IMPERIAL COLLEGE LONDON

ULTRASONIC INSPECTION OF HIGHLY ATTENUATING MEDIA

by

Mr. Jack Samuel Egerton, MSci., ARCS

A thesis submitted to the Imperial College London for the degree of
Doctor of Engineering

Department of Mechanical Engineering
Imperial College London
London SW7 2BX
UK

April 2018

Declaration of Originality

The entire content presented in this thesis is the result of my independent research in the past four years under the supervision of Professor Mike Lowe and Doctor Peter Huthwaite. I have provided appropriate references wherever required in the thesis.

Jack Samuel Egerton 28/03/2018

Copyright Declaration

Abstract

The aim of the project was to improve the ultrasonic array inspection of high-density polyethylene (HDPE) heat-fused pipe joints of cooling water pipework that is installed in EDF Energy's nuclear power stations. Whereas ultrasound array inspection is now established for safety-critical metal components, HDPE poses a hugely challenging problem, that the ultrasound waves are heavily attenuated by the material. This impacts multiple aspects of the inspection and of the modelling that is needed to design and qualify inspection. The thesis reports a range of research that was needed to overcome this challenge.

The work of the thesis has:

- obtained accurate acoustic properties of HDPE that are necessary for improved simulated or real ultrasonic array imaging of HDPE pipe joints
- developed a simulation technique for representing ultrasound in such inspections that has both high accuracy and efficiency
- extended analytical analysis of ultrasound scattering from cylindrical voids from elastic media to general, attenuative media
- used the Huygens-Fresnel principle to represent ultrasound scattering from volumetric and planar voids, to image sub-wavelength features of these defects in an ideal circular array setup, and to image angled ultrasonic array nondestructive evaluation (NDE) of potential defects occurring in HDPE pipe joints
- devised an automated and antidispersive system for reducing coherent and incoherent noise in waveforms with an isolated wave reflection signal
- produced an imaging and analysis method for ultrasonic array NDE that can represent defects in a refractive, reflective, and scattering environment in attenuating media, which is applied to data from the above developed simulation technique
- applied much of the above imaging and analysis method to defects machined into HDPE pipe material, with an experimental ultrasonic array controller, yet with an array of limited suitability
- specified parameters for ultrasonic arrays and a water-filled wedge, which are optimum for HDPE pipe joint inspection, and have been designed and built by Imasonic SAS, France, for research use at Imperial College London

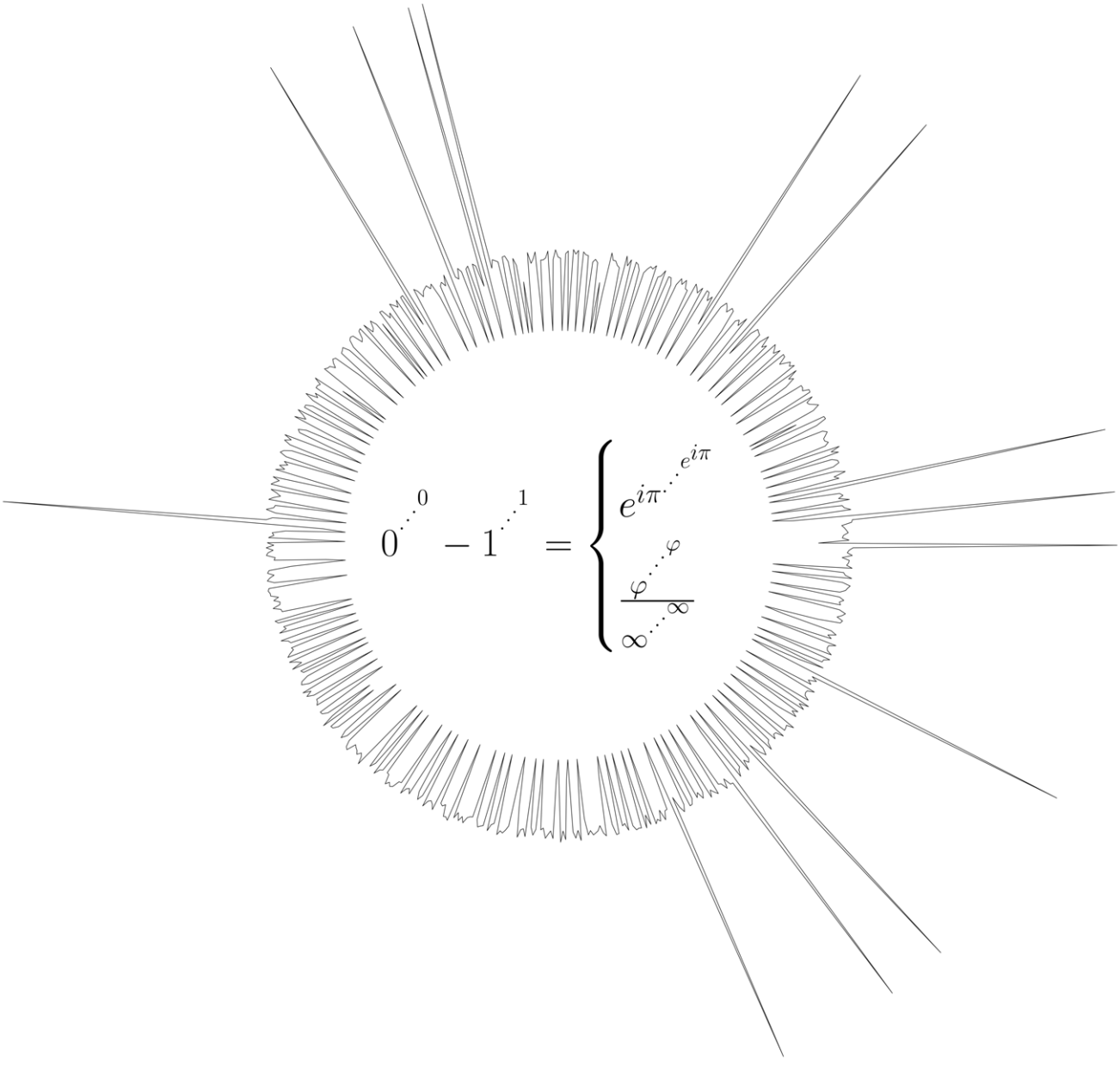
$0^{\cdot^{\cdot^{0}}} - 1^{\cdot^{\cdot^{1}}} = \begin{cases} e^{i\pi^{\cdot^{\cdot^{e^{i\pi}}}}} \\ \varphi^{\cdot^{\cdot^{\varphi}}} \\ \overline{\infty^{\cdot^{\cdot^{\infty}}}} \end{cases}$

Acknowledgement

I would like to thank everyone who has contributed to the four years of my Engineering Doctorate with Imperial College London and EDF Energy. These include, in an organic order,

Mike, for his contribution, not only my to project and time so far in the NDE Group, but also to ensuring the group always operates as intended. Peter H, for the right guidance at the right time on many elements of my work. Tariq, for proposing the project and getting everything up and running, also with much initial help from Harshad. Thank you also Tariq for introducing me to the Offshore Wind team of EDF R&D UK Centre – my placement there with you all was a great experience, and thanks to Erwan, Ellen, and everyone at Croydon. Harshad, thank you for getting me into Torness for the outage so I could see many of the inspections first hand, and for the time observing the trial inspections with Doosan at AMEC. Thank you John for taking up the role of my third industrial supervisor and thank you for organising the data collection with TWI.

For ensuring that the EngD scheme was possible and that the courses were useful and engaging, thank you Chris and Keith. All course lecturers helped ensured that this was the case. For those extra hours at each course, where we found plenty of joy in exploring the towns and cities where our fellow RCNDE members are based, thanks to the EngD 2013 cohort and other cohorts. The same for all who I have enjoyed time with at QNDE and other conferences.

Thank you to the NDE Group members for work and social events – five-a-side, go karting, many discussions over a beer or two at Eastside, and much more. Thanks to some of the senior members and group alumni for welcoming us all. Thank you Anton for a lot of significant help with experiments and simulations. Peter C and Fred for your major contributions to the lab, also. Thanks for the great annual dinners, Peter C. Nina, for ensuring so many things operated as they should.

Relating to some key aspects of work and progress, Julio, Fred, and Gabor were very kind in allowing us trial use of the experimental array controller they developed. Thanks very much Julio for the data acquisition help. This provided positive results. James, for his Introduction to Abaqus notes. Wonjae, for a useful Python script that worked well with Abaqus simulations. Craig and Plasflow, for all the help producing

our representative defective HDPE pipe joints. Romain, Frederic, and everyone at Les Renardières and Chatou, for highly constructive HDPE inspection discussions and pipe samples. At Doosan, thank you Colin, David, and Kathlene at Doosan, for industrial guidance. For academic guidance, thank you Peter N, Richard C, and Tony M. Thank you Miles, Phillip, and co. at TWI for your help with UT and CT data collection. Ruth and Paul, for optical transmission microscopy help. Suresh, for much help getting C-T samples made. Maria, for the People in NDE, BINDT interview. Thank you Fan for the thesis template.
Thank you again, all who have contributed, and apologies to anyone I may have missed.

Specific acknowledgements and thanks relating to published and submitted articles are as follows,

Improved FE simulation of ultrasound in plastics

The authors acknowledge EPSRC and the UK Research Centre for NDE (EPSRC grant no. EP/L022125/1) for funding this work. P. Huthwaite is funded under EPSRC grant no. EP/M020207/1.

Ultrasonic attenuation and phase velocity of high-density polyethylene (HDPE) pipe material

The authors acknowledge EPSRC and the UK Research Centre for NDE (EPSRC grant no. EP/L022125/1) for funding this work. P. Huthwaite is funded under EPSRC grant no. EP/M020207/1. The authors thank Dr. Edward Cohen of the Imperial College London Statistics Group and Dr. Kostas Zaragoulidis of the Imperial College London NDE Group for their advice on neural networks and multiparameter regression.

A multiband approach for accurate numerical simulation of frequency dependent ultrasonic wave propagation in the time domain

The authors acknowledge EPSRC and the UK Research Centre for NDE (EPSRC grant no. EP/L022125/1) for funding this work. P. Huthwaite is funded under EPSRC grant no. EP/M020207/1.

Analytical simulation of viscoelastic ultrasonic bulk longitudinal and shear wave scattering from heterogeneities using Huygens principle, demonstrated with image reconstruction of sub-wavelength features and nondestructive evaluation of high-density polyethylene pipe joints

The authors acknowledge EPSRC and the UK Research Centre for NDE (EPSRC grant no. EP/L022125/1) for funding this work. P. Huthwaite is funded under EPSRC grant no. EP/M020207/1.

Automated and antidispersive coherent and incoherent noise reduction of waveforms that contain a reference signal

The authors acknowledge EPSRC and the UK Research Centre for NDE (EPSRC grant no. EP/L022125/1) for funding this work. P. Huthwaite is funded under EPSRC grant no. EP/M020207/1. The authors thank Dr. Glenn Jones and Dr. Artem Kashubin of the Mechanical Engineering Department of Imperial College London for discussing with us relevant procedures within the fields of geophysics and seismology.

Numerical simulation of ultrasonic NDE of sound-damping materials using a multi-band time domain approach

The authors acknowledge EPSRC and the UK Research Centre for NDE (EPSRC grant no. EP/L022125/1) for funding this work. P. Huthwaite is funded under EPSRC grant no. EP/M020207/1. The authors thank Mr. Sam Horne of the Mechanical Engineering Department of Imperial College London for suggesting an expanded solution to equation (7.7.4). The authors thank Dr. Richard Phillips and Dr. Fan Shi for discussions about their developments of hybrid simulation techniques.

Contents

List of Figures

Chapter 1

Introduction

1.1 Overview

EDF Energy is one of the 'big 6' energy providers in the UK. All 8 of EDF Energy's nuclear power stations in UK and potentially some in mainland Europe may be affected by the outcomes of this project. EDF Energy, similar to some nuclear energy organisations in the US and Europe, is currently undergoing a phase of replacement of much of its cast iron pipework with high-density polyethylene (HDPE). Some of the pipework is in safety-critical regions of the nuclear island (the immediate surrounding area enclosing a nuclear power station) where failure of the pipes could be highly undesirable and consequently safety standards are very high. HDPE pipe welds, necessary during manufacture and installation, are the most common regions of localised reduced pipe strength because of the potential existence of defects within the weld volume. It is therefore necessary, and consequently required by national and international safety standards, that reliable NDE is performed on current and future HDPE pipe installations in nuclear power stations. Currently, the majority of reliable NDE inspection techniques have been developed and optimised for use on metals and composites, with HDPE and other plastics requiring more work. Consequently, this Imperial College London Engineering Doctorate (EngD) project involves the modelling of phased array ultrasonic testing and other improvements to the inspection of HDPE welds. It should increase NDE inspection reliability in a cost-effective and efficient way when compared with current methods of extensive or exhaustive destructive and nondestructive evaluation of potential defective pipes.
This introduction first covers the context and motivation for the EngD research

project from the industrial context of EDF Energy and its use of HDPE in replacement of cast iron pipework in its nuclear power stations in the UK. Next, a review of the relevant literature covered to date is presented, including the pros and cons of HDPE pipework, welding procedures, weld failure mechanisms, destructive evaluation of welds, representative fabricated HDPE joint defects, nondestructive evaluation of welds including traditional visual and surface inspections as well as high sensitivity volumetric NDE, the relevant acoustic properties of HDPE, and current relevant examples of modelling of ultrasound applicable to HDPE joints.

1.2 Industrial Context and Motivation for Research

EDF is a large international energy provider based in France of which EDF Energy is the UK subsidiary and one of the 'big 6' energy providers in the UK. EDF Energy provides the large majority of the UK's nuclear energy from its 8 nuclear power stations (of the 9 in the UK) situated throughout the country.

EDF Energy is undergoing a significant overhaul of the pipework used in its nuclear power stations from cast iron to high-density polyethylene (HDPE). Although there are many benefits to using HDPE, discussed in section 1.3, if produced to a substandard quality, the butt fusion welds joining HDPE pipes can be a point of reduced strength and so a potential location of pipe failure. Consequently, Doosan Babcock has worked with EDF Energy to develop a nondestructive evaluation (NDE) technique using a phased array ultrasonic testing (PAUT) probe, detailed in section 1.3.9, for detecting certain defects which may potentially occur in butt fusion joints. The present pipework replacement does not include any safety critical pipework within the nuclear island but there is much drive towards these replacements also being made in the UK, Europe, and the US (see section 1.3). If this occurs, further need of validation of the PAUT inspection technique will likely be required.

Validation on this scale can be expensive and so it is more cost-effective to experimentally validate only certain cases of importance, which may be bounding cases or cases of specific significance. In conjunction, it is necessary to create a tool for modelling PAUT inspection of HDPE that, after validation using the experimental cases, can be straightforwardly and reliably applied to all other important cases. Before this EngD project, no such modelling tool existed for ultrasonic inspection of HDPE, so its development is a valuable contribution to this area of inspection.

This project benefits from relevant and potentially applicable developments existing in recent NDE technology, operation, and data analysis. This work also contributes to a wider body of understanding required to develop rejection criteria for flawed fusion joints, such that sentencing can be performed with more confidence and less wastefulness than the default approach used where no criteria exist, whereby all pipe sections containing joints deemed potentially defective with established NDE methods must be removed and replaced at significant monetary and time cost to EDF Energy.

In early project reports, the aim was stated as follows, "By the end of this EngD project the aim is to have developed a fully functioning modelling tool of ultrasound from a phased array probe in HDPE that draws upon research into the acoustic properties of HDPE, the way in which ultrasound from a phased array probe propagates in HDPE, and the way the wave interacts with defects experienced in HDPE butt welds such that predictions can be made that lead to faster, more reliable defect characterisation and sentencing."

1.3 Literature Review

1.3.1 HDPE pipework – justification for use and associated problems

Existing cast iron pipework used in EDF Energy's nuclear power stations is susceptible to corrosion, fouling, and microbial attack [1–9, 11–13]. They consequently require continual replacement and maintenance [14]. Along with the above issues, the labour costs for installing and maintaining cast iron pipes can be 10 times greater than for HDPE, the material considered the best alternative [15]. The 2012 global annual production rate of plastic pipes was 7.5bn metres and the projected growth from then until 2017 is expected to be 8.5% [1]. Similarly, in the nuclear power industry significant amounts of HDPE pipework are being installed to replace existing cast iron pipes. This is occurring in the UK with EDF Energy, mainland Europe, the US, and elsewhere because of the many benefits of HDPE over conventional pipework. Unlike cast iron, HDPE is not susceptible to the above issues and has a longer predicted service life, is cheap, lightweight, flexible, and relatively straightforward to install [1–9, 11–13]. One other important advantage of many is

that HDPE removes the need for rubber ring joints used with other pipework, as these are often a source of degradation and leakage [16]. Some potential problems include, sensitivity to UV radiation, thermal expansion, low operating temperature, and being susceptible to cracking stress [4]. Although EDF Energy does not bury its pipes in the UK, the pipes are often under roof cover so UV is not a concern. The pipes also contain 2.5% carbon as an industry standard, which is employed for UV protection. Given the merits outweigh the few demerits, it is suggested that the increased reliability achieved through introducing HDPE pipework will reduce the nuclear reactor core damage frequency (CDF) [3] a key figure of merit for nuclear safety.

HDPE pipework has already successfully, and in many cases extensively, been installed for transporting water, gas, sewage, chemicals and hazardous substances, and water in non-safety-critical nuclear applications [4, 17–19] with few failures in low temperature and pressure applications [15]. Recent efforts have also been made to introduce HDPE pipework for safety-critical applications within the nuclear island by EDF Energy in the UK. In the US, two major plants, AmerenUE's Callaway plant and Duke Energy's Catawba plant, have introduced HDPE for use in safety-critical applications [11]. This has been done subject to approval by the Nuclear Regulatory Commission (NRC) but with conditions to be met concerning the fabrication, NDE, and qualifications of procedures, equipment, and personnel [19]. The permission was granted in agreement with the American Society of Mechanical Engineers (ASME) Code Case N-755 concerning the use of Class III (safety-critical) HDPE pipes [20], for example those in figure 1.1. The design temperature of 60°C [20, 21] might be exceeded in Class III applications and so a higher grade of HDPE (PE-4710) used

Figure 1.1: HDPE pipes with complex geometry butt welds in power plant [15].

in Europe was adopted by the US to increase the safe operating temperature [19]. Further concern regarding fusion weld integrity is raised through the use of larger pipe diameters which may be more susceptible to brittle failure because of slow crack growth [22]. Thicker pipes have also been shown to be more sensitive to flaws present in the welds [23]. EDF Energy's Sizewell B pressurised water reactor (PWR) has installed HDPE pipework for the safety-critical service water system but is running at suboptimal temperatures to remain below the HDPE design temperature [19].
The ASME Code Case does not specify a favoured reliable NDE technique for inspecting weld flaws because more work is necessary to support and advance the high probability of detection (PoD) and low false call rate of volumetric methods [19, 20] such as the ultrasonic and electromagnetic radiation techniques covered in section 1.3.9. Being limited to considering only commercially available NDE solutions further reduces choice [17].
The benefits of fusion welding include a permanent flow-efficient and economical weld [8] and the ability to fuse long sections of pipe, which reduces the monetary and time cost of welding relative to other equivalent pipe installation and welding [24]. When produced correctly a heat fused HDPE weld can be as strong as the extruded pipe material [15, 24]. To minimise the number of defective welds, PE manufacture is very strictly regulated [15, 25] but the welding procedure is only semi-automated so operator error can still occur [26]. Also, use of the incorrect parameters for a given weld shape and size as well as machine faults can lead to systematically flawed welds.

1.3.2 Butt fusion welding procedure

EDF Energy has chosen and favours butt fusion, or butt welding, as its chosen HDPE jointing process, over alternative methods such as electrofusion. HDPE butt welds are produced in a butt welding machine, for use in EDF Energy's nuclear power stations, as follows [15, 24, 27, 36]:

1. two HDPE pipes are clamped with their ends aligned
2. the sawn pipe ends are planed smooth
3. the pipe ends and the heater plate may be cleaned with an alcoholic spray

4. the heater plate is brought between the two ends (figure 1.2) which are brought together and pressure is applied until a small weld bead forms

5. the pressure is removed but contact is maintain during a heat soak period

6. the heater plate is then removed, resulting in temporary exposure of the melted ends during the dwell period

7. the ends are slowly brought together again and the pressure is gradually increased until the full bead forms

8. the pressure is maintained for an extended welding and cooling period

9. the inner and outer weld beads may be optionally removed using a manual run-around planing tool or power planer

Including the final debeading step, these are the standards adhered to by Plasflow plc., EDF Energy's chosen HDPE heat fusion weld manufacturer. Debeading is performed to prevent invertebrates or plants being trapped in certain pipework sections that can occur near seawater or freshwater inlets [36] as well as reduce the risk of high shear stress on the weld from the high pressure flow. As further quality control, at the beginning of a welding session a dummy weld can be produced to remove fine contaminants from the heater plate.

Figure 1.2: HDPE pipes (∼500mm diameter) with heater plate between in butt fusion process at Plasflow plc.

1.3.3 Butt fusion weld potential defects

Despite the benefits of using HDPE pipework, as with cast iron there are also potential problems that can occur and defects that can arise in butt fusion joints during manufacture. These defects occur around the whole circumference of the pipe and are aligned radially parallel to the fusion surface [7], as shown in figure 1.3. In butt welds lack of fusion (LoF) is the most probable defect that can arise [2]. It is a planar region (that is defined as having no extent in the axial direction) between the welded pipe end surfaces where fusion has not occurred. LoF is generally caused by the fusion temperature being too low, pressure being too high, fusion time being too short, misalignment of the pipe ends, or planar contaminant inclusions on the pipe end surfaces. Often caused by similar but less extreme conditions than LoF, cold fusion is the incomplete crossing of polymer bonds within the HDPE weld [11, 19, 33]. Similar to LoF, cold welds, formed in the same plane as LoF, can be significantly weaker than an optimal weld [11, 26, 34]. Inclusions are a concern when producing butt fused welds. These are contaminants that enter the weld during the dwell period when the pipe ends are exposed and partially melted, but also after the planing stage when the pipe ends are electrically charged by the planing, thus attracting fine airborne particulates [24]. Other larger inclusions such as dirt, grit, or grease can also contaminate the pipe ends [2, 24, 35]. Inclusions are a concern because they can create volumetric voids in the weld that can grow under long-term fatigue loading [24]. Because of the way the bead forms in butt fusion, in the rare case where welds are defective, contaminants will often exist within roughly the inner and outer thirds of the through-wall thickness [36, 37] because the heated surface is stretched into the bead but not squeezed out entirely [38]. The probability of all major contaminants being squeezed into the weld bead is also significantly reduced for thicker pipes [16].

The environment in which butt welds are produced has a significant impact on the number of expected flaws. Producing welds in controlled factory conditions is favourable compared with the unavoidable environmental effects experienced on site [24]. For example, welding is often carried out at the same time as other work that produces contamination, such as sources of cement dust and other fine particulates. On site butt welds are often produced in small trenches where dirt and other contaminants can easily be introduced to the weld. It is common for on site

butt welding to be performed in tents, which helps reduce some of these factors. Well trained operators who are encouraged to follow all procedures correctly and well maintained fusion equipment will also improve the quality of on and off site welds [8, 12, 24, 25].

In general, to reduce the number of flawed welds produced, essential fabrication variables need to be better understood and optimised based on pipe properties [19]. For example, a given pressure specified in the US ISO standards can be approximately triple that of the recommendation in the UK ISO standards [27]. This is suggested to cause a higher rate of cold fusion and lack of fusion in welds in the US by forcing too much melted pipe out of the weld. Despite continual efforts to understand the causes of flaws and improve the procedure accordingly, at present it is not possible to ensure all butt fused joints are produced without flaws [16, 28] and so efforts to detect and characterise these flaws must be made to prevent pipe failure and improve quality assurance [1, 3, 36]. Furthermore, the larger HDPE pipes necessary for nuclear applications are more difficult to weld because of stricter tolerances on dimensions, complications when preparing the pipe ends, and the lack of agreed parameters for these pipes [13].

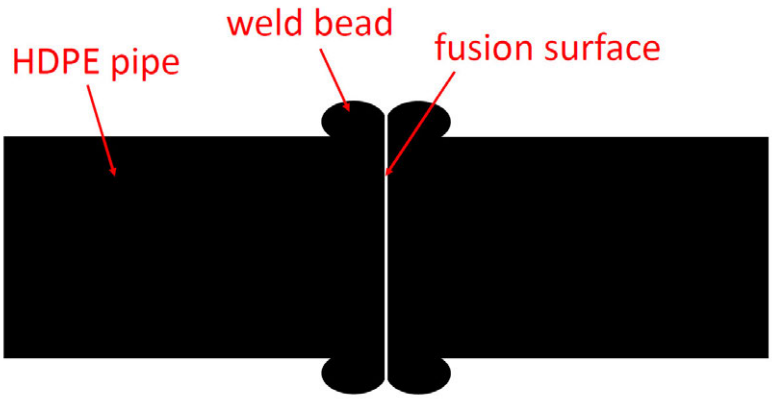

Figure 1.3: Depiction of cross-section in through wall radial-axial plane (fixed circumference) of upper half of a butt jointed HDPE pipe showing the fusion surface where known potential manufacturing joint defects occur.

1.3.4 Electrofusion welding procedure

The other major way HDPE pipes can be welded, which is not currently used by EDF Energy, is electrofusion [1, 4, 12, 26], where two pipe ends are fused within a larger diameter coupler covering the joined pipe ends, shown in figure 1.4. The

process is as follows [9, 28, 29]:

1. the pipe outer surfaces which are fused to the coupler are scraped to remove oxides

2. the two pipes may be optionally clamped to improve fusion contact surface area

3. the two pipe ends are forced together in the coupler until they meet internal plastic stops

4. a current is passed through coiled wires in the coupler to heat the coupler and pipes, bringing them into contact via thermal expansion

5. further resistive heating in a heat soaking period occurs to locally melt the coupler and pipe surfaces

6. as the joint cools, fusion occurs

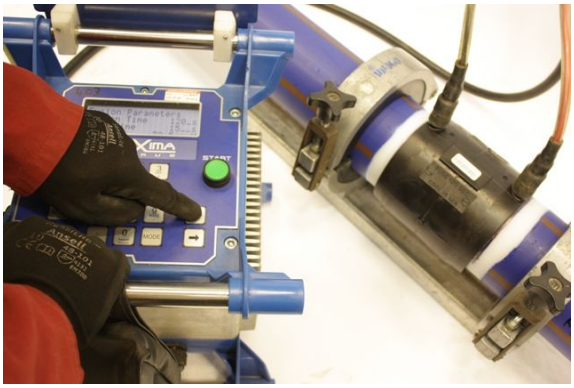

Figure 1.4: Electrofusion welding procedure. Coupler containing heating wires is connected to external current supply. [30]

1.3.5 Electrofusion weld potential defects

In electrofusion, flaws can occur such as lack of fusion between the coupler and the pipe ends, cold fusion, and voids around the heating wires (see figure 1.5). As with butt fusion, the flaws occur along the fusion surface, which is in the axial direction for electrofusion [7], with the exception of the volumetric flaws that are local to the heating wires. Electrofusion defects can be caused by pipe misalignment or lack of penetration (LoP) where the pipe ends and not in contact with the plastic stops in

the centre of the electrofusion coupler, resulting in potential bunching of the heating wires that leads to shorting and local overheating [39]. Many of these defects can also be caused by using the incorrect heat cycle [9] or not completely scraping the oxide layer off the pipe end surfaces [4, 28]. In electrofusion, operators may rely on barcodes attached to the couplers for the correct fusion parameters but these can potentially be misread or the wrong barcode scanned [4]. HDPE pipes often have a slightly oval cross-section, which is especially pronounced in larger pipe diameters. This can lead to a high probability of flawed welds because of the incomplete contact between the coupler and pipe ends, but the risk of this can be reduced by clamping the joint during electrofusion welding [39].

Similar to butt welds, producing electrofusion welds on site significantly increases the risk of contamination via environmental influences. The fusion surface is larger in electrofusion than butt fusion and so more care must be taken to ensure minimal levels of weld contamination.

1.3.6 HDPE joint failure mechanisms

The effect of many of the flaws in heat fused HDPE welds is to increase the probability of failure via fracture when slow crack growth reaches critical levels. This failure occurs earlier for larger initial defect sizes and so the critical defect size that a viable NDE technique needs to detect can be defined based on an expected failure

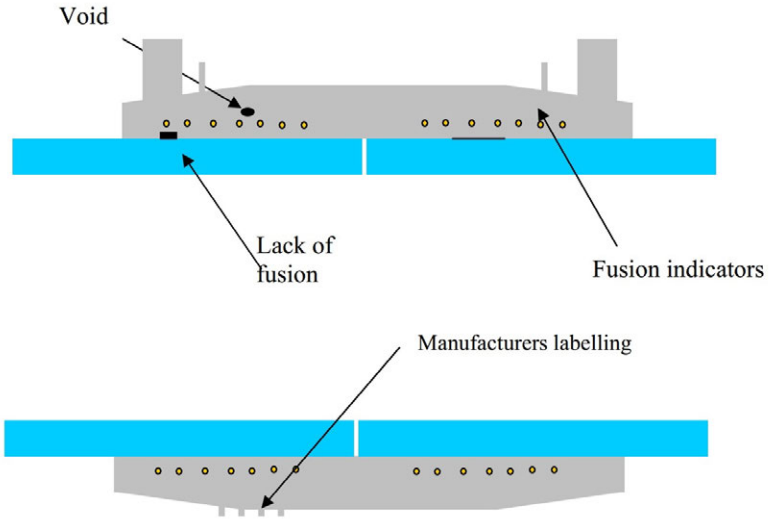

Figure 1.5: Depiction of cross-section in through wall radial-axial plane (fixed circumference) of electrofusion welded HDPE pipe showing the locations of known potential weld defects [9]

at 50 years [1, 16].

If HDPE is subject to high stress it is most likely to fail in a ductile manner where a significant amount of plastic deformation occurs. If lower stress is applied but for a longer time, small cracks slowly grow larger until large surface areas yield at once via brittle failure with low plastic deformation [1]. The existence of defects in HDPE welds allows for potential slow crack growth to occur and for the pipe to fail prematurely in a brittle manner [16, 24].

1.3.7 Destructive evaluation of HDPE welds

Flawed HDPE welds can be evaluated destructively in a number of ways to confirm how influential that flaw would be on the service lifetime of that weld as well as to determine material characteristics of different regions of the failed weld. It is impractical and expensive to run tests for multiple years on HDPE pipes, for example running a constant pressure test for that duration, and so fracture mechanics can be used to extrapolate failure times for higher pressure or cyclic fatigue tests [1]. In this way it can be meaningful to run tests where the part fails in a number of days or hours. These can, for example, be performed on multiple sections from the circumference of the weld to build a complete picture of the failure mechanism. As well as destructive tests performed on defective welds, certain mechanical tests can be performed on HDPE pipes before they are installed. For example, hydrostatic tests are often performed, which involve flowing water through the pipe at a minimum of 1.5 times the design pressure of the pipe [35, 42, 43]. These tests do not predict long term performance of the welds but can eliminate highly defective welds before installation. A less extreme flaw such as cold fusion would not generally be detected by hydrostatic testing [12].

Whole pipe or specimen (circumferential section) creep tensile rupture tests of HDPE butt welds (see figure 1.6) can be performed to determine the influence of planar flaws [16, 21, 35]. The latter is more common than whole pipe tests as more tests can be performed on circumferential sections and simpler apparatus can be used. However, whilst being more expensive, performing whole pipe tests removes the need to extrapolate the failure characteristics of sections to that of the whole pipe, which include factors such as residual stresses in the pipe [21]. It is suggested that in destructive testing of HDPE, approximately 30% of welds should be under low

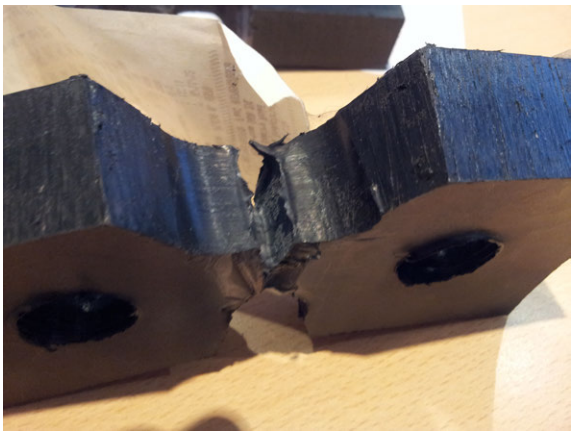

Figure 1.6: HDPE butt weld tensile test failure in a both brittle (large central region of weld) and ductile (edges and bottom) manner at Plasflow plc. The brittle failure is a cleaner break with less extension of the polymer chains than the ductile failure.

enough stress but for a longer duration such that they experience brittle rather than ductile failure. However, this process can still be sped up via surfactant solutions [21]. When performing tensile tests the force applied or the displacement resulting from a given force can be measured to determine the weld strength [26]. With knowledge of the stress applied and the strain measured, the tensile energy to break (TEB) can be determined and equivalently used as a measure of weld strength [24]. Visual analysis of the separated weld determines which parts fail in a brittle or ductile manner, where brittle failure suggests a weakened defective joint.

Although tensile tests do have value, it has been suggested that side-bend test results for butt welds may correlate better with the true brittle or ductile nature of the weld section [19]. A side-bend test, as the name suggests, involves bending both sides of the weld in the direction where the through-wall edges are in tension or compression about a central column located at the weld. Bend tests are also said to be good at measuring the strength of brittle materials [44], which are of concern here. By the nature of bend tests (though not for the side-bend tests mentioned above) it is clear that the highest stresses are near the inner and outer pipe surfaces where compression and tension occur respectively, rather than in tensile testing where stress is equal throughout the cross-section. Bend tests can therefore concentrate stresses where flaws are more likely (as covered in section 1.3.3) and also where real stress concentrations occur when the pipe is in operation because pressure is radial.

As the fusion surface of electrofusion welds is different, so are the destructive tests. Some of the common tests include crush/decohesion, peel, long-term creep and

hydrostatic pressure tests [9, 21]. The crush test involves applying a pressure to the weld and recording the pressure it fails at, where the failure occurs, and the appearance of the defect [45]. Peel tests involve cutting circumferential sections of the electrofusion weld and applying tension at one end and recording the force required to peel apart the two fused layers as well as analysing how brittle or ductile the failure was and locating any potential defects. Creep tests involve a constant stress where the strain is the measured variable. As covered above, hydrostatic tests involve flowing high pressure water through the pipe to potentially induce failure. Other material tests of welds include taking sliced cross-sections through the weld and analysing them with an optical transmission microscopy (OTM) setup or equivalent. The material structure and expected differences observed for welded material, unwelded material, and flawed material can provide information on the acoustic properties and failure mechanisms of HDPE welds [12]. Similarly, a simple smoothed cross-sectional slice of the through-wall of the weld can provide information about macroscopic features such as LoF [34, 35]. To improve this technique, thin slices ($\sim$30μm) can be cut using a microtome, similar to the first technique, but then visually analysed for evidence of LoF and other defects [19].

1.3.8 Representative defects in butt welds

To improve the capabilities of nondestructive and destructive evaluation techniques a combination of real and fabricated representative defects must be analysed. Real defects are valuable because they are produced via real failure in the production of the weld by equipment, operator, or both. The downside is that real defects are often not repeatable or cannot be controlled in terms of level or type of inclusion. Beneficially, real cold welds and LoF can generally be repeated because the parameters input into the fusion apparatus are often retrievable when produced in factory conditions. However, when trying to recreate the same weld using the same parameters there is no guarantee that the same degree of LoF or cold weld will occur. This can be somewhat alleviated by the production of many welds using the same parameters. Fabricating welds with inclusions is more challenging. For example, representative inclusions have been produced using talc to represent fine particulates [16, 24, 33], sand for coarse particulates [16, 24], and mineral oil and WD-40 [33]. Talc particles are very small ($\sim$15μm) so they represent fine airborne particulates. Also, they do

not polymerise and the melting point is much higher than the fusion temperature, so they are a good choice for this type of contaminant [33]. Talc is difficult to detect directly using ultrasonic testing (UT) as particle scattering is weak for diameters less than 1/10 wavelength [32]. Mineral oil is a useful liquid contaminant because it is does not polymerise. Similarly, nor does WD-40 [33], yet its high boiling point means it will not form volumetric voids as might be expected for other liquids.

Representative flaws must be controlled and repeatable. Techniques for producing these flaws vary between experiments but many emphasise the need to control volume of applied inclusion. The degree to which the volume is controlled varies significantly. Examples include using a fan with variable speeds to blow particulates onto the pipe ends [24]; using a paintbrush to apply heavy, medium, and light quantities that were compared with controlled samples to estimate contamination [16]; and cutting square holes of known dimensions in the pipe ends then adding weighed quantities of inclusion material, yet this approach was applied only to an alternative process to conventional butt fusion [33]. Also, cutting square holes itself alters the weld integrity in a way uncharacteristic to real defects.

Other inserted materials include thin aluminium discs [16, 23, 47] and solid stainless steep oval inserts [36]. Thin aluminium discs are useful for representing planar flaws but may become warped or displaced from the weld. This can also be the case when using PTFE tape to represent planar flaws [36]. One way to help maintain the position of the insert is to use an adhesive [16] but this may alter the defect characteristics. While steel inserts are useful for ultrasonic NDE, and potentially other techniques, as they do not deform, they are also useful in representing tip diffraction, detectable from real defects. This is because their oval shape means the diffracted signal is conservatively small and therefore not larger than that of a small defect. Using steel also means a lower difference in sound speed than that of an air gap [36], again showing a degree of conservativeness. Their high thickness means these flaws cannot be considered planar.

By varying fusion parameters such as temperature, pressure, and time of different steps in the fusion process, cold welds can be produced to varying severity. As mentioned above, using the same parameters does not necessarily lead to cold fusion or LoF with the same area but repeating the process multiple times can reduce the problem of variability. To create partial or complete lack of fusion any combination of reduced heating time, reduced temperature, or excessively high or low pressures

can be used.

There is value to producing calibration blocks from HDPE with side-drilled holes and slots of known dimensions [36, 40]. They do not represent real defects but are highly controlled in terms of size and shape and so an inspection standard can be formed. These regular, repeatable, simple geometry flaws are a useful first test for a model of NDE of HDPE as they are straightforward to implement and unambiguous to analyse. From this basis, more complicated geometries can be characterised with increased confidence.

1.3.9 Nondestructive evaluation of HDPE welds

Visual evaluation

Many traditional NDE techniques have limited to no applicability to HDPE fusion welds. For example, dye penetrants are useful in locating some surface flaws but in HDPE welds the majority of flaws are located within the volume of the weld and some important flaws such as cold fusion and LoF are planar with minimal through-wall thickness and so the dye cannot penetrate even surface flaws [1, 19].

Some tests can be performed at the point of weld production. For example, while the weld bead remains on the weld it can be visually analysed to ensure the bead appears qualitatively correct based on its height, width, whether the beads, pipes, or both are misaligned, whether it has made contact with the pipe, and whether it is uneven around the circumference including bead shape or voids in the fusion zone [15, 19, 21, 40]. During debeading any brittleness or separation of the bead may suggest a similar situation internally. The removed bead is often subject to a bend back test where it is bent against its curvature to determine if there is any inclusions or gross LoF evident, similar to the previous technique [16, 21]. For thicker pipes the chance of contaminants passing into the weld bead is significantly reduced, as covered in section 1.3.3.

Many of the visual tests, bend tests, and also hydrostatic testing were directly transferred from analysis of steel welds but are not necessarily directly transferable to testing of HDPE welds, which are very different in many ways [48]. It is the lack of reliable NDE in the past that has maintained the dominance of visual and other non-volumetric NDE techniques [49].

A case study on the reliability of visual NDE determined that of 132 HDPE field

samples there was a 19% false acceptance and 63% false call rate [50]. However, this was compared with ultrasonic time of flight diffraction (TOFD) ultrasonic testing (UT) not mechanical testing, so there would be some discrepancy still between the TOFD and the real flaws.

Visual tests are useful for detecting some highly flawed welds (to the degree that they may fail a hydrostatic test) at the time of production. They are simple and have some success but have a low probability of detection (PoD) and significant false calls [19, 50]. Because of the safety concerns and stringent requirements placed on the use of HDPE in safety-critical nuclear applications, there is urgent need for reliable, high quality NDE [13, 19]. Specifically, volumetric NDE can be the solution to many concerns including saving costs associated with pipe failure or incorrect replacement, saving time via automated data capture, quality assurance, detection of internal flaws, the ability to perform the inspection on site or in controlled conditions, and the potential to perform the inspections whilst the pipe is in operation, thus dramatically reducing the costs to time and money associated with ceased operation [50]. Modelling must also be performed to corroborate experimental data with theoretical expectations and other existing data without the time and monetary costs of running many more tests to cover all likely cases of defective welds. Validation of NDE techniques by this approach helps ensure they are made reliable as soon as possible.

Near-infrared imaging (NIR)

Unlike thermographic imaging, Near-infrared imaging (NIR) relies on the transmission of radiation in the 700-900nm range and is most applicable to materials with low electrical conductivity [51]. As mentioned above, this includes HDPE. NIR can be performed using cheap, readily available hardware that is already commercially available and compact in size. As well as measuring amplitude transmission through the material thickness, by using a range of transmitted wavelengths, absorption spectra can be generated and compared with known spectra to potentially determine the chemical composition of the absorbing region [51]. If a crack formed in a HDPE pipe that allowed water to enter via the inner or outer face then the absorption spectra of water could potentially be used to detect this. However, optically dark materials, such as black HDPE pipes used by EDF Energy, which contain 2.5% carbon, may be

more difficult to apply NIR to [51]. HDPE pipes are also produced in other colours such as yellow, blue, and white that do not contain carbon. These could potentially be used in nuclear applications as well as the conventional black pipes.

Radiography

Radiographic NDE involves passing x-rays through a material that are detected on an imaging screen that plots the amplitudes of the transmitted rays in a greyscale 2D image or otherwise via film that is exposed by the rays. Applicable to both digital and filmed-based radiography, the higher the density and thickness of the material the x-rays pass through the more they are absorbed by the material and so the lower the amplitude of the measured ray. Using this variation in transmission, an image can be composed of areas where there is a notable change in density through the thickness. The contrast variations of the image are based on the average absorption through the thickness that the ray has travelled through and so no depth measurements can be made without multiple tests at different angles that are then used to build up a 3D CT (computed tomography) image via a suitable reconstruction algorithm. This approach allows better defect characterisation since, subject to the resolution of the system, the full 3D shape of any defect can be produced.

Because radiography is based on averaging through the thickness, it is best suited to flaws aligned with their greatest extent being radial. This is the case for planar flaws such as LoF in butt fused welds, yet the very small through-wall thickness of the flaws makes these flaws hard to resolve and highly dependent on the angle of the x-rays from the source [52]. It is clear physically that a small displacement of the source from perpendicular to the pipe surface will result in a large reduction in variation in x-ray absorption compared with the unflawed material because the beam is passing at an angle through the planar through-wall thickness not the tip to tip extent of the flaw. This amounts to a significant drop in image contrast. Volumetric flaws are less dependent on the incident angle of the x-rays and so can be reliably detected provided the absorption of the flaw deviates detectably from the absorption of the parent material. This means larger pipe diameters are more challenging for radiography.

Radiography is less feasible for electrofusion HDPE welds than in butt fusion welds discussed above. This is because many of the flaws are planar in the axial direction

whilst inspection is radial. Also, the volumetric flaws and voids that may otherwise be detectable can be obscured if near the metal heating wires, which themselves have a strong radiographic contrast to the parent material [1].
Although 3D CT of HDPE would require about 20% of the intensity necessary in steel, because of HDPE's lower density, the technique is still costly in terms of time to perform the multiple shots required for large pipe imaging and the time lost for health concerns as local evacuation occurs when tests are conducted [21].

Microwave interferometric method

This approach uses the change in the relative permittivity between flaws and the HDPE pipe. Microwaves are reflected from flaws because of the change in refractive index at the boundary, much like in ultrasonic NDE [12, 52, 53]. The image received is a combination of spatially varying voltage drops based on the interference of the transmitted and received wave. There are two receivers in a pulse-echo configuration with a microwave path difference of 1/4 wavelength. This allows the feature to be resolved via interferometry [37].
The technique was developed at a time when ultrasonic testing of attenuative plastics was considered infeasible [52]. It is highly sensitive to flaws (and inspection surfaces) containing water [7] because the microwaves are at the frequency of the molecular excitation modes. Microwave interferometric NDE has potential as a complementary technique with a method that has higher probability of detection and image quality if it is used for the detection of cold welds. The technique has shown some flaw indication in welds with significant LoF [12, 54].
Gouges and other heterogeneities in the weld surface caused by debeading can significantly distort the microwave image [37]. Also, direct comparison with phased array ultrasonic testing (PAUT) has shown it is not currently capable of detecting some other harder to access flaws PAUT can detect [37]. A significant disadvantage shared with 2D radiography is that the data obtained from this technique is a spatial average, in this case in the through-wall direction, and so it provides no information about the depth of any potential defect [37]. Knowledge of depth helps determine how a flaw may evolve in time and what the consequences of that evolution would be, suggesting when failure may occur. The data analysis is more straightforward but also more limited than that which can be applied to techniques such as PAUT,

covered in 1.3.9. Changes to the colour and scale of figures can be made [37], yet this can potentially make the analysis more convoluted and subjective. The data collection can be automated, reducing the dependence on the operator and the risk of human error. Microwave NDE can be performed in service as no couplant is required [37], yet in order to reliably detect flaws it is considered that the technique must at best be complementary to other NDE [15], because of the above disadvantages. This could lead to complications because it cannot be used on joints with residual ultrasonic probe couplant as this has a different permittivity to HDPE [37]. Qualitative preliminary inspection of HDPE electrofusion welds using Evisive Scan Technology show the potential to detect incorrect pipe locations within the coupler yet no direct flaw detection capabilities are demonstrated [55].

Capacitive method

Ultrasonic inspection requires changes in acoustic impedance. Specifically, ultrasonic inspection is considered unsuitable for the accurate and reliable detection of cold fusion in HDPE pipe joints, where the pipe joint may be mechanically weaker, because of incomplete crossing of polymer chains within the material, but where this is minimal acoustic impedance variation. Alternative methods, such as the capacitive method of [56], are said to have the potential to detect certain instances of cold fusion defects in HDPE pipe joints.

Guided Lamb wave ultrasonic testing

Before major adoption of current ultrasonic testing techniques of HDPE, it was suggested that guided Lamb waves that propagate axially along the pipe could be excited at multiple circumferential positions to inspect large areas of HDPE pipe and weld volume [1]. Many Lamb wave modes have dispersion curves (phase velocity vs. frequency) that pass nearby or cross each other. To excite one such mode would result in partial excitation of the other and therefore an impure, hard to interpret transmitted and received pulse [1]. Other modes were too high frequency and so were heavily attenuated over the long distances covered by the guided waves. The result was that a single Lamb mode (S_2) was most suitable, yet its frequency-thickness was 1.536MHzmm so for a 50mm pipe thickness the longitudinal ultrasonic wavelength would be roughly 75mm, making the resolution low. Longitudinal and

shear waves of such wavelength are also very highly attenuated in HDPE [3], such that signal-to-noise ratio (SNR) would be low for these propagation distances. It is still possible to detect and size a defect with these wavelengths, possibly leading to defect characterisation and correct sentencing, but the technique is best used in permanent monitoring as well as detection of defects in welds well beyond the reach of local inspection techniques. Neither of these circumstances apply to EDF Energy's general HDPE pipe weld inspection scenario, whereby pipe welds are inspected locally upon installation and periodically in future in routine checks or if there is cause for concern.

Time of flight diffraction technique (TOFD)

Time of flight diffraction (TOFD) of HDPE butt welds involves two probes either side of the weld where one transmits and the other receives. An undefective weld will register the signal from the surface wave from the outer surface followed later by the wave reflected off the back wall (inner surface). When a flaw is present the tips at maximum and minimum radial extent in the weld will also diffract some of the wave towards the receiver, resulting in two more compressional (L-wave) signals between the surface and back wall responses. S-waves are too highly attenuated for use in NDE of HDPE [3]. The L-wave signals allow for depth measurement and flaw sizing. TOFD is therefore better suited to detecting radial flaws like LoF [16]. Certain welds cannot be accessed from both sides and so the application of TOFD is limited in general to simple geometry butt welds [17]. Also, responses near the outer and inner surfaces are difficult to distinguish from those of the surface and back wall, yet signals still maintain some differentiability as the tip signals are often parabolic, if they have negligible extent in the scan direction, not flat like the surface and back wall [19]. The received signals in TOFD are circumferentially stitched amplitude scans, known as a D-scans and the frequencies used in HDPE TOFD are relatively low compared with steel, so for smaller defects the two tip signals become hard to differentiate [21]. Also, TOFD necessarily uses a divergent ultrasonic wave and so much energy is lost to the receiver, resulting in low signal-to-noise (SNR) in HDPE which is already highly attenuative. TOFD is suggested to be a viable complementary technique that requires the addition of NDE with a higher PoD throughout the weld [15, 19]. Its advantage lies in the relatively small

amount of data and equipment cost compared with techniques using a higher PoD PAUT setup or equivalent.

WINDEPP: Combined creeping wave, tandem and TOFD ultrasonic testing

Before PAUT had been widely adopted in NDE, especially of HDPE, there was a desire to use different hardware to increase the weld inspection coverage compared with that of individual techniques such as TOFD. Consequently, a set of three complementary ultrasonic techniques were combined together by TWI to form the Welding with Integrated Non-Destructive Examination of Polyethylene Pipes (WINDEPP) approach. The first was the use of creeping waves, which travel below the outer surface of the pipe and can be used to detect defects within that shallow sub-surface region. These waves are highly attenuative as there is significant mode conversion to shear waves and so produce poor signal-to-noise (SNR) in anything but inspection close to the weld [16]. TOFD is also used, which is best suited for radially aligned flaws away from the outer and inner pipe surfaces. The third method is the tandem technique, where as with TOFD two probes are used but the receiver detects reflected not diffracted signals via a pitch-catch setup where both probes are the same side of the weld with one behind the other in the axial direction [16]. This is advantageous for detecting defects where the refracted signal is low or undetectable given the defect geometry and the probe orientation(s). WINDEPP proves capable of detecting some aluminium foil inclusions and sand down to 3% contamination by area but not fine particulates (talc) or cold or LoF welds [16].
The WINDEPP approach is designed to be performed when the weld is first produced and still undergoing cooling, therefore the significant temperature dependence of the acoustic properties of HDPE will distort the time of flight calculations. Also, these complementary techniques can today all be performed using PAUT probes but with the added versatility of being able to use PAUT-specific data acquisition and analysis techniques, covered in section 1.3.9.

Phased array ultrasonic testing (PAUT)

Phased array ultrasonic testing (PAUT) involves the use of an array of many transducers capable of transmitting and receiving ultrasonic signals. Common array types

include 1-D linear arrays and 2-D matrix arrays but many others exist. Time delay laws for transmission and reception allow manipulation such as focusing the beam at certain locations for better SNR [57] and steering to different directions. Like Huygens' wavelets, the full wavefront is the sum of the individual transmitted wavefronts. When focusing there is a compromise between the area covered, the spatial resolution, and the attenuation based on the choice of frequency [1, 9]. The SNR can also be improved using more elements but these probes are more expensive and require higher data storage capacity.

PAUT can be used to cover a large volume of butt welds and the surrounding heat affected zone (HAZ) in one scan, improving reliability and repeatability [59]. A commonly used PAUT technique is to perform a sectorial scan (S-scan) where multiple A-scans are taken through a large swept angle. One variable focal distance exists throughout the sweep [58] and the large coverage significantly increases the flaw PoD. The signals near the surface are specular reflections whilst deeper signals are mainly caused by tip diffraction [35]. Tip diffracted signals can yield through-wall thickness of planar flaws such as LoF [2]. When performing single-sided inspection, PAUT can be used on pipe-to-pipe and pipe-to-fitting welds, adding to its versatility [13]. Another key advantage of PAUT is that it is much quicker than convention scanning using single-element probes because of the larger coverage of a PAUT S-scan, for example [45, 59, 60]. Also, by automating the circumferential scanning the dependence on the operator and risk of human error are reduced.

In an approach similar to WINDEPP above, multiple conventional UT techniques may be used to cover the whole weld volume. The advantage of having many transducer elements adds flexibility to this. For example, it is possible to perform self-tandem where the array is divided into two sub-arrays for transmitting and receiving the tandem signal [59]. Two probes with steering wedges with different refractive indices can be used to cover the majority of the weld volume, which is especially useful in large thickness pipes [34]. This approach has been suggested to have the potential to detect cold fusion in butt welds [34], despite cold fusion being challenging to detect nondestructively [11, 16].

PAUT scans provide a lot of data which can be analysed and manipulated after scan completion. A technique commonly used is full matrix capture (FMC) where each element is fired separately and each time all elements are also used to receive the returned signal. This data can be processed in many ways to increase the detection

capabilities of PAUT, covered in section 1.3.9.

In electrofusion welds, incorrect fusion conditions that lead to cold fusion or LoF can be inferred from the size of the HAZ [9, 28]. PAUT can detect voids formed at the solid-liquid interface at the HAZ boundary [9]. PAUT of electrofusion welds requires no steering and so the beam pitch can be large without reducing the probe performance, whereas with butt fusion welds, wedges are used to minimise the need for beam steering via delay laws [17].

In collaboration with EDF Energy, Doosan Babcock have developed an automated circumferential scanning system (figure 1.7) for PAUT with a custom water wedge for forward beam steering that has successfully detected target locations and edges, the latter allowing for through-wall defect sizing [36]. This marks significant progress towards versatile, reliable volumetric NDE of HDPE that is required by regulation [17, 19].

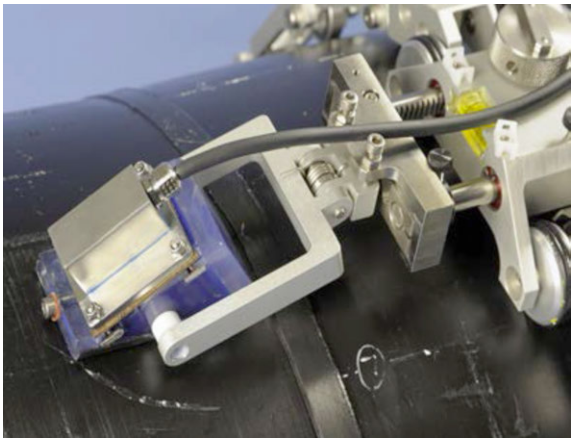

Figure 1.7: Doosan Babcock's automated PAUT butt weld scanning system with bespoke water wedge for beam steering [36].

Data analysis and PAUT enhancements

The large data acquisition capabilities of PAUT add versatility in terms of data analysis that can improve resolution, SNR (contrast), coverage, and other NDE figures of merit. In combination with delay laws mentioned in section 1.3.9, gain laws have been used to perform techniques such as dynamic depth focusing (DDF), which improves the depth of field and the SNR of PAUT [59, 61, 62]. The combination of delay and gain laws is known as a focal law. In DDF there is one focal law for transmission and different delay laws for reception at each element [62].

A commonly used technique for processing FMC data is to use the total focusing method (TFM). This involves using delay laws to steer and focus a beam comprising the sum of the FMC wavelets. The result is a scan that is focused at every location not just focused along a swept line as with S-scans [6]. Adjustment to the amplitude of the signal represented in the scan can be made by correcting for attenuation (proportional to path length) by altering the gain laws of the FMC data. The background noise local to the amplified area will also be enhanced via this approach. To achieve resolution beyond the classical diffraction limit techniques can be used to achieve superresolution [64]. This can be performed with the full matrix of data to enhance all points in the scanned weld volume. Given the large amounts of data generated in FMC, the high costs associated with arrays with a large number of elements, the time taken to transmit and receive with all elements, and the limitations of some hardware used to activate the array elements, it can be beneficial to use only a select few elements. This can be relevant to 2D arrays where randomised patterns can be used to determine which elements are used. The consequence of this is improved detection capabilities relative to ordered or grouped activation of specific array elements [65]. These are referred to as sparse arrays. Firing single elements for FMC rather than an aperture of a set element width will reduce the SNR by a factor of the square root of the number of elements in the aperture, N. This already accounts for an improvement due to the random noise averaging of FMC by firing N times [60]. However, this SNR penalty can be removed by firing multiple elements at once with different phase characteristics to generate an alternative full matrix of data [66].

Further improvements can be made to the SNR by firing coded pulses rather than a conventional single time-windowed pulse. Techniques include a Golay sequence, which involves firing a sequence of pulses, followed by its complementary sequences. The received signals are then cross-correlated with the transmitted sequences and the results of the two complementary sequences are summed to remove the sequence self-noise. Another, suggested to be an improvement on Golay is to linearly vary the frequency of the pulse during emission in what is known as a frequency chirp [67]. A straightforward further improvement to SNR is achieved by averaging the data from multiple FMCs. Storing this extra data could potentially be infeasible but it would be sufficient to retain only the averaged data once this process is completed, reducing the data requirements back to those of one FMC dataset.

All UT mentioned until now considers only the linear component of the wave, the fundamental harmonic, but there is a branch of UT known as nonlinear ultrasonics that evaluates the contribution of other harmonics [68–70]. These are invariably of (often significantly) smaller amplitude than the fundamental harmonic and so in highly attenuative media such as HDPE at the frequencies and pipe thicknesses used in the NDE of pipe joints these are at most negligible contributors compared with the fundamental harmonic or otherwise almost entirely undetectable.

Miscellaneous techniques

Of the remaining NDE techniques that might be applicable to inspection of HDPE welds, eddy current and magnetic methods are considered infeasible as HDPE is an electrical insulator. Also considered unsuitable, thermographic NDE involves the material in question being exposed to a flash or prolonged exposure of thermal radiation that, when re-emitted from the material surface, is measured using thermal imaging. Generally, this can only be applied to surface defects at depths of up to a few millimetres, which is inapplicable to HDPE pipes of interest that are tens of millimetres thick. Also, nuclear magnetic resonance imaging (NMR/MRI) is not considered feasible because it is very costly and requires large, localised hardware. Other NDE techniques exist that are not considered here. They have in common an incompatibility with HDPE pipes in terms of, for example, physical properties, pipework dimensions, and time and monetary cost constraints.

1.4 Thesis Outline

The aim of the project is to improve the ultrasonic array inspection of high-density polyethylene (HDPE) heat-fused pipe joints of cooling water pipework that is installed in EDF Energy's nuclear power stations. Whereas ultrasound array inspection is now established for safety-critical metal components, HDPE poses a hugely challenging problem, that the ultrasound waves are heavily attenuated by the material. This impacts multiple aspects of the inspection and of the modelling that is needed to design and qualify inspection. The thesis reports a range of research that was needed to overcome this challenge, with overall successful outcomes.

The work of the thesis does:

1. obtain accurate acoustic properties of HDPE that are necessary for improved simulated or real ultrasonic array imaging of HDPE pipe joints
2. develop a simulation technique for representing ultrasound in such inspections that has both high accuracy and efficiency
3. extend analytical analysis of ultrasound scattering from cylindrical voids from elastic media to general, attenuative media
4. use the Huygens-Fresnel principle to represent ultrasound scattering from volumetric and planar voids, to image sub-wavelength features of these defects in an ideal circular array setup, and to image angled ultrasonic array nondestructive evaluation (NDE) of potential defects occurring in HDPE pipe joints

5. devise an automated and antidispersive system for reducing coherent and incoherent noise in waveforms with an isolated wave reflection signal
6. produce an imaging and analysis method for ultrasonic array NDE that can represent defects in a refractive, reflective, and scattering environment in attenuating media, which is applied to data from the above developed simulation technique
7. apply much of the above imaging and analysis method to defects machined into HDPE pipe material, with an experimental ultrasonic array controller, yet with an array of limited suitability
8. specify parameters for ultrasonic arrays and a water-filled wedge, which are optimum for HDPE pipe joint inspection, and have been designed and built by Imasonic SAS, France, for research use at Imperial College London

Chapters 2 to 9 sequentially cover the above 8 outcomes of this thesis.

References

[1] *Plastic Pipe Market*, PlastEurope, `http://v.ht/oxvD`, accessed November 6, 2017.

[2] EDF Energy Nuclear Generation, *Hunterston B Power Station Specific NDT Procedure for the Phased Array Ultrasonic Examination of HDPE Butt Weld*, Central Engineering Support Function Branch Instruction, E/PROC/ENG/BI/1442, Revision 000, 2012.

[3] *An Integrated Project Plan to Obtain Code and Regulatory Approval to Use High-Density Polyethylene in ASME Class 3 Piping Applications*, EPRI, Palo Alto, CA, 2006. 1013572.

[4] S.S. Say and A.A. Akgungor, *Welding Defects and their Reasons Observed in Electrofusion Welding of Polythene Pipes*, 24th World Gas Conference, Argentina, 2009.

[5] *Fatigue and Capacity Testing of High Density Polyethylene Pipe Material*, EPRI, Palo Alto, CA, 2007. 1014902.

[6] *An Integrated Project Plan to Obtain Code and Regulatory Approval to Use High-Density Polyethylene in ASME Class 3 Piping Applications*, EPRI, Palo Alto, CA, 2006. 1013572.

[7] D. Naujock, C. Basavaraju, *Safety Evaluation by the Office of Nuclear Reactor Regulation, Relief Request No. I3R-10, Third 10-Year Inservice Inspection Interval, Union Electric Company, Callaway Plant, Unit1*, Docket No. 50-483, United States Nuclear Regulatory Commission, Washington, D.C., 2008.

[8] *Plastic Pipe Institute: Second Edition Handbook of PE Pipe*, Plastic Pipe Institute, `http://v.ht/MT3K`, accessed November 6, 2017.

[9] D.S. Caravaca, C. Bird, and D. Kleiner, *Ultrasonic phased array inspection of electrofusion joints in polyethylene pipes*, NDT 2006, 45th Annual British Conference on NDT, Stratford-upon-Avon, UK, September 2006.

[10] C.W. Chan, *The Ultrasonic Nondestructive Evaluation of Welds in Plastic Pipes*, Ph.D. Thesis, Imperial College London, London, March 1996.

[11] *Nondestructive Evaluation: NDE for High Density Polyethylene (HDPE) Pipe for Cold Fusion*, EPRI, Palo Alto, CA, 2009. 1019141.

[12] R. Stakensborghs, *New method to detect cold fusion joints in high density polyethylene*, Evisive, Inc., Baton Rouge, LA, 2012.

[13] *Development and validation of an automated non-destructive evaluation (NDE) approach for testing welding joints in plastic pipes*, Research for SME-Association Groups, Stage 1 Proposal, 2008.

[14] D. Naujock, C. Basavaraju, *Safety Evaluation by the Office of Nuclear Reactor Regulation, Relief Request No. 06-CN-003, Catawba Nuclear Station, Units 1 and 2, Duke Energy Carolinas, LLC*, Docket Nos. 50-413 and 50-414, United States Nuclear Regulatory Commission, Washington, D.C., 2008.

[15] *Technical Support for Proposed Polyethylene Pipe Code Case*, EPRI, Palo Alto, CA, 2005. 1011628.

[16] M.J. Troughton, *Welding with integrated non-destructive examination of polyethylene pipes*, TWI Ltd., Cambridge, 2001.

[17] F. Hagglund, M. Spicer, and M. Troughton, *Development of Phased Array Ultrasonic Inspection Techniques for Testing Welded Joints in Plastic (PE) Pipes*, 18th World Conference on Nondestructive Testing, South Africa, April 2012.

[18] *High-Density Polyethylene Pipe Solutions*, Plastic Pipe Institute, `http://v.ht/m8sb`, accessed November 6, 2017.

[19] S.L. Crawford, S.R. Doctor, A.D. Cinson, M.W. Watts, S.E. Cumblidge, T.E. Hall, and M.T. Anderson, *Assessment of NDE Methods on Inspection of HDPE Butt Fusion Piping Joints for Lack of Fusion*, United States Nuclear Regulatory Commission, JCN N6398, NUREG/CR-7136, PNNL-20300, May 2012.

[20] *Code Case N-755: Cases of ASME boiler and pressure vessel code, Use of Polyethylene (PE) Plastic Pipe Sections III, Division I and XI*, ASME, March 2007.

[21] *Plastic Joining – Butt fusion and electrofusion welding*, Training and Examination Services, TWI Ltd., Cambridge, 2006.

[22] G. Sandilands and J. Bowman, *An examination of the role of flaw size and material toughness in the brittle fracture of polyethylene pipes*, Journal of Materials Science, **21**, 2881 (1986).

[23] J.P. Marshall, *The influence of welding parameters on the toughness of butt fusion welds in MDPE*, In Advances in Joining Plastics and Composites, Proceedings of the International TWI Conference, Bradford, June 1991.

[24] J.Q. Zhao, L. Daigle, and D. Beaulieu, *Effect of Joint Contamination on the Quality of Butt-Fused HDPE Pipe Joints*, Canadian Journal of Civil Engineering, **29**, No. 5, 787 (2002).

[25] G.P. Marshall, E. Ingham, et al., *The crack growth resistance of PVC and PE*, Plastic Pipes IX, 77 (1995).

[26] A. Prakash T.K., R.L. O'Leary, and A. Gachagan, *Ultrasonic Imaging of Electrofusion Welded Polyethylene Pipes Employed in Utilities Industry*, NDT 2012, 51st Annual British Conference on NDT, Daventry, UK, September 2012.

[27] *Plastics pipes and fittings – Butt fusion jointing procedures for polyethylene (PE) pipes and fittings used in the construction of gas and water distribution systems*, ASME ISO 21307:2011.

[28] C. Bird and M. Troughton, *Non-destructive testing of PE pipe joints*, TWI Ltd., Cambridge, 2008.

[29] *Specification for the Fusion Jointing of Polyethylene Pressure Pipeline Systems Using PE80 and PE100 materials*, Water Industry Specification 4-32-08, Issue 3, April 2002.

[30] *Electrofusion fittings*, Radius Systems, `http://v.ht/1XnB`, accessed November 6, 2017.

[31] R.J. Stakenborghs, *NDT Report RGE Polyethylene Piping Weld Scans*, Evisive, Inc., July 2004.

[32] J. Krautkramer and H. Krautkramer, *Ultrasonic Testing of Materials*, 4th ed., Berlin: Springer (1990).

[33] *Nondestructive Evaluation: High-Density Polyethylene NDE Technology*, EPRI, Palo Alto, CA, 2013. 3002000439.

[34] C. Frederick, A. Porter, and D. Zimmerman, *Ultrasonic Phased Array Examination of Butt-Fusion Joints in High Density Polyethylene*, Proceedings of the 17th International Conference on Nuclear Engineering, ICONE17, July 2009.

[35] W.J. O'Hagan, *Capability Statement for the Use of Phased Array Ultrasonics in the Examination of Hunterston 450 mm and 630 mm (Outside Diameter 38 mm and 60 mm thick respectively) HDPE Butt Welds*, Doosan Power Systems, June 2012.

[36] D. MacLennan, J. Allen, I.G. Pettigrew, C.R. Bird, *Phased Array Inspection Solution for HDPE Butt Welds*, BINDT, 2012.

[37] K. Murphy, *Evisive Microwave inspection of Butt fusion welds*, Exova, Salford, Feb. 2013.

[38] Reynolds, N.D., Jenkins, P.W., Burgess, P., and Attwood, J. 1998. *Fast weld field trials, high productivity butt fused jointing of polyethylene pipes*, In Plastic Pipeline Systems for the Millennium, Proceedings of the 10th International Conference on Plastics Pipes, Gteborg, Sweden, IOM Communications, London, 565 (1998).

[39] C. O'Connor, *Polyethylene Pipeline Systems – Avoiding The Pitfalls of Fusion Welding*, at the 7th Pipeline Technology Conference, Hannover, Germany, March 2012.

[40] *NDE Program Highlights for August 2008*, EPRI, Palo Alto, CA, 2008. 1018005.

[41] S.L. Crawford, S.E. Cumblidge, S.R. Doctor, T.E. Hall, and M.T. Anderson, *Preliminary Assessment of NDE Methods on Inspection of HDPE Butt Fusion Piping Joints for Lack of Fusion*, JCN N6398, Task 2D, Pacific Northwest National Laboratory, Richland, WA, May 2008.

[42] *ASME code development roadmap for HDPE pipe in nuclear service*, STP-NU-057, ASME Standards Technology Llc., Jan. 2013.

[43] E.A. Gimmler, R. Farrage, et al., *Manual for polyethylene pipe systems for water supply applications*, Section 8 – Installation: Testing and Commissioning, 2nd edition, WRc Publications, Swindon, UK, 1994.

[44] G.M. Swallowe, *Mechanical Properties and Testing of Polymers: An A-Z Reference*, Polymer Science and Technology Series, Vol. 3, Springer, 1999.

[45] C. Bird and D. Caravaca, *The Ultrasonic Phased Array Inspection of Electrofusion Joints in Polyethylene Pipes*, ECNDT, 2006.

[46] J. Wu, *Determination of velocity and attenuation of shear waves using ultrasonic spectroscopy*, J. Acoust. Soc. Am. **99**, 2871 (1996).

[47] I.J. Munns and G.A. Georgiou, *Ultrasonic and radiographic NDT of butt fusion welded polyethylene pipes*, Insight **41**(5), 291 (1999).

[48] *Technical Note 802 Leak Testing of Polyethylene Pipe For Municipal and Industrial Applications*, Performance Pipe, Chevron Phillips Chemical Company LP, 2002.

[49] *Generic Butt Fusion Joining Procedure for Field Joining of Polyethylene Pipe*, TR-33, The Plastic Pipe Institute, Irving, US, 2012.

[50] B. Messer, M. Yarmuch, and P. den Boer, *Novel High Resolution Defect Detection For Thermoplastic Butt-Welds*, Pipeline & Gas Journal *230*, 46 (2003).

[51] G.G. Diamond, D.A. Hutchins, P. Pallav, and R. Gohel, *Near Infrared (NIR) Spectral Imaging for NDE*, AIP Conference Proceedings **1096**, 447 (2009).

[52] B. Stakenborghs, *Specific Application NDE Method Leads to Development of Novel Microwave NDE Technique*, Inspectioneering Journal **11**(1), 11 (2005).

[53] S.L. Crawford, S.R. Doctor, A.D. Cinson, M.W. Watts, T.L. Moran, and M.T. Anderson, *Assessment of NDE Methods on Inspection of HDPE Butt Fusion Piping Joints for Lack of Fusion with Validation from Mechanical Testing*, JRC-NDE 2010, Berlin, Germany, Nov. 2010.

[54] J.P. Pan, X.W. Zhu, and L.J. Tan, *Detecting Cold Weld Defects in HDPE Piping Thermal Fusion Welds Based on Microwave Technique*, Applied Mechanics and Materials *423-426*, 852 (2013).

[55] *HDPE Pipe Electro-Fusion Coupling Inspection and Imaging Using Evisive Scan Technology*, Evisive, Inc., Baton Rouge, LA, 2009.

[56] T. Bore, D. Placko, F. Taillade, and P. Sabouroux, *Electromagnetic characterization of grouting materials of bridge post tensioned ducts for NDT using capacitive probe*, NDT&E International **60**, 110-120, 2013.

[57] *Advances in Phased Array Ultrasonic Testing Applications*, Olympus NDT, Waltham, USA, 2007.

[58] *Introduction to Phased Array Ultrasonic Testing Applications*, Olympus NDT, Waltham, USA, 2004.

[59] G. Neau and D. Hopkins, *The promise of ultrasonic phased arrays and the role of modeling in specifying systems*, at the ASNT Fall Conference & Quality Testing Show, Houston, USA, Oct. 2006.

[60] B.W. Drinkwater and P.D. Wilcox, *Ultrasonic arrays for non-destructive evaluation: A review*, NDT&E International **39**, 525 (2006).

[61] H.J. Shin, Y.H. Jang, J.R. Kwan, and E.J. Lee, *Nondestructive Testing of Fusion Joints of Polyethylene Piping by Real Time Ultrasonic Imaging*, NDT.net **10**(3), (2005).

[62] A. Lamarre and F. Mainguy, *Dynamic Focusing of Phased Arrays for Nondestructive Testing: Characterization and Application*, NDT.net *4(9)*, (1999).

[63] C. Holmes, B.W. Drinkwater, and P.D. Wilcox, *Post-processing of the full matrix of ultrasonic transmitreceive array data for non-destructive evaluation*, NDT&E International **38**, 701 (2005).

[64] F.K. Gruber, E.A. Marengo, and A.J. Devaney, *Time-reversal imaging with multiple signal classification considering multiple scattering between the targets*, J. Acoust. Soc. Am. **115**(6), 3042 (2004).

[65] J.T. Yen and S.W. Smith, *Real-Time Rectilinear 3-D Ultrasound Using Receive Mode Multiplexing*, IEEE Transactions on Ultrasonics, Ferroelectrics, and Frequency Control, *51*(2), 216 (2004).

[66] R.A. Smith, J.M. Bending, L.D. Jones, T.R.C. Jarman, D.I.A. Lines, *Rapid ultrasonic inspection of ageing aircraft*, Insight, **45**(3), 174 (2003).

[67] T. Misaridis and J.A. Jensen, *Use of Modulated Excitation Signals in Medical Ultrasound. Part I: Basic Concepts and Expected Benefits*, IEEE Transactions on Ultrasonics, Ferroelectrics, and Frequency Control, *52*(2), 177 (2005).

[68] R. Lencioni, D. Cioni, and C. Bartolozzi, *Tissue harmonic and contrast-specific imaging: back to gray scale in ultrasound*, Eur. Radiol. **12**, 151 (2002).

[69] P.J.A. Frinking, A. Bouakaz, J. Kirkhorn, F.J. Ten Cate, N. de Jong, *Ultrasound contrast imaging: current and new potential methods*, Ultrasound in Med. & Biol., **26**(6), 965 (2000).

[70] E. Escobar-Ruiz, A. Ruiz, W. Hassan, D.C. Wright, I.J. Collison, P. Cawley, and P.B. Nagy, *Non-linear Ultrasonic NDE of Titanium Diffusion Bonds*, J. Nondestruct. Eval. **32**(4), (2013).

Chapter 2

Ultrasonic attenuation and phase velocity of high-density polyethylene (HDPE) pipe material

The formulation, implementation, and evaluation of some concepts covered in chapter are published Open Access as: J.S. Egerton, M.J.S. Lowe, H.V. Halai, and P. Huthwaite, *Ultrasonic attenuation and phase velocity in high-density polyethylene (HDPE) pipe material*, J. Acoust. Soc. Am. **141**(3), 1535-1545 (2017).

2.1 Abstract

Knowledge of acoustic properties is crucial for ultrasonic or sonic imaging and signal detection in nondestructive evaluation (NDE), medical imaging, and seismology. Accurately and reliably obtaining these is particularly challenging for the NDE of high density polyethylene (HDPE), such as is used in many water or gas pipes, because the properties vary greatly with frequency, temperature, direction and spatial location. Therefore the work reported here was undertaken in order to establish a basis for such a multiparameter description. The approach is general but the study specifically addresses HDPE and includes measured data values. Applicable to any such multiparameter acoustic properties dataset is a devised regression method that uses a neural network algorithm. This algorithm includes constraints to respect the

Kramers-Kronig causality relationship between speed and attenuation of waves in a viscoelastic medium. These constrained acoustic properties are fully described in a multidimensional parameter space to vary with frequency, depth, temperature, and direction. Example figures from this dispersion multidimensional parameterisation are shown in appendix 2.8.6. The resulting uncertainties in acoustic properties dependence on the above variables are better than 4% and 2% respectively for attenuation and phase velocity and therefore can prevent major defect imaging errors.

2.2 Introduction

Knowledge of acoustic properties is crucial for ultrasonic or sonic imaging and signal detection in nondestructive evaluation (NDE) [1], medical imaging [2], and seismology [3]. Specifically, in many industrial applications it is necessary to conduct nondestructive evaluation (NDE) to detect potential defects in engineering components such that the likelihood of critical damage or failure is minimised. Consequently, it is necessary to develop accurate and reliable NDE methods to ensure integrity of such components.

On occasion, manufacturing defects can occur within the joints of high-density polyethylene (HDPE) pipes. This is of particular importance to the nuclear industry where safety is a high priority. In EDF Energy's UK nuclear power stations, existing cast iron pipes are being replaced by those made of HDPE in their tertiary cooling circuits. Much of the existing NDE of HDPE pipe joints involves ultrasonic array inspection [4–6] with some inspections also performed via the microwave interferometric method [7]. When a HDPE pipe joint is heat fused, defects can occur. These include volumetric inclusions and voids, as well as planar lack of fusion defects that have negligible axial extent. Ultrasonic array inspection is superior at defect detection and sizing in HDPE joints compared with microwave imaging because it can be used to produce an image covering all depths within the joint whereas microwave inspection only detects an average discrepancy in relative permittivity through the depth. In this way ultrasonic inspection can locate planar defects with axial normals, while microwave NDE cannot. This is critical to defect sizing, which itself is necessary for determining whether a defective joint should be replaced.

The current HDPE pipe joint ultrasonic array inspection techniques are often based on default imaging methods provided by the hardware. The main example of this

is a sector scan. This process provides good weld volume coverage by sweeping over a range of transmit and receive angles but only focuses the ultrasonic beam at one depth. Consequently, any defect image is inherently unfocused, resulting in inaccurate defect sizing. Also, no known HDPE pipe joint inspection technique accounts for variations in acoustic properties – attenuation and phase velocity – with ultrasonic frequency, propagation depth in the pipe, temperature of the pipe, and propagation direction. Previous viscoelastic and dispersive acoustic properties experiments that have included frequency dependence are on occasion based on multiple measurements; have defined uncertainty bounds; conform to some or all of the constraints detailed in section 2.3; or partially account for some of the above environmental, geometric, or material considerations [8–18].

The purpose of this chapter is to address the current lack of accurate HDPE pipe acoustic properties. It is here determined that all these variations are significant and that by accounting for these, discrepancies can be reduced between predicted and actual defect size. Further to this, without such acoustic properties characterisation, current HDPE pipe joint inspection procedures often require much time consuming calibration to determine and account for the variation of the attenuation and phase velocity of the ultrasonic wave with temperature or frequency and are unable to account for the influence of beam steering and diversion caused by heterogeneity and anisotropy; with such acoustic properties characterisation, all the above can be accounted for in calibration and data analysis. It is suggested that acoustic properties variation between different batches of HDPE pipework is small and the variation of different batches is not investigated in this study.

As part of this investigation, this author will consider the dispersion relations of viscoelastic waves that are constrained to be causal by the Kramers-Kronig relation that may depend not only on wave frequency, but also other parameters – an example being the temperature of the viscoelastic medium in which such waves propagate. Such acoustic properties must be obtained accurately and reliably via a suitable experimental method for suitable ranges of parameter values. Then, if numerical descriptions of such dispersion relations are to be obtained from such multiparameter empirical acoustic properties data, any accurate regression method that discards none of the multiparameter dataset must inherently be multivariate. Multivariate regression is necessarily nonlinear in frequency for viscoelastic media, and the regression coefficients are not all independent for causal Kramers-Kronig constrained

dispersion relations. A suitable and efficient approach to tackling a multiparameter problem such as this is to employ a neural network algorithm [19, 20] to obtain such a numerical description of such dispersions relations.

This chapter is set out as follows. Succeeding background theory in section 2.3; the principles of the method for obtaining and analysing the acoustic properties of HDPE and other such viscoelastic media are provided in section 2.4; the procedure for obtaining HDPE acoustic properties, their dependence on frequency, propagation depth within the pipe, temperature, and propagation direction within the pipe, and the method for fully determining this multiparameter variation are provided in section 2.5; in section 2.6, the empirical phase velocity and attenuation of HDPE are characterised and a neural network algorithm is implemented as a method of constrained, multiparameter regression; and conclusions are drawn in section 2.7.

2.3 Theory

Here this author summarises a theoretical description of an ultrasonic bulk wave that propagates in a viscoelastic medium such as HDPE. This description includes the theoretical constraints to which such an ultrasonic wave in a viscoelastic medium must adhere. These constraints are necessarily imposed in the frequency domain, and so this is how the wave description is formulated.

The spectrum of a 1-D harmonic plane wave can be expressed as

$$S_x(x, f) = S_x(0, f) \exp(ik_x(f)x), \tag{2.3.1}$$

where x is location, f is frequency, and $k_x(f)$, or tersely $k(f)$, is the dispersion relation,

$$k(f) = \frac{2\pi f}{v_p(f)} + i\alpha(f), \tag{2.3.2}$$

where $v_p(f)$ is phase velocity and $\alpha(f)$ is attenuation. For this entire study, the following units are used, $[v_p] = \mathrm{ms}^{-1}$ and $[\alpha] = \mathrm{m}^{-1}$; alternative, unused unit conventions do exist, including $[\alpha] = \mathrm{Np} \cdot \mathrm{m}^{-1}$.

Much time has been given to the study of how best to describe the dispersion relation of viscoelastic media [8, 11, 14, 17, 21, 23–27]. From which, it is usual to conclude that the most suitable description for attenuation of ultrasonic waves in a viscoelastic medium follows a power law,

$$\alpha(f) = \alpha_1 f^y, \tag{2.3.3}$$

where $0 < \alpha_1$ and $1 < y < 2$ are coefficients to be determined. One such example of a commonly used damping model is Kelvin-Voigt, but this loses accuracy via restriction to f^2 proportionality at ultrasonic frequencies. Causality is a necessary constraint on dispersion that couples the real and imaginary components of dispersion via the Kramers-Kronig relations [27–29],

$$v_p(f) = v_{p1} + \left(\frac{v_{p1}}{\pi}\right)^2 \int_{f_1}^{f} \frac{\alpha(f')}{f'^2} df', \tag{2.3.4}$$

which, via use of equation (2.3.3) and selecting zero reference frequency, $f_1 = 0$, results in the following power law description of ultrasonic viscoelastic phase velocity,

$$v_p(f) = v_{p1} + \left(\frac{v_{p1}}{\pi}\right)^2 \frac{\alpha_1}{y-1} f^{y-1}, \tag{2.3.5}$$

where positive phase velocity at zero frequency, $0 < v_{p1}$, is to be determined. Importantly, the above constraint, $1 < y < 2$, ensures that the description of phase velocity in equation (2.3.5) remains finite for all positive frequencies. Only with these frequency dependent descriptions of attenuation and dispersion can any regression be applied to these data that is constrained via the above requirements for viscoelasticity and for causality.

Appropriate multiparameter regression to these acoustic properties should simultaneously use all data that contain dependent parameters; a parameter fit will be inaccurate if, for example, regression is conducted on a subset of data, where all but one parameters are fixed, and then the obtained 1D fit is extrapolated in the other dimensions. This is so because the regression only remains accurate for the

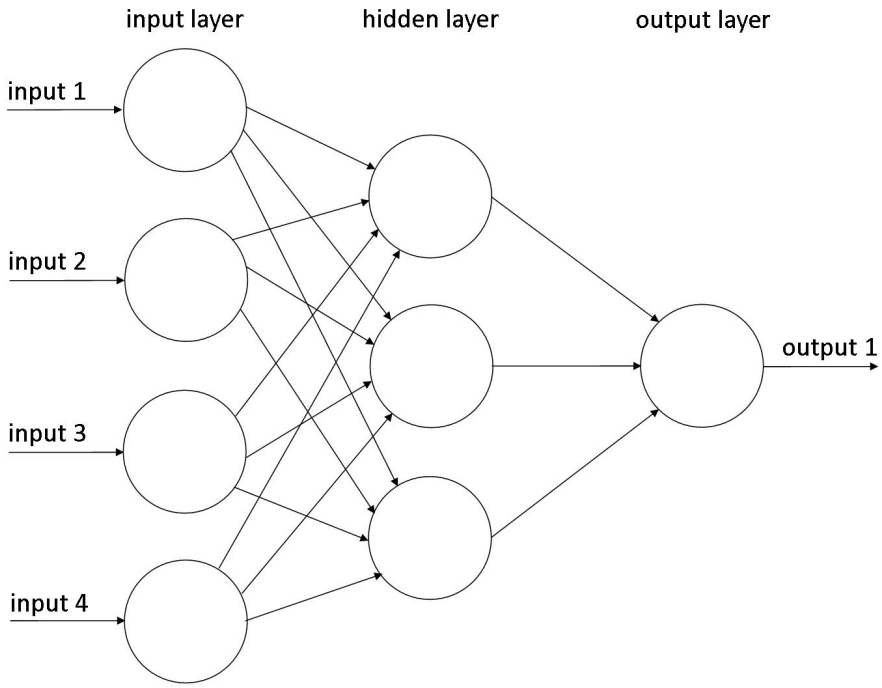

Figure 2.1: Cartoon of an artificial neural network, including input, hidden, and output nodes and their interconnects and layers.

initial parameter set and not the extrapolated values. Alternatively, multivariate linear or nonlinear regression techniques are capable of fitting multiple dimensions of the dataset simultaneous, but these are also considered unsuitable for two reasons. First, they do not accurately represent power law functional forms as found in equations (2.3.3) and (2.3.5). Second, they do not determine coupled regression coefficients, such as y and α_1.

A suitable regression technique [19], chosen here, is to implement a neural network algorithm on the multiparameter acoustic properties dataset that has previously been constrained via 1D power law fits in frequency to adhere to equations (2.3.3) and (2.3.5); these conditions impose viscoelastic and causality constraints on the input, and thus also the output, of the neural network algorithm. Example figures from this dispersion multidimensional parameterisation are shown in appendix 2.8.6. High accuracy and high confidence in interpolation and extrapolation can be achieved through suitable selection of the quantity of hidden layers in the neural network regression, shown in figure 2.1, where fits could otherwise range from linear in each parameter to overspecified fits such as those obtained from piecewise cubic splines. The appropriate neural network parameterisation therefore exhibits minimal unphysical high order fluctuations while still having a high closeness to the data, which is, for

example, quantifiable via the coefficient of determination, R^2 [30]. The two dimensional analogue to such an appropriate multidimensional fit is a smooth surface with low curvature on the scale of the parameter sample length.

2.4 Principles of method

The standard ASTM E664 is acknowledged as an associated technique. However, the ASTM E664 time-domain method for obtaining ultrasonic attenuation does not directly inform the spectroscopic (frequency-domain) requirements of this method. The acoustic properties measurement principles and procedure are presented here for longitudinal waves in HDPE; shear waves are found by Wu to propagate negligible distances in HDPE [12] and therefore only cause mode conversion losses for the propagating longitudinal waves upon reflection or scattering.

First, the chosen ultrasonic signal is defined. The wave described in equation (2.3.1) is continuous and consequently does not represent a conventional 'toneburst' output from a piezoelectric longitudinal ultrasonic transducer. When within their linear operating range and driven with a single, often half-period square or spiked, voltage impulse, these longitudinal wave transducers oscillate sinusoidally with an approximately Gaussian amplitude envelope. Simulation of this enveloped sinusoid toneburst requires windowing of equation (2.3.1). A Gaussian envelope has infinite duration and truncations to this are mathematically cumbersome.

Consequently, a commonly used window is a half-period sinusoid known as a Hann function. The amplitude spectrum of this function has side lobes either side of the central peak at pulse centre frequency, f_0.

This is unsuitable when general frequency dependent dispersion in attenuative materials is assumed, as is necessary to describe viscoelastic media such as HDPE. This is because, during wave propagation, the frequency content of the main lobe can be attenuated more than the unphysical side lobes, resulting in dominance of these erroneous frequencies in propagated pulses. This is avoided through selection of an envelope that generates an amplitude spectrum closer to the single-peak Gaussian approximation to the spectrum of the transducer.

One such suitable envelope is the Blackmann-Harris window [27]. This is the chosen window for all time domain signals analysed here, owing to the relative smallness of the side lobes immediately adjacent to the main lobe at f_0. Using an input pulse

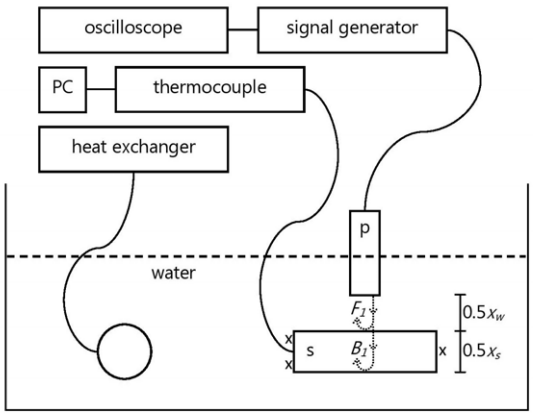

Figure 2.2: Cartoon of immersion tank with pulse-echo single probe setup. Label 'p' is the probe, 's' is the sample, F_1 and B_1 are the first front wall and back wall reflections, and x_w and x_s are the propagation paths in the water and the sample. The crosses beside the sample represent a G-clamp.

with accurate frequency content relaxes the filtering requirements in post-processing of the simulated wave; if large side lobes are present the high- and low-pass filters used necessarily have corner frequencies close to f_0, resulting in greater filtering of the frequency content of the main spectrum.

The immersion tank setup used to obtain waveforms that include reflections from the front and back walls of a cuboid-shaped sample cut from HDPE pipe inspected with a pulse-echo ultrasonic configuration at normal incidence to the sample surfaces is depicted in figure 2.2. The ratio between front and back wall pulse amplitudes coupled with the difference in time of flight between the front and back wall reflections infer the attenuation and phase velocity in the test sample.

Below are equations used to obtain attenuation and phase velocity and their dependences on frequency, propagation depth, temperature, and propagation direction from these HDPE pipe sample waveforms. These equations can also readily be applied to other highly attenuative media.

To yield a general description of damped bulk plane wave attenuation and phase velocity, equations (2.3.1) and (2.3.2) can be combined using $\ln(a^b) \equiv b\ln(a)$ and $c \equiv |c|\exp(i\phi_c)$ to yield,

$$\ln\left|\frac{S(f)}{S_0(f)}\right| + i(\phi_S(f) - \phi_{S_0}(f)) = i\frac{2\pi f x}{v_p(f)} - \alpha(f)x, \tag{2.4.1}$$

where $\phi_S(f)$ and $\phi_{S_0}(f)$ are phases of the spectra. By equating real and imaginary

components of equation (2.4.1) it follows that for a 1-D propagating wave the general forms of attenuation and phase velocity are,

$$\alpha_{gen}(f) = -\frac{1}{x} \ln \left| \frac{S(f)}{S_0(f)} \right| \tag{2.4.2}$$

and

$$v_{p,gen}(f) = \frac{2\pi f x}{\phi_S(f) - \phi_{S_0}(f)}. \tag{2.4.3}$$

Equations (2.4.2) and (2.4.3) are adapted to describe attenuation and dispersion of the sample in figure 2.2, as follows. First, for an ultrasonic probe, with a flat circular transmission-reception surface that has finite radius, a, such as is used here to characterise HDPE pipe acoustic properties, it is necessary to account for diffraction of the transmitted and reflected waves. For such transducers, this can be achieved using Lommel diffraction correction [32]

$$D(s) = 1 - \exp\left(-i\left(\frac{2\pi}{s}\right)\left[J_0\left(\frac{2\pi}{s}\right) + iJ_1\left(\frac{2\pi}{s}\right)\right]\right), \tag{2.4.4}$$

where

$$s = \frac{xc}{fa^2}, \tag{2.4.5}$$

given c is a general variable that represents the longitudinal phase velocity in either one or other medium – here water or HDPE. A smaller path in each medium, x, results in less beam spread. However, Lommel diffraction correction is valid only in the far field of the wave, the distance of which is known to be,

$$d_{far} = \frac{a^2}{\lambda_{min}}. \tag{2.4.6}$$

The spectra of the signals reflected off the front wall, $F_1(f) = S(x_w, f)$, and back

wall, $B_1(f) = S(x_w + x_s, f)$, replace $S_0(f)$ and $S(f)$, where

$$F_1(f) = S_0(f) \exp(ik_w(f)x_w) A_{11} \frac{1}{D_{F_1}} \tag{2.4.7}$$

and

$$B_1(f) = S_0(f) \exp(ik_w(f)x_w) \exp(ik_s(f)x_s) A_{12}A_{22}A_{21} \frac{1}{D_{B_1}}, \tag{2.4.8}$$

given $k_{w,s}$ are dispersion in both media, A_{11} is the water-HDPE plane wave normal incidence reflection coefficient, $A_{22} = -A_{11}$ is that of HDPE-water, A_{12} is the water-HDPE transmission coefficient, and A_{21} is that of HDPE-water. The transmittance of a plane wave at normal incidence to the interface is,

$$A_{121} = A_{12}A_{21} = \frac{4\rho_s v_{p,est} \rho_w c_w}{(\rho_s v_{p,est} + \rho_w c_w)^2}, \tag{2.4.9}$$

where $\rho_{w,s}$ are density in both media, and $v_{p,est}$ is an estimate of phase velocity in HDPE. Estimating phase velocity has a small associated error given the following approximation, $A_{121} \propto (v_{p,est})^{-1}$ for $\rho_s v_{p,est} > \rho_w c_w$, varies with a low order power in $v_{p,est}$ and therefore is not strongly dependent on it. For this reason, uncertainty can be neglected in estimated phase velocity, and by the same reasoning, all other parameters in equation (2.4.9). It is assuming that plane wave conditions are valid for the beam profile, given the geometry of the transducer diameter, $2a$, the minimum propagation, x_w, and the wavelength. Normal incidence is a valid assumption because the solid angle subtended in wave reception by the transducer is small. Lommel diffraction correction, equation (2.4.4), is introduced to equations (2.4.7) and (2.4.8) given $D_{F,B_1} = D(s_{F,B_1})$ where $s_{F_1} = s(x_w c_w, f, a)$ and $s_{F_1} = s(x_w c_w + x_s v_{p,est}, f, a)$. The resulting empirical descriptions of attenuation and phase velocity are,

$$\alpha_{emp}(f) = -\frac{1}{x_s} \ln \left| \frac{B_1(f)}{F_1(f)} \frac{1}{A_{121}} \frac{D_{B_1}}{D_{F_1}} \right| \tag{2.4.10}$$

and

$$v_{p,emp}(f) = \frac{x_s}{\Delta\tau + \frac{\Delta\phi(f)}{2\pi f}} \tag{2.4.11}$$

where $\Delta\phi(f) = \hat{\phi}_{B_1}(f) - \phi_{F_1}(f)$, for which the 'hat' of $\hat{\phi}_{B_1}(f)$ signifies phase inversion for the reflected pulse that occurs for $\rho_1 c_1 > \rho_2 c_2$. Subscripts '1' and '2' represent before and beyond the interface, which for B_1 is HDPE-water. In contrast with equation (2.4.3), the empirical description of phase velocity is expressed with the extra term, $\Delta\tau$. This is introduced to alleviate the $2n\pi$ ambiguity inherent in phase, where n is an integer. This adaptation is achieved as follows:

1. circularly shift the front wall waveform by duration, τ_{F_1}, such that the peak amplitude of its Hilbert envelope occurs at $t = 0$
2. repeat for the back wall to obtain τ_{B_1}
3. calculate the difference between the shifts $\Delta\tau = \tau_{B_1} - \tau_{F_1}$
4. determine ϕ_{F_1} and $\hat{\phi}_{B_1}$
5. refine $\Delta\tau$ by finding the shift closest to $\Delta\tau$ for which $\Delta\phi(f)$ is continuous over a bandwidth that bounds the majority of frequency content
6. introduce $\Delta\tau$ to equation (2.4.11)

Consequently, $\Delta\tau$ in equation (2.4.11) accounts for the net shift of this duration applied in the above circular shifts. This is a time domain shift and is therefore the same for all frequencies; it is alike to shifting by the difference in travel time of pulses moving at the group velocity, $\Delta t_{g,emp} = x_s / v_{g,emp}$, but rather its duration is optimised to be that which provides continuous phase over a specified bandwidth. In this way, it can be considered to be the frequency independent offset to phase velocity, from which the phase terms are perturbed, to yield phase velocity over the specified bandwidth. Procedures such as the above also remove the additional need to phase unwrap [13].

2.5 Implementation of method

The procedure for accurately and reliably obtaining the acoustic properties of HDPE (grade PE-100) pipe material where variations with frequency, anisotropy via direction relative to the pipe geometry, temperature, and heterogeneity via depth in the radial (throughwall) direction are characterised is described here. These variations can then be described with full dependence on the above parameters through regression analysis conducted on all parameters simultaneously.

Only with this accurate full description of acoustic properties can specific values for these conditions be input into a function that generates the associated attenuation and phase velocity outputs.

This procedure is optimised such that it is inherently readily applicable to other highly attenuative media.

As depicted in figure 2.2, the signal generator that transmits half-cycle square impulses is an *Olympus 5077PR (Tokyo, Japan)*, the single probe used to transmit and receive ultrasound is a *GE Inspection Technologies ISS Gamma 10MHz (NY, USA)*, the oscilloscope used to digitise the data is a *Teledyne LeCroy waverunner 44Xi (Geneva, Switzerland)*, the tank heat exchanger is a *Thermo Fisher Haake DC10 (Hemel Hempstead, UK)*, and the thermocouple is a *Pico Technologies TC-08 (Eaton Socon, UK)*. A probe with $f_0 = 10$MHz is chosen because higher f_0 probes have higher absolute bandwidths for the same percentage bandwidth. This makes regression analysis to fit equation (2.3.3) more accurate, because local random variations become relatively less significant where more data is available.

In equation (2.4.6), for $a = 3.175$mm and assuming a maximum frequency of $f_{max} = 15$MHz with corresponding wavelength $\lambda_{min} = 0.16$mm after propagation through water, $d_{far} = 60$mm – this is the chosen water path, x_w, for all measurements. Via probe tilt screws the angle of alignment of the probe is varied in both axes of rotation such that the signal amplitude is maximised, while linearity of the signal is maintained through input voltage reduction in the presence of signal saturation. Multiple coherent time averages of independently obtained waveforms within a measurement increase the signal-to-noise ratio (SNR) of the averaged waveform relative to any one waveform used in obtaining said average. Applying central limit theorem to these independent random variables, the increase in SNR is known to be proportional to the square root of the number of time averages. Consequently,

there is a diminished improvement for larger numbers of time averages. Further, environmental conditions within the immersion tank that affect acoustic properties measurements can change significantly over longer durations. Consequently, it is found that reducing the random noise with 1000 time averages of each waveform is optimal for this compromise. The digital sampling in both voltage and time have maximised bit depths because the recorded waveforms extend close to full screen height and width. Other due diligence includes letting the water in the tank settle to minimise air bubble content and letting the water temperature reach equilibrium with the samples submerged. Temperature gradients remained within the tank, but accurate temperature control is ensured by moving the heat exchanger far from the sample such that local gradients are smaller, and by ensuring the thermocouple is in contact with the sample. The samples are submerged using a G-clamp with minimal contact pressure and angled such that minimal tilt screw adjustment from vertical is required.

Three HDPE pipe samples are cut with thicknesses, h, detailed in appendix 2.8.3, that each extend in a direction orthogonal to the thicknesses of the other two samples – the resulting samples have orientations labelled, $O = \mathbf{I}, \mathbf{II}, \mathbf{III}$, in the circumferential, axial, and radial directions, shown in figure 2.3. The samples are cut distant from the fusion joint, and its heat affected zone (HAZ), in the bulk pipe material. This is done such that the bulk wave propagation characteristics distant from the HAZ are isolated from those of wave propagation in the HAZ. The wave propagation path external to the HAZ constitutes a large majority of the total wave propagation path. Consequently, any difference in acoustic properties internal and external to the HAZ, and their corresponding variations with frequency, anisotropy, temperature, and heterogeneity, only result in wave path and arrival time perturbations for a small proportion of the total propagation path. Therefore, the effect of the HAZ on wave propagation is here neglected for the application of ultrasonic inspection of HDPE pipe joints.

This size of h is a compromise between a small fractional error, inherent in thicker samples where machining tolerances are fixed, and the ideal value for attenuation over a propagation path, $x_s = 2h$, of $\alpha x_s = 1$ [33]. The precursory study conducted by this author informed that $\alpha(5\text{MHz}) \approx 140\text{m}^{-1}$ at room temperature, suggesting $h_{ideal} \approx 3.6\text{mm}$ but, with this, the machining tolerance of approximately 0.1mm would cause too large a reduction in accuracy, because it would contribute

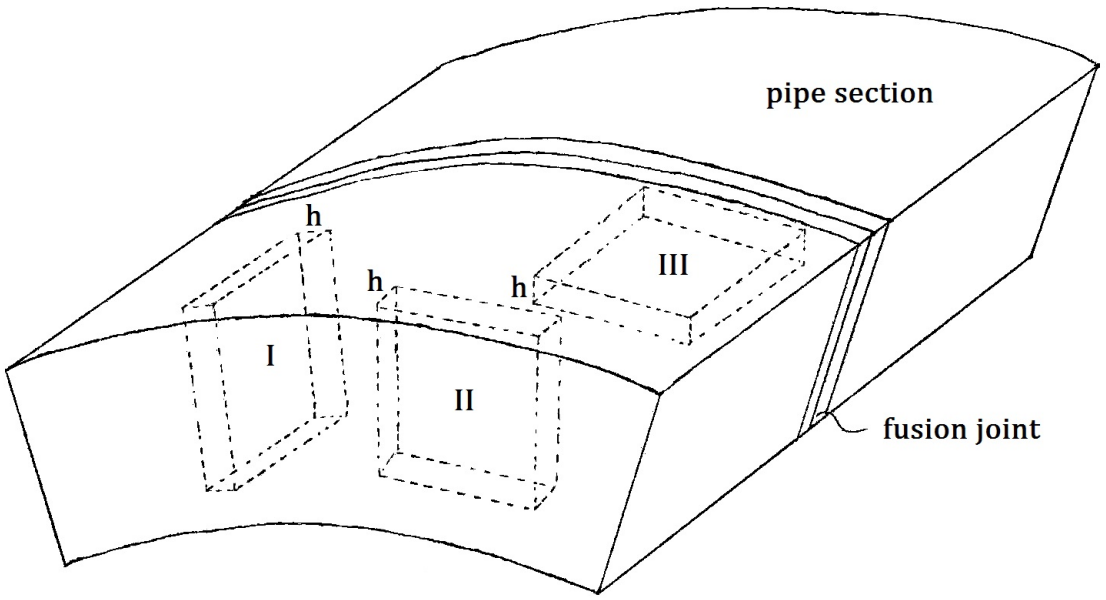

Figure 2.3: Sketch of HDPE pipe samples **I**, **II**, and **III** oriented with their thicknesses in the circumferential, axial, and radial directions. Samples are cut distant from the fusion joint, and its heat affected zone (HAZ), in the bulk pipe material.

approximately 0.03 fractional uncertainty, in quadrature, to acoustic properties uncertainties. Therefore, $h \approx 10$mm is the favoured compromise, with an approximate fractional uncertainty contribution of 0.01. Each sample has 5 independent sampling rows, $i = 1, 2, ..., 5$, and 5 columns, $j = 1, 2, ..., 5$, resulting in 25 independent measurement locations with pitches (spacings) of 10mm. The region of unique measurement consequently has a 10mm diameter. This is greater than the front wall transmission spot size of B_1, where the majority of the ultrasonic flux passes, which is marginally larger than $2a = 6.35$mm after beam spread. The 75 measurements are repeated 3 times at temperatures close to $T = 8, 21, 42°$C, representing a range that includes the majority of ambient temperatures at which NDE of HDPE pipe joints is conducted. The samples are finished with approximately 10 micron surface roughness to minimise scattering at higher frequencies, which have associated wavelengths close to the roughness amplitudes.

Acoustic properties data for all frequencies, temperatures, measurement locations, and sample orientations is collectively defined $[k]_{f,T,ij,O}$. To determine the radial heterogeneity of the acoustic properties at these temperatures, the mean and standard deviation of each row of each set of 25 measurements must be determined, yielding $[k]_{f,T,j,O}$. From these, the radial heterogeneity sets are defined $[k]_{f,T,j,\mathbf{I}}$ and $[k]_{f,T,j,\mathbf{II}}$, and the axial heterogeneity set is $[k]_{f,T,j,\mathbf{III}}$. Axial heterogeneity should not exist

for an extrusion cooled HDPE pipe, therefore this set is a control for comparison with those of radial heterogeneity. For the sets $[k]_{f,T,j,\mathbf{I}}$ and $[k]_{f,T,j,\mathbf{II}}$, i increases from pipe outer diameter, OD, to inner diameter, ID. To determine anisotropy, the mean and standard deviation of all 25 measurements for each sample and temperature are obtained, yielding $[k]_{f,T,O}$. Analysis of the standard deviation of acoustic properties when the mean of all geometric properties is taken requires $[k]_{f,T}$.

2.6 Results and analysis

Attenuation and phase velocity variations with frequency, depth, temperature, and direction are quantified here. Associated uncertainties are provided that give high statistical significance to these acoustic properties descriptions. A neural network algorithm is used to apply a multidimensional fit to these acoustic properties that adhere to viscoelastic and causality constraints. These dispersion characteristics are therefore fully parameterised. In doing so, for the user's chosen HDPE pipe joint inspection application, attenuation and phase velocity are described for the ranges found in current ultrasonic inspection and that cover the vast majority of potential HDPE pipe sizes that may be used in the nuclear industry and elsewhere.
All empirical frequency dependences are obtained using equations (2.4.10) and (2.4.11). All frequency regressions are constrained by equations (2.3.3) and (2.3.5). The frequency regressions are calculated only from the bandwidth over which significant spectral content exists – this is taken to be the mean for all spectra of the range spanning two half-width-half-maxima above and below the modal frequency of the reflection from the back wall,

$$\overline{f_{0,B_1}} \pm 2\overline{HWHM_{B_1}} = 7.0 \pm 3.0\text{MHz}. \tag{2.6.1}$$

All mean regressions have associated standard deviations but for clarity the standard deviations are omitted from figures with many nearby curves. All regressions are obtained via a least squares algorithm.
The frequency dependence of attenuation and phase velocity for all temperatures where the mean has been taken of all sample orientations and measurement locations – dataset $[k]_{f,T}$ – are shown in figures 2.4 and 2.5. For each temperature, empirical

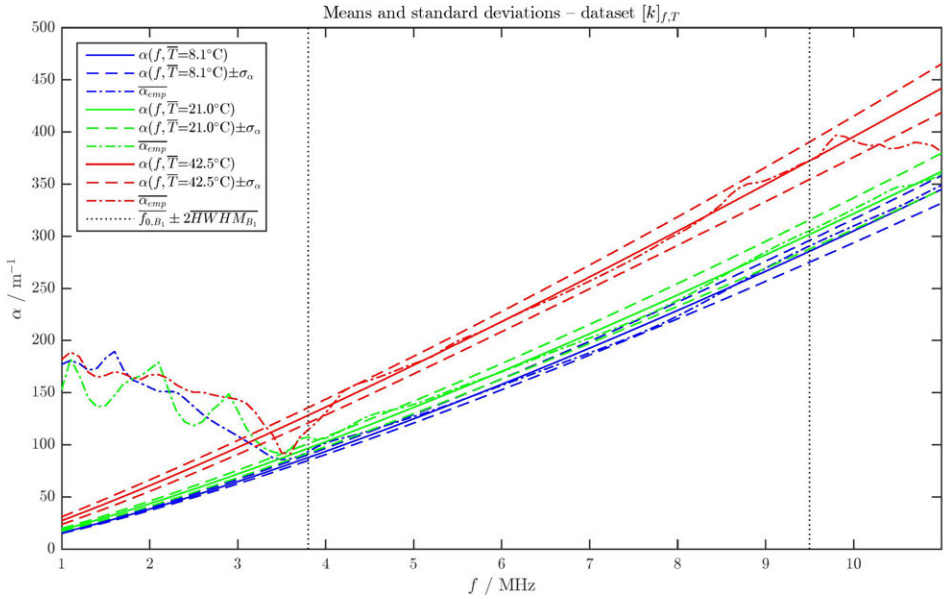

Figure 2.4: Power-law regression means and standard deviations fitted to empirical attenuation vs. frequency curves that are the mean of all sample orientations and measurement locations, for three individual temperatures. Regression interval, $4 \leq f/\text{MHz} \leq 10$. For the three sets of curves each containing solid, dashed, and dot-dashed curves, the top set corresponds to $\overline{T} = 42.5°\text{C}$, the middle to $\overline{T} = 21.0°\text{C}$, and the bottom to $\overline{T} = 8.1°\text{C}$.

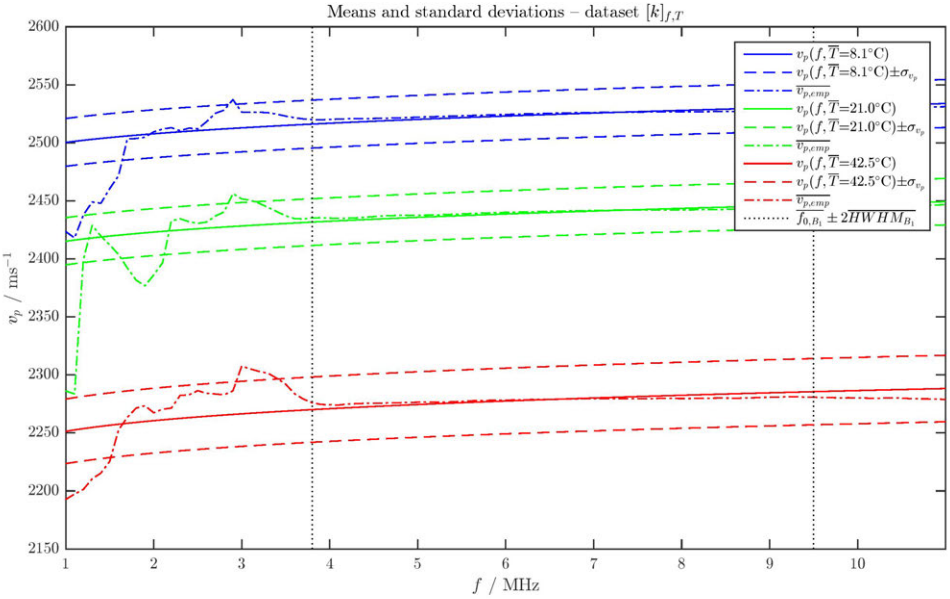

Figure 2.5: Power-law regression means and standard deviations fitted to empirical phase velocity vs. frequency curves that are the mean of all sample orientations and measurement locations, for three individual temperatures. Regression interval, $4 \leq f/\text{MHz} \leq 10$. For the three sets of curves each containing solid, dashed, and dot-dashed curves, the top set corresponds to $\overline{T} = 8.1°\text{C}$, the middle to $\overline{T} = 21.0°\text{C}$, and the bottom to $\overline{T} = 42.5°\text{C}$.

attenuation, α_{emp}, and phase velocity, $v_{p,emp}$, vary smoothly with frequency over the regression interval for which significant frequency content exists. Least squares regressions of attenuation with free parameters α_1 and y of equation (2.3.3) are obtained with associated regression standard deviations. The same are found for phase velocity with the single free parameter, v_{p1}. The goodness of fit is quantified via the coefficient of determination, R^2, in table 2.1. For attenuation $|1 - R^2| \ll 1$,

	$\overline{T} = 8.1°\text{C}$	$\overline{T} = 21.0°\text{C}$	$\overline{T} = 42.5°\text{C}$
$R^2(\alpha_{emp}(f), \alpha(f))$	0.996	0.996	0.997
$R^2(v_{p,emp}(f), v_p(f))$	0.686	0.512	-7.93

Table 2.1: Coefficients of determination, R^2, for the means of attenuation, $\alpha(f)$, and phase velocity, $v_p(f)$, that include all sample orientations and measurement locations, for three individual temperatures.

suggesting very good agreement between that predicted in equation (2.3.3) and that obtained empirically via the method in section 2.5. The R^2 is not close to unity for phase velocity, and a slight negative gradient of velocity with frequency in the data for $\overline{T} = 42.5°\text{C}$ yields a negative R^2 value. This is probably in part caused by constraint of the function form of velocity with frequency to a single free variable imposed by the causality constraint of the Kramers-Kronig relation expressed in equation (2.3.4), compared with attenuation that has two free variables. These R^2 values can be brought into context through analysis of the fractional uncertainties in standard deviations of these regressions to highlight their relative uncertainty ranges and consistency of measurement. These are obtained for attenuation for all depths, temperatures, and directions via,

$$\epsilon_{\alpha(f)} = \frac{\sigma_\alpha(f)}{\alpha(f)}, \tag{2.6.2}$$

and for phase velocity via,

$$\epsilon_{v_p(f)} = \frac{\sigma_{v_p}(f)}{v_p(f)}, \tag{2.6.3}$$

and shown in figure 2.6. The fractional uncertainties are low and approximately constant other than the inherent behaviour $\epsilon_\alpha \to \infty$ as $f \to 0$ because $\alpha(f = 0) = 0$. Importantly, the inferior R^2 values of $v_p(f)$ are of low significance because

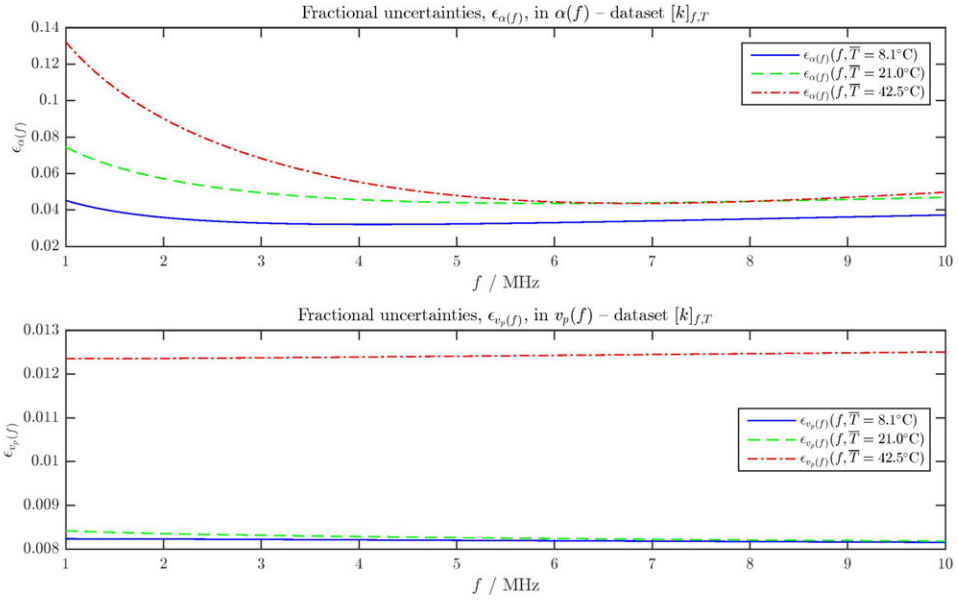

Figure 2.6: Attenuation (top) and phase velocity (bottom) frequency dependence fractional uncertainties, ϵ, in standard deviations that are the mean of all sample orientations and measurement locations, for three individual temperatures.

discrepancies between v_p and $v_{p,emp}$ over the regression interval in figure 2.5 are much smaller than the now quantified, small standard deviation fractional uncertainties. Uncertainties in measurement of acoustic properties parameters shall now be determined, such that overall uncertainties can be obtained for empirical attenuation and phase velocity. Sample thickness is measured at 24 inspection locations, excluding the centre that is unreachable with a micrometer screw gauge. The central thickness is taken to be the mean of the adjacent 8. The micrometer has a measurement uncertainty of $\delta_h = 0.01\text{mm}$. The thicknesses of samples **I**, **II**, and **III** are $x_{s,\mathbf{I}} \pm \sigma_{x_{s,\mathbf{I}}} = 10.15 \pm 0.02\text{mm}$, $x_{s,\mathbf{II}} \pm \sigma_{x_{s,\mathbf{II}}} = 10.64 \pm 0.03\text{mm}$, and $x_{s,\mathbf{III}} \pm \sigma_{x_{s,\mathbf{III}}} = 10.66 \pm 0.02\text{mm}$. These adhere to the favoured, $h \approx 10\text{mm}$, specified in section 2.5. Any variation in thickness for different i and j is not important because acoustic properties measurements are independent at each location. A fractional uncertainty can be obtained for all 75 locations, the mean of which constitutes a single estimate of this,

$$\epsilon_h = \overline{\left(\frac{\delta_h}{h}\right)} = 9.54 \times 10^{-4}. \tag{2.6.4}$$

Because $x_s = 2h$, the same fractional uncertainty applies to the propagation path

in the sample,

$$\epsilon_{x_s} = \epsilon_h = 9.54 \times 10^{-4}. \tag{2.6.5}$$

The linear thermal expansion coefficient of HDPE is of the order $\kappa \sim 10^{-4}\mathrm{K}^{-1}$ therefore the sample, or HDPE pipe, would only expand approximately 0.1% if its temperature increased by 10°C. Consequently, thermal expansion is a source of negligible measurement uncertainty. Uncertainties in the velocities and densities that describe transmittance in equation (2.4.9) are shown to be negligible in the discussion associated with that equation, therefore the overall uncertainty in transmittance can be neglected.

Temperatures at three times during each set of 25 measurements are shown in table 2.2. A single fractional uncertainty is obtained by taking the mean of the 9 indi-

	first time	**second time**	**third time**	**mean**	**standard deviation**
I	8.3	7.8	8.0	8.0	0.3
II	8.4	8.5	8.0	8.3	0.3
III	8.3	7.9	7.8	8.0	0.3
I	20.6	20.8	20.9	20.8	0.2
II	21.0	21.3	21.1	21.1	0.2
III	21.1	21.2	21.1	21.1	0.1
I	42.1	42.5	42.3	42.3	0.2
II	42.5	42.6	42.7	42.6	0.1
III	42.5	42.4	42.5	42.5	0.1

Table 2.2: Temperatures recorded at three times during 25 measurements for all samples, the mean of each set of three, and their standard deviations.

vidual fractional uncertainties for the three temperature ranges and three samples, where lower temperatures have above mean fractional uncertainties and vice versa for higher temperatures. The temperature fractional uncertainty is

$$\epsilon_T = \overline{\left(\frac{\sigma_T}{T}\right)} = 1.60 \times 10^{-2}, \tag{2.6.6}$$

where σ_T are the standard deviations of each set of three temperature measurements. While three measurements are few, the favoured and implemented standard deviation formulation is unbiased and therefore remains relatively accurate for few

samples. Using quadrature, the total measurement fractional uncertainty is

$$\epsilon_m = \left(\epsilon_{x_s}^2 + \epsilon_T^2\right)^{\frac{1}{2}} = 1.61 \times 10^{-2}, \tag{2.6.7}$$

where ϵ_T is the dominant term. The upper limit on the mean total attenuation and phase velocity fractional uncertainties for all pipe temperatures, directions, and radial depths taken at inspection frequency $f = 2.25$MHz that incorporates both variation in repeat measurements and uncertainty in individual measurements are

$$\epsilon_{\alpha(f=2.25\text{MHz})} \rightarrow \left(\epsilon_{\alpha(f=2.25\text{MHz})}^2 + \epsilon_m^2\right)^{\frac{1}{2}} = 5.81 \times 10^{-2}; \tag{2.6.8}$$

and

$$\epsilon_{v_p(f=2.25\text{MHz})} \rightarrow \left(\epsilon_{v_p(f=2.25\text{MHz})}^2 + \epsilon_m^2\right)^{\frac{1}{2}} = 1.88 \times 10^{-2}. \tag{2.6.9}$$

These frequency regression fractional uncertainties should be considered an upper limit on acoustic properties uncertainty. This is because the variation in acoustic properties datasets resulting from different propagation depths and directions are here being treated as incoherent noise rather than as physically meaningful variations and are therefore contributing to a larger standard deviation about the mean of these variations rather than being kept as separate datasets.

In progression, what follows is a full parameterisation of dispersion, that incorporates dependence on frequency, depth, temperature, and direction. It uses all acoustic properties data obtained and can provide accurate estimates of attenuation and phase velocity for the ranges of these parameters that are relevant to HDPE pipe inspection. This dispersion parameterisation improves upon the upper limit of acoustic properties uncertainty provided in equation (2.6.8).

To fully describe the simultaneous variation of attenuation and phase velocity with all their parameters, and theoretical constraints in these parameters, requires application of a multivariate regression technique with constrained inputs. As such, a neural network regression algorithm is used to obtain six descriptions of acoustic properties, which are of attenuation and phase velocity in three directions, $\alpha_{\mathbf{I},\mathbf{II},\mathbf{III}}^{NN}$

and $v_{p,\mathbf{I},\mathbf{II},\mathbf{III}}^{NN}$, from three parameters, which are frequency, f, depth, l, and temperature, T.

The neural network algorithm is validated with a fair statistical test by reserving a certain proportion of dataset samples for validation, while the majority is used to train the algorithm [34]. The acoustic properties to which the algorithm is applied are not the raw datasets but the Kramers-Kronig and viscoelastic constrained regressions with frequency, $\alpha(f)$ and $v_p(f)$, described in equations (2.3.3) and (2.3.5), for which regressions exist for all combinations of depth, temperature, and direction. This constraint must be applied on the neural network inputs because the neural network parameters are themselves only constrained by the number of 'hidden layers' it uses. These are equivalent to the number of times the algorithm generates an output from one parameter then uses this output for the input to describe the variation with the next parameter.

Consequently, the algorithm is here optimised by using an equal number of hidden layers to the number of parameters, which is three, excluding direction, for which three separate outputs are generated for attenuation and three for phase velocity. For each acoustic property, the three directions may be blended in a spherical coordinate system where, for HDPE joint inspection, the azimuthal angle is the angle of tilt of the array away axial alignment, which should ideally be 0° for current pipe joint inspections, and the polar angle is the angle of wave propagation within HDPE that is refracted towards the axial direction via Snell's law applied to the water wedge angle. Neural network algorithms may have stochastic outputs, which can be exploited by repeating the algorithm on the dataset until an optimal solution is obtained. The outputs are optimised by this approach for the following constraints:

1. the fractional discrepancies from the unconstrained datasets α_{emp} and $v_{p,emp}$ are minimised where peak frequency content occurs, $f = 7$MHz, as specified in equation (2.6.1)

2. the fractional discrepancies from $\alpha(f)$ and $v_p(f)$ are accepted or rejected based on a threshold value for discrepancy at the specified inspection frequency, $f = 2.25$MHz

The combination of the two criteria ensures strong, direct adherence to the raw data acoustic properties at the frequency where this data is most reliable and also

adherence to the constrained acoustic properties at a frequency relevant to ultrasonic NDE of HDPE pipe joints.

These fractional differences are now quantified and shown in figures 2.9 to 2.20. At an inspection frequency, the mean over all parameters of the fractional difference between the neural network regression of attenuation and the associated Kramers-Kronig and viscoelastic constrained frequency power-law fit is $\epsilon_{\alpha_{reg}}(f{=}2.25\text{MHz}) = 1.13{\times}10^{-2}$. The equivalent fractional difference for phase velocity is $\epsilon_{v_{p,reg}}(f{=}2.25\text{MHz}) = 1.46{\times}10^{-3}$. At the raw dataset modal spectral amplitude, the mean fractional difference of the attenuation parameterisation from the raw dataset is $\epsilon_{\alpha_{emp}}(f{=}7\text{MHz}) = 3.26 \times 10^{-2}$ and similarly for phase velocity, $\epsilon_{v_{p,emp}}(f{=}7\text{MHz}) = 2.03 \times 10^{-3}$. The fractional differences from the frequency regressions and those from the raw datasets are independent measures of uncertainty in the same neural network parameterisations. Consequently, the maxima of the two associated fractional differences are conservative estimators of uncertainty in these parameterisations. These are, for both attenuation and phase velocity, the differences from the raw datasets, which are $\epsilon_\alpha = 3.26 \times 10^{-2}$ and $\epsilon_{v_p} = 2.03 \times 10^{-3}$. The result is single estimates of uncertainty in acoustic properties descriptions for HDPE pipe joints that incorporate all parameters and are, at their core, quadrature combinations of uncertainties from standard deviations in regressions to parameterised datasets and from the associated physical measurement uncertainties used to obtain these datasets, given in equation (2.6.7). For attenuation and phase velocity these are

$$\epsilon_\alpha \rightarrow \left(\epsilon_\alpha^2 + \epsilon_m^2\right)^{\frac{1}{2}} = 3.64 \times 10^{-2}; \tag{2.6.10}$$

and

$$\epsilon_{v_p} \rightarrow \left(\epsilon_{v_p}^2 + \epsilon_m^2\right)^{\frac{1}{2}} = 1.62 \times 10^{-2}. \tag{2.6.11}$$

The attenuation and phase velocity of HDPE pipe material has been determined to within an uncertainty of better than 4% and 2% respectively for a large range of inspection frequencies, depths, and temperatures, for the three orthogonal directions within the pipe.

Example values generated, using the above acoustic properties parameterisation, for attenuation and phase velocity for the case of nondestructive evaluation of a HDPE pipe joint using a directive ultrasonic source, for example an array or an angled single probe are provided in appendix 2.8.1. The acoustic properties, obtained there for a specific source location where peak wave amplitude occurs, are concluded to be applicable to a large range of inspection scenarios. Within the associated uncertainty bounds, this, for example, includes any inspection from parallel to normal in the axial-radial plane.

Between typical ultrasonic inspections of HDPE pipes the temperature, for example, can vary by many degrees. Also, if inspections are conducted in service, there may be temperature gradients between the external and internal surfaces of the pipe. Some exemplar benefits of the novel acoustic properties descriptions to image of HDPE pipe joints are provided here.

From appendix 2.8.1, for a signal that has propagated a total of 200mm through the pipe, the amplitude ratio between 10 and 20°C pipe temperatures for the 1MHz components of the waves is of the order of 1.6 and for the 5MHz components of the waves is 9.6. The difference in time of arrival between signals recorded at 10 and 20°C for the 1MHz and 5MHz components are 2.8% and 2.6% respectively. As well as the associated reduction in sizing and location errors yielded by the provided temperature dependence of attenuation and phase velocity, the frequency dependence of the phase velocity prevents dispersive effects within the image that otherwise cause defects signatures to become highly nonlocal. Consequently, these acoustic properties provide the means to image accurately and reliably.

2.7 Discussion and conclusions

Provided above is the method for obtaining accurate and reliable acoustic properties of viscoelastics and other similar media. The approach is here applied to HDPE pipes but it is readily applicable to other such materials. This HDPE pipe dispersion data is novel because it accurately describes dependence on wave frequency, propagation depth within the pipe (radial heterogeneity), temperature of the pipe, and propagation direction within the pipe (anisotropy). Uncertainty in such real data is unavoidable and is ideally reduced to an extent that these variables can be described with statistical significance using such a dataset as this. The set contains

5 spatially independent waveforms for every potential parameter combination and in total contains records of 225 fully independent spatial measurement locations, where each recorded waveform is temporally averaged 1000 times to reduce noise. Detailed in the procedures for obtaining the experimental data and the analysis and data processing are multiple refinements and optimisations that also increase accuracy and reliability. Consequently, uncertainties in acoustic properties dependence on the above variables are better than 4% and 2% respectively for attenuation and phase velocity. The variation of dispersion with these properties is, in some cases, as little as a few percent over the range of values expected for HDPE pipe joint inspection, and therefore these low data uncertainties are necessary and sufficient for these novel acoustic properties descriptions and the provided full parameterisation of them.

These functional descriptions of HDPE pipe attenuation and phase velocity are a specific implementation of a more generally applicable formulation derived here for ultrasonic viscoelastic bulk wave propagation that adheres to the causality constraint imposed by the Kramers-Kronig relation.

In ultrasonic NDE of HDPE pipe joints, as with much other ultrasonic NDE, it is critical for accurate and reliable inspection that the acoustic properties are well characterised in this way. For example, potential daytime temperature variations are shown here to result in amplitude discrepancies of up to a factor of 10. Also, daytime temperature variation can result in a few percent difference in wave arrival time. Only with these accurate acoustic properties can the propagation and interaction of waves in the target medium be understood, such that potential defects can be located, sized, or characterised without major errors that could otherwise lead to incorrect decisions concerning replacement or repair of defective components. Simulation of waves in complex media such as HDPE informs the development of an inspection system, and for the system itself to be accurate and reliable, the well characterised acoustic properties must be accurately represented.

References

[1] E. Leinov, M.J.S. Lowe, P. Cawley, *Ultrasonic isolation of buried pipes*, Journal of Sound and Vibration, **363**, 2016.

[2] M.L. Palmeri, A.C. Sharma, R.R. Bouchard, R.W. Nightingale, and K.R. Nightingale, *A finite-element method model of soft tissue response to impulsive acoustic radiation force*, Ultrasonics, Ferroelectrics, and Frequency Control, IEEE Transactions on, **52**(10), 2005.

[3] P. Moczo, J. Kristek, M. Galis, P. Pazak, and M. Balazovjech, *The finite-difference and finite-element modelling of seismic wave propagation and earthquake motion*, Acta Physica Slovaca, **57**(2), 2007.

[4] D. MacLennan, J. Allen, I.G. Pettigrew, C.R. Bird, *Phased Array Inspection Solution for HDPE Butt Welds*, 51st Annual Conference of the British Institute of Non-destructive Testing, Northamptonshire, 335-343 (2012).

[5] F. Hagglund, M. Spicer, and M. Troughton, *Development of Phased Array Ultrasonic Inspection Techniques for Testing Welded Joints in Plastic (PE) Pipes*, 18th World Conference on Nondestructive Testing, Durban, 2782-2791 (2012).

[6] Nondestructive Evaluation: Technique Development to Evaluate the Joint Strength of High-Density Polyethylene Butt Fused Pipe Joints, Electric Power Research Institute, Palo Alto, CA, 2014. 3002003032.

[7] R.J. Stakensborghs, *Validation of a microwave inspection system for HDPE butt fusions*, Proceedings of the ASME 2014 Pressure Vessel & Piping Conference, California, Vol. 5 (2014).

[8] W. Sachse and Y.-H. Pao, *On the determination of phase and group velocities of dispersive waves in solids*, J. Appl. Phys, **49**(8), 1978.

[9] R.A. Kline, *Measurement of attenuation and dispersion using an ultrasonic spectroscopy technique*, J. Acoust. Soc. Am., **76**(2), 1984.

[10] V.K. Kinra and V.R. Iyer, *Ultrasonic measurement of the thickness, phase, velocity, density or attenuation of a thin-viscoelastic plate. Part I: the forward problem*, Ultrasonics, **33**(2), 1995.

[11] T.L. Szabo, *Causal theories and data for acoustic attenuation obeying a frequency power law*, J. Acoust. Soc. Am., **97**(1), 1995.

[12] J. Wu, *Determination of velocity and attenuation of shear waves using ultrasonic spectroscopy*, J. Acoust. Soc. Am., **99**(5), 1996.

[13] P. He, *Experimental verification of models for determining dispersion from attenuation*, Ultrasonics, Ferroelectrics, and Frequency Control, IEEE Transactions on, **46**(3), 1999.

[14] T.L. Szabo and J. Wu, *A model for longitudinal and shear wave propagation in viscoelastic media*, J. Acoust. Soc. Am. **107**(5) Pt. 1, 2000.

[15] P. He and J. Zheng, *Acoustic dispersion and attenuation measurement using both transmitted and reflected pulses*, Ultrasonics, **39**, 2001.

[16] H. Wang, *Improved ultrasonic spectroscopy methods for characterization of dispersive materials*, Ultrasonics, Ferroelectrics, and Frequency Control, IEEE Transactions on, **48**(4), 2001.

[17] R. Raisutis, R. Kazys, and L. Mazeika, *Application of the ultrasonic characterization methods for highly attenuating plastic materials*, NDT&E International, **40**, 2007.

[18] J.D. Ferry, *Viscoelastic properties of polymers*, 3rd ed., John Wiley & Sons, New York, 168-176 (1980).

[19] D.F. Specht, *A general regression neural network*, Neural Networks, IEEE Transactions on, **2**(6), 1991.

[20] Y. Lecun, L. Bottou, Y. Bengio, and P. Haffner, *Gradient-based learning applied to document recognition*, Proceedings of the IEEE, **86**(11), 1998.

[21] T.L. Szabo and J. Wu, *A model for longitudinal and shear wave propagation in viscoelastic media*, J. Acoust. Soc. Am., **107**(5), Pt. 1, 2000.

[22] X. Zhang, W. Chen, and C. Zhang, *Modied Szabo's wave equation for arbitrary frequency-dependent viscous dissipation in soft matter with applications to 3D ultrasound imaging*, Acta Mechanica Solida Sinica, **25**(5), 2012.

[23] F. Mainardi, *Fractional calculus and waves in linear viscoelasticity*, 1st ed., Imperial College Press, UK, 77-107 (2010).

[24] B.E. Treeby, J. Jaros, A.P. Rendell, and B.T. Cox, *Modeling nonlinear ultrasound propagation in heterogeneous media with power law absorption using a k-space pseudospectral method*, J. Acoust. Soc. Am. **131**(6), 2012.

[25] S. Holm and S.P. Nasholm, *A causal and fractional all-frequency wave equation for lossy media*, J. Acoust. Soc. Am., **130**(4), 2011.

[26] S.P. Nasholm and S. Holm, *On a fractional Zener elastic wave equation*, Fractional Calculus & Applied Analysis, **16**(1), 2013.

[27] S. Holm and S.P. Nasholm, *Comparison of fractional wave equations for power law attenuation in ultrasound and elastography*, Ultrasound in Med. & Biol., **40**(4), 2014.

[28] M. O'Donnell, E.T. Jaynes, and J.G. Miller, *Kramers-Kronig relationship between ultrasonic attenuation and phase velocity*, J. Acoust. Soc. Am. **69**(3) , 1981.

[29] K.R. Waters, J. Mobley, and J.G. Miller, *Causality-imposed (Kramers-Kronig) relationships between attenuation and dispersion*, Ultrasonics, Ferroelectrics, and Frequency Control, IEEE Transactions on, **52**(5), 2005.

[30] N.J.D. Nagelkerke, *A note on a general definition of the coefficient of determination*, Biometrika, **78**(3), 1991.

[31] J.O. Smith III, *Spectral Audio Signal Processing* (W3K Publishing, Lewiston, NY, USA), 57-63 (2011).

[32] P.H. Rogers and A.L. Van Buren, *An exact expression for the Lommel diffraction correction integral*, J. Acoust. Soc. Am., **55**(4), 1974.

[33] A.N. Kalashnikov and R.E. Challis, *Errors and uncertainties in the measurement of ultrasonic wave attenuation and phase velocity*, Ultrasonics, Ferroelectrics, and Frequency Control, IEEE Transactions on, **52**(10), 2005.

[34] C.M. Bishop, *Novelty detection and neural network validation*, IEE Proceedings - Vision, Image and Signal Processing, **141**(4), 1994.

[35] A.C. Taylor, *Structure, Properties & Applications of Polymers* lecture notes, Imperial College London, 2013.

2.8 Appendices

Figures from appendices are found in section 2.8.6.

2.8.1 Acoustic properties look-up tables

Provided in tables 2.3 and 2.4 are values generated, using the above acoustic properties parameterisation, for attenuation and phase velocity for the example of nondestructive evaluation of a HDPE pipe joint using an ultrasonic source, for example an array. The peak wave amplitude is directed towards the centre of the joint through-wall height, $h = 60$mm, and on the pipe surface the peak wave amplitude is offset from the fusion surface in the axial direction by an amplitude peak datum offset, $APDO = 57.5$mm. This is approximated as the sum of the distance from the datum to the front of the array wedge, the standoff, and half the wedge length. The chosen values of h and $APDO$ are used to specify an inspection angle with the HDPE pipe, which itself determines the relative contributions of the three anisotropic directions of dispersion, where here the circumferential contribution is set to zero to agree with the majority of such HDPE joint inspections. The two parameters, h and $APDO$, together define the angle of wave propagation in HDPE after forward beam diffraction at the water-HDPE interface.

These provided values are applicable, within uncertainty bounds, to all angles from parallel to normal in the axial-radial plane. This is because, varying either h or

$APDO$ by large fractions of the specified values used in tables 2.3 and 2.4 results in a relatively small change in propagation angle. For example, for throughwalls $h = (20, 100)$mm and $APDO = 57.5$mm the corresponding HDPE propagation angles are $\theta = (80, 50)^\circ$. This 30° difference in axial-radial relative contribution is a small fraction of the total anisotropy – exhibited with a 90° difference – which itself is a few percent. Therefore, the corresponding variation in acoustic properties at half throughwall height for different pipe thickness is for the majority of cases less than 1% for attenuation and less than a fraction of a percent for phase velocity, and so, for both acoustic properties, this is not statistically significant compared with the associated dispersion fractional uncertainties. As a result, the dispersion values presented in tables 2.3 and 2.4 are, within the provided fractional uncertainty ranges, applicable to the majority of radial depth, h, and amplitude peak datum offset, $APDO$, values.

2.8.2 Dispersion multidimensional parameterisation

As described above, a neural network algorithm on the multiparameter acoustic properties dataset that has previously been constrained via 1D power law fits in frequency to adhere to equations (2.3.3) and (2.3.5); these conditions impose viscoelastic and causality constraints on the input, and thus also the output, of the neural network algorithm. Example figures from this dispersion multidimensional parameterisation are shown here. The orientations of wave propagation through the pipe, **I**, **II**, and **III**, are blended with equal weighting to yield these examples. In figures 2.7 and 2.8, the stars represent a full acoustic properties dataset for each frequency surface, while more than the five depicted frequency increments, $f_0 = 1, 2, ..., 5$MHz, exist in the data used for the neural network regression. The regression hypersurface – multidimensional parameter space – has contour slices that are depicted for the same frequencies as the data points. These contours pass near the data points, demonstrating closeness of fit. The quantified greyscale duplicates the z-axis information.

In figure 2.7, the attenuation is again seen to vary with frequency for the family of five curves, where the lower frequencies result, as in the main text, in lower attenuations. Attenuation is also again seen to increase with temperature. The variation of attenuation is observable as not differing more than the 3.64% uncertainty of equa-

tion (2.6.10) and therefore the ultrasonic bulk wave longitudinal attenuation is not considered measurably anisotropic in HDPE pipe material. Using the same reasoning, ultrasonic bulk wave longitudinal attenuation is also not considered measurably heterogeneous in HDPE pipe material.
In figure 2.8, the phase velocity is again seen to vary slightly with frequency for the family of five curves, where the lower frequencies result, as in the main text, in lower phase velocities. Phase velocity is also again seen to decrease with temperature. The variation of phase velocity is observable as not differing more than the 1.62% uncertainty of equation (2.6.11) and therefore the ultrasonic bulk wave longitudinal phase velocity is not considered measurably anisotropic in HDPE pipe material. Using the same reasoning, ultrasonic bulk wave longitudinal phase velocity is also not considered measurably heterogeneous in HDPE pipe material.
The attenuation and phase velocity data and regression uncertainties used to obtain equations (2.6.10) to (2.6.11) are shown in figures 2.9 to 2.20. The datasets for temperatures close to $T = 8, 21, 42°\text{C}$ respectively are blue (dark in greyscale print), red (medium in greyscale print), and green (light in greyscale print). The data acquisition radial depths, $l = -20, -10, 0, 10, 20\text{mm}$ have respective datasets, circles, pluses, crosses, squares, and diamonds.

2.8.3 HDPE pipe sample thicknesses

The thicknesses of samples **I**, **II**, and **III** are shown in figures 2.21, 2.22, and 2.23. These adhere to the favoured, $h \approx 10\text{mm}$, specified in section 2.5. Any variation in thickness for different i and j is not important because acoustic properties measurements are independent at each location.

2.8.4 Polymers theory

Notes from a third year undergraduate Mechanical Engineering course on polymers by Dr Ambrose Taylor of Imperial College London [35] were studied and relevant information was extracted. Some of the key points include that:

1. Extruded semicrystalline thermoplastics such as HDPE should exhibit some anisotropy in sound velocity and attenuation.

2. Thermoplastics (particularly semicrystalline) have high volumetric shrinkage

when cooling. This leads to residual stresses being locked in. This is exacerbated by variable spatial cooling rates. Stresses occur when contraction occurs in different directions. Slow cooling reduces the lock in effect.

3. High pressure during the welding process may add residual stress.

4. In extrusion the first layer to cool is left in compression while the last is in tension.

5. In extrusion crystallisation is incomplete on the outer (rapidly) water-cooled surface.

6. HDPE is well described by a standard linear solid spring-dashpot model using a combination of parallel and series alignment.

7. Brittle failure is promoted by stress concentrations including sharp corners, holes, slots, welds, and inserts.

8. Pressurised components like pipes are susceptible to slow crack growth, especially where toughness is lower. For example, perpendicular to polymer chains or across weld lines.

2.8.5 High-density polyethylene (HDPE) polymer structure using optical transmission microscopy (OTM)

The HDPE pipe joint defect known as cold fusion is very challenging to detect using conventional NDE techniques, including with an ultrasonic array. Discussed in chapter 1, cold fusion is said to arise from the incomplete crossing of polymers in the region local to the fusion line where the two pipe ends meet. This could be potentially detected directly or otherwise inferred by the size of the weld heat affected zone (HAZ), where a smaller HAZ could suggest less heat energy and therefore a higher change of cold fusion. Both the incomplete polymer crossing and HAZ characteristics could potential be detected via direct inspection of the polymer structure using optical transmission microscopy (OTM) performed on slices of HDPE tens of nanometres thick. This destructive analysis can validate assumptions made about defects made on the nanometre scale.

Pursuing this aim, a microtome has been used to cut slices of HDPE from parent and weld material ranging from 25 to 100nm thick with the in-plane lengths being of the order of a few millimetres. These slices were transferred to glass slides and inspected using an OTM setup at 100× zoom with two polarising filters crossed at an angle of 65°, an angle chosen based on maximum image contrast. The polarising filters are used to express the birefringent nature of the polymer lamellae (ordered crystalline structure) because the crystalline structure refracts light by different degrees at different polarisations (oscillatory orientations). The result is brightly illuminated lamellae under crossed polarising filters where none were otherwise detectable, as shown in figures 2.25 and 2.26 where the former is the weld material with an angle between the polarisers of 0° and the latter is of the same slice at 65°. Figure 2.25 shows no discernible ordered polymer structure. Present instead is a relatively uniform distribution of light and dark patches where more and less light has transmitted across the entire in focus region which spans tens of microns.
In figure 2.26 the ordered polymer structure is evident in the form of lamellae. These bunches of polymer chains snake at right angles with major and minor lengths between right angles of approximately 3000 and 800nm. These span the 50μm height of the sample. Under crossed polarisers the parent material shows the same lamellae structure as the weld material, as seen in figure 2.27. Neither region was found to exhibit amorphous polymer structure that is expected to connect the highly ordered crystalline regions. Further investigation is required to determine whether there exists an appreciable difference in polymer structure at this scale. Future analysis of the polymer structure of cold welds and other defects could provide discernible differences.

2.8.6 Appendices figures

Found here are all the tables and figures of the appendices of chapter 2.

$T/°\mathrm{C}$ f/MHz	1	2	3	4	5
5	14.55	36.15	60.95	89.01	120.23
10	17.56	40.12	65.94	95.02	127.19
15	19.30	42.88	69.78	99.93	133.10
20	19.89	44.64	72.78	104.17	138.48
25	19.84	46.02	75.66	108.52	144.19
30	20.02	47.96	79.39	113.96	151.15

Table 2.3: HDPE pipe joint attenuation, α/m^{-1}, with fractional uncertainty, $\epsilon_\alpha = 3.64 \times 10^{-2}$, for a wave with its peak amplitude directed at half throughwall depth, $l = 0$, where $h/2 = 30\mathrm{mm}$, with pipe surface peak amplitude datum offset, $APDO = 57.5\mathrm{mm}$.

$T/°\mathrm{C}$ f/MHz	1	2	3	4	5
5	2514	2523	2526	2528	2529
10	2488	2498	2502	2504	2506
15	2457	2468	2473	2475	2477
20	2420	2432	2438	2441	2442
25	2380	2393	2399	2402	2404
30	2340	2354	2360	2363	2365

Table 2.4: HDPE pipe joint phase velocity, v_p/ms^{-1}, with fractional uncertainty, $\epsilon_{v_p} = 1.62 \times 10^{-2}$, for a wave with its peak amplitude directed at half throughwall depth, $l = 0$, where $h/2 = 30\mathrm{mm}$, with pipe surface peak amplitude datum offset, $APDO = 57.5\mathrm{mm}$.

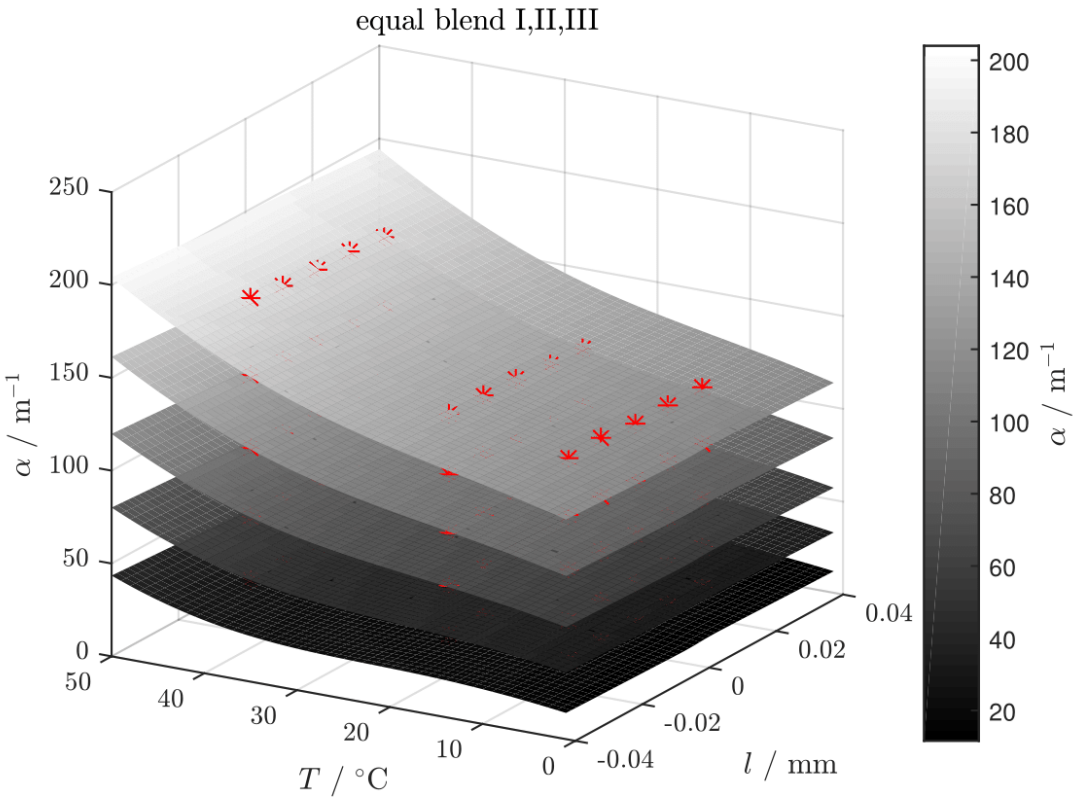

Figure 2.7: The multidimensional parameterisation of HDPE pipe material attenuation, α, varying with temperature, T, radial location through the pipe, l, and blended over wave propagation orientations through the pipe, **I**, **II**, and **III**. Some experimental data points are represented with stars. The corresponding parameterisations are the greyscale curves with duplicate information on the z-axis. From lowest to highest attenuation, the family of curves are at $f_0 = 1, 2, ..., 5$MHz.

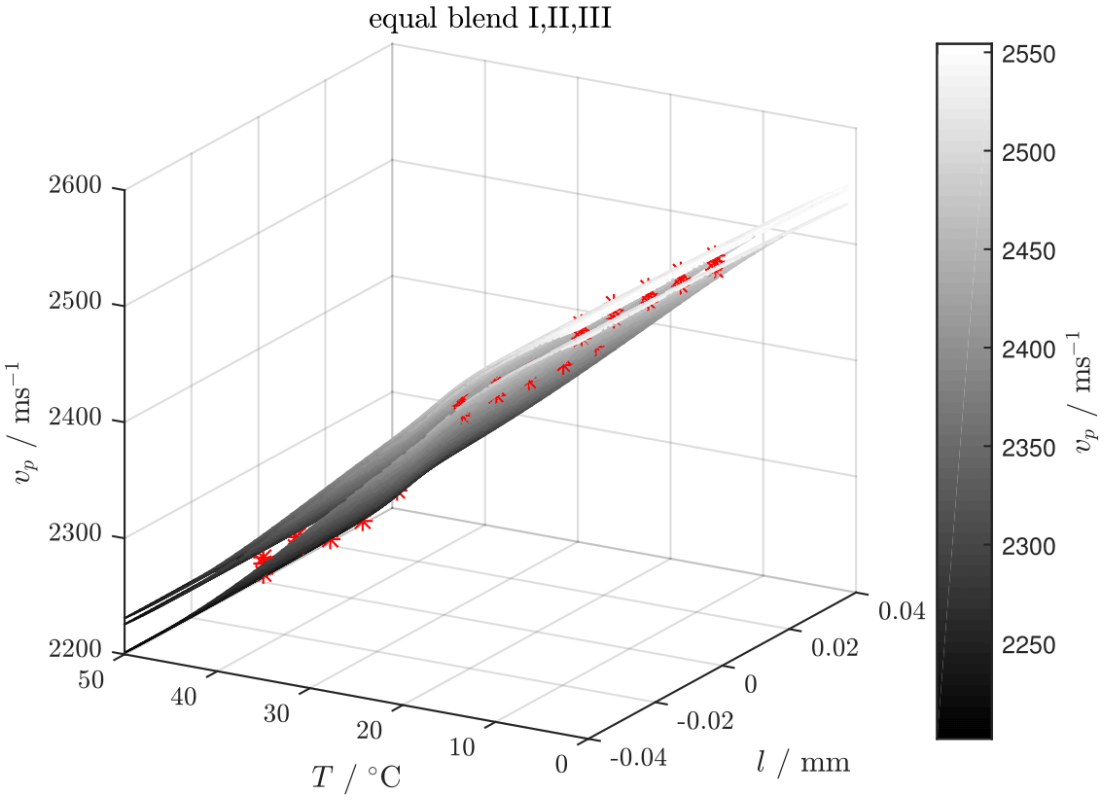

Figure 2.8: The multidimensional parameterisation of HDPE pipe material phase velocity, v_p, that is otherwise the same as for attenuation in figure 2.7.

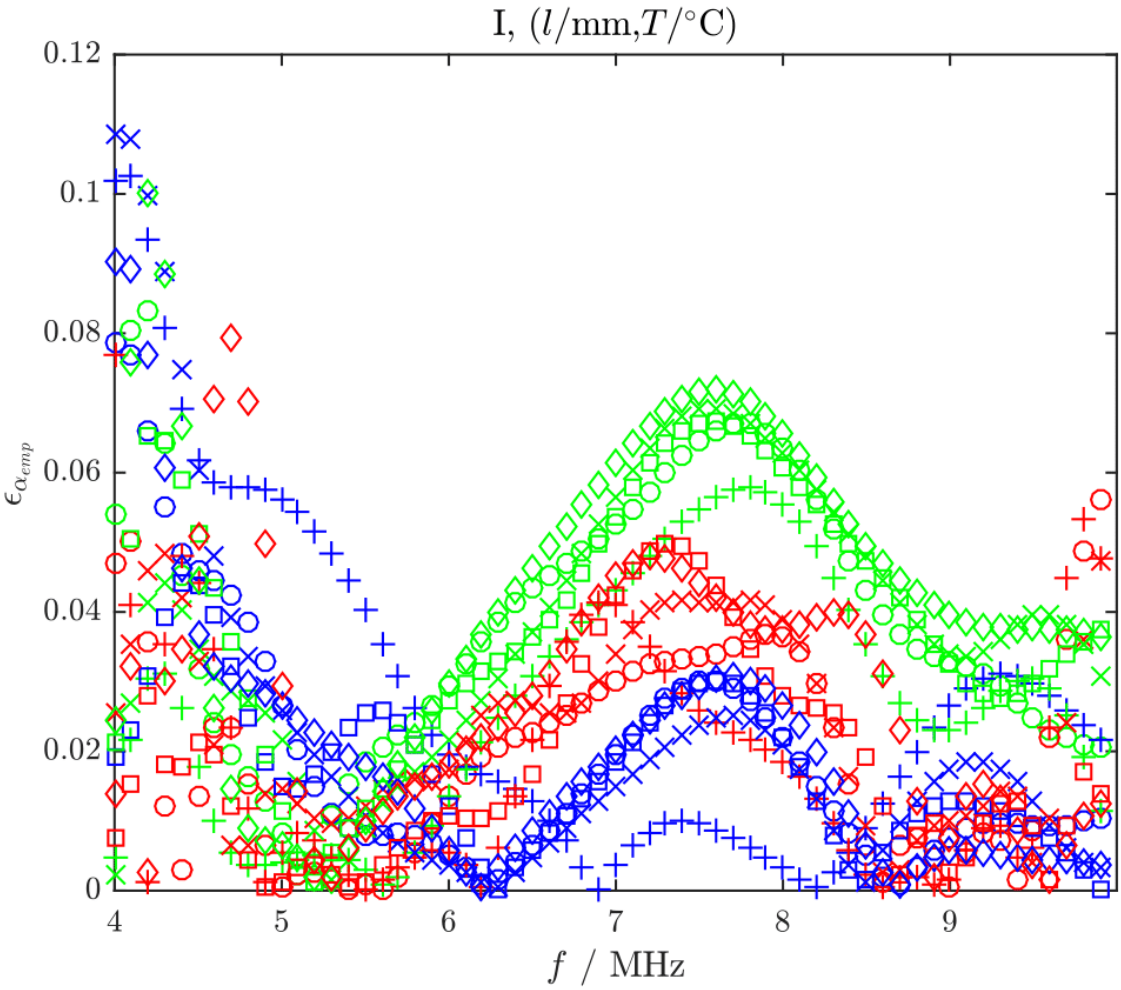

Figure 2.9: The attenuation data uncertainties, $\epsilon_{\alpha_{emp}}$, for wave propagation orientation **I** that is used to obtain equation (2.6.10). The datasets for temperatures close to $T = 8, 21, 42$°C respectively are blue (dark in greyscale print), red (medium in greyscale print), and green (light in greyscale print). The data acquisition radial depths, $l = -20, -10, 0, 10, 20$mm have respective datasets, circles, pluses, crosses, squares, and diamonds.

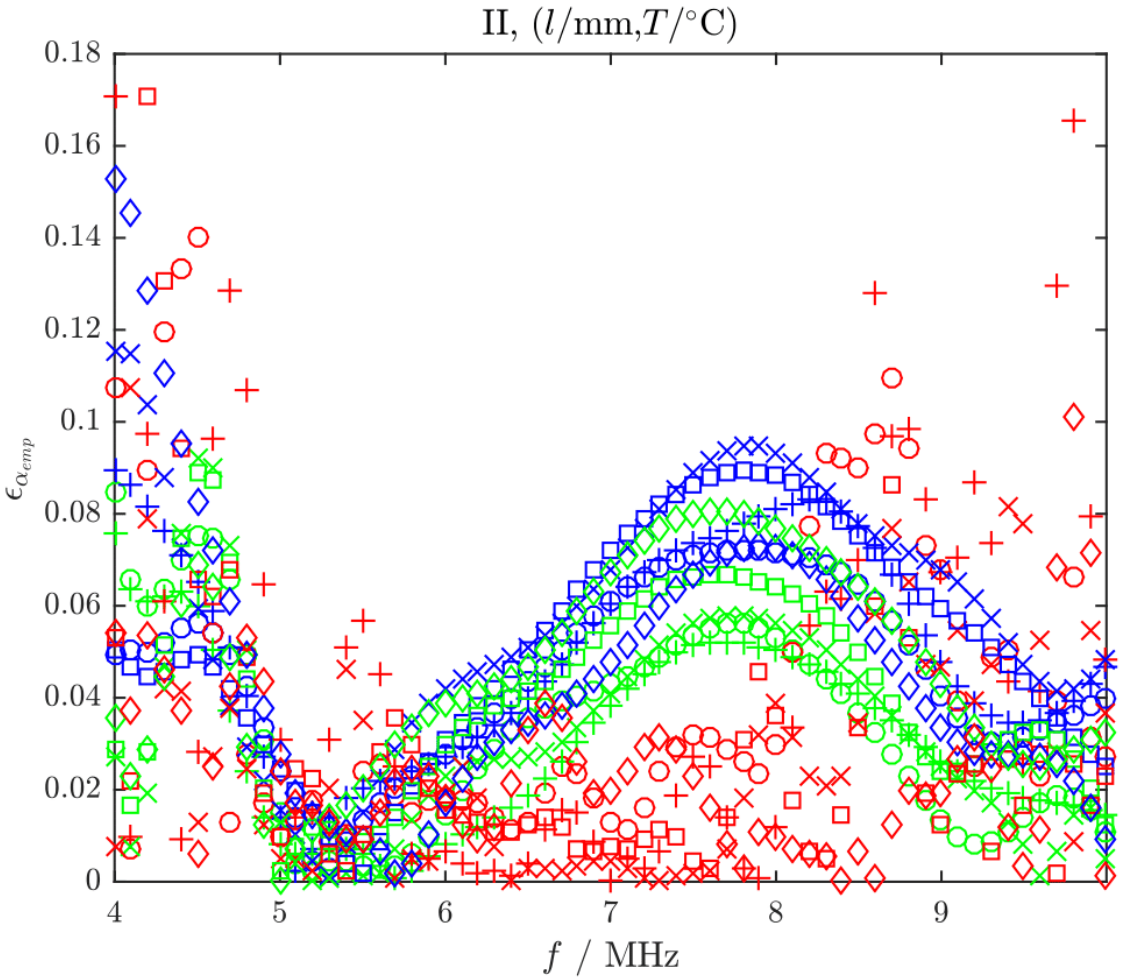

Figure 2.10: The attenuation data uncertainties, $\epsilon_{\alpha_{emp}}$, for wave propagation orientation **II** that is used to obtain equation (2.6.10). This figure is otherwise the same as figure 2.9.

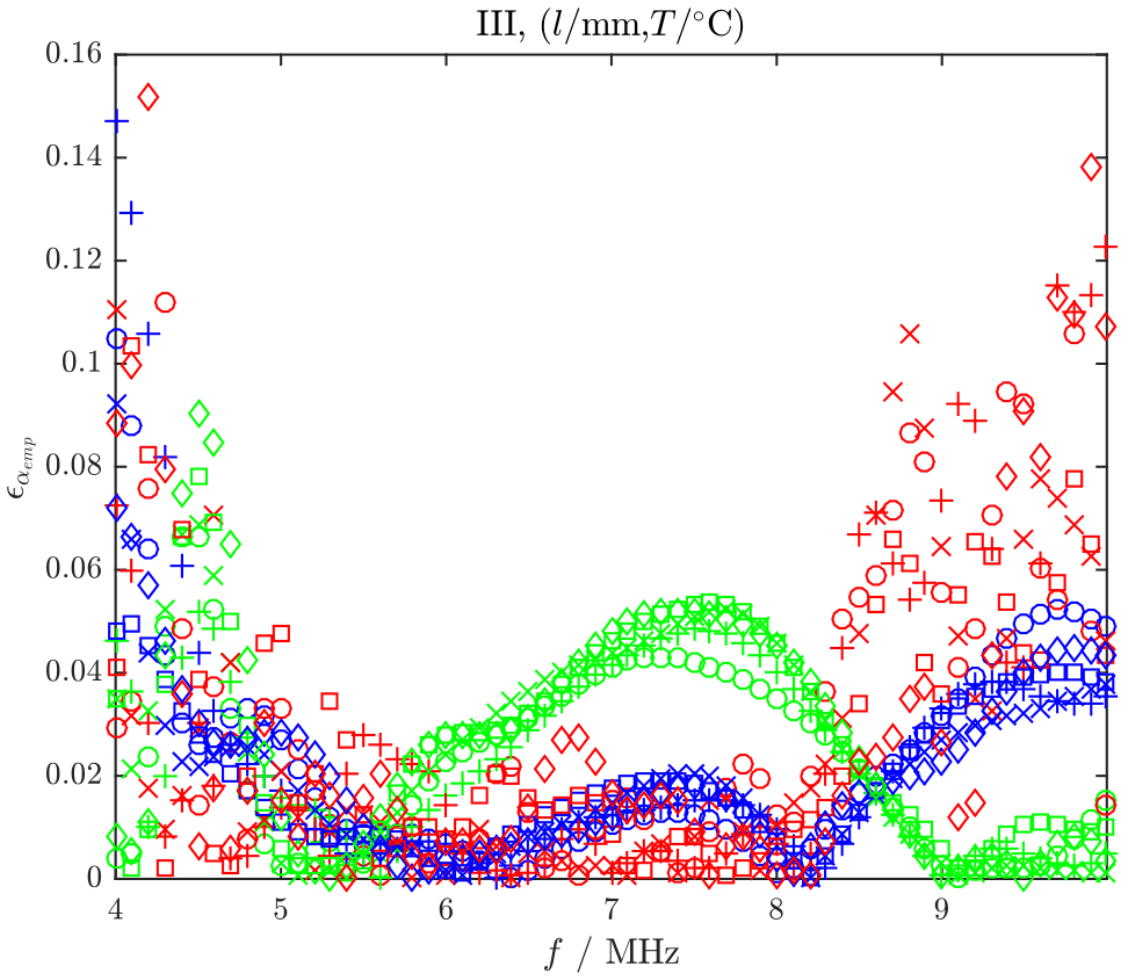

Figure 2.11: The attenuation data uncertainties, $\epsilon_{\alpha_{emp}}$, for wave propagation orientation **III** that is used to obtain equation (2.6.10). This figure is otherwise the same as figures 2.9 and 2.10.

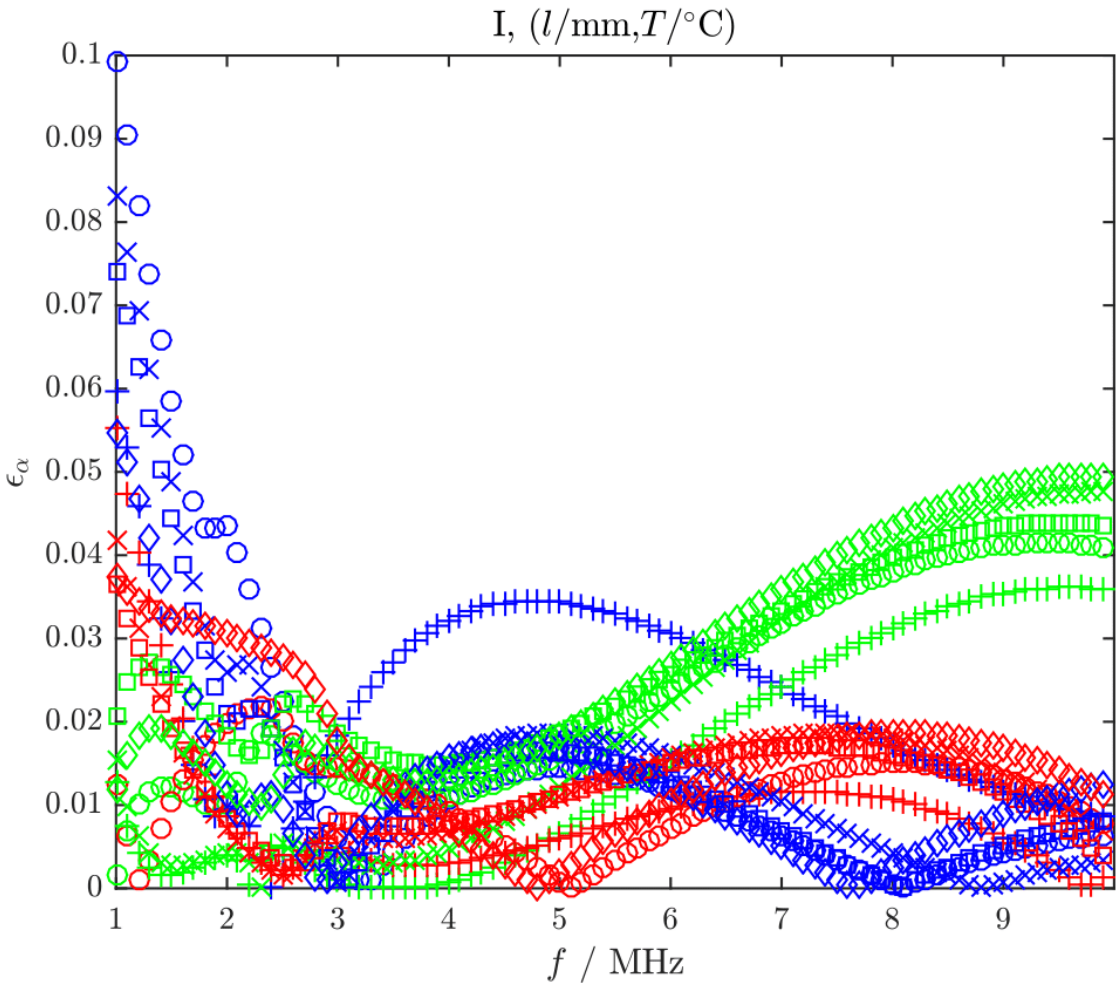

Figure 2.12: The attenuation regression uncertainties, ϵ_α, for wave propagation orientation **I** that is used to obtain equation (2.6.10). This figure is otherwise the same as figures 2.9 to 2.11.

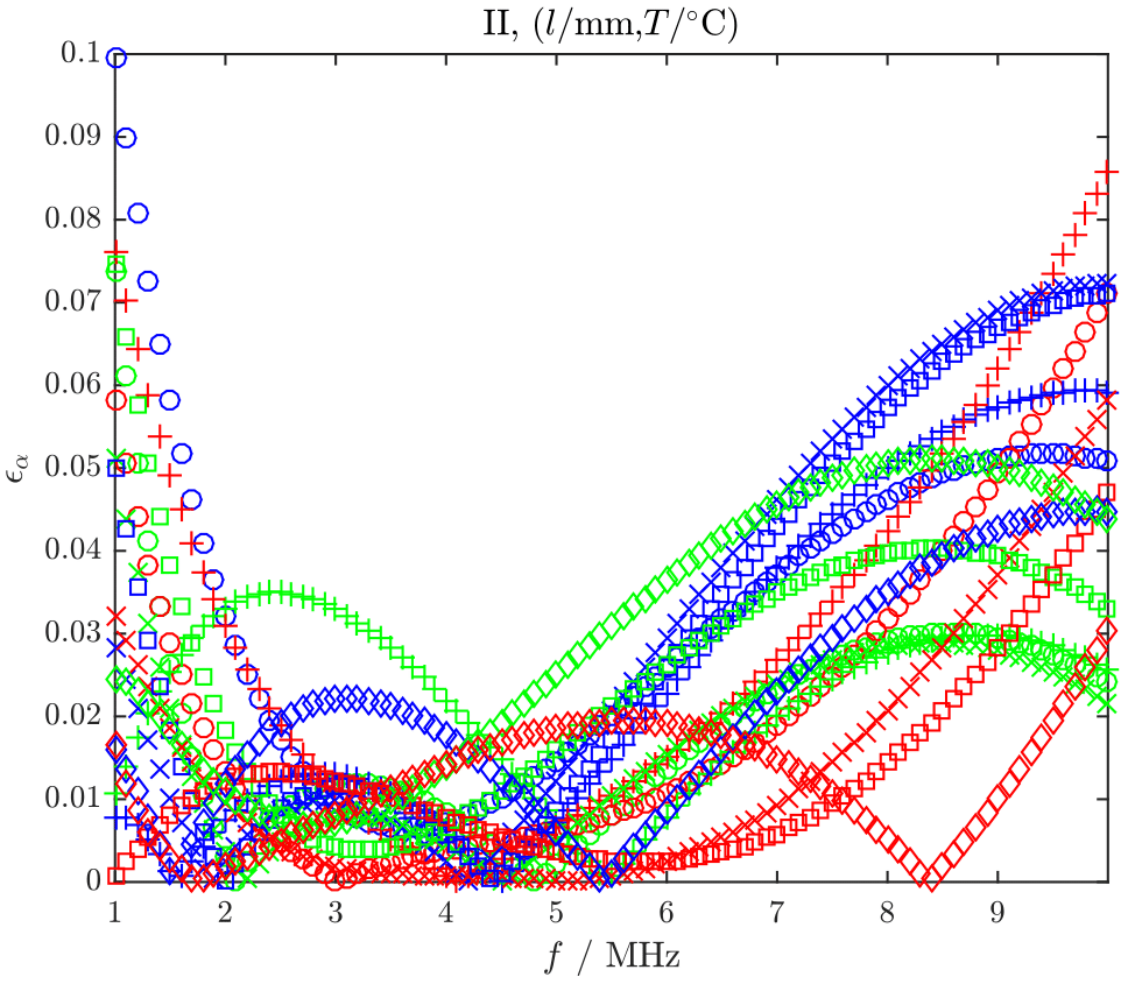

Figure 2.13: The attenuation regression uncertainties, ϵ_α, for wave propagation orientation **II** that is used to obtain equation (2.6.10). This figure is otherwise the same as for figures 2.9 to 2.12.

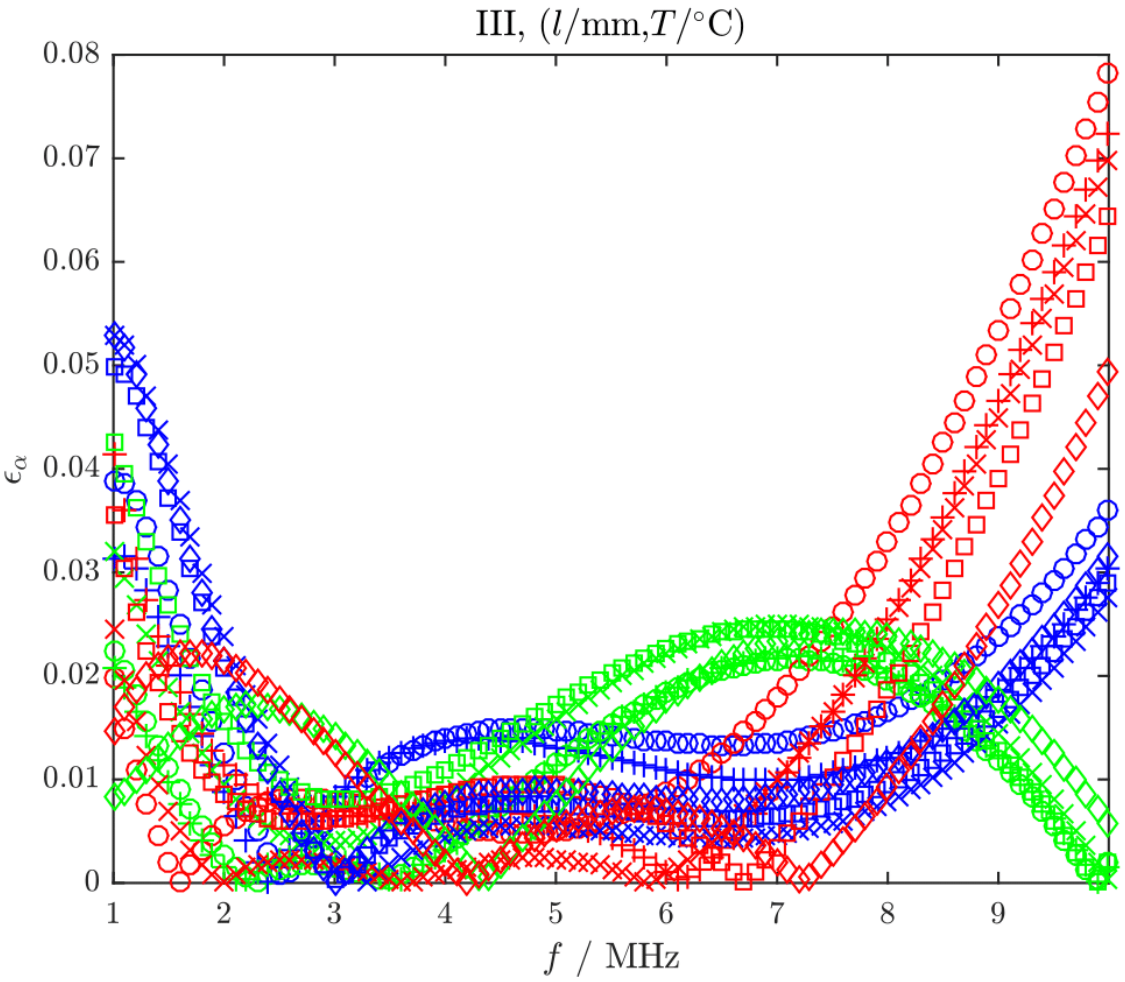

Figure 2.14: The attenuation regression uncertainties, ϵ_α, for wave propagation orientation **III** that is used to obtain equation (2.6.10). This figure is otherwise the same as figures 2.9 to 2.13.

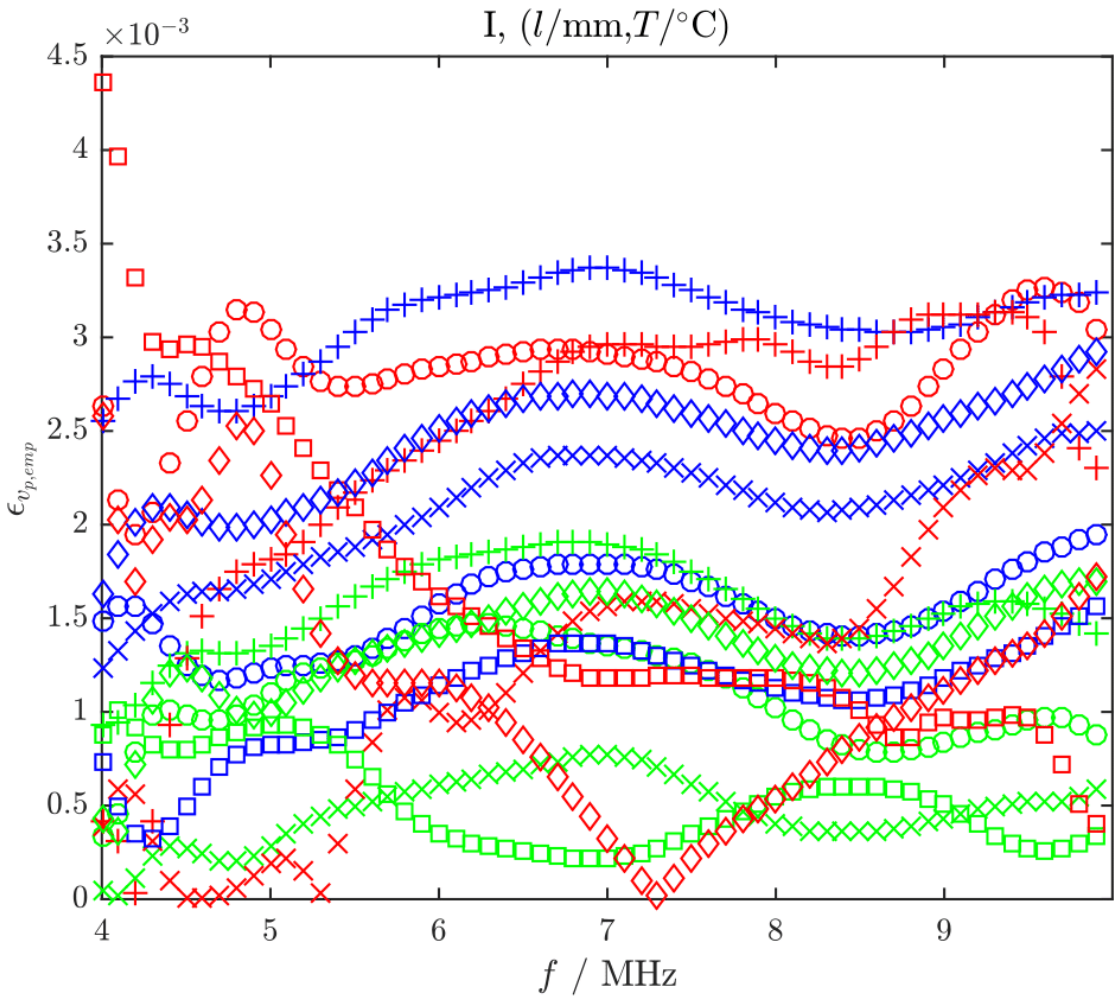

Figure 2.15: The phase velocity data uncertainties, $\epsilon_{v_{p,emp}}$, for wave propagation orientation **I** that is used to obtain equation (2.6.11). This figure is otherwise the same as figures 2.9 to 2.14.

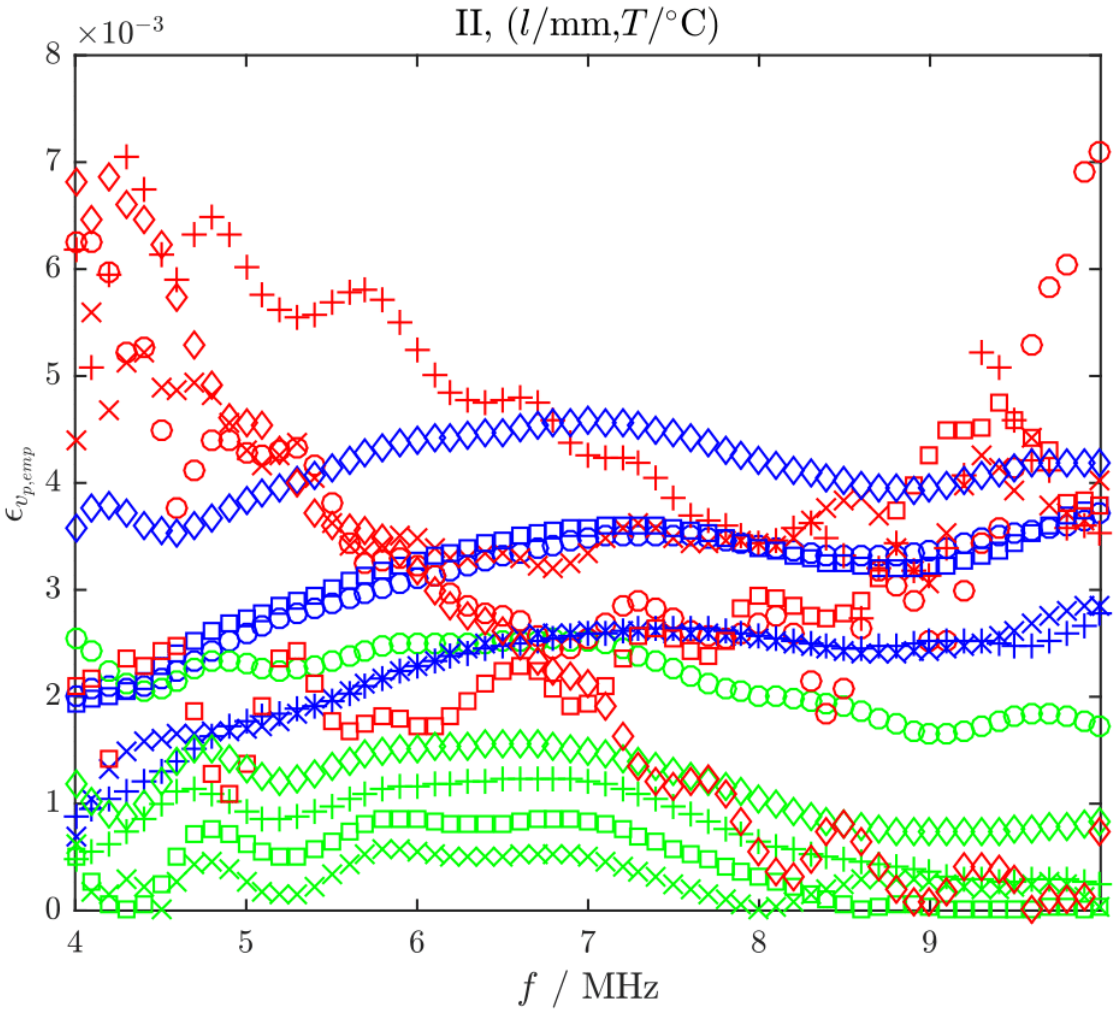

Figure 2.16: The phase velocity data uncertainties, $\epsilon_{v_{p,emp}}$, for wave propagation orientation **II** that is used to obtain equation (2.6.11). This figure is otherwise the same as figures 2.9 to 2.15.

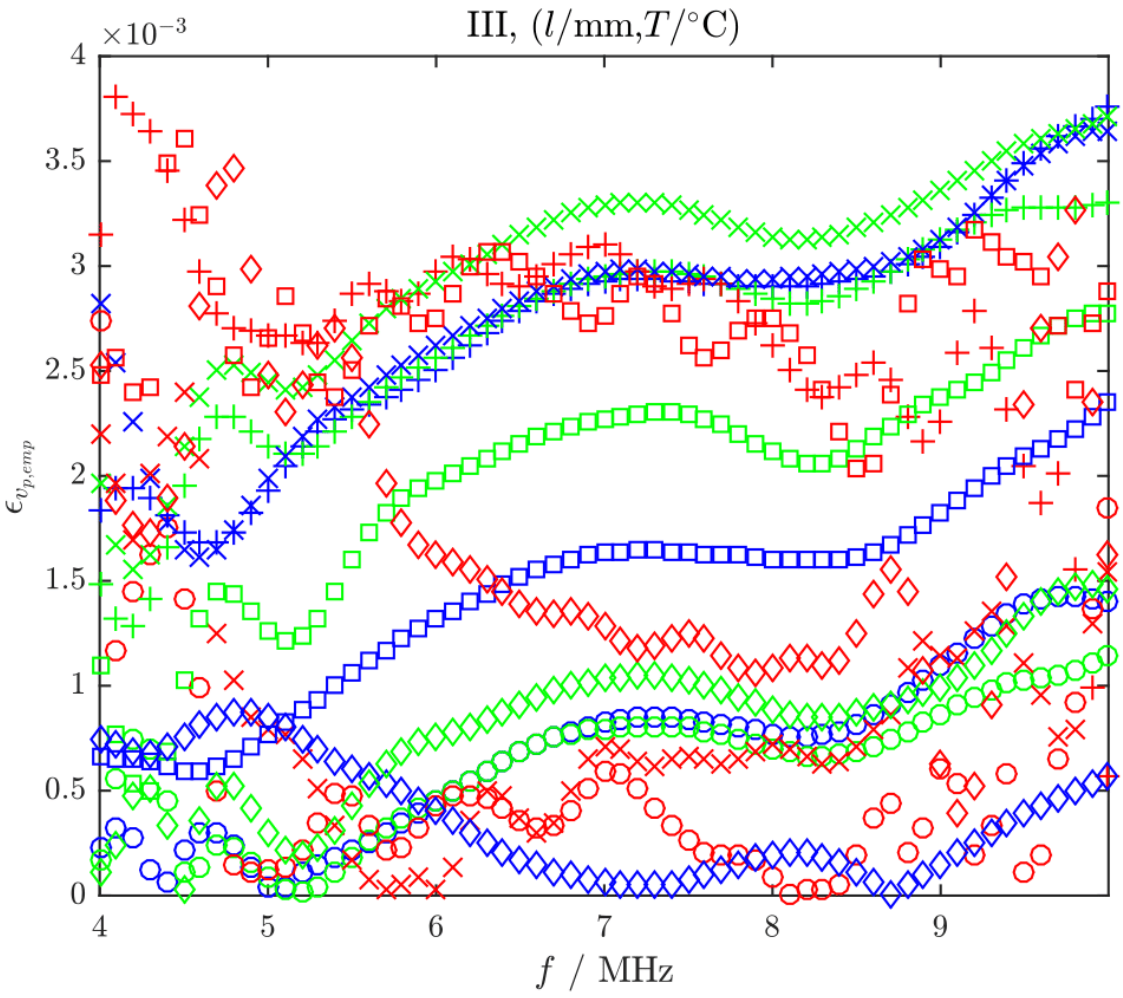

Figure 2.17: The phase velocity data uncertainties, $\epsilon_{v_{p,emp}}$, for wave propagation orientation **III** that is used to obtain equation (2.6.11). This figure is otherwise the same as figures 2.9 to 2.16.

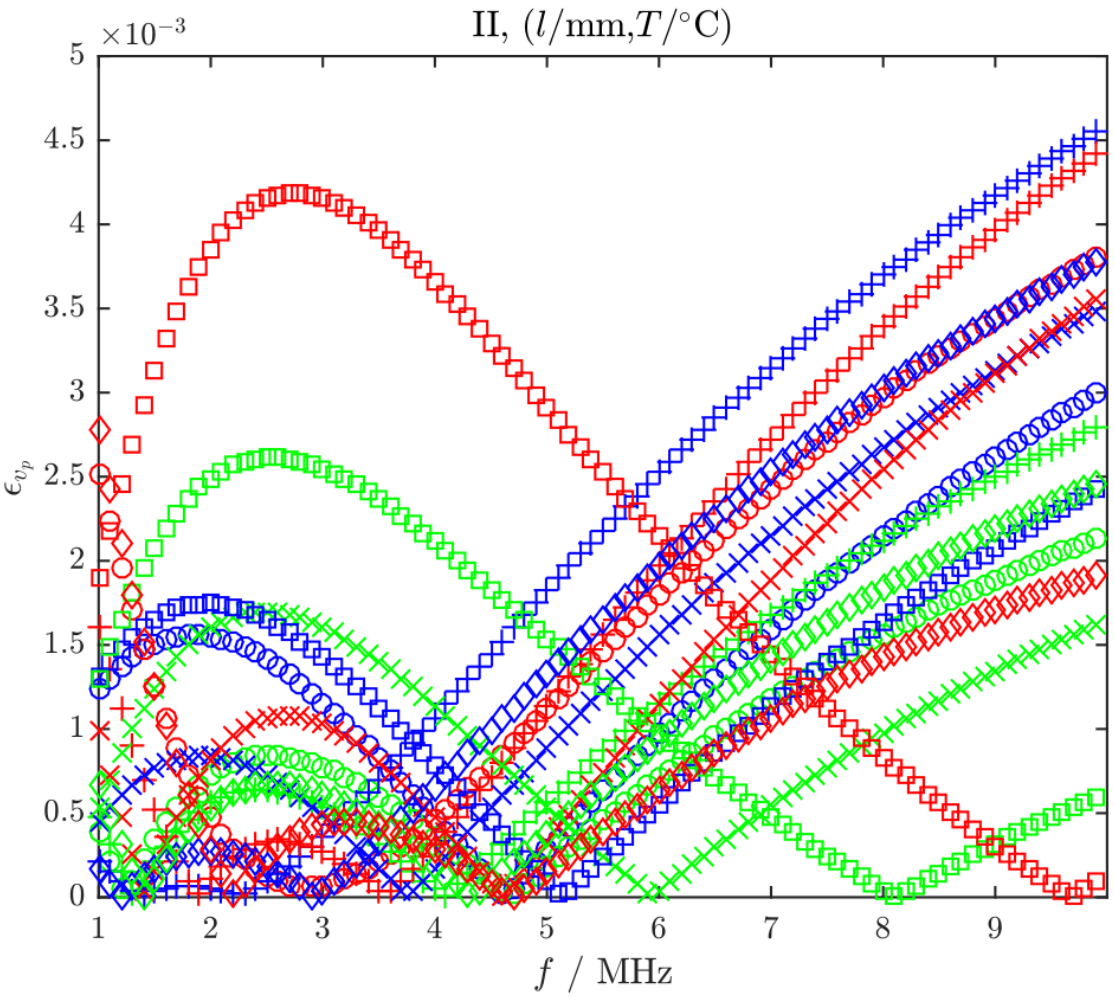

Figure 2.18: The phase velocity regression uncertainties, ϵ_{v_p}, for wave propagation orientation **I** that is used to obtain equation (2.6.11). This figure is otherwise the same as figures 2.9 to 2.17.

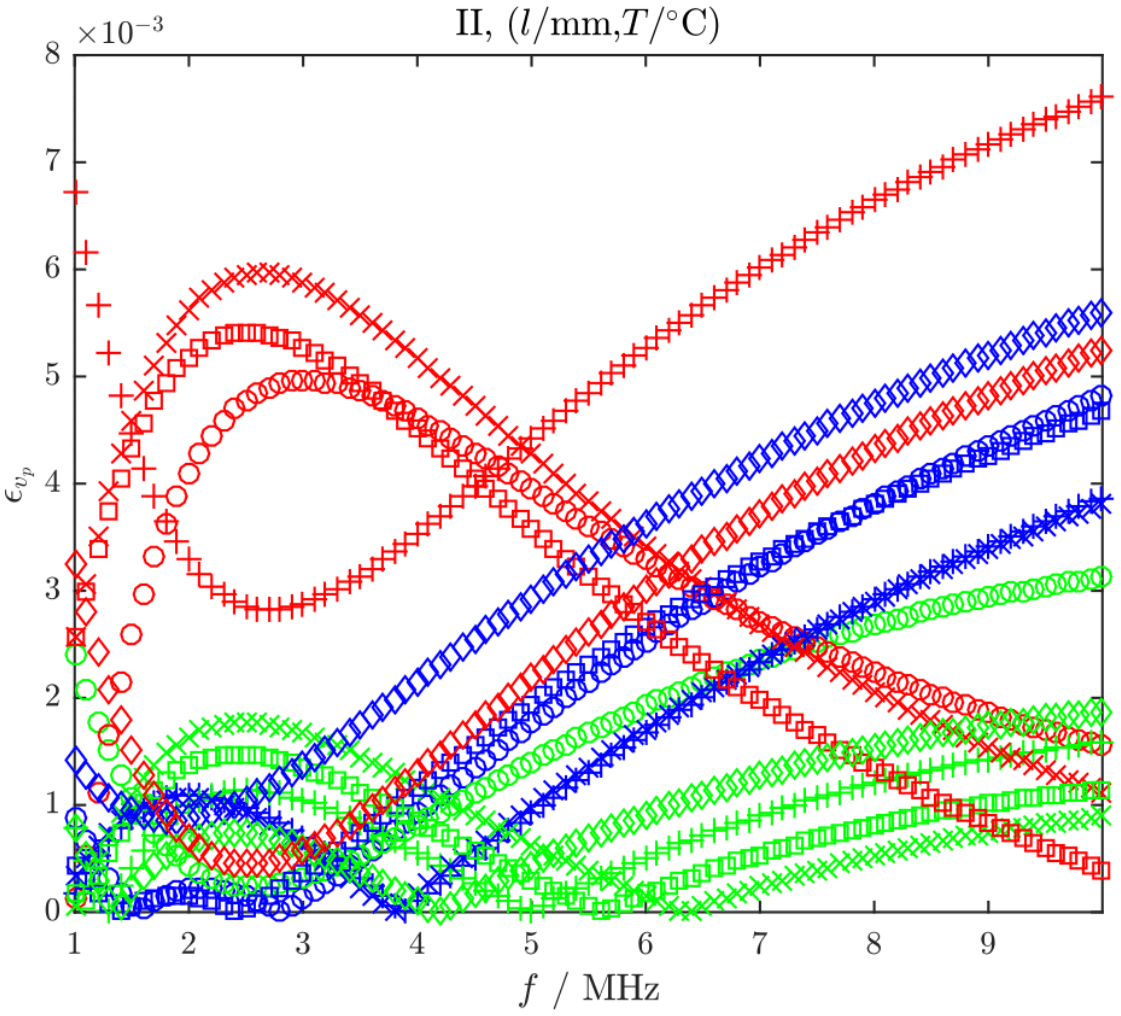

Figure 2.19: The phase velocity regression uncertainties, ϵ_{v_p}, for wave propagation orientation **II** that is used to obtain equation (2.6.11). This figure is otherwise the same as figures 2.9 to 2.18.

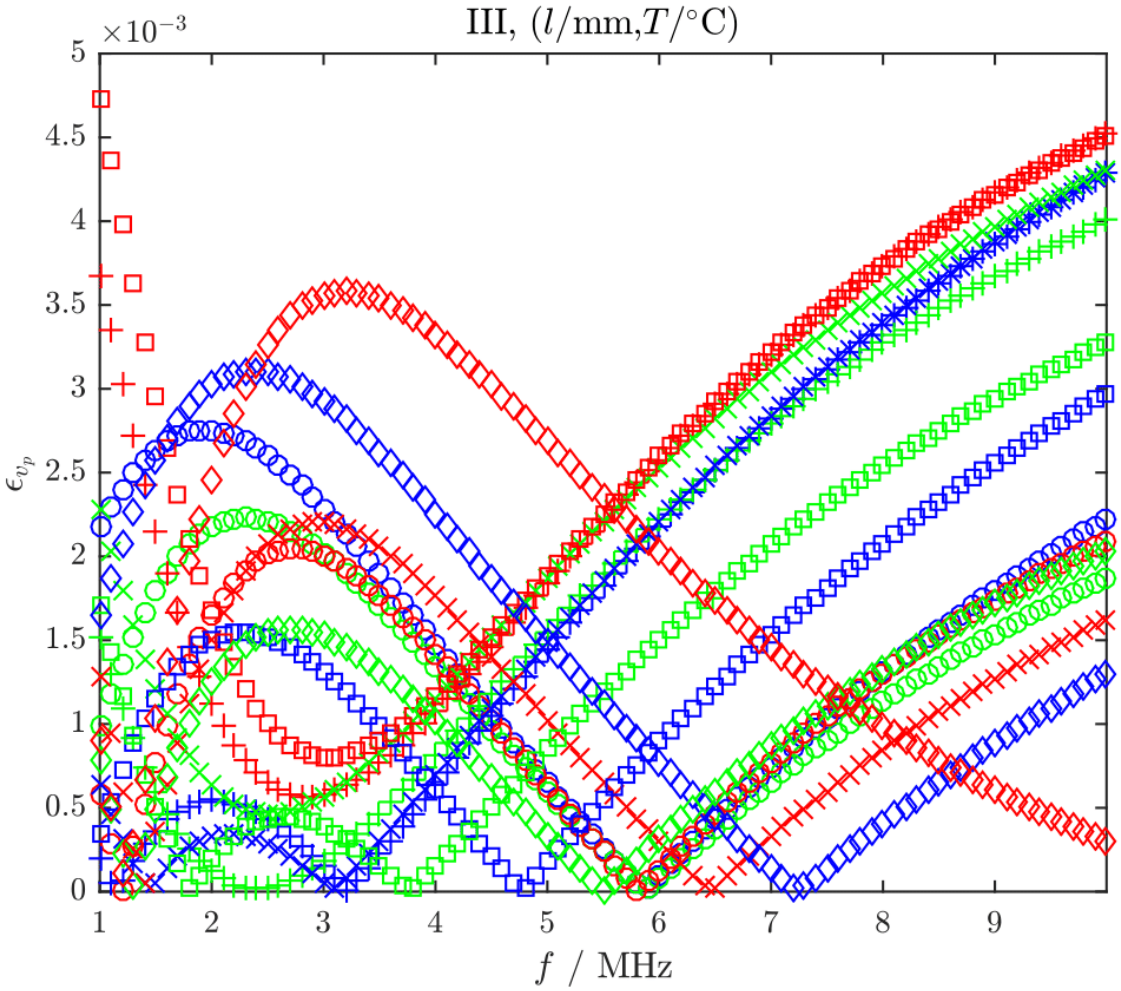

Figure 2.20: The phase velocity regression uncertainties, ϵ_{v_p}, for wave propagation orientation **III** that is used to obtain equation (2.6.11). This figure is otherwise the same as figures 2.9 to 2.19.

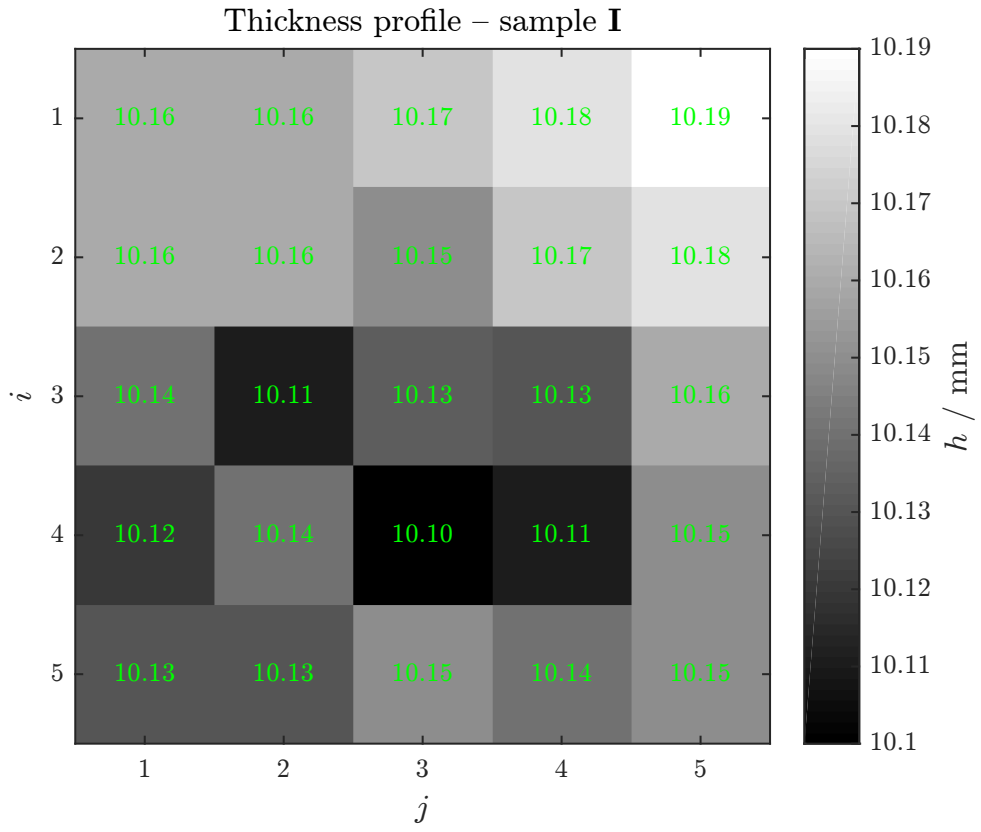

Figure 2.21: Thickness profile of sample **I** obtained at $T = 21°\text{C}$ using a micrometer screw gauge. The central thickness is the mean of the adjacent 8. Each ij measurement region has a height and width of 10mm.

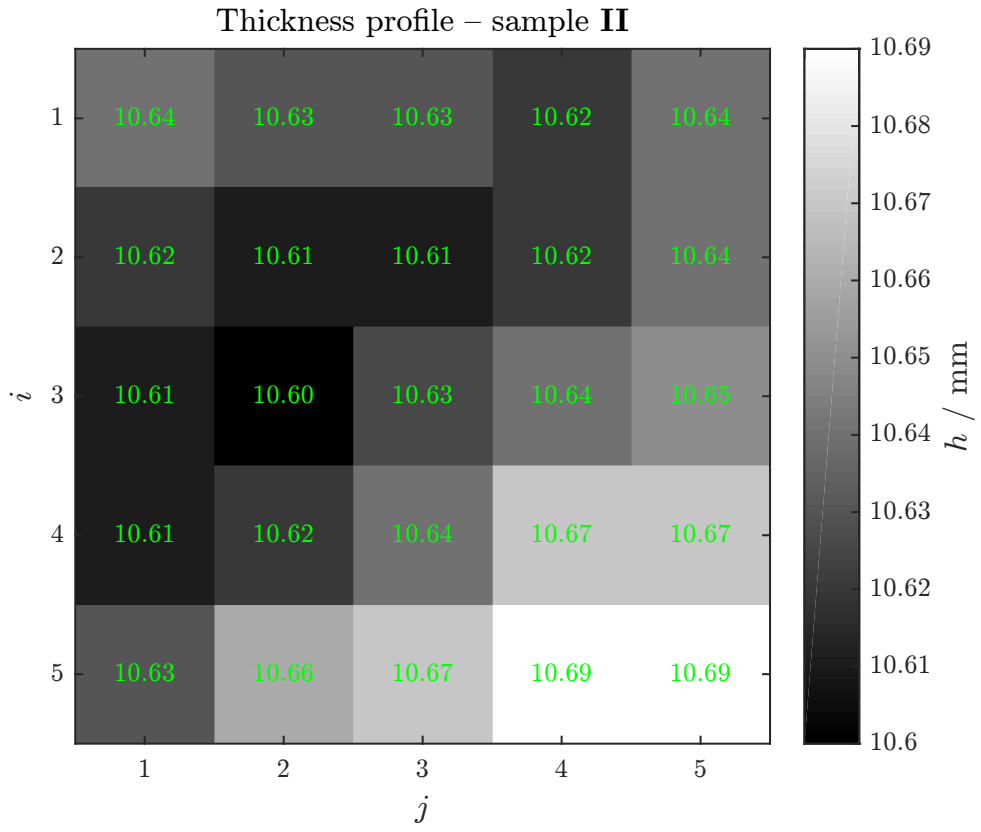

Figure 2.22: Thickness profile of sample **II** obtained $T = 21°\text{C}$ using a micrometer screw gauge. The central thickness is the mean of the adjacent 8. Each ij measurement region has a height and width of 10mm.

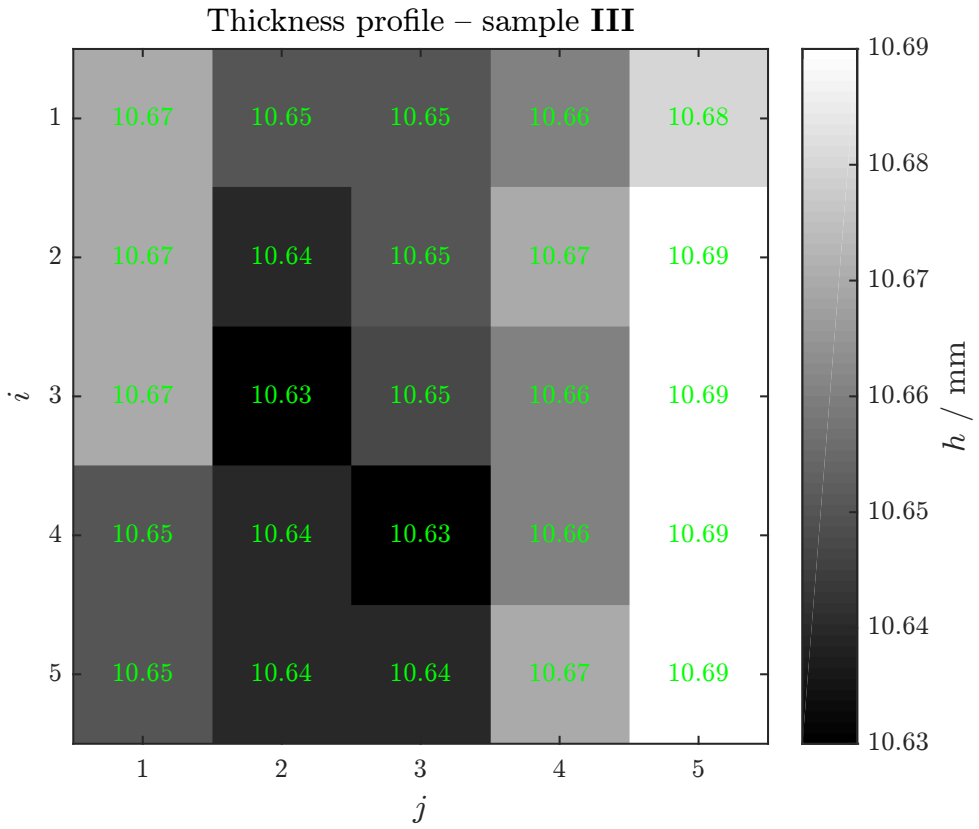

Figure 2.23: Thickness profile of sample **III** obtained $T = 21°\text{C}$ using a micrometer screw gauge. The central thickness is the mean of the adjacent 8. Each ij measurement region has a height and width of 10mm.

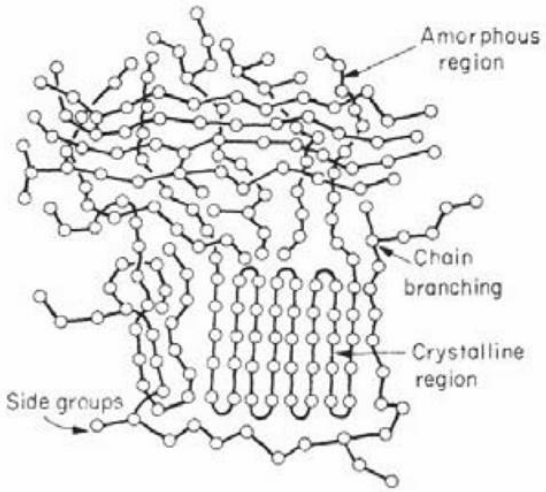

Figure 2.24: Structure of a semicrystalline polymer such as HDPE [35].

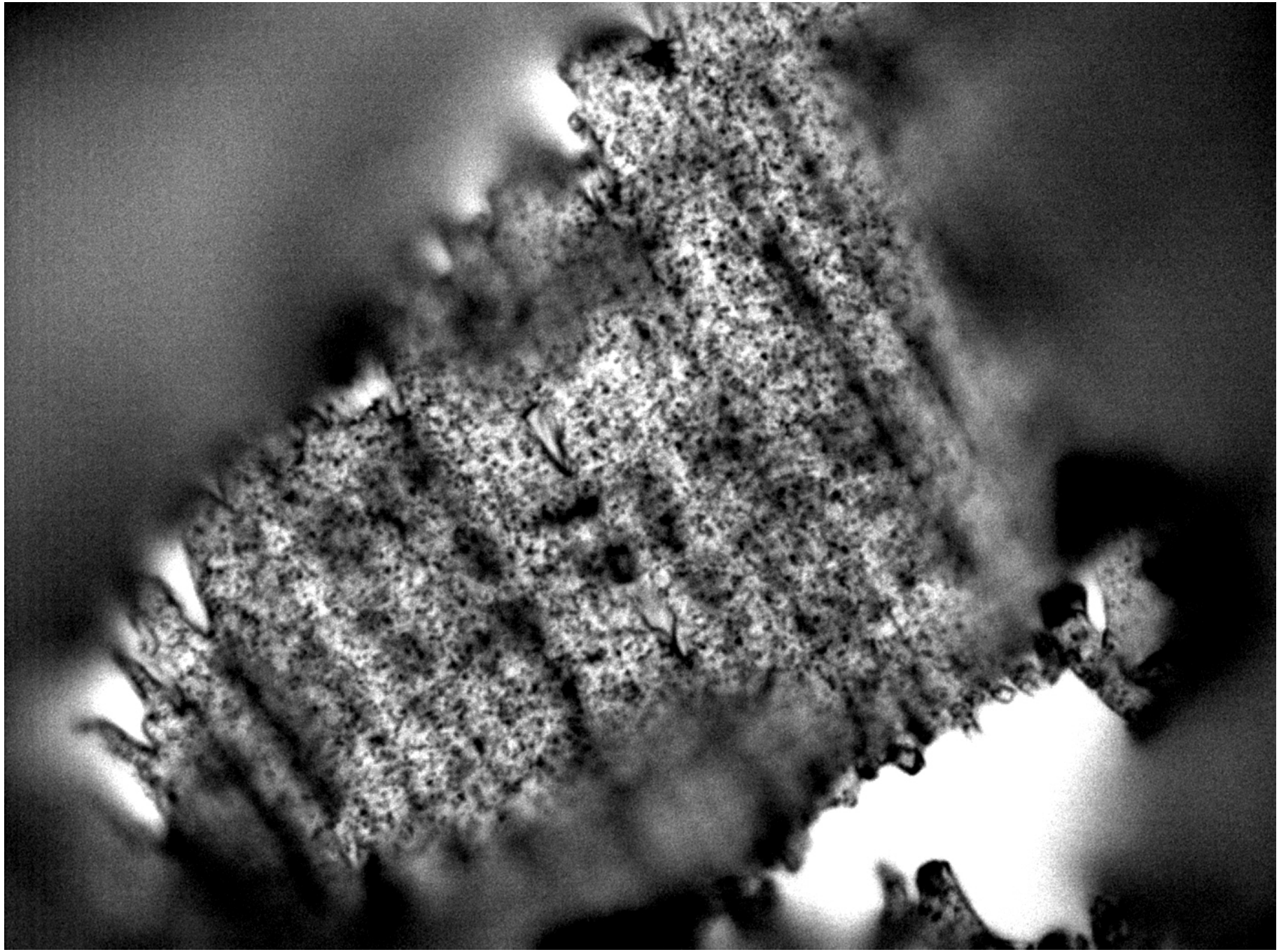

Figure 2.25: OTM of 100nm thick slice (approximately 80×50μm focused in-plane) from HDPE pipe weld material at 100× zoom with 0° between the two crossed polarising filters.

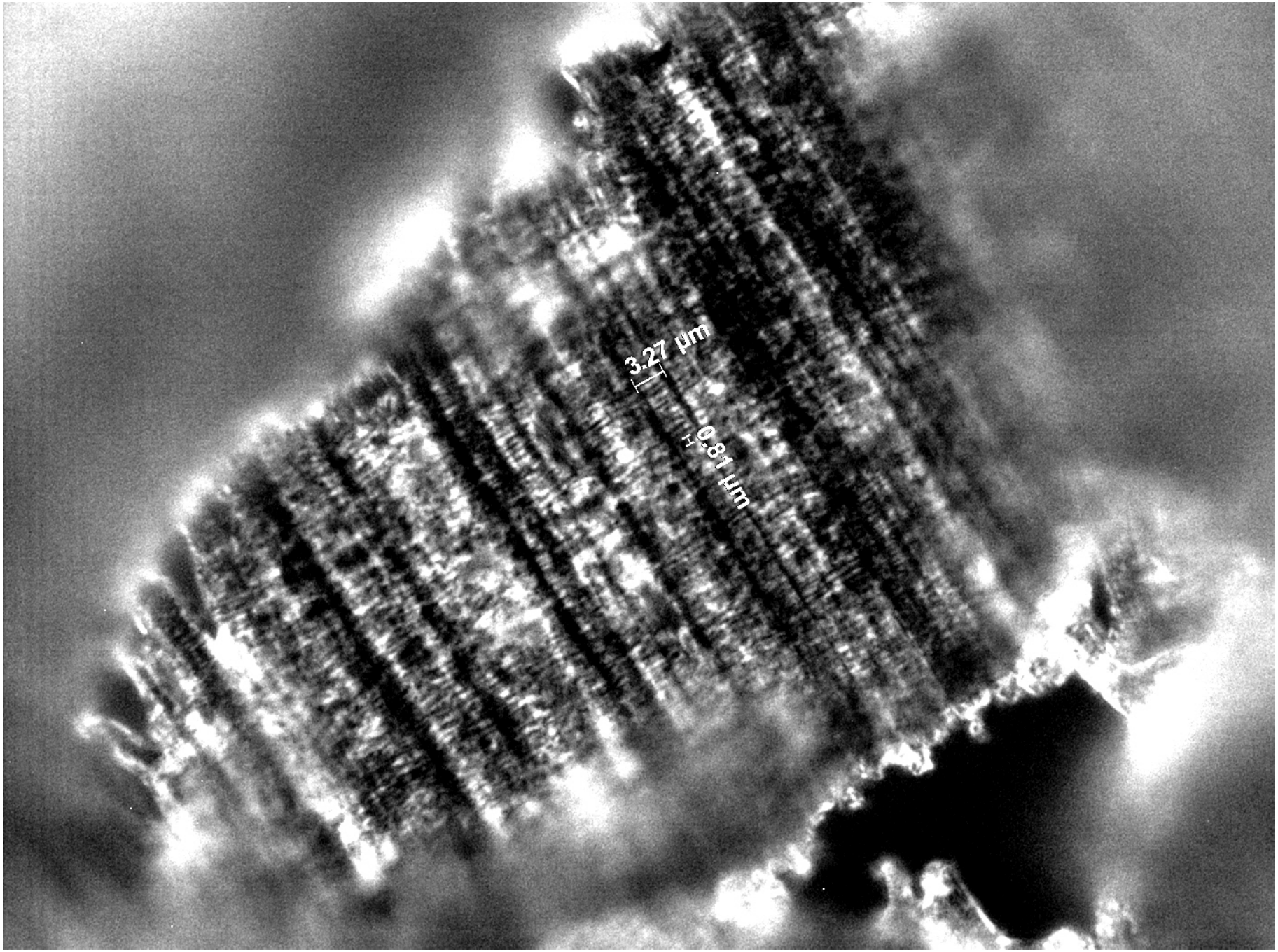

Figure 2.26: OTM of 100nm thick slice (approximately 80×50μm focused in-plane) from HDPE pipe weld material at 100× zoom with 65° between the two crossed polarising filters.

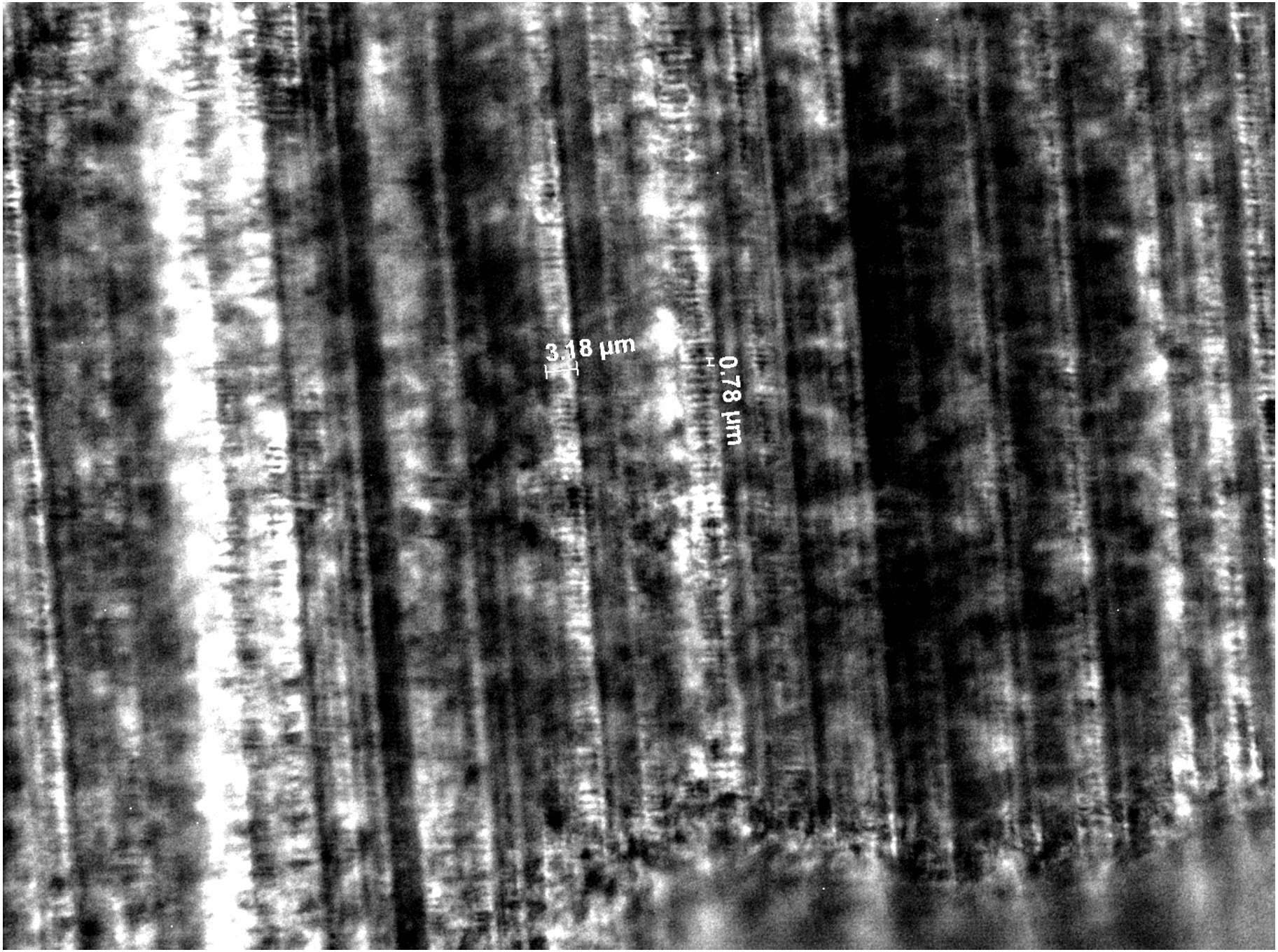

Figure 2.27: OTM of 25nm thick slice (approximately 100×80μm focused in-plane) from HDPE pipe parent material at 100× zoom with 65° between the two crossed polarising filters.

Chapter 3

A multiband approach for accurate numerical simulation of frequency dependent ultrasonic wave propagation in the time domain

The formulation, implementation, and evaluation of some concepts covered in chapter are published Open Access as: J.S. Egerton, M.J.S. Lowe, H.V. Halai, and P. Huthwaite, *Ultrasonic attenuation and phase velocity in high-density polyethylene (HDPE) pipe material*, J. Acoust. Soc. Am. **141**(3), 1535-1545 (2017).

3.1 Abstract

Finite element (FE) simulations are popular for studying propagation and scattering of ultrasonic waves in nondestructive evaluation. For a large number of degrees of freedom, time domain FE simulations are much more efficient than the equivalent frequency domain solution. However, unlike frequency domain simulations, time domain simulations are often poor at representing the speed and the attenuation of waves if the material is strongly damping or highly dispersive. Here, this author demonstrates efficient and accurate representation of propagated and scattered waves, achieved by combining a set of time domain solutions that are obtained for a set of frequency ranges known as bands, such that, in combination, the multiband solution of the author accurately represents the whole wave spectrum. Consequently,

high accuracy is achieved, at minor computational cost, using a modest number of bands. The multiband technique is implemented for ultrasonic wave propagation in highly attenuating polyethylene material, using 3 frequency bands, and can yield a reduction in empirical acoustic properties fractional error compared with respective time domain simulations, in propagation duration, of a factor of 1.4, and in full-width-half-maximum, of a factor of 10. Lastly, the accuracy of this approach is further exemplified in a wave scattering simulation.

3.2 Introduction

Nondestructive evaluation (NDE) is widely used in industry to detect potential defects in engineering components such that the likelihood of critical damage or failure is minimised. The development of accurate and reliable NDE methods increasingly uses numerical model simulations. The work presented here arose from a need to perform simulations of ultrasound NDE of high-density polyethylene (HDPE) pipes. The simulations were performed using finite element (FE), but this was not straightforward because HDPE is a highly attenuating material. The methodology presented here was the result of developments to enable accurate FE simulations for this problem, but it is presented here as a general methodology as it has wide value for applications with damping materials.

FE simulations can be performed in either time or frequency domains. It is usual that time domain calculations are performed explicitly, such that current solutions are obtained directly from previous solutions, and under certain preferred conditions – central difference time marching, with diagonal mass representation [3] – this can be done by spatially local calculations without ever needing to assemble or invert a full system matrix. With no loss of accuracy or generality, the efficiency is further improved through the use of parallel processing. A particularly effective approach is to use graphics processors (GPUs), such as is done by the Pogo FEA [32] software. High efficiency is of particular significance when modelling wave propagation in large regions where a fine FE mesh is required, necessitating field solutions for a large quantity of elements; multiple millions can be used in many current applications.

The principle FE alternative, frequency domain FE (FDFE) simulations, are solved implicitly and for a large number of harmonic solutions. This is highly computationally expensive, particularly for large modelled geometries, requiring the assembly

and inversion of system matrices [3]. Further to this, some large models cannot be solved practically at all using FDFE because the system matrix is too large for the computer memory, and inversion is not possible within a practical timescale, even though the matrix is sparse.

The problem for the modeller arises because explicit TDFE solutions are often poor at accurately representing the variation with frequency of acoustic properties – specifically the dispersion relation, which comprises attenuation and phase velocity – and therefore for many such applications, neither TDFE or FDFE are suitable.

Consequently, this author developed the multiband FE (MBFE) approach to simulation, with which a full, accurate dispersion relation can be modelled by blending the solutions from multiple separate TDFE solutions that are obtained at different frequency bands. MBFE couples both the accuracy and efficiency of FE analysis of waves with dispersion relations that can exhibit frequency dependence of general form. The multiband approach is developed to recover the lost accuracy of explicit TDFE without incurring the heavy computational penalty of FDFE, or the limitations in model size of the latter.

The example application material, HDPE, is viscoelastic. The properties of materials such as this can be described by extrapolation and inference – often from multiple decades below ultrasonic frequencies – of frequency-dependent material property parameters, such as storage and loss moduli [1, 2], provided that the modelling constraints described above do not apply. This author also achieves an accurate description of ultrasonic wave propagation and scattering in the MBFE methodology without need for extrapolation across many frequency decades and the consequent inference of material properties, and without such modelling constraints as model size, found in similar FDFE models, using acoustic properties – attenuation and phase velocity.

In the preceding study conducted by this author, the ultrasonic viscoelastic acoustic properties of HDPE pipe material [5], this author provides a unique, accurate and reliable description of the viscoelastic properties of HDPE, covering the range of frequencies and temperatures needed for practical ultrasound NDE of this material. The properties are presented there in the desired manner as spectra of attenuation and phase velocity. The variation in properties with frequency is the modelling challenge which this author aims to address here; while this will take the specific

example of HDPE properties, the approach is general and can be used for any dispersive medium.

The multiband technique may be used with dispersion relations of general frequency dependence, because it places no constraint on the frequency dependence of the acoustic properties – attenuation and phase velocity – used to define the dispersion relation. The multiband technique is here applied to the example of viscoelastic HDPE, in which bulk longitudinal waves propagate. More generally, such application of FE analysis – to the accurate description of viscoelastic or highly attenuating wave propagation, and to other waves for which attenuation and phase velocity have frequency dependence – is important to many areas of research, including NDE [6], medical imaging [7], and seismology [8].

This chapter is set out as follows. First, in section 3.3, is the background theory required to formulate MBFE; next, in section 3.4, is the outline of the MBFE method; in section 3.5 are the results and analysis of MBFE applied to wave propagation and scattering examples in HDPE pipe material; and in section 3.6 conclusions are drawn.

3.3 Material Model

The theory used to define the ultrasonic acoustic properties of viscoelastic HDPE pipes is provided here to form the basis for exemplification of the MBFE model.

The spectrum of a 1-D harmonic plane wave can be expressed as

$$S_x(x, f) = S_x(0, f) \exp(ik_x(f)x), \tag{3.3.1}$$

where x is location, f is frequency, and $k_x(f)$, or tersely $k(f)$, is the dispersion relation,

$$k(f) = \frac{2\pi f}{v_p(f)} + i\alpha(f), \tag{3.3.2}$$

where $v_p(f)$ is phase velocity and $\alpha(f)$ is attenuation. For this entire study, the following units are used, $[v_p] = \text{ms}^{-1}$ and $[\alpha] = \text{m}^{-1}$; alternative, unused unit

conventions do exist, including $[\alpha] = \mathrm{Np} \cdot \mathrm{m}^{-1}$.

In the preceding study conducted by this author, HDPE pipe acoustic properties study [5] this author presented a description of ultrasonic viscoelastic bulk wave dispersion that conforms to theoretical viscoelastic constraints and that is necessarily causal, using the Kramers-Kronig relation. The variation in properties with frequency is the modelling challenge which this author aims to address here; while this will take the specific example of HDPE properties, the approach is general and can be used for any dispersive medium. Consequently, attenuation and phase velocity vary with frequency using,

$$\alpha(f) = \alpha_1 f^y, \tag{3.3.3}$$

and

$$v_p(f) = v_{p1} + \left(\frac{v_{p1}}{\pi}\right)^2 \frac{\alpha_1}{y-1} f^{y-1}, \tag{3.3.4}$$

where $0 < \alpha_1$, $1 < y < 2$, and positive phase velocity at zero frequency, $0 < v_{p1}$, are all known empirical coefficients. It is shown in the prior analysis conducted by this author [5] that from equation (3.3.1), general forms of attenuation and phase velocity are,

$$\alpha_{gen}(f) = -\frac{1}{x} \ln \left| \frac{S(f)}{S_0(f)} \right| \tag{3.3.5}$$

and

$$v_{p,gen}(f) = \frac{2\pi f x}{\phi_S(f) - \phi_{S_0}(f)}, \tag{3.3.6}$$

where ϕ_{S_0} and ϕ_S are phases of the initial and propagated waves.

3.4 Method

The method for obtaining the multiband finite element model is described here, followed by its validation using wave propagation simulations that well match those of the empirical acoustic properties obtained above. The simulation technique is also applied to a scattering example.

3.4.1 Multiband finite element (MBFE)

The underlying concept of the MBFE methodology is to solve the simulation multiple times in the time domain, in each case covering only a subset of the frequency bandwidth, and then assemble the multiple results to obtain the outcome for the broader bandwidth problem. Each of the narrow band solutions needs to be narrow enough to achieve acceptable accuracy, given the frequency-varying properties, and at the same time wide enough to avoid the need for large numbers of contributing bands.

The wave characteristics used in the described implementation of the multiband finite element model are chosen to be suited to real inspection requirements. Piezoelectric ultrasonic transducers are designed with a Q-factor – the degree of damping of an object oscillating at resonance – that results in a single pulse duration that is generally of the order of 3-4 cycles. These short duration pulses have broad frequency bandwidths, and consequently exhibit greater variation in frequency-dependent dispersion within their non-negligible frequency range. FE simulations in this study are therefore conducted with cycles, $n_{cyc} = 4$, such that meaningful comparison can be made between accurately represented frequency-dependent dispersion, using the MBFE approach, and otherwise, using time domain FE (TDFE).

A commonly used pulse window is a half-period sinusoid given by a Hann function. The amplitude spectrum of this function has large peaks, known as side lobes, either side of the central peak at pulse centre frequency, f_0. This is unsuitable when general frequency dependent dispersion is assumed, as it is necessary to describe viscoelastic media such as HDPE, because during wave propagation the frequency content of the main lobe can be attenuated more than the unphysical side lobes, resulting in dominance of these erroneous frequencies in propagated pulses. This is avoided through selection of an envelope that generates an amplitude spectrum

with smaller side lobes, such as the Blackmann-Harris window [27],

$$\Pi(n) = a_0 - a_1 \cos\left(\frac{2\pi n}{N-1}\right) + a_2 \cos\left(\frac{4\pi n}{N-1}\right) - a_3 \cos\left(\frac{6\pi n}{N-1}\right), \quad (3.4.1)$$

for samples $n = 1, .., N$, where $a_0 = 0.35875$, $a_1 = 0.48829$, $a_2 = 0.14128$, $a_3 = 0.01168$. This is the chosen window for all FE simulations in this chapter. Using an input pulse with accurate frequency content relaxes the filtering requirements in post-processing of the simulated wave; if large side lobes are present the high- and low-pass filters used necessarily have corner frequencies close to f_0, resulting in greater undesired filtering of the frequency content of the main spectrum.

The low accuracy of the frequency dependent acoustic properties obtained using TDFE result from the necessary reduction of equation (3.3.2) to a fixed frequency solution. This fixed frequency representation is also used in the MBFE procedure, but accuracy is improved because each band is relatively narrow. The fixed frequency for this approximation is justifiably chosen to be that which the wave contains most of – the modal value of its amplitude spectrum – which is f_0 for approximately single-peak pulses, such as the tonebursts used here. The resulting simplified dispersion is

$$k(f_0) = \frac{2\pi f_0}{v_p(f_0)} + i\alpha(f_0), \quad (3.4.2)$$

with corresponding terse variables, k_0, v_{p0}, and α_0. Rayleigh damping is a damping model available in many commercial explicit TDFE software packages that is appropriate to the dispersion in equation (3.4.2), and that does not compromise the efficiency of the explicit time marching scheme, which is described using the equation of dynamic equilibrium [10],

$$[M]\ddot{u} + [C]\dot{u} + [K]u = [F] \quad (3.4.3)$$

where $[M]$, $[C]$, $[K]$, and $[F]$ are mass, damping, stiffness, and loading matrices respectively. The following, u, $\dot{u}$, $\ddot{u}$ are particle displacement and its first and second time derivatives. The damping matrix can be expressed in terms of both the mass

and stiffness matrices [10],

$$[C] = C_M[M] + C_K[K], \tag{3.4.4}$$

where $[C]$, $[M]$, and $[K]$ are the damping, mass, and stiffness coefficients and C_M and C_K are the Rayleigh coefficients, which can be defined in terms of attenuation for a fixed frequency using [11],

$$C_M = 2\alpha_0 v_{p0} \tag{3.4.5}$$

and

$$C_K = \frac{C_M}{\omega_0^2}, \tag{3.4.6}$$

where the centre angular frequency is $\omega_0 = 2\pi f_0$. Assuming a harmonic displacement solution to equation (3.4.3),

$$u(t) = u_0 \exp(i\omega_0 t), \tag{3.4.7}$$

where the angular frequency is $\omega = 2\pi f$, and using equation (3.4.4), the equilibrium equation becomes,

$$-[M]\left(1 + i\frac{C_M}{\omega_0}\right)\omega_0^2 u + [K](1 - i\omega_0 C_K)u = [F], \tag{3.4.8}$$

implying the following transformations from an undamped to damped system for density,

$$\rho \to \rho\left(1 + i\frac{C_M}{\omega_0}\right) \tag{3.4.9}$$

and Young's modulus,

$$E \to E(1 - i\omega_0 C_K). \tag{3.4.10}$$

The low accuracy of TDFE results from the following. Describing the general frequency dependence of wave acoustic properties in HDPE using power law viscoelastic dispersion is highly accurate, as shown in [5]. Conversely, it is inaccurate to reduce these acoustic properties to a fixed frequency description. Much of the accuracy of the power law description, or other dispersion relations, is recovered using MBFE. The favoured approach to conducting MBFE, known as 'k-blending', is outlined here with relevant equations:

1. Divide the amplitude of the spectrum of the initial signal into a set number of bands, n_{band}, containing equal frequency content (equal area under $|S_{init}|$ vs. f curve)

2. Perform separate TDFE simulations with centre frequencies equal to the frequency at the centre of each band

3. Window and filter all waveform outputs such that distinct initial and latent signals are isolated

4. Calculate attenuation and phase velocity from these separated signals

5. Combine these acoustic properties using the dispersion relation of equation (3.3.2)

6. Blend together the dispersion relations of all bands using weighting functions, yielding k for the whole bandwidth

7. Calculate an accurate description of the transfer function, $H(f)$, that maps an initial pulse to a propagated pulse

The window used in step 3 is a Tukey window, which is a rectangular window with Hann (sinusoidal) leading and trailing edges. Unlike for the above example of toneburst generation, where significant attenuation and corresponding dominance of amplitude spectrum side lobes results, windowing of waveforms is not subject to this

complication, therefore Hann edges are no issue. A rectangular function is accurate because it does not alter pulse amplitude within the window range. However, it does sharply truncate the signal, which can alter the pulse frequency content. By contrast, use of Hann edges in Tukey windowing smooths truncation, minimising this effect. The corner frequency of the filters in step 3 are distant from significant frequency content and have first-order roll-off. Approaches to multiband blending that are deemed inferior to k-blending are described in appendix 3.7.1.

The attenuation and phase velocity in step 4 are those of equations (3.3.5) and (3.3.6). The blending described in step 6 involves linear weighting functions for the n^{th} band, b_n, that equal 1 at band centres where TDFE simulations are most accurate, equal 0.5 at adjacent band edges and equal 0 at adjacent band centres. In the outer halves of the first and last bands all frequency content is used – equivalently $b_n = 1$ there. Using this blending, the whole bandwidth can be described with high use of accurate frequency content and low use of inaccurate content. Frequency content beyond the first and last band is alternatively linearly extrapolated for comparison of accuracy.

Below, this author describes and formulate general methods this author has considered for the blending of attenuations and phase velocities, as well as blending of dispersion relations. Blending of propagated spectra, attenuations and phase velocities, dispersion relations, and transfer functions are all inequivalent. For example, the blends of attenuations and phase velocities are not the same as the blends of dispersion relations, as follows,

$$\alpha_{blend} = \sum_n \alpha_n b_n \tag{3.4.11}$$

and

$$v_{p,blend} = \sum_n v_{pn} b_n \Leftrightarrow \frac{2\pi f}{v_{p,blend}} = \frac{2\pi f}{\sum_n v_{pn} b_n}, \tag{3.4.12}$$

while the dispersion blending used in MBFE is,

$$k_{blend} = 2\pi f \sum_n \frac{b_n}{v_{pn}} + i \sum_n \alpha_n b_n, \tag{3.4.13}$$

such that,

$$k_{blend} \neq \frac{2\pi f}{v_{p,blend}} + i\alpha_{blend}. \tag{3.4.14}$$

The mapping of initial pulse to propagated pulse described in step 7 includes both the amplitude and the phase of the spectra and is defined as follows,

$$H(f) = \frac{S(f)}{S_0(f)}. \tag{3.4.15}$$

To ensure the k-blending MBFE technique is most suitable, other approaches to MBFE are also developed for comparison of accuracy, generality, and to a lesser degree, simplicity. These unfavoured approaches are listed here.
The first omitted approach takes the transfer function of each band evaluated at solely the band centre frequencies then assigns these fixed values, obtained from each TDFE simulation, to all frequencies within their corresponding band. The second approach is to linearly interpolate the transfer function between the band centre values. The next approach is logarithmic interpolation of the transfer function. Of blending approaches, first the propagated spectra of each band are blended, then the phase velocities and attenuations are blended, followed by dispersions, and finally the transfer functions. Of these, blending the dispersion relations (k-blending) proves accurate, general, and simple to implement and use.

3.4.2 Finite element meshing and geometries

The FE models described here represent the propagation and scattering of plane longitudinal waves in HDPE pipe material in two dimensions. In figure 3.1, the propagation FE simulations are in 2-D; at the top and bottom model boundaries, displacement normal to these boundaries is set to zero; and HDPE is approximated

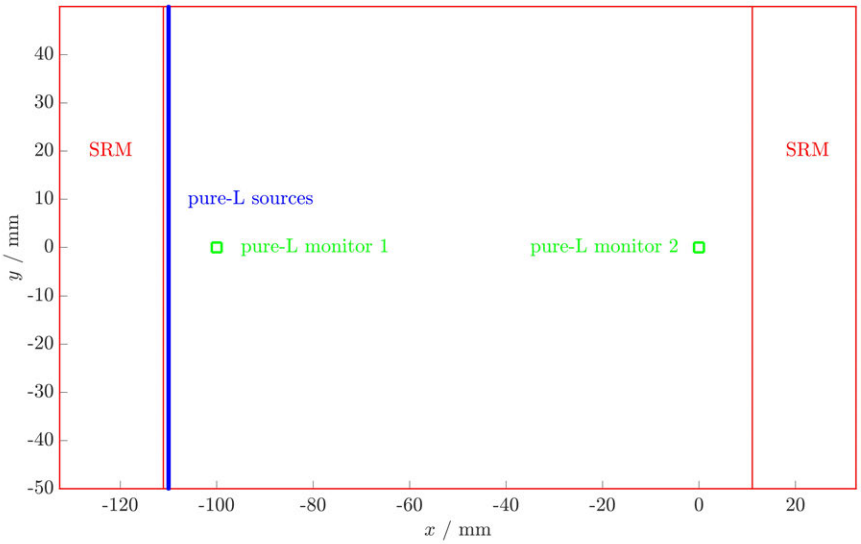

Figure 3.1: Geometry of FE simulation of wave propagation in the material of the wall of a HDPE pipe. The two large rectangles are the boundaries of the absorbing region (SRM), all pure-L point sources are aligned vertically near the inner left boundary, and the monitoring nodes are depicted by squares centred at (-100,0) and (0,0).

as homogeneous and isotropic. A plane wave is approximated by a 100mm linear source oriented 90° to the axial direction. The model is set within the FE software to have no displacements normal to the direction of wave propagation. The wave is monitored at two locations, one 10mm from the source in the propagation direction, the next 100mm beyond that.

The sum of all point sources along the source line approximates a plane wave, which is most suitable for HDPE where shear waves are attenuated of the order of 10 times that of the already highly attenuated longitudinal waves [12]. The simulated region is bounded by a large absorptive region that has decreasing stiffness towards the boundary, known as the stiffness reduction method (SRM) [29]. This highly attenuates waves propagating in this region such that boundary reflections are minimal and the resulting wave is not complicated by undesired signals. The SRM was primarily designed for use with elastic materials. In such cases, the damping of the SRM decreases to zero towards the modelled region. This author has adjusted the implementation of the SRM to decrease damping towards the viscoelastic damping of HDPE at the inner edges of the SRM. This ensure damping continuity at the boundary.

The optimal frequency for ultrasonic inspection of HDPE pipes is selected based on the following compromise. Higher frequencies can increase spatial resolution. Also,

higher frequencies produce more directive beams. Lastly, attenuation in HDPE, and many other media, increases with frequency. Because of this, MBFE and TDFE simulations of both wave propagation and scattering are conducted with median propagation paths of $x_s = 100$ and 53.5mm respectively, all at frequency, $f = 2.25$MHz. Frequencies similar to this are often used in current industrial inspection of HDPE pipe joints.

The chosen FE mesh comprises structured triangular plane strain elements. The mesh is describable as fine [30] with element size,

$$\mathrm{d}x \leq \frac{\lambda_0}{20}, \tag{3.4.16}$$

where the wavelength at centre frequency, f_0, is $\lambda_0 = v_{p0}/f_0$ and v_{p0} is the phase velocity at centre frequency. This mesh refinement, and the other chosen refinement, which is half the spatial step of this, are sufficiently fine for the purpose of demonstrating the improvements in accuracy of MBFE over TDFE simulations, for given mesh refinements. Given that for all simulations the time step is 2.5 times as refined as the spatial step,

$$\mathrm{d}t \leq \frac{1}{50 f_0}, \tag{3.4.17}$$

the time step contributes negligible computational error, while ensuring numerical stability.

For increased FE simulation accuracy in both TDFE and MBFE, shown in figure 3.2, at the four square-oriented corners of two adjacent triangular source or monitor elements, four nodes are displaced parallel to lines that project to the centre of the squares that comprise two triangular elements. After summation of the displacements at the four nodes, where two nodes are common to both elements, this excitation approximates that of a purely longitudinal (pure-L) wave point source [30].

Following the study of the propagation and attenuation of plane waves, this author has also demonstrated the MBFE methodology on a simulation of scattering from a discontinuity, in a study relevant for NDE. Shown in figure 3.3, the scattering

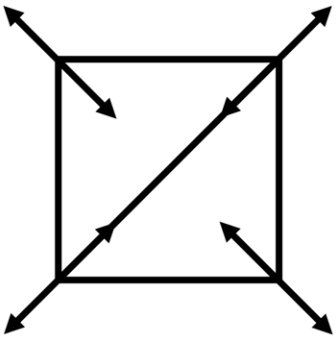

Figure 3.2: Cartoon of two adjacent square-oriented triangular source or monitor elements with four nodal displacements, depicted by arrows, which are directed parallel to lines that project to the centre of the squares that comprise the two triangular elements.

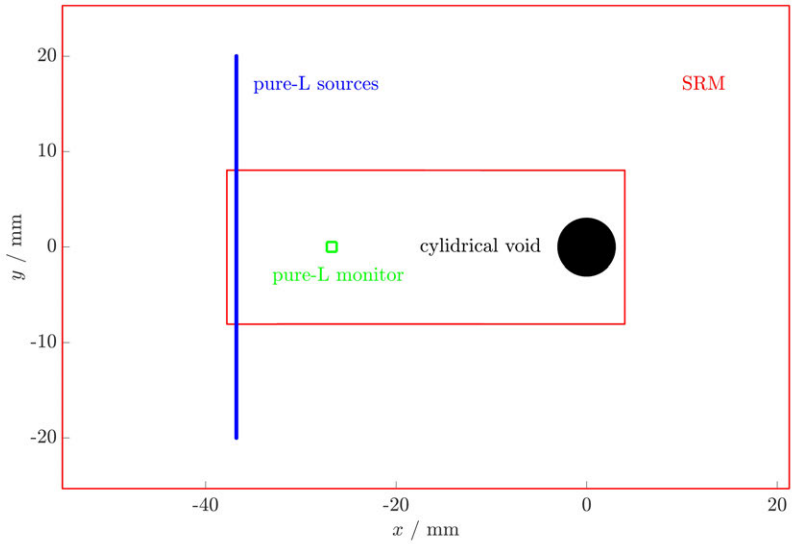

Figure 3.3: Geometry of FE simulation of scattering from a cylindrical void defect in the material of the wall of a HDPE pipe. The inner rectangle is the boundaries of the absorbing region (SRM), the defect is depicted as a solid circle, all pure-L point sources are aligned vertically near the left absorbing region, and the monitoring nodes are centred at (-26.75,0) and depicted by a square.

FE simulations are in 2-D and the scatterer is a cylindrical void with a radius of 3mm. This is an approximation to a pertinent defect example, where a void may form around a liquid or solid manufacturing inclusion in the HDPE pipe joint. The FE mesh comprises triangular elements with the size stated in equation (3.4.16). Before and after scattering off the cylindrical void, the wave is detected at a pure-L monitor.

3.5 Results and analysis

Provided here are the results and analysis of MBFE applied to the wave propagation and scattering examples.

3.5.1 Wave propagation

Shown in figure 3.4 are 4-cycle tonebursts propagated 100mm in the FE geometry depicted in figure 3.1. The solid curve is the benchmark propagated pulse, u, predicted using equation (3.3.2) with select acoustic properties obtained from the procedure described in the preceding HDPE pipe acoustic properties study conducted by this author [5]. The dashed curve is the TDFE pulse, u_{TD}, $\mathrm{d}x = \lambda_0/40$, and a time increment of $\mathrm{d}t = 1/(100f_0)$. The dot-dashed curve is the MBFE pulse with $n_{band} = 3$, $u_{MB,3}$.

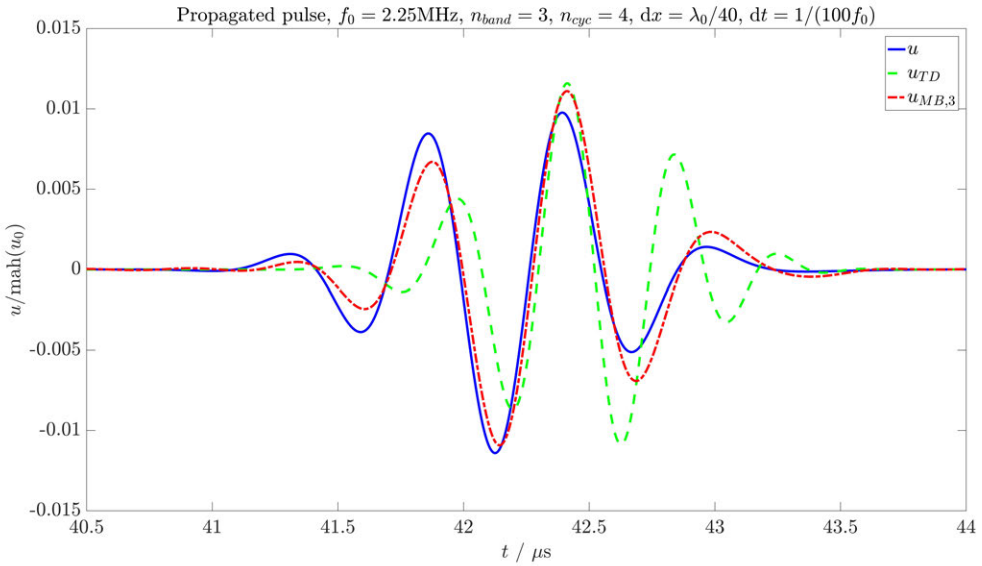

Figure 3.4: Empirical, from section 3.3, and FE simulated longitudinal wave pulses propagated in HDPE. The input pulses are 4-cycle tonebursts with Blackman-Harris envelopes. The centre frequency of the input pulse is $f_0 = 2.25$MHz and for the FE pulses the mesh spacing is $\mathrm{d}x = \lambda_0/40$ and the time increment is $\mathrm{d}t = 1/(100f_0)$. The pulse amplitudes are normalised to the maximum of the amplitude of the Hilbert transform of the analytical initial pulse, $\mathrm{mah}(u_0)$. The solid curve is the empirical pulse, u, the dashed curve is the TDFE pulse, u_{TD}, and the dot-dashed curve is the MBFE pulse with $n_{band} = 3$, $u_{MB,3}$.

Qualitatively, it is clear that there is significantly improved matching to u for $u_{MB,3}$ compared with u_{TD}, specifically in both the amplitude and the phase of the pulse. Also the period is visibly much shorter for u_{TD} than it should be, because the

low frequencies are attenuated too much and the high frequencies too little with frequency independent attenuation.

In summary, using as few as three bands in MBFE results in a significantly improved representation of ultrasonic wave propagation relative to that of TDFE simulation. The TDFE and MBFE attenuations are exemplified in figures 3.5 and 3.6 for $n_{band} = 3$ and $n_{cyc} = 4$, $\mathrm{d}x = \lambda_0/40$, and $\mathrm{d}t = 1/(100f_0)$. The attenuation of TDFE is

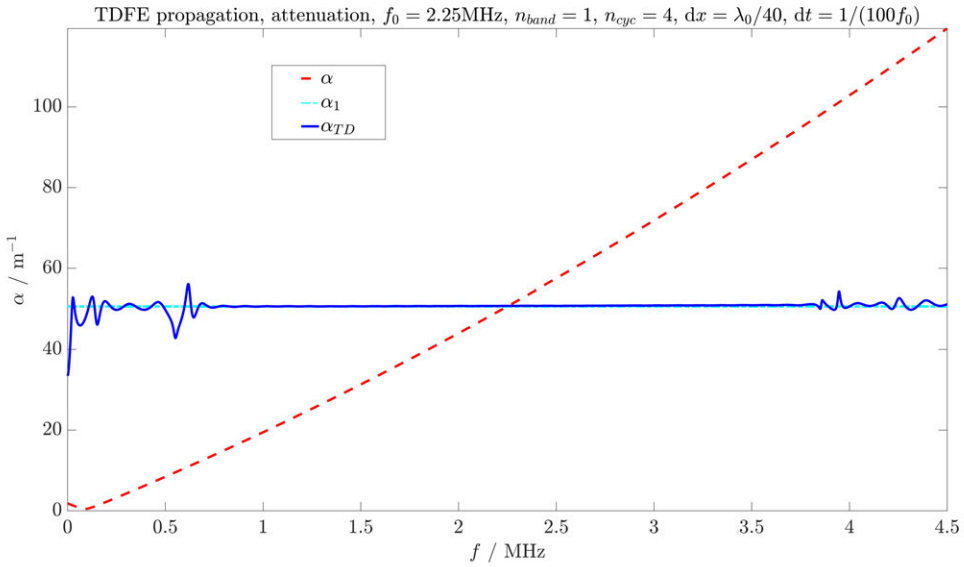

Figure 3.5: TDFE attenuation frequency dependence for HDPE wave propagation where $\mathrm{d}x = \lambda_0/40$ and the time increment is again $\mathrm{d}t = 1/(100f_0)$. The dashed curve is the empirical attenuation frequency power-law, the dot-dashed curve is the empirical attenuation at f_0, and the solid curve is the TDFE solution obtained at $f_0 = 2.25$MHz, where non-negligible wave frequency content exists between $1 \leq f/\mathrm{MHz} \leq 3.5$.

approximately equal to the empirical attenuation at f_0, resulting in attenuation being too high at frequencies below f_0 and too low at frequencies above f_0.

The blending of attenuation in figure 3.6 shows close agreement with the desired empirical solution, obtained in the acoustic properties study conducted by this author [5], over the frequency range covered by the bands. The bands are defined such that equal frequency content of the initial pulse exists in each band. However, the dispersion blending solution between bands cannot be an ideal linear approximation to the empirical dispersion because other sources of computational error exist in FE simulation. An example of this is the error associated with approximating the modelled geometry with finite elements, where a coarser mesh decreases the FE accuracy; the accuracy increases as the mesh is refined. Similar results are expected for refinement of the time increment, $\mathrm{d}t$.

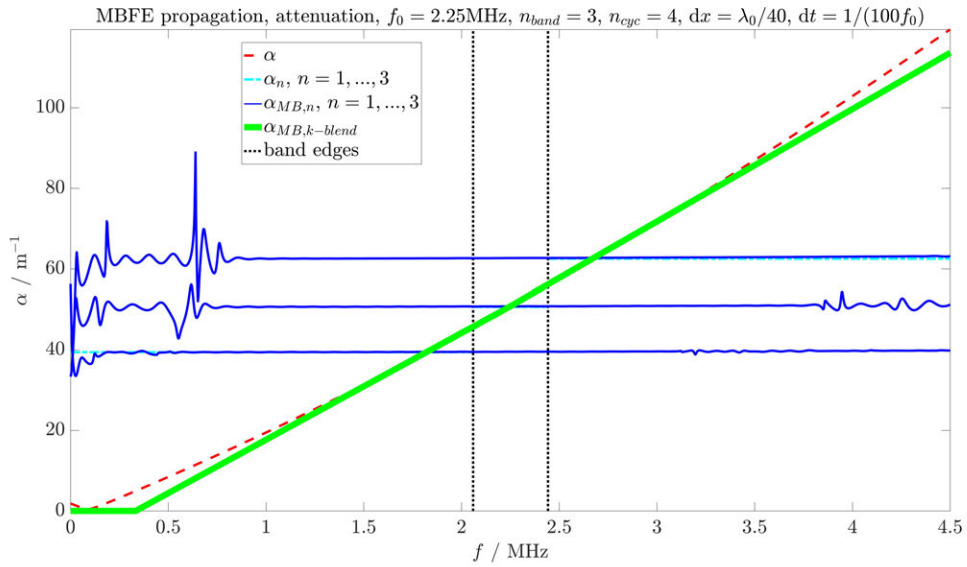

Figure 3.6: MBFE attenuation frequency dependence for HDPE wave propagation where $\mathrm{d}x = \lambda_0/40$ and the time increment is again $\mathrm{d}t = 1/(100f_0)$. The dashed curve is the empirical attenuation frequency power-law, the dot-dashed curves are the empirical attenuations at f_0 of each band, the solid curves are time domain finite element solutions obtained at f_0 of each band, the thick solid curve is the MBFE dispersion blend solution to describe general frequency dependence, and the vertical dots are the edges between bands and the outer bands contain the remaining frequency content.

In summary, using as few as three bands in MBFE results in a significantly improved representation of ultrasonic attenuation relative to that of TDFE simulation.

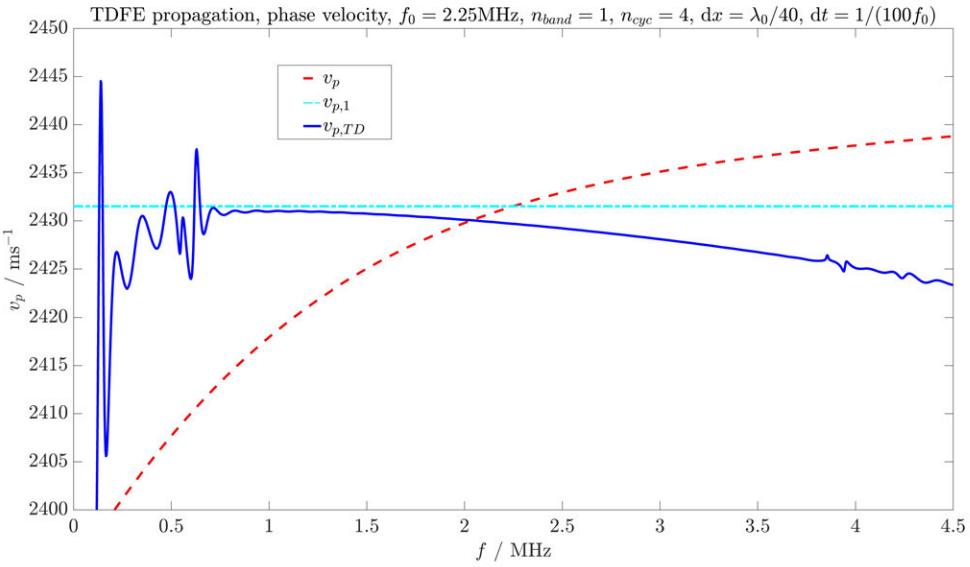

Figure 3.7: TDFE phase velocity frequency dependence for HDPE wave propagation where $\mathrm{d}x = \lambda_0/40$ and the time increment is again $\mathrm{d}t = 1/(100f_0)$. The dashed curve is the empirical phase velocity frequency power-law, the dot-dashed curve is the empirical phase velocity at f_0, and the solid curve is the TDFE solution obtained at $f_0 = 2.25$MHz, where non-negligible wave frequency content exists between $1 \leq f/\mathrm{MHz} \leq 3.5$.

In figure 3.7, the phase velocity of TDFE is approximately equal to the empirical phase velocity at f_0, resulting in velocity being too high at frequencies below f_0 and too low at frequencies above f_0. For increasing frequency, the TDFE velocity error relative to the frequency independent ideal solution, $v_{p,1}$, increases because the number of elements per wavelength, $\lambda/40$, decreases. In figure 3.8, as with MBFE

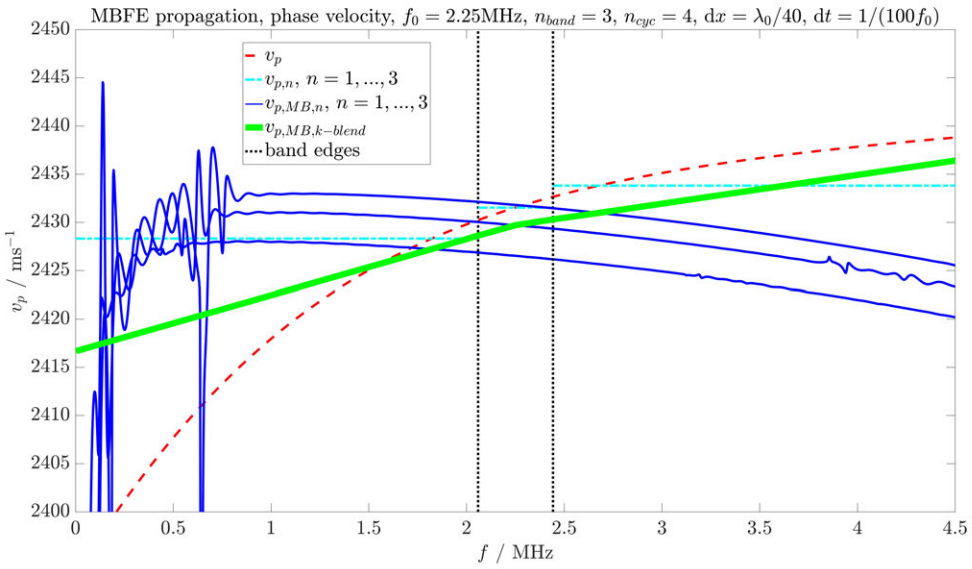

Figure 3.8: MBFE phase velocity frequency dependence for HDPE wave propagation where $dx = \lambda_0/40$ and the time increment is again $dt = 1/(100f_0)$. The dashed curve is the empirical phase velocity frequency power-law, the dot-dashed curves are the empirical phase velocities at f_0 of each band, the solid curves are time domain finite element solutions obtained at f_0 of each band, the thick solid curve is the MBFE dispersion blend solution to describe general frequency dependence, and the vertical dots are the edges between bands and the outer bands contain the remaining frequency content.

attenuation, MBFE phase velocity shows close agreement to the empirical curve and improved accuracy at frequencies above and below f_0 compared with any of the three individual TDFE solutions that this blend is obtained from.

In summary, using as few as three bands in MBFE results in a significantly improved representation of ultrasonic phase velocity relative to that of TDFE simulation.

To further quantify the improved accuracy of MBFE over TDFE, for a given number of frequency bands, n_{band}, mesh spacing, dx, and time increment, dt, the full-width-half-maxima (FWHM) and propagation durations (PD) of the FE pulses are obtained as fractional differences from those of the empirical propagated pulse, u, for a 4-cycle toneburst, shown in figures 3.9 and 3.10 respectively. The FWHM corresponds to a 6dB drop in amplitude on a logarithmic scale and the PD can infer wave propagation distance using knowledge of the wave velocity in the medium. The

TDFE solutions are threshold lines for comparison with 3, 7, and 15 bands. The two alternative MBFE techniques, with and without extrapolation of the solution beyond the edge bands, are also compared.

In figure 3.9, the FWHM discrepancy is

$$\epsilon_{FWHM} = \left| \frac{\mathrm{FWHM}(u) - \mathrm{FWHM}(u_{FE})}{\mathrm{FWHM}(u)} \right|, \tag{3.5.1}$$

where $\mathrm{mah}(u)$ is the maximum amplitude of the Hilbert transform of the longitudinal wave displacement, and in figure 3.10, the PD discrepancy is

$$\epsilon_t = \left| \frac{t_{\mathrm{mah}(u)} - t_{\mathrm{mah}(u_{FE})}}{t_{\mathrm{mah}(u)} - t_{\mathrm{mah}(u_0)}} \right| \tag{3.5.2}$$

where $t_{\mathrm{mah}(u_{P0})}$ is the time that the maximum amplitude of the Hilbert envelope of the initial pulse, u_{P0}, occurs, and the other times correspond to the maxima for the other pulses.

In figure 3.9, the TDFE solution with less mesh refinement has unexpectedly low

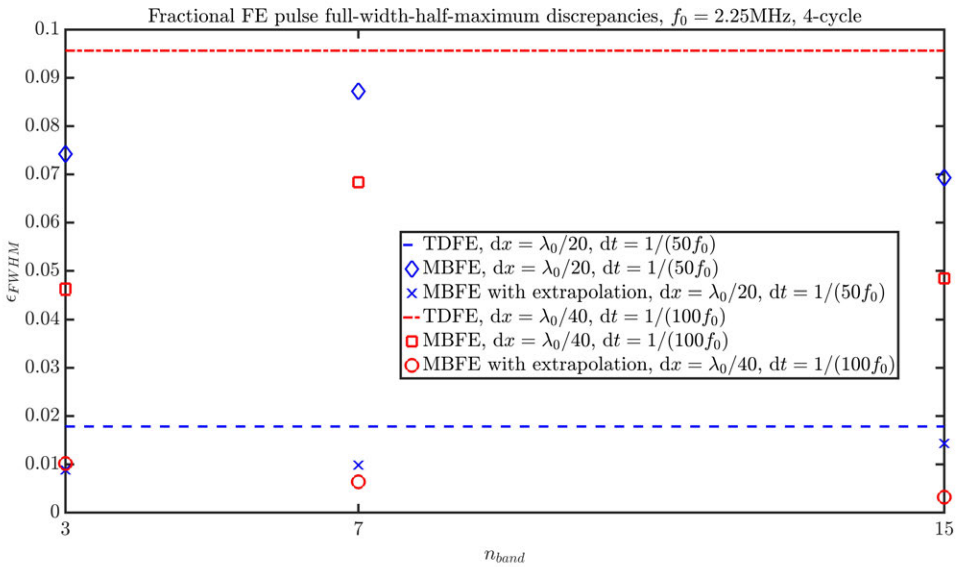

Figure 3.9: Full-width-half-maximum discrepancies between the empirical propagation of a 4-cycle toneburst and the TDFE and MBFE approximations to this. The dotted line is the TDFE fractional error with $\mathrm{d}x = \lambda_0/20$. For the same mesh refinement, the diamonds are the MBFE FWHM fractional errors and the crosses are the fractional errors for MBFE with extrapolation. The dot-dashed line is the TDFE fractional error with $\mathrm{d}x = \lambda_0/40$. For the same mesh refinement, the squares are the MBFE fractional errors and the circles are the fractional errors for MBFE with extrapolation.

fractional error. This is because, as is shown in figures 3.4 and 3.5 for $\mathrm{d}x = \lambda_0/40$, the pulse does not have the required frequency down shift, and therefore no pulse broadening in the time domain. However, an equal and opposite error occurs with the velocity, as also shown in figures 3.4 and 3.7, where high frequencies are significantly more dispersive than for the empirical velocity, resulting in erroneous pulse broadening.

These two errors counteract one another to produce a coincidentally accurate FWHM, where $\epsilon_{FWHM} = 0.018$. By increasing the mesh refinement of the TDFE solution, and therefore decreasing numerical error, the fractional uncertainty in FWHM shown in figure 3.9 actually increases to $\epsilon_{FWHM} = 0.096$. This is because the two numerical errors described above that have equal and opposite contributions to pulse dispersion in the time domain reduce at different rates with increased mesh refinement.

Because of these various contributing sources of error in FWHM, MBFE has high accuracy for 3 bands but there is no consistent trend towards increasing accuracy with increasing bands for FWHM. With 3 bands the FWHM errors for the coarse and fine mesh refinements of MBFE without extrapolation are $\epsilon_{FWHM} = 0.074$ and 0.046. With extrapolations these errors reduce to $\epsilon_{FWHM} = 0.010$ and 0.009, which are approximately a factor of 2 more accurate than the erroneously high accuracy of the coarse refined TDFE solution and approximately a factor of 10 more accurate than the TDFE solution with less computational error.

In summary, using as few as three bands in MBFE results in significantly improved representations of ultrasonic pulse full-width-half-maxima relative to those of TDFE simulation, with the exception of one anomalously accurate TDFE result, explained above.

In figure 3.10, the coarse and fine mesh TDFE PD errors are $\epsilon_t = 0.047$ and 0.038. The MBFE errors asymptote towards the highest accuracy achievable for a given mesh refinement. With 3 bands the PD errors for the coarse and fine mesh refinements of MBFE without extrapolation are $\epsilon_t = 0.042$ and 0.035. With extrapolations these errors reduce to $\epsilon_t = 0.040$ and 0.033, which are approximately a factor of 1.1 more accurate than the coarse refined TDFE solution and approximately a factor of 1.4 more accurate than the TDFE solution with less computational error.

In summary, using as few as three bands in MBFE results in significantly improved representations of ultrasonic pulse propagation duration relative to those of TDFE simulation.

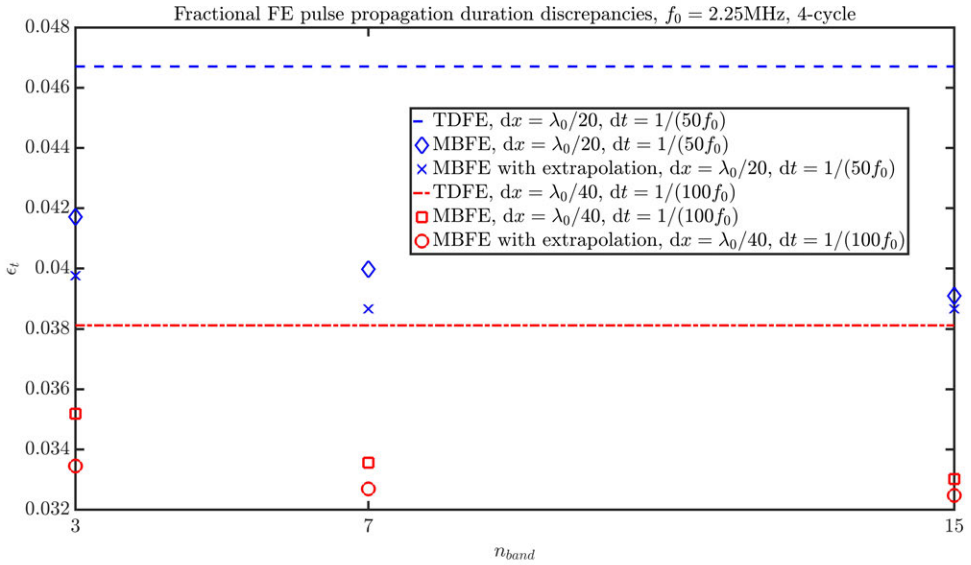

Figure 3.10: Propagation duration discrepancies between the empirical propagation of a 4-cycle toneburst and the TDFE and MBFE approximations to this. The dotted line is the TDFE fractional error with $dx = \lambda_0/20$. For the same mesh refinement, the diamonds are the MBFE PD fractional errors and the crosses are the fractional errors for MBFE with extrapolation. The dot-dashed line is the TDFE fractional error with $dx = \lambda_0/40$. For the same mesh refinement, the squares are the MBFE fractional errors and the circles are the fractional errors for MBFE with extrapolation.

The absolution reduction in error from TDFE to MBFE is greater for FWHM than PD because FWHM is influenced by attenuation and phase velocity accuracy while PD error is only influenced by phase velocity; for viscoelastic media with dispersion relations that adhere to the Kramers-Kronig causality constraint, as with equations (3.3.3) and (3.3.4), attenuation varies more than phase velocity with frequency and is therefore less well represented by the TDFE frequency independent solution. Extrapolation provides the largest reduction in MBFE FWHM error because of the high frequency dependence of attenuation, while mesh refinement provides the largest reduction in MBFE PD error because of the relatively large reduction in velocity accuracy when the number of elements per wavelength is lower.

Consequently, MBFE has been quantitatively validated using the example of ultrasonic wave propagation in HDPE that has a known general functional form for frequency dependent dispersion. MBFE has also been shown to provide significant improvements over TDFE for as few as 3 bands.

3.5.2 Wave scattering

Wave scattering is a second case where dispersion characteristics, including the influence of the scatterer, follow general frequency dependence describable by MBFE. The scattered pulse shapes of TDFE simulations will be compared with those of MBFE with 3 bands. The convergence of the 3 band solution to a 15 band solution will be depicted for a high mesh refinement MBFE example with extrapolation at the outer band edges.

The following analysis is of simulations using the cylindrical void scattering geometry shown in figure 3.3, where the wave is monitored at the same location before incidence on the scatterer and after scattering. In figure 3.11, the solid curve is the

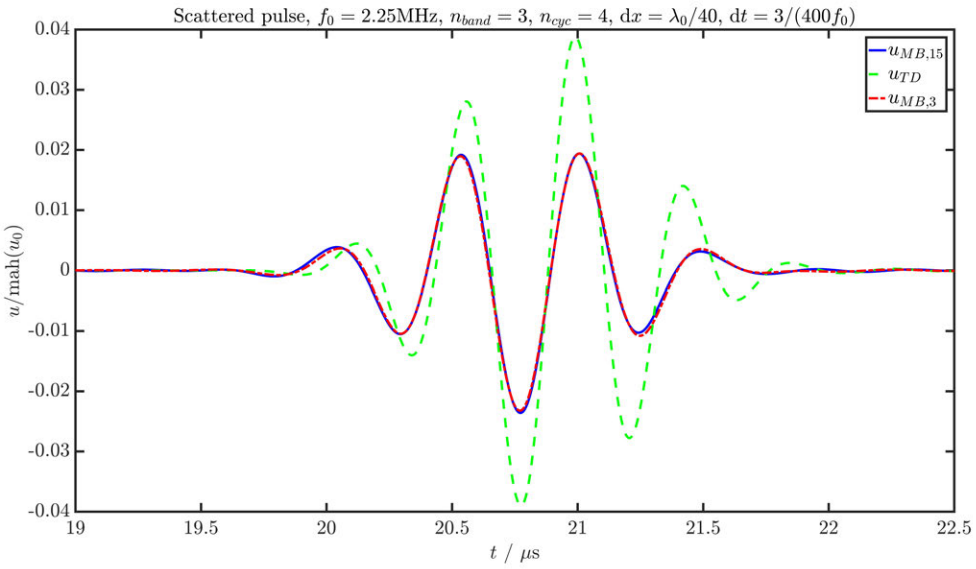

Figure 3.11: FE simulated longitudinal wave pulses propagated in HDPE and scattered from a 3mm cylindrical void. The input pulses are 4-cycle tonebursts with Blackman-Harris envelopes. The centre frequency of the input pulse is $f_0 = 2.25$MHz and the mesh spacing is $\mathrm{d}x = \lambda_0/40$ and the time increment is $\mathrm{d}t = 3/(400f_0)$. The pulse amplitudes are normalised to the maximum of the amplitude of the Hilbert transform of the input pulse, $\mathrm{mah}(u_0)$. The solid curve is the 15 band MBFE scattered pulse, $u_{MB,15}$, the dashed curve is the TDFE scattered pulse, u_{TD}, and the dot-dashed curve is the 3 band MBFE scattered pulse, $u_{MB,3}$.

15 band MBFE scattered pulse, $u_{MB,15}$, the dashed curve is the TDFE scattered pulse, u_{TD}, and the dot-dashed curve is the 3 band MBFE scattered pulse, $u_{MB,3}$. The TDFE has an amplitude that is approximately double that of the 15 band MBFE pulse. Also, its period is too short, which will result in a FWHM that is too low. The phase is approximately one quarter of a cycle wrong. The propagation duration is approximately equal to that of the 15 band MBFE pulse. The 3 band MBFE solution has fully converged to the 15 band MBFE pulse, within uncertainty

bounds much smaller than the computational error caused by the finite mesh size. In summary, using as few as three bands in MBFE results in a significantly improved representation of ultrasonic wave scattering relative to that of TDFE simulation.

3.6 Discussion and Conclusions

Conventional TDFE simulations provide insufficient accuracy when describing ultrasonic waves in materials where wave propagation results in a large reduction in wave amplitude, because they are limited to restrictive damping models, such as Rayleigh damping. FDFE is discussed as an alternative approach to such simulation, but this method is inherently highly computationally expensive for large model sizes and, using usual implementation in many commercial software packages, FDFE can also be limited in its description of different frequency dependent dispersion relations. Accurate application of FDFE to, for example, viscoelastic waves often requires prior accurate knowledge of the frequency dependence of storage and loss moduli, rather than just the frequency dependence of attenuation and phase velocity. The MBFE approach is beneficial because such material properties as storage and loss moduli require significant materials testing to obtain. The inference of these acoustic properties using specific relations to material properties can result in increased uncertainty or error, potentially caused by such a mathematical description using unsuitable approximations to variations in, or unsuitable operating ranges in, the parameters with which the acoustic properties vary. For example, these material properties must usually be inferred using extrapolation from data obtained at frequencies significantly below ultrasonic frequencies. In wave simulation, use of accurate and reliable fully parameterised acoustic properties inherently bypasses these potential complications and sources of uncertainty or error. MBFE is consequently devised and proposed as an appropriate approach to modelling ultrasonic viscoelastic waves, and other such dispersion relations with general frequency dependence, only using prior knowledge of acoustic properties.

The MBFE approach is validated using a wave propagation example and shown to significantly increase accuracy over the TDFE example. For HDPE pipe material, while the large variation of its attenuation with frequency results in improved accuracy, even for a high number of MBFE bands, the smaller variation with frequency of its phase velocity leads to higher achievable absolute accuracy; using MBFE with 3

bands is highly beneficial for sizing accuracy, for example using a 6dB drop in amplitude, and also beneficial for location accuracy because of its improved propagation duration accuracy.

Scattering from a cylindrical void is demonstrated as an alternative case where MBFE is implemented to simulate waves with transfer functions that have general frequency dependence. The MBFE 3 band solution is fully converged to the 15 band pulse shape, within uncertainty bounds, while the TDFE solution features significant discrepancy.

MBFE is shown to improve accuracy over TDFE without incurring high computational cost. Furthermore, MBFE can be significantly more computationally efficient than FDFE for similar accuracy, or potentially more efficient with higher accuracy than an FDFE simulation implemented in many current commercial software packages.

References

[1] K.-J. Bathe, *Finite Element Procedures in Engineering Analysis*, Prentice-Hall, New Jersey, 887-1012, 1982.

[2] P. Huthwaite, *Accelerated finite element elastodynamic simulations using the GPU*, Journal of Computational Physics, **257**(A), January 2014.

[3] R.E. Challis, F. Blarel, M.E. Unwin, J. Paul, and X. Guo, *Models of ultrasonic wave propagation in epoxy materials*, Ultrasonics, Ferroelectrics, and Frequency Control, IEEE Transactions on, **56**(6), June 2009.

[4] S. Holm and S.P. Nasholm, *Comparison of fractional wave equations for power law attenuation in ultrasound and elastography*, Ultrasound in Med. & Biol., **40**(4), April 2014.

[5] J.S. Egerton, M.J.S. Lowe, H.V. Halai, P. Huthwaite, *Ultrasonic attenuation and phase velocity in high-density polyethylene (HDPE) pipe material*, J. Acoust. Soc. Am. **141**(3), 1535-1545 (2017).

[6] S.I. Rokhlin, D.E. Chimenti, and P.B. Nagy, *Physical Ultrasonics in Composites*, Oxford University Press, Oxford, 3-368, 2011.

[7] M.L. Palmeri, A.C. Sharma, R.R. Bouchard, R.W. Nightingale, and K.R. Nightingale, *A finite-element method model of soft tissue response to impulsive acoustic radiation force*, Ultrasonics, Ferroelectrics, and Frequency Control, IEEE Transactions on, **52**(10), October 2005.

[8] P. Moczo, J. Kristek, M. Galis, P. Pazak, and M. Balazovjech, *The finite-difference and finite-element modelling of seismic wave propagation and earthquake motion*, Acta Physica Slovaca, **57**(2), February 2007.

[9] J.O. Smith III, *Spectral Audio Signal Processing* (W3K Publishing, Lewiston, NY, USA), 57-63 (2011).

[10] L. Meirovitch, *Fundamentals of Vibration*, McGraw Hill Publications, 77-144 (2003).

[11] C. Ramadas, K. Balasubramaniam, A. Hood, M. Joshi, and C.V. Krishnamurthy, *Modelling of attenuation of Lamb waves using Rayleigh damping: Numerical and experimental studies*, Composite Structures, **93**, 2011.

[12] J. Wu, *Determination of velocity and attenuation of shear waves using ultrasonic spectroscopy*, J. Acoust. Soc. Am., **99**(5), May 1996.

[13] J.R. Pettit, A. Walker, P. Cawley, and M.J.S. Lowe, *A stiffness reduction method for efficient absorption of waves at boundaries for use in commercial finite element codes*, Ultrasonics, **54**(7), September 2014.

[14] M.B. Drozdz, *Efficient finite element modelling of ultrasound waves in elastic media*, Ph.D. Thesis, Imperial College London, 182-203, January 2008.

3.7 Appendices

3.7.1 Blending techniques inferior to k-blending

The first omitted approach takes the transfer function of each band evaluated at solely the band centre frequencies then assigns these fixed values, obtained from each TDFE simulation, to all frequencies within their corresponding band. The resulting propagated spectrum is sharply stepped, therefore much precise band filtering is necessary. This is a cumbersome approach that requires many specific parameters, making it less immediately general. The second approach is to linearly interpolate the transfer function between the band centre values. This is less accurate than k-blending. The next approach is logarithmic interpolation of the transfer function. This is accurate for propagation of a power law dispersive wave but not generalisable to scattering. The propagated spectrum may also be linearly interpolated. This is less accurate than k-blending. Of blending approaches, first the propagated spectra of each band are blended, then the phase velocities and attenuations are blended,

followed by dispersions, and finally the transfer functions. Of these, blending the dispersion relations proves accurate, general, and simple to implement and use.

Chapter 4

Analytical ultrasonic scattering from a cylindrical void in a highly attenuating medium, with image reconstruction of such scatterers

4.1 Abstract

This work was conducted to extend a method for describing ultrasonic scattering from cylindrical voids, which is used in the nondestructive evaluation (NDE) industry, from its existing elastic formulation to a novel general formulation for highly attenuating media. While multiband FE is more general, the generalised formulation provided here remains applicable only to cylindrical voids. For cylindrical void scattering, this method is expected to be more computationally efficient than multiband FE, with similar accuracy. This novel formulation is exemplified with cylindrical voids in high-density polyethylene (HDPE), which is viscoelastic. Further to this, novel formulation for image reconstruction of such scatterers is also provided and analysed. The improved waveform simulation accuracy of the general attenuative formulation, which is used to represent the viscoelastic HDPE medium, also results in higher amplitude difference between the image reconstruction of the cylinder and its surrounding artefacts.

4.2 Introduction

Analytical simulations can be more computationally efficient, with similar accuracy, than equivalent FE approaches, for the specific scattering problems to which they are applicable. There exist many studies on the analytical scattering of waves from elastic cylindrical voids, for example, [1–6], but fewer for highly attenuating media, such as these viscoelastic examples, [7, 8]. The viscoelastic examples use Kelvin-Voigt or Maxwell models and these functional forms cannot describe general viscoelasticity, and less so general attenuation in highly attenuating media.
First, the existing formulation of analytical elastic ultrasonic cylinder scattering is provided, then these equations are here generalised to highly attenuating media, and exemplified with ultrasound scattering from cylindrical voids in viscoelastic high-density polyethylene (HDPE).

4.3 Theory

The theory for the scattering of elastic waves from cylindrical voids and image reconstruction of such scatterers is presented as follows. First, the existing published theory is set out. Next, this is extended in a general way to enable it to predict the scattering when the material is attenuative. Finally, the image reconstruction of cylindrical discontinuities from ultrasonic scattered pulses is formulated.

4.3.1 Existing elastic theory

Detailed here is existing analytical theory for elastic ultrasonic wave scattering from cylindrical voids. This existing formulation is not generally applicable to scattering from cylindrical voids in attenuative media. Figure 4.1 shows the analytical cylindrical void scattering simulation geometry. The cylinder is central and marked by the circular line, the scattered wave monitor locations are marked by squares, and the source location, at $\theta = 180°$, is marked by a cross.
For a longitudinal wave incident on a cylindrical void of radius a, the total particle displacement field may be defined as the sum of the incident longitudinal (L) and

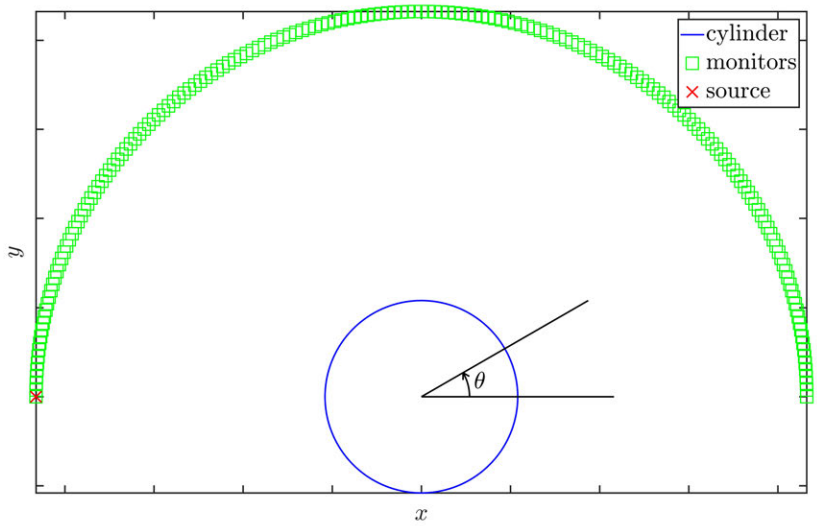

Figure 4.1: Analytical cylindrical void scattering simulation geometry. The cylinder is central and marked by the circular line, the scattered wave monitor locations are marked by squares, and the point source location, at $\theta = 180°$, is marked by a cross.

scattered longitudinal and shear (S) waves,

$$u = u_L^{inc} + u_L^{scat} + u_S^{scat}. \tag{4.3.1}$$

Defining the incident and scattered particle displacement fields in equation (4.3.1) – in cylindrical coordinates in 2-D, the particle displacement, at a radius, r, angle, θ, time, t, angular frequency, ω, and wavenumber, k, is [3, 4]

$$u_L^{inc}(r,t) = ik_L u(0,0,0)\left[\sum_{n=0}^{\infty}(2-\delta_{0n})i^n J_n(k_L r)\right]\exp(-i\omega t), \tag{4.3.2}$$

$$u_L^{scat}(r,\theta,t) = \left[\sum_{n=0}^{\infty} A_n H_n^{(1)}(k_L r)\cos(n\theta)\right]\exp(-i\omega t), \tag{4.3.3}$$

and

$$u_S^{scat}(r,\theta,t) = \left[\sum_{n=0}^{\infty} B_n H_n^{(1)}(k_S r)\sin(n\theta)\right]\exp(-i\omega t), \tag{4.3.4}$$

where δ_{0n} is the Kronecker delta, J_n and $H_n^{(1)}$ are the Bessel and Hankel functions of the first kind of order n. The amplitude coefficients of the particle displacement fields are

$$A_n = -(2-\delta_{0n})i^{n+1}k_L u(0,0,0)\frac{\begin{vmatrix} E_{11}^{(1)} & E_{12}^{(3)} \\ E_{41}^{(1)} & E_{42}^{(3)} \end{vmatrix}}{D_n} \tag{4.3.5}$$

and

$$B_n = -(2-\delta_{0n})i^{n+1}k_S u(0,0,0)\frac{\begin{vmatrix} E_{11}^{(3)} & E_{11}^{(1)} \\ E_{41}^{(3)} & E_{41}^{(1)} \end{vmatrix}}{D_n}, \tag{4.3.6}$$

where

$$D_n = \begin{vmatrix} E_{11}^{(3)} & E_{12}^{(3)} \\ E_{41}^{(3)} & E_{42}^{(3)} \end{vmatrix} \tag{4.3.7}$$

and

$$E_{11}^{(j)} = \left(n^2 + n - \frac{1}{2}k_S^2 a^2\right) F_n^{(j)}(k_L a) - k_L a F_{n-1}^{(j)}(k_L a), \tag{4.3.8}$$

$$E_{12}^{(j)} = n(n+1)F_n^{(j)}(k_S a) - nk_S a F_{n-1}^{(j)}(k_S a), \tag{4.3.9}$$

$$E_{41}^{(j)} = n(n+1)F_n^{(j)}(k_L a) - nk_L a F_{n-1}^{(j)}(k_L a), \tag{4.3.10}$$

and

$$E_{42}^{(j)} = -\left(n^2 + n - \frac{1}{2}k_S^2 a^2\right) F_n^{(j)}(k_S a) + k_S a F_{n-1}^{(j)}(k_S a), \tag{4.3.11}$$

for which $F_n^{(1)} = J_n$ and $F_n^{(3)} = H_n^{(1)}$. The angle θ is zero for wave propagation in the incident direction and marked by the rightmost monitor in figure 4.1.

4.3.2 Generalised attenuative theory

The task now is to extend the elastic wave scattering theory so that attenuation, such as material damping, can be taken into account. This will be done here in a general way by introducing an imaginary part to the wavenumber k. The wavenumber is here used to define ultrasonic bulk wave longitudinal and shear dispersion relations for highly attenuating media, including viscoelastic media,

$$k_{L,S} = \frac{\omega_{L,S}}{v_{p,L,S}} + i\alpha_{L,S}, \tag{4.3.12}$$

where $v_{p,L,S}$ are longitudinal and shear phase velocities and $\alpha_{L,S}$ are attenuation coefficients. The general form of equation (4.3.12) is suited to highly attenuating waves, as for viscoelastic waves in HDPE. It is noted that the real components of $k_{L,S}$, not the complex $k_{L,S}$ of equation (4.3.12), are used in the Bessel arguments to prevent unphysical dephasing of the wave that would be seen as low-level ripples in the pulse occurring earlier than the first arrival of the pulse. Also, the existing elastic wave formulation may be yielded by taking the real components of the dispersion relations, $k_{L,S}$, of equation (4.3.12). For HDPE, k_L is obtained with high accuracy in [4] and k_S is approximated from the results of [10].

4.3.3 Cylinder image reconstruction

Having identified the equations for elastic wave scattering from cylindrical voids in attenuative material, the target now is to use these formulae to perform image reconstruction from monitored scattered longitudinal or shear pulses and knowledge of the ultrasonic propagation dispersion relation, $k_{L,S}$, in the medium. Such image

reconstruction requires

$$S_0(\theta, \nu_x) = \frac{S(\theta, \nu_x)}{H(\theta, \nu_x)}, \tag{4.3.13}$$

where the back-propagated pulse spectrum is S_0 in the spatial frequency domain, given

$$\nu_x = \frac{f}{v_{p,L,S}}; \tag{4.3.14}$$

the monitored pulse spectrum is S; and the transfer function that maps the propagation of S_0 to S is

$$H(\theta, \nu_x) = \exp\left[ik_{L,S}(\nu_x)\overline{x}(\theta)\right], \tag{4.3.15}$$

given that $\overline{x}$ is the mean propagation path travelled by the ultrasonic pulse to and from the cylindrical discontinuity.

4.4 Results

Provided below are simulated scattered pulses of the above elastic and general cylindrical void scattering formulations, as well as cylindrical void spatial image reconstructions that use these simulated waveforms.

4.4.1 Viscoelastic and elastic high-density polyethylene scattered pulses

Presented here are scattered pulse waveforms from a simulated implementation of the above cylindrical void scattering formulation that, first, uses the existing elastic model and, second, accounts for viscoelastic damping in HDPE. Figures 4.2 to 4.5 show back-scatters, from $\theta = 180°$ – with longitudinal incidence and longitudinal scatter, LL – from cylindrical voids in viscoelastic and elastic representations of HDPE. The four figures show results respectively for four different sizes of the

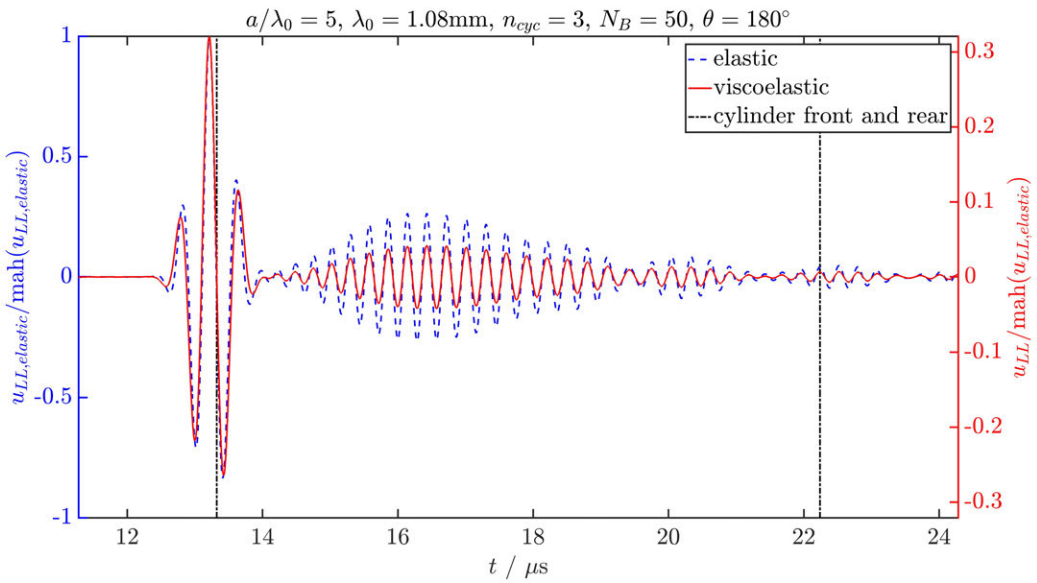

Figure 4.2: Back-scattered pulses, from $\theta = 180°$, from cylindrical voids in viscoelastic and elastic HDPE, with radii per wavelength, $a/\lambda_0 = 5$. The dashed line, associated with the left y-axis, is the elastic approximation; the solid line, associated with the right y-axis is the viscoelastic full representation of the medium; and the vertical dot-dashed lines mark the arrival times for the front and rear of the cylinder for a centre wavelength, $\lambda_0 = 1.08$mm, wave component travelling to and from the cylinder extrema at the centre bulk longitudinal phase velocity, $v_{p,L,0}$. Viscoelastic and elastic LL pulses are normalised by the maximum amplitude of the absolute of the Hilbert transform, mah$(\cdot)$, of the elastic LL pulse. The ultrasonic pulse has three periods, or cycles, $n_{cyc} = 3$. The infinite sums of equations (4.3.2) to (4.3.4) are truncated to $N_B = 50$.

cylindrical void, from a/λ_0=5 to a/λ_0=0.5. These voids are centred $20\lambda_0$ from the ultrasonic point source, which is also the location at which the wave is monitored, after scattering from the cylindrical void. Viscoelastic HDPE results are here the reference comparator, as detailed in [4]. The dashed line, associated with the left y-axis, is the elastic approximation; the solid line, associated with the right y-axis is the viscoelastic full representation of the medium; and the vertical dot-dashed lines mark the front and rear of the cylinder arrival times for a centre wavelength, $\lambda_0 = 1.08$mm, wave component travelling to and from the cylinder extrema at the centre bulk longitudinal phase velocity, $v_{p,L,0}$. The first arriving components of the pulse, from the front of the cylinders, coincide with the vertical lines.

The Huygens-Fresnel principle allows a cylindrical void to be decomposed into a superposition of point scatterers. Oblique scattered waves from scatterers at angles away from normal arrive later, because of the curved surface of the cylinder. For the point source, such oblique incidence angles result in reduced wave content re-radiated towards the monitor point, compared with the content from the points aligned at normal incidence to the frontmost edge of the cylindrical void. This may

be understood through consideration of the pressure wave oscillation of the particles, or point scatterers. These oscillations are, first, partially restricted, being partially directed into the solid medium and partially into the void, and, second, unrestricted, being directed into the void, or halfspace, respectively for the oblique and normal cases.

In figures 4.2 to 4.5 the maximum amplitudes of the attenuated viscoelastic pulses, shown on the righthand y-axes, are less than those of the non-attenuated elastic pulses, shown on the lefthand y-axes, because the pulses propagate with a mean path, $\overline{x}$, that is $20\lambda_0$ to, and $20\lambda_0$ from, the cylindrical voids, through a damping medium, HDPE. Also, the two y-axes scale the amplitudes of the pulses that first arrive at the monitor, for the viscoelastic and elastic simulations, such that the pulses are of comparable height. The amplitudes of later arriving components of the scattered pulses are reduced in amplitude more in the viscoelastic cases than in the elastic cases. This is as expected for pulse components arriving later, from oblique angles, because some of the wave oscillation is converted from longitudinal to shear, which is very highly attenuated in viscoelastic media such as HDPE.

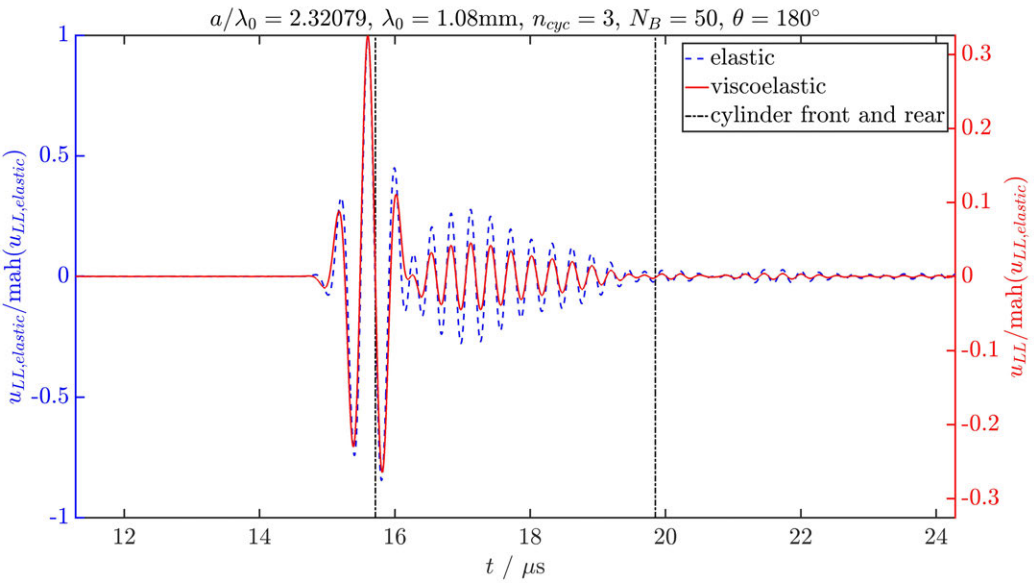

Figure 4.3: Back-scattered pulses, as in figure 4.2, except with radii per wavelength, $a/\lambda_0 = 2.32079$.

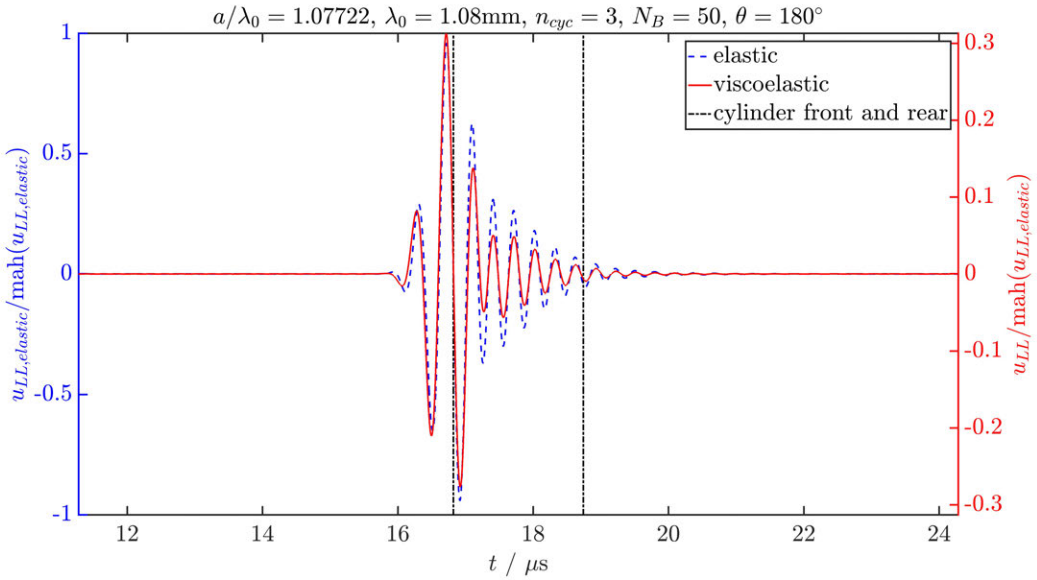

Figure 4.4: Back-scattered pulses, as in figures 4.2 and 4.3, except with radii per wavelength, $a/\lambda_0 = 1.07722$.

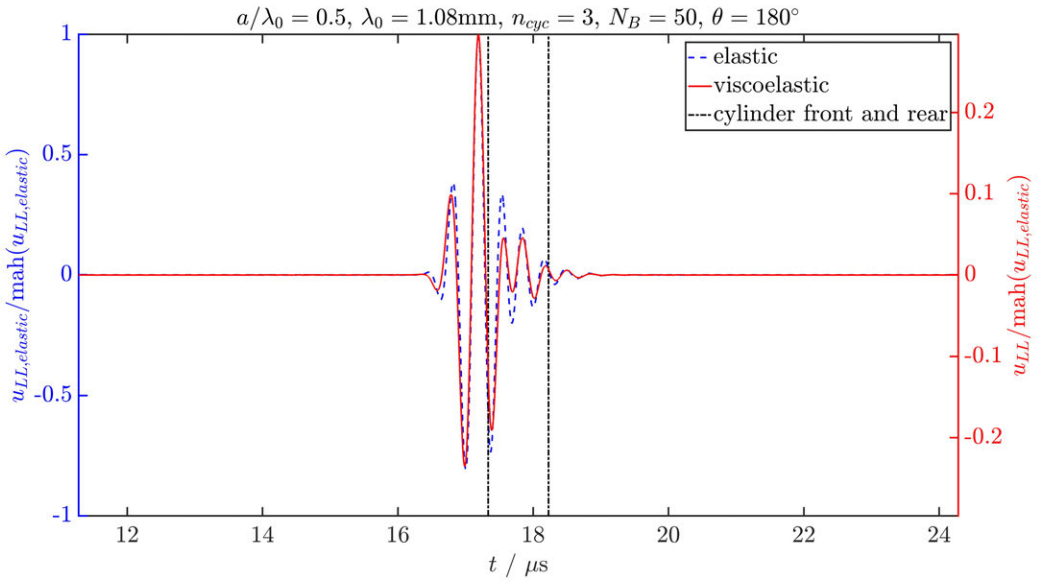

Figure 4.5: Back-scattered pulses, as in figures 4.2 to 4.4, except with radii per wavelength, $a/\lambda_0 = 0.5$.

4.4.2 Viscoelastic and elastic high-density polyethylene cylindrical void reconstructions

Detailed here are cylindrical void reconstructions from a simulated implementation of the above cylindrical void scattering formulation that, first, accounts for viscoelastic damping in HDPE and, second, uses the existing elastic model. Figures 4.6 to 4.9 show viscoelastic and elastic image reconstructions of the cylinders obtained

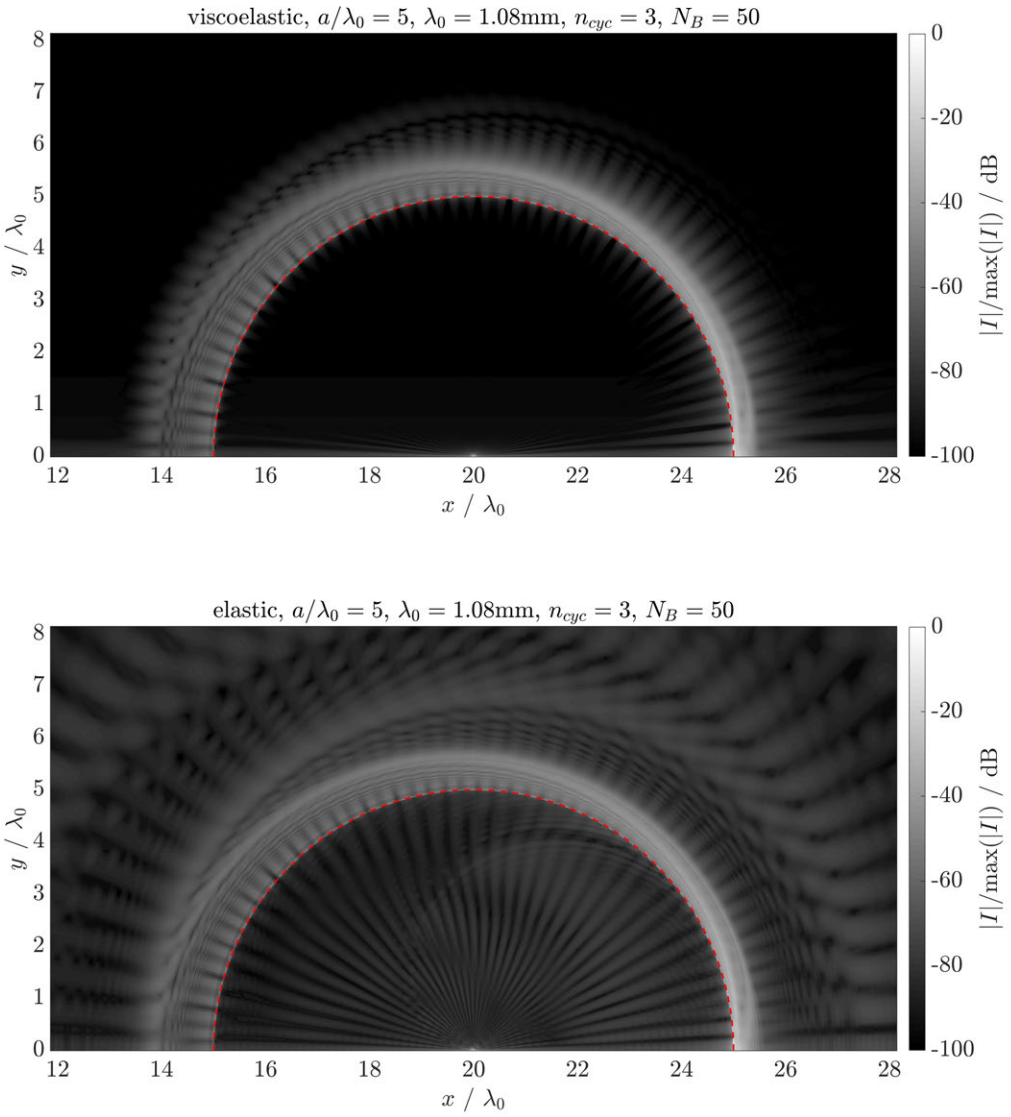

Figure 4.6: Viscoelastic (top) and elastic (bottom) HDPE reconstructions of the cylinders obtained by deconvolving, by the input pulse, the scattered waveforms, exemplified in figures 4.2 to 4.5, using equation (4.3.13). Cylinder radius per wavelength is $a/\lambda_0 = 5$. The cylinder boundaries area marked by the dotted lines.

by deconvolving, by the input pulse, using equation (4.3.13), the scattered waveforms, exemplified in figures 4.2 to 4.5. While some sampling artefacts exist in the images, for all cylinders the viscoelastic and elastic reconstruction boundaries are coincident with the cylinders, marked with dotted lines. For both the viscoelastic and the elastic simulations, the pulse characteristics are deconvolved from the waveform, before imaging. However, especially for the larger cylinders, the viscoelastic cylinder reconstructions have higher amplitude difference between the cylinders and their surrounding artefacts than do the elastic cylinder reconstructions. This could

be because the accurate representation of attenuation in the viscoelastic waveform simulation inherently results in decreasing wave amplitude with increasing time, which continues up to the latest time represented in the waveform. In the elastic simulation, at the latest simulated time, there may be an abrupt step in amplitude of any wave content present at that time, which leads to unintended, additional broadband frequency content. Such broadband frequency content could be the source of the noise exhibited in the elastic image reconstructions of figures 4.6 to 4.9 that is less prominent in the viscoelastic image reconstructions.

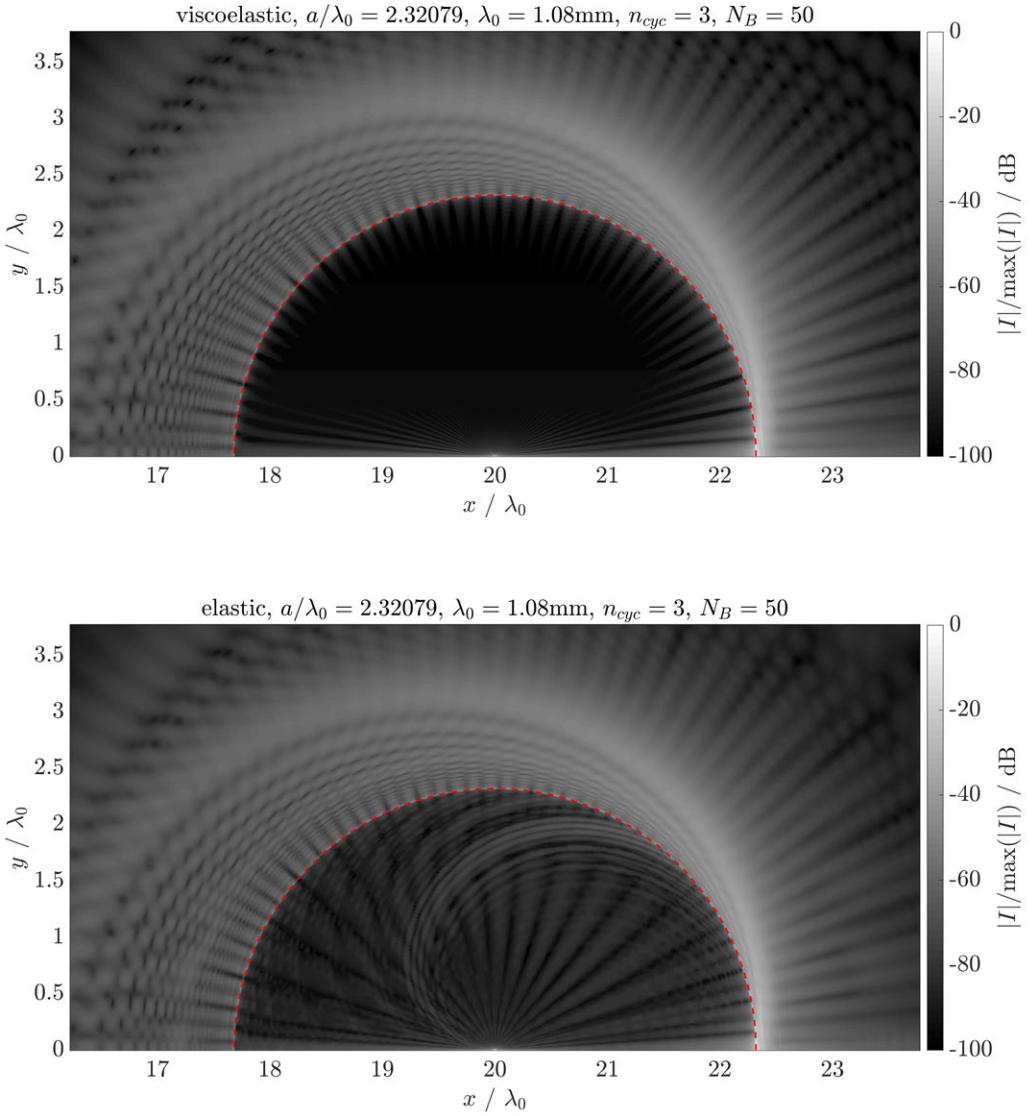

Figure 4.7: Viscoelastic (top) and elastic (bottom) HDPE reconstructions of the cylinders, as in figure 4.6, except with radii per wavelength, $a/\lambda_0 = 2.32079$.

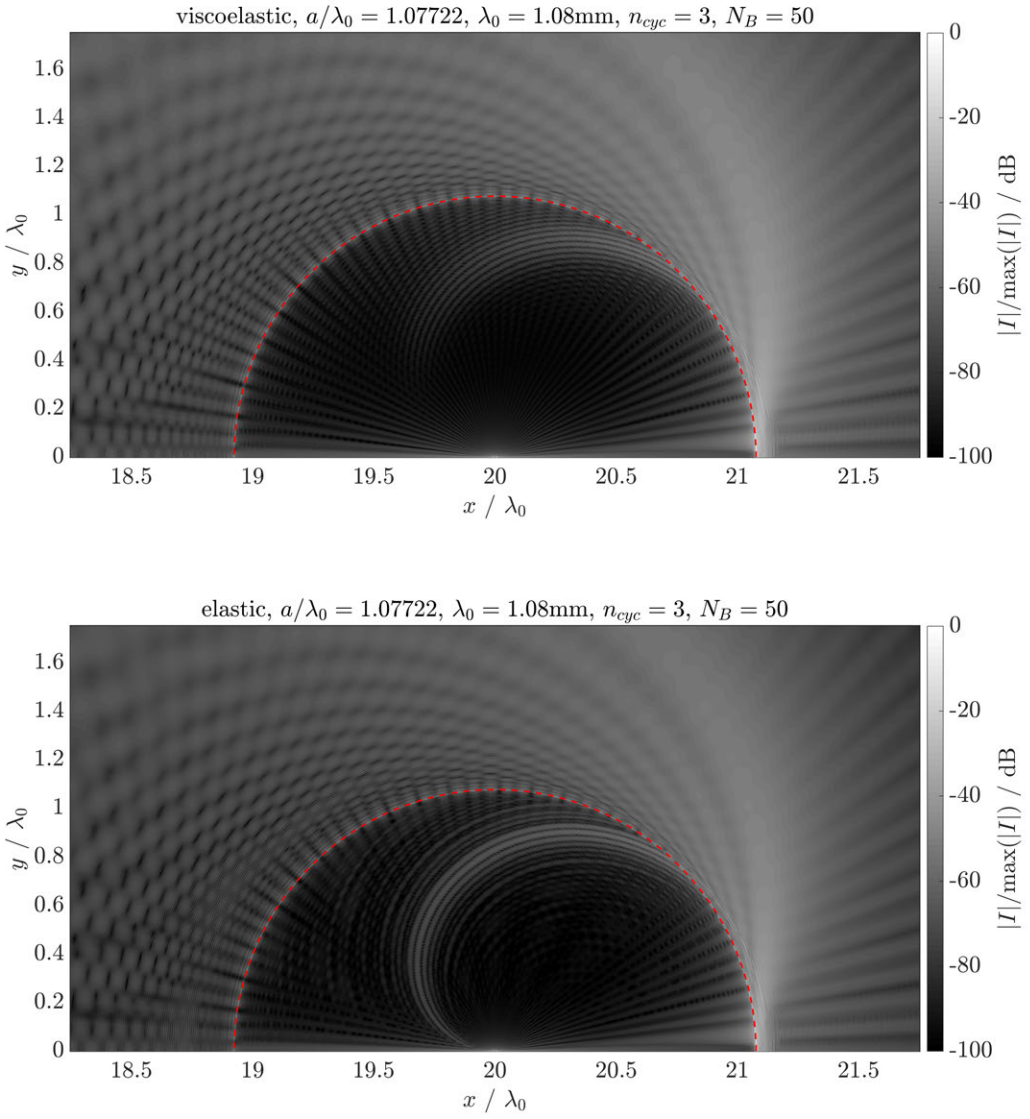

Figure 4.8: Viscoelastic (top) and elastic (bottom) HDPE reconstructions of the cylinders, as in figures 4.6 and 4.7, except with radii per wavelength, $a/\lambda_0 = 1.07722$.

4.5 Conclusion

The analytical theory for ultrasonic scattering from a cylindrical void has been extended from an elastic formulation, as seen in current literature, to a general formulation that is accurate for highly attenuating media, such as HDPE, which is viscoelastic. Both viscoelastic and elastic simulated ultrasonic waveforms are shown to be reconstructible as cylinders, by deconvolution by the input pulse. For HDPE, the viscoelastic cylinder image reconstructions are both much more accurate for such materials and also have a higher amplitude difference between the cylinders

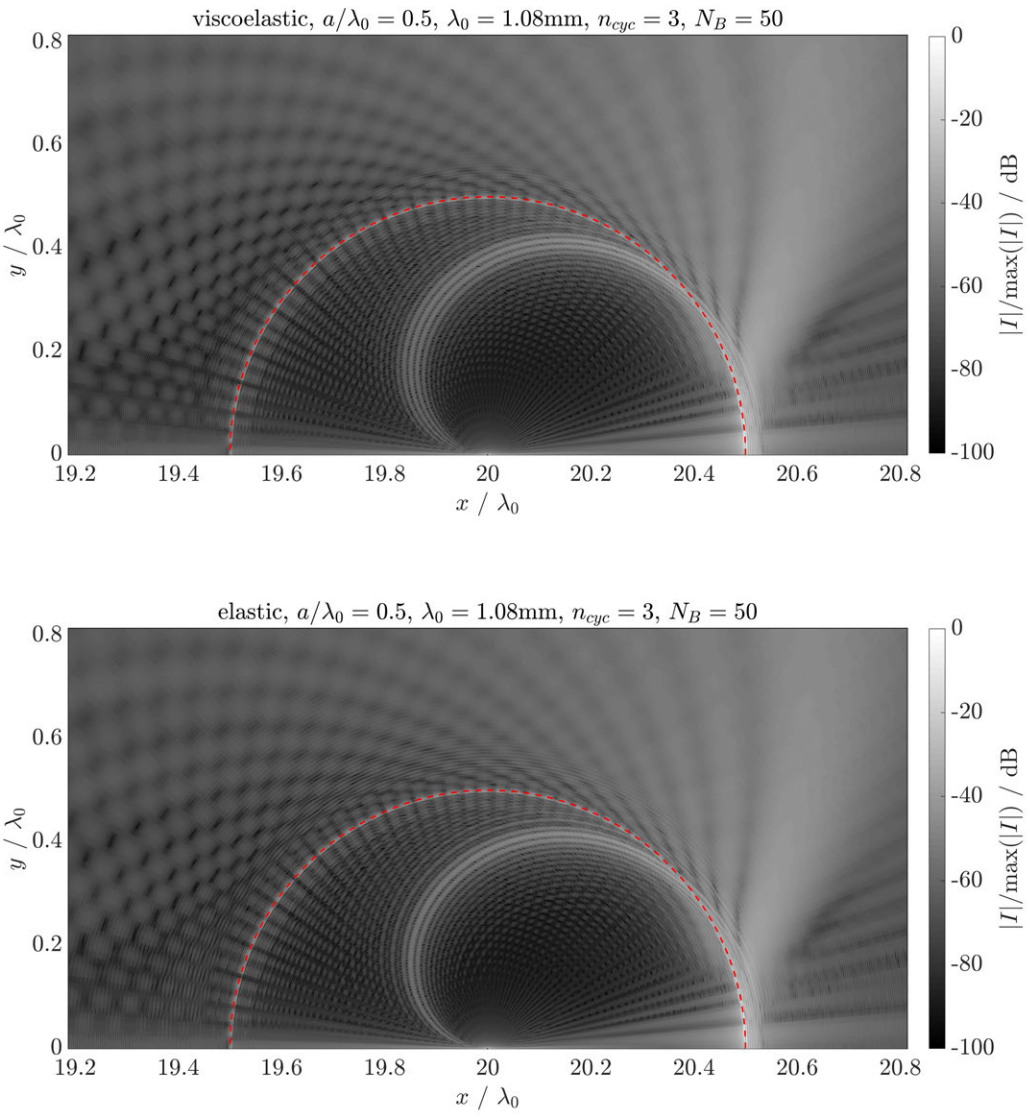

Figure 4.9: Viscoelastic (top) and elastic (bottom) HDPE reconstructions of the cylinders, as in figures 4.6 to 4.8, except with radii per wavelength, $a/\lambda_0 = 0.5$.

and their surrounding artefacts.

References

[1] K. Sezawa, *Scattering of elastic waves and some allied problems*, Earthquake Research Institute, (1927).

[2] R.M. White, *Elastic wave scattering at a cylindrical discontinuity in a solid*, J. Acoust. Soc. Am. **30**(8), 771-785 (1958).

[3] R.D. Doolittle, H. Überall, and P. Ugničius, *Sound scattering by elastic cylinders*, J. Acoust. Soc. Am., **43**(1), 1-14 (1968).

[4] C-C. Mow and Y-H. Pao, *The diffraction of elastic waves and dynamic stress concentrations*, A report prepared for United States Air Force Project Rand, R-482-PR, (1971).

[5] R.J. Brind, J.D. Achenbach, and J.E. Gubernatis, *High-frequency scattering of elastic waves from cylindrical cavities*, Wave Motion, **6**, 41-60 (1984).

[6] A.L. Lopez-Sanchez, H-J Kim, L.W. Schmerr Jr., and A. Sedov, *Measurement models and scattering models for predicting the ultrasonic pulse-echo response from side-drilled holes*, Journal of Nondestructive Evaluation, **24**(3), 83-96 (2015).

[7] G.C. Gaunaurd, *Methods for solving the viscoelasticity equation for cylinder sphere problems*, Naval Surface Weapon Center, (1976).

[8] G.C. Gaunaurd and H. Überall, *Theory of resonant scattering from spherical cavities in elastic and viscoelastic media*, J. Acoust. Soc. Am., **63**(6), 1699-1712 (1978).

[9] J.S. Egerton, M.J.S. Lowe, H.V. Halai, P. Huthwaite, *Ultrasonic attenuation and phase velocity in high-density polyethylene (HDPE) pipe material*, J. Acoust. Soc. Am. **141**(3), 1535-1545 (2017).

[10] J. Wu, *Determination of velocity and attenuation of shear waves using ultrasonic spectroscopy*, J. Acoust. Soc. Am., **99**(5), 1996.

Chapter 5

Analytical simulation of viscoelastic ultrasonic bulk longitudinal and shear wave scattering from heterogeneities using Huygens principle, demonstrated with image reconstruction of sub-wavelength features and nondestructive evaluation of high-density polyethylene pipe joints

5.1 Abstract

The Huygens-Fresnel principle is applied to generalise the simulation of ultrasonic attenuative pulse scattering from two-dimensional volumetric and planar hetero-

geneities, exemplified with voids, for which the anisotropy and orthogonality of longitudinal and shear wave emission from a point region in a solid is accounted for with the introduction of viscoelastic point scatterers. The viscoelastic point scatterer method is supported with evidence by finite element (FE) analysis, and more is sought – first, the applicability of the anisotropy of the viscoelastic point scatterers for longitudinal wave incidence and scattering and, second, the scattering amplitudes obtained with viscoelastic point scatterer superposition for longitudinal wave incidence and scattering. Further, image reconstruction in an example viscoelastic medium, high-density polyethylene (HDPE), is conducted with viscoelastic point scattering to demonstrate sub-wavelength features of heterogeneities in an ideal ultrasonic circular array imaging setup. Last, this scattering approach is demonstrated with simulated waveform generation and imaging in a HDPE pipe joint setup for the nondestructive evaluation of potential defects.

5.2 Introduction

Using the Huygens-Fresnel principle, ultrasonic wave scattering from a planar defect tip has been simulated in existing studies, such as [1]. The Huygens principle – where waves radiate solely isotropically, or omnidirectionally, from a single location and without account for the longitudinal and shear wave angular dependence and orthogonality of solid media – has been applied to the simulation of ultrasonic wave fields in fluids and elastic solids with the distributed point source method (DPSM) or other comparable methods using the Green's function, which is cumbersome if it incorporates anisotropy [2–9, 9]. Other similar approaches also exist, such as the pencil method, which is demonstrated for the commercial ultrasonic simulation software CIVA [11]. However, such formulations do not represent ultrasonic waves in general, attenuative media, but only specific attenuative cases; the pencil method does provide treatment of longitudinal and shear waves. Further, the viscoelastic point scattering method does not require computationally intensive numerical methods, such as finite element (FE) analysis, that may otherwise be used to obtain the correct ultrasonic bulk longitudinal and shear wave behaviour of scattering [6]. Also, such FE methods are conventionally less accurate at representing wave propagation in attenuative and dispersive media, without the multiband finite element (MBFE) time domain wave propagation and scattering, and imaging method [5, 5].

The aim of this study in this chapter is to provide a highly efficient, general ultrasonic bulk longitudinal and shear wave scattering simulation method that can also provide accurate wave propagation behaviour. This analytical method is inherently computationally rapid, more so than MBFE. This is because it involves the repeat application of operators to single waveforms, rather than explicit time stepping for a FE mesh of the geometry of the defect. Also, the practical implementation, including the movement and storage of data, of a combined FE and analytical method, such as MBFE, can have a reduced efficiency compared with a purely analytical approach. However, the viscoelastic point scatterer method currently suffers partially reduced accuracy, because of temporary storage requirements, to simulate defects significantly larger than a wavelength, while MBFE does not. In this way the methods are considered complementary.

First, existing theories are highlighted that are necessary for such waveform generation and imaging. Next, said theory is applied to the ultrasonic imaging of simulated two-dimensional volumetric and planar heterogeneities, exemplified with voids, which have sub-wavelength features. Last, this approach is applied to non-destructive evaluation (NDE) of HDPE pipe joint for simulated potential defects. While here being exemplified with viscoelastic high-density polyethylene (HDPE) material, this approach is applicable for general, attenuative media.

5.3 The Huygens and Fresnel principles

Existing theories that define interface reflection and refraction, and that define the scattering of waves from heterogeneities through decomposition into point scatterers, are here combined in a formulation that yields ultrasonic bulk longitudinal and shear wave scattering from points in a viscoelastic, or elastic, medium, as predicted by the Huygens-Fresnel principle.

First, Fresnel principle reflection and refraction is formulated for an interface between two general, attenuative materials [15] and an interface between two general, elastic materials [25]. These full formulations are large and, for the specific described example of HDPE pipe joint material containing two-dimensional volumetric and planar voids, for which a stress-free boundary exists, the elastic reflection coefficient

for longitudinal (L) wave incidence and scattering can more simply be given as [25],

$$\Gamma_{LL}(\theta_L, \theta_S, v_{p,L}, v_{p,S}) = \frac{\sin 2\theta_S \sin 2\theta_L - \left(\frac{v_{p,L}}{v_{p,S}}\right)^2 \cos^2 2\theta_S}{\sin 2\theta_S \sin 2\theta_L + \left(\frac{v_{p,L}}{v_{p,S}}\right)^2 \cos^2 2\theta_S} \tag{5.3.1}$$

where θ_L, shown in figure 5.1, is the angle between the path – source to point

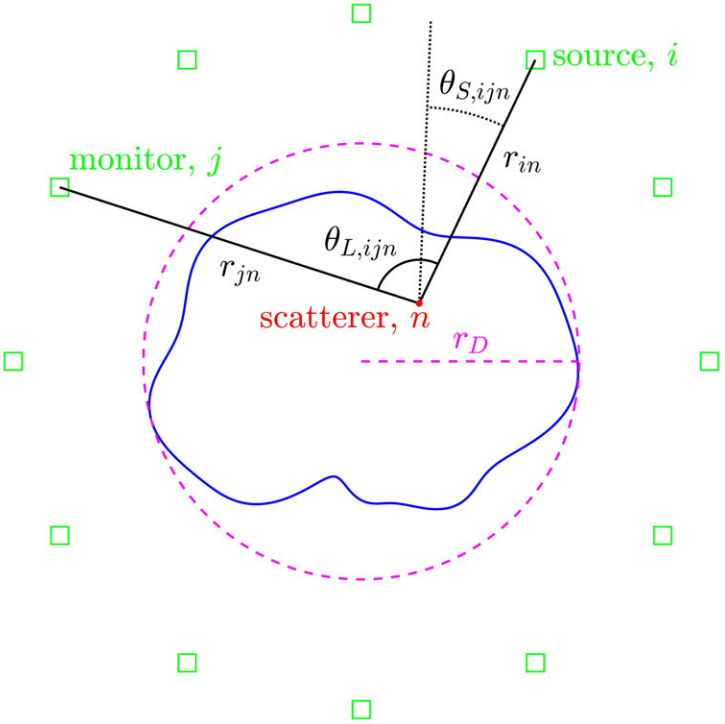

Figure 5.1: Point scattering simulation geometry. All source and monitor locations are squares. The heterogeneity is the solid curve. The enclosing circle radius, r_D of maximum heterogeneity extent is the dashed line that meets the dashed circle. The point scatterer is the circular point that is met by the incident distance from source to point, r_{in}, and scattered distance from point to monitor, r_{jn}, for all source, monitor, and point scatterer combinations. These distances are solid lines. The longitudinal scattering angle, $\theta_{L,ijn}$, is from source to monitor and the shear scattering angle is $\theta_{S,ijn}$.

scatterer then point scatterer to monitor – of the longitudinal incident then scattered waves; θ_S is the angle that the shear component of the wave scatters at after longitudinal incidence on the point scatterer; and $v_{p,L,S}$ are the longitudinal and shear phase velocities in the medium, HDPE, found in [2, 3]. The reflection coefficient of equation (5.3.1) is elastic, but because acoustic impedance change caused by attenuation mismatch is very small relative to the change in bulk modulus and density at the discontinuity, and therefore can be neglected, the approximation to elastic of these local scattering interactions is taken to be a valid assumption. For a

two-dimensional wave field, equation (5.3.1) specifies a plane wave of infinite extent normal to its propagation direction, which is incident on an infinite extent planar interface. A wave component that propagates from point source to point scatterer then from point scatterer to point monitor differs from the same wave component for plane waves and plane interfaces by two beam spread factors. In two dimensions, for a given point scatterer, n, these factors, for longitudinal incidence, i, and scattering, j, are

$$B_{LL,i,j,n} = \frac{1}{\sqrt{r_{i,j,n}}} \tag{5.3.2}$$

where $r_{i,j,n}$ are the incident and scattered pulse propagation distances for all source, i, monitor, j, and point scatterer, n, combinations.

Second, upon wave incidence on the heterogeneity within the medium, the Huygens principle is applied, through the linear superposition of adjacent quantised point heterogeneities, or point scatterers, that collectively define the two-dimensional scatterer – in the case of a two-dimensional simulation. Huygens principle is used to represent scattering from a finite extent void in the medium. Any nonlinear components of the scattered wave that arise from a high amplitude incident wave are expected to be low, and any such nonlinearities that are of higher frequency shall be more highly attenuated in HDPE than the linear content of the wave [2]. Consequently, linearity is seen to be a valid assumption.

For all simulations here, the spacing between superposed point scatterers is much less than the wavelength at the centre frequency of the wave,

$$\frac{\mathrm{d}x}{\lambda_0} \ll 1. \tag{5.3.3}$$

Therefore, because of the closeness of adjacent point scatterers, and because each scattering interaction with a point scatterer results in a loss of wave amplitude with distance from the scatterer, in accordance with equation (5.3.2), multiple scattered waves from the point scatterers of the heterogeneity are seen to contribute negligibly to the total scattered wave content from said heterogeneity. A concave defect face might direct some scattered wave content towards the monitor after multiple

scattering, and is not simulated here as doing such. However, it would be highly computationally expensive to simulate all relevant possible combinations of multiple scatterers.

For a volumetric heterogeneity, the viscoelastic point scatterer method superposes heterogeneity quanta, or cells, within the heterogeneity volume, or area in two dimensions. The Born approximation, used with penetrable scatterers, relies on this approach, and this is a fundamental assumption in diffraction tomography [2]. It is alternatively possible to superpose boundary heterogeneity quanta without superposing the volume, which is similar to certain treatments of electromagnetic wave diffraction [19] or that of the DPSM method [3–5]. The viscoelastic point heterogeneity approach is exemplified with impenetrable scatterers that represent voids, and hence the above argument that just the boundary scatterers contribute to wave scattering. It has been proposed in the viscoelastic point scatterer method that the elemental scatterers are placed throughout the volume of the scatterer, because just permitting scatterers around the boundary of the domain will enable both inward and outward radiating waves from each boundary location. This could enable interference between the waves on one side of the domain with the waves on the opposite side. This full volume approach could also be considered to match the penetrable scattering technique, at the extreme limit of infinite difference in ultrasonic impedance. An alternative is given, that it may be possible to implement an angular nullification factor for said inwardly propagating waves, so they no longer propagate through the heterogeneity, or void in this example. The suggestions described here are yet to be validated, therefore, while both a volume of viscoelastic point scatterers and a ring of viscoelastic point scatterers produce the same gross wave scattering, at present it is not clear which approach would best represent said behaviour. This is work in progress and more work will be needed to confirm and validate this model.

5.4 The Huygens-Fresnel principle for simulating ultrasonic scattering and heterogeneity imaging

The method here provides the means for the simulation of ultrasonic bulk longitudinal waves and bulk shear waves scattering from volumetric and planar heterogeneities, followed by some real world considerations for waveform simulation, and last, a description of the chosen, existing method for image reconstruction of the heterogeneities.

5.4.1 Scattering from viscoelastic points within the heterogeneity

Described here is the method used to simulate ultrasound scattered from volumetric and planar heterogeneities using the Huygens-Fresnel principle, followed by the imaging method used to reconstruct said heterogeneities from the ultrasonic waveforms.

The point scattering simulation geometry is detailed in figure 5.1. The longitudinal ultrasonic waveforms are analytically propagated in the frequency, f, domain from a source to a point scatterer, with distance, r_{in}, then from the scatterer to a monitor, with distance, r_{jn}, yielding the longitudinal propagated point scatter spectrum,

$$S_{LL,ijn}(\theta_{L,ijn}, f) = B_{LL,jn} \exp(ik_L(f) r_{jn}) \Gamma_{LL}(\theta_{L,ijn}, \theta_{S,ijn}, v_{p,L}, v_{p,S}) B_{LL,in} \exp(ik_L(f) r_{in}) S_{L0}, \tag{5.4.1}$$

where k_L is the wavenumber that defines the longitudinal dispersion relation and S_{L0} is the initial longitudinal pulse spectrum.

Using the principle of superposition to apply Huygens principle, the total longitu-

dinal scattered spectrum, for a given source and given monitor, is

$$S_{LL,ij} = \sum_{n=1}^{N} S_{LL,ijn}, \tag{5.4.2}$$

for N point scatterers. This superposed waveform, $S_{LL,ij}$, represents that which would be obtained in one transmit and receive pair in the acquisition of real ultrasonic array data.

5.4.2 Additional random electric noise and other considerations

Additionally, to represent random noise from electrical components, which is inherent in the acquisition of real waveforms, Gaussian white noise is added to all simulated waveforms. The noise is added at an example, achievable level of -20dB, as could be found from figure 6.8. The specific noise level in real waveform acquisition varies with the ultrasonic equipment used, and its configuration. The simulated noise is minimised with a low pass filter – specifically a hyperbolic tangent filter [20]. It is noted that the post-processing of the simulated waveforms, and the imaging algorithm applied to this data, should be considered equally as applicable to experimental data as to said simulated data. Also, the chosen configuration of the sources and monitors in this example is idealised, as seen in figure 5.1. This is done to demonstrate the current maximum capability of this waveform simulation method.

5.4.3 Finite element model for the validation of the anisotropy of the viscoelastic point scatterer

The viscoelastic point scattering simulation geometry of figure 5.1 is also used for the MBFE configuration used to validate the anisotropy of the viscoelastic point scatterer; in place of the point scatterer in figure 5.1, there exists an FE region with a simulated void in the HDPE pipe material that is obtained through the removal of finite elements, as shown in figure 5.2.

Next, the FE parameters for the model are given. The cylinder representing the point scatterer is significantly smaller than the ultrasonic bulk longitudinal wave-

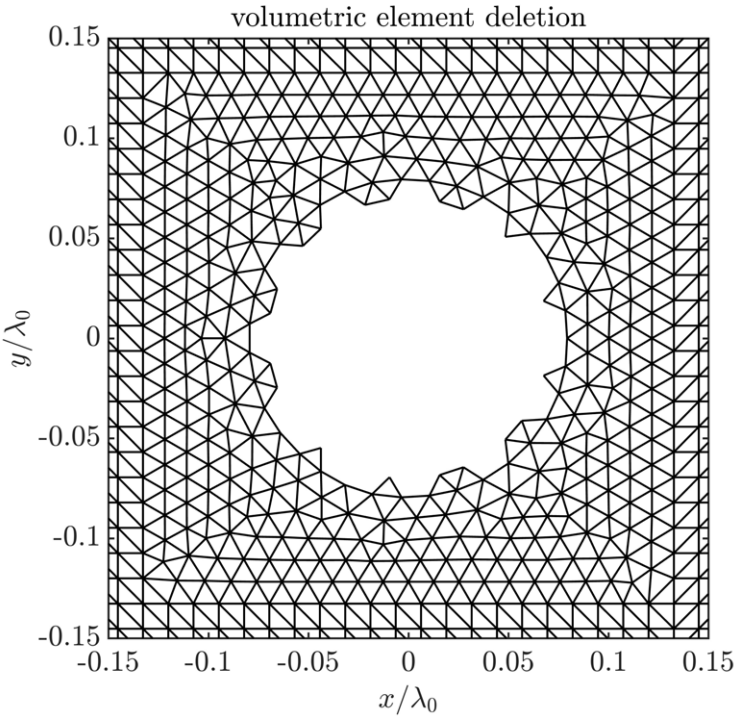

Figure 5.2: Volumetric element deletion where element are triangles. The cylinder radius is $r_d = 7\lambda_0/100$ and the mesh spacing is $\mathrm{d}x = \lambda_0/60$.

length at centre frequency, f_0, with radius,

$$r_d = \frac{7\lambda_0}{100}. \tag{5.4.3}$$

Also, the chosen FE mesh comprises structured triangular plane strain elements. The mesh is describable as fine [30] when element size satisfies,

$$\mathrm{d}x \leq \frac{\lambda_0}{20}; \tag{5.4.4}$$

the chosen mesh resolution is,

$$\mathrm{d}x = \frac{\lambda_0}{60}. \tag{5.4.5}$$

This is also the maximum surface roughness of the cylindrical void. It is seen in figure 5.2 that other elements of the surface of the void could be removed to reduce

roughness to below one sixtieth of the centre wavelength. This could be attempted again in a continuation of this study. The CFL condition [31] for numerical method stability is adhered to with time step,

$$\mathrm{d}t = \frac{3}{400 f_0}. \tag{5.4.6}$$

For each frequency band in MBFE there exists a different set of FE simulated waveforms. Collectively these provide a standard deviation on an expected value that is given by the blending process central to MBFE. These sets of FE simulated waveforms are obtained at different scattering angles. These are interpolated for other angles by adding zero amplitudes to frequency bins in the spectra of the waveforms that are of higher frequency than the sampling frequency. This is known as spectral zero-padding.

Next, because of the symmetry of the defect, source location, and surrounding medium about $y = 0$, the scattering amplitudes obtained, for source and monitor angles, θ_i and θ_j, at $180 \leq (\theta_j - \theta_i)^\circ < 360$ are reversed, $360 > (\theta_j - \theta_i)^\circ \geq 180$, given a 180° circular arc phase reduction, $180 > (\theta_j - \theta_i)^\circ \geq 0$, and then averaged with the symmetric results at $0 \leq (\theta_j - \theta_i)^\circ < 180$ to yield the scattering amplitudes presented in this study. This is equally done for all viscoelastic point scatterer method scattering amplitudes presented in this study. Also, the FE scattering amplitudes are normalised by a constant value to have minimum discrepancy from the viscoelastic results, such that angular behaviour of the scatterer can be directly compared without scaling discrepancy. Last, the chosen FE software, Pogo FEA [32], is highly computationally efficient because it uses graphics processors (GPUs) for its time domain calculations.

5.4.4 Finite element model for the validation of the scattering amplitudes of viscoelastic point scatterer superposition

Again, the viscoelastic point scattering simulation geometry of figure 5.1 is used for the MBFE configuration used to validate the scattering amplitudes of viscoelastic point scatterer superposition; in place of the point scatterer in figure 5.1, there

exists an FE region with a simulated planar void in the HDPE pipe material that is obtained through the duplication of finite element vertex nodes, as shown in figure 5.3. The process of duplication of finite elements vertex nodes along a line or other

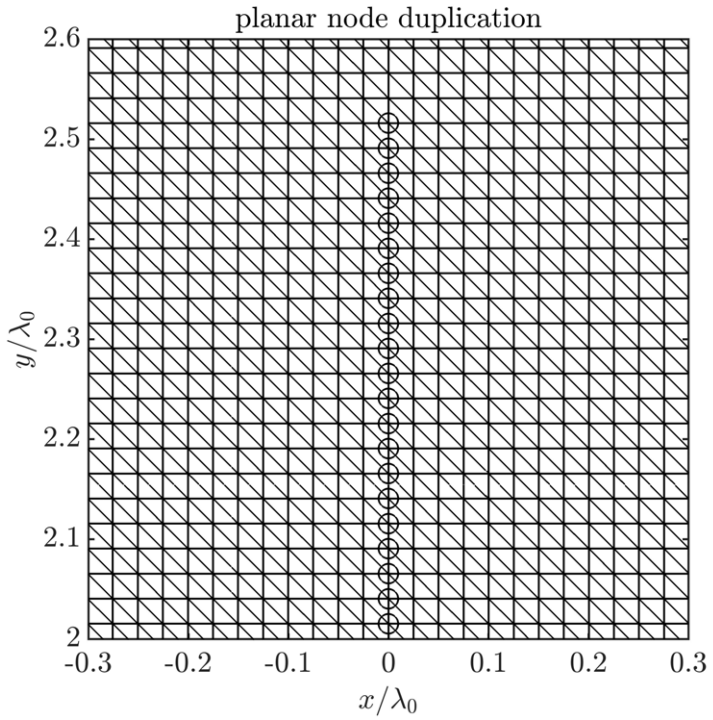

Figure 5.3: Planar node duplication where elements are triangles and duplicate nodes are circles. The defect length is $r_d = 5\lambda_0$, while only the top tip is shown, and the mesh spacing is $\mathrm{d}x = \lambda_0/40$.

geometry results in the whole region being meshed, as is required for a zero-volume planar defect, but also results in a detachment of elements that were adjoining before this duplication, such that, at these elements, a stress free boundary is created. The minimum encircling radius is

$$r_d = 5\lambda_0, \tag{5.4.7}$$

as for the large planar defect used for the ideal circular ultrasonic array example. The chosen FE mesh comprises structured triangular plane strain elements. The chosen mesh resolution is,

$$\mathrm{d}x = \frac{\lambda_0}{40}. \tag{5.4.8}$$

Last, the CFL condition [31] for numerical method stability is adhered to with time step,

$$\mathrm{d}t = \frac{3}{400 f_0}. \tag{5.4.9}$$

The interpolation, symmetric averaging, and normalisation of the point scatterer results are applied to these planar defect point scatterer superposition scattering amplitudes.

5.4.5 Chosen method for ideal circular array image reconstruction of heterogeneities

An image reconstruction of the heterogeneity from the scattered waveforms is obtained using the total focussing method (TFM) [6]. This imaging algorithm is here described in brief. The scattered pulses in the waveform are seen to arrive after a given wave propagation duration. For an ultrasonic pulse that is travelling from a given source to a given monitor, there is a circular arc of possible locations from which the pulse could have scattered for that propagation duration. The image of this arc forms one component of the total TFM image. The sum of all such arcs from all source and monitor combinations yields the TFM image of the scatterer.

5.4.6 Chosen defect image reconstruction method for angled ultrasonic array NDE of HDPE pipe joints

In the angled ultrasonic NDE of HDPE pipe joints, the array and water-filled wedge configuration depicted in figure 5.4 is used. To model this, the approach of the MBim method is used but with viscoelastic point scattering in place of MBFE scattering. By using MBim, inspection characteristics including array and wedge influences on ultrasonic longitudinal bulk waves are accounted for: the reflection and refraction at the water-HDPE interface using Fermat's principle, attenuation losses with the use of the acoustic properties of HDPE pipe material [4] and consequent attenuation correction that is based on wave propagation distance, and, last, wave dispersiveness with frequency domain imaging. For this, imaging is conducted at a number of independent frequencies, $n_{f,im}$, and these images are superposed to

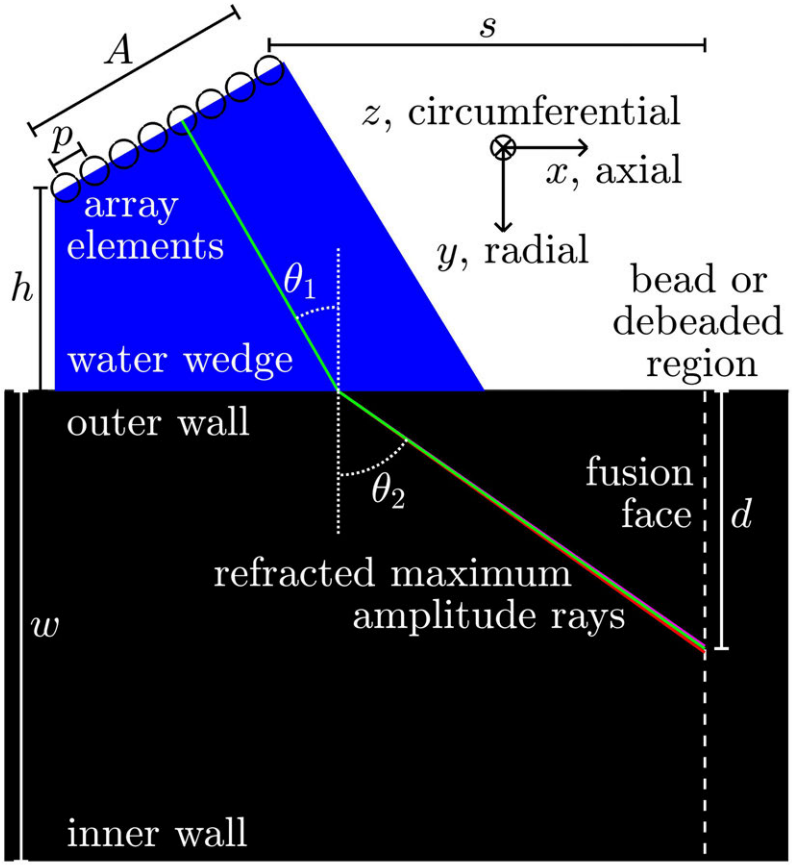

Figure 5.4: Angled ultrasonic array inspection of HDPE pipe heat fused joints where the array is offset from the bead or debeaded region of the joint and the array is mounted on an angled, water-filled wedge directed towards the heat fusion face of the joint. The array elements are the circles, which are separated by a pitch, p, and active aperture, A. The base height of the water wedge is h, the array is offset axially from the fusion face by standoff, s, the wall thickness between the outer and inner wall of the HDPE pipe is w, and the radial depth on the fusion face of the target region is d. The water wedge is angled at θ_1 from normal to the pipe outer wall. The angle at which the maximum amplitude of the ultrasound propagates in the HDPE pipe is θ_2. This is depicted at half, once, and twice the centre frequency to show the dispersiveness of the medium; the angle at $f_0/2$, f_0, and $2f_0$ are respectively the bottom, middle, and top rays.

yield the frequency domain image. Such frequency domain imaging should be a modest correction relative to time domain imaging in the case of HDPE pipe material because, in such viscoelastic media, dispersiveness is low, as seen in figure 5.4.

5.5 Results

First, a MBFE validation of the Huygens-Fresnel principle approach to viscoelastic point scatterer superposition is considered. Next is the ideal case of ultrasonic imaging using a circular array that surrounds the heterogeneity. This is a best case example of imaging potential heterogeneities in the example HDPE pipe material. In this, sub-wavelength features are identified. Last, viscoelastic point scatterer superposition is applied to waveform generation for the angled ultrasonic array NDE image reconstruction of volumetric and planar voids in viscoelastic HDPE.

5.5.1 Finite element validation of the anisotropy of the viscoelastic point scatterer

In figure 5.5 are viscoelastic point and FE simulated ultrasonic longitudinal bulk

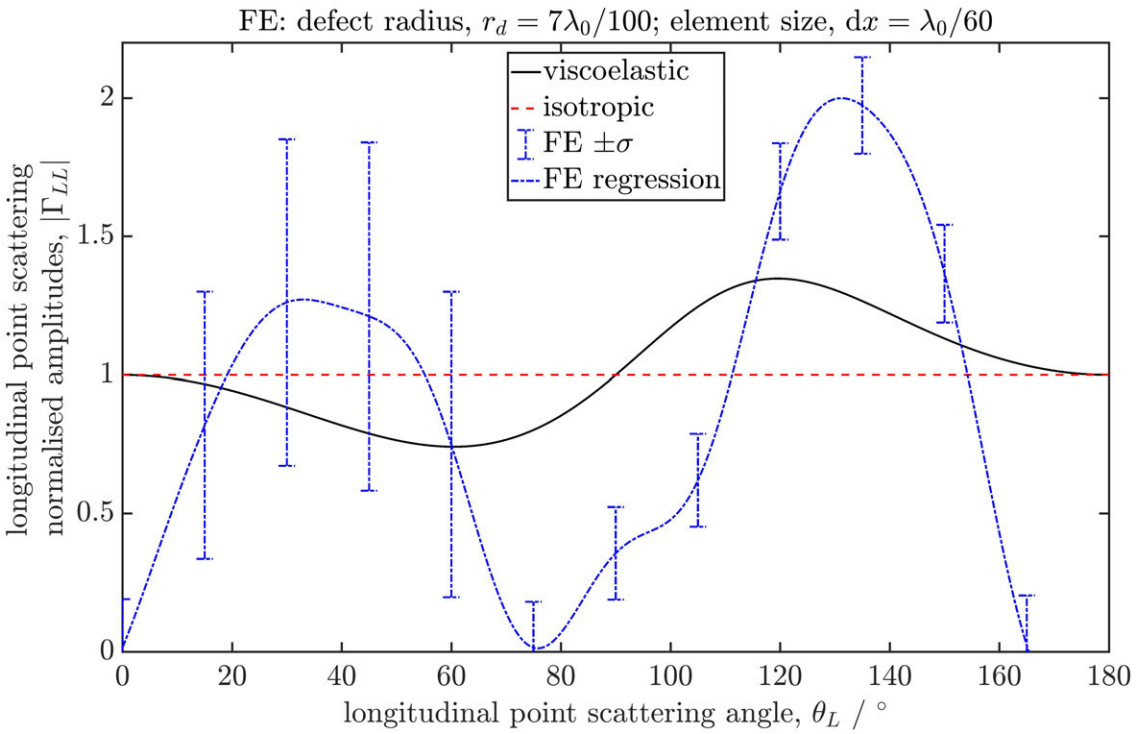

Figure 5.5: Simulated ultrasonic longitudinal bulk viscoelastic point scattering amplitudes, $|\Gamma_{LL}|$, varying with scattering angle, θ_L. The viscoelastic amplitudes are the solid curve, the isotropic or omnidirectional amplitudes are the dashed line, the normalised FE amplitudes are given with dot-dashed standard deviation uncertainty bounds, and the spectrum zero-padded regression to these FE amplitudes is the dot-dashed curve. The FE defect radius is $r_d = 7\lambda_0/100$ and the element size is $\mathrm{d}x = \lambda_0/60$.

viscoelastic point scattering amplitudes, $|\Gamma_{LL}|$, varying with scattering angle, θ_L. The viscoelastic amplitudes are the solid curve, the isotropic amplitudes are the

dashed line, and the normalised FE amplitudes are given with standard deviation uncertainty bounds – the spectrum zero-padded regression to the FE amplitudes is the dot-dashed curve.

The viscoelastic point scatterer amplitudes are in closer agreement with the FE point scatter amplitudes than those of the isotropic point scatterer of existing methods. Though this method seems more accurate, there remain some differences. The FE amplitudes are zero at 0, 90, and 180°. This could be caused by the finite mesh size, $\mathrm{d}x = \lambda_0/60$, or defect radius, $r_d = 7\lambda_0/100$, but both are considered small relative to the centre wavelength, λ_0. It could otherwise be caused by the rectangular geometry of regular FE meshes – in this case two adjacent triangles form the rectangle. This is more likely because this would probably be invariant with FE element size, $\mathrm{d}x$. Without these unexplained zeros at said angles in the FE results, there would be significantly higher agreement between the scattering amplitudes of the viscoelastic point scatterer and the FE point scatterer. This would require more data to be validated.

5.5.2 Finite element validation of the scattering amplitudes of viscoelastic point scatterer superposition

In figure 5.6 are simulated ultrasonic longitudinal bulk viscoelastic planar defect scattering amplitudes, $|\Gamma_{LL}|$, varying with scattering angle, θ_L. The viscoelastic amplitudes are the crosses, the spectrum zero-padded regression to these viscoelastic amplitudes is the solid curve, the normalised FE amplitudes are given with dot-dashed standard deviation uncertainty bounds, and the spectrum zero-padded regression to these FE amplitudes is the dot-dashed curve. The FE defect enclosing radius is $r_d = 5\lambda_0$ and the element size is $\mathrm{d}x = \lambda_0/20$.

The FE scattering amplitudes again feature the zeros at 0, 90, and 180° found in the FE point scatterer in figure 5.5, suggesting that the mesh geometry, not defect geometry, is causing this. The exact cause of the discrepancies needs to be identified and, if possible, corrected for. In the viscoelastic planar defect scattering amplitudes there exist relatively strong specular reflections and transmissions at 0 and 180° angle between source and monitor respectively, which is expected for the planar defect geometry. This is because reflected and transmitted waves has greater amplitudes than scattered waves, such as found at the planar defect tips at 90 and

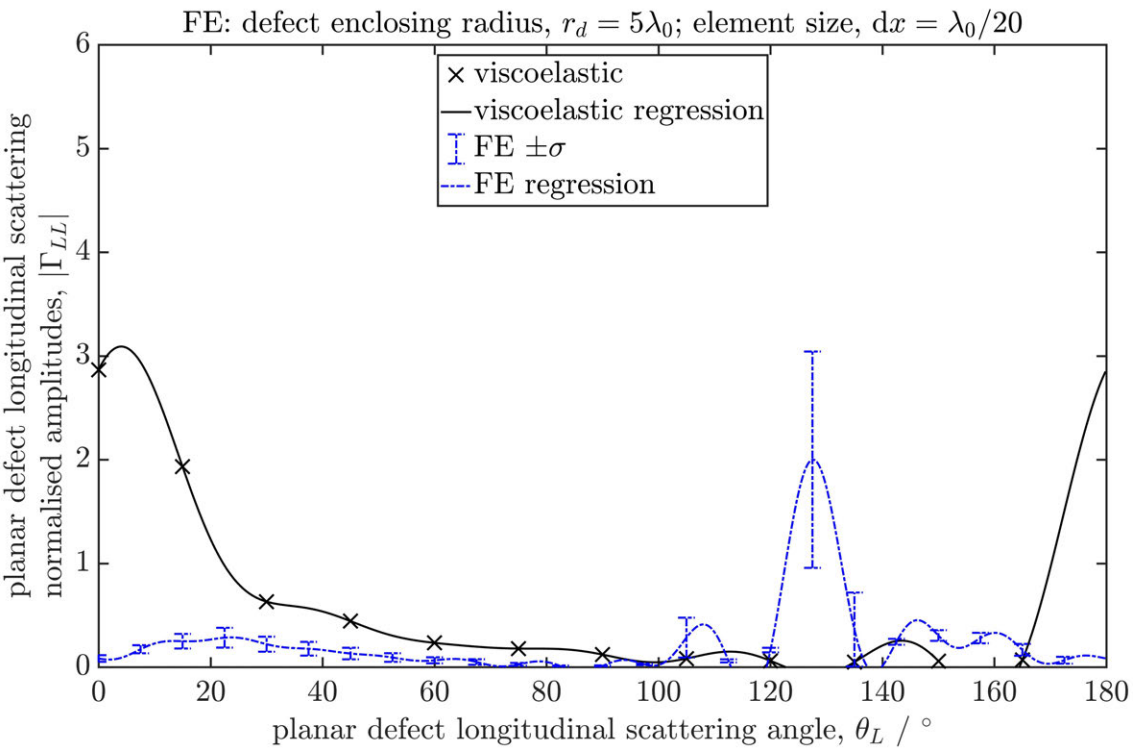

Figure 5.6: Simulated ultrasonic longitudinal bulk viscoelastic planar defect scattering amplitudes, $|\Gamma_{LL}|$, varying with scattering angle, θ_L. The viscoelastic amplitudes are the crosses, the spectrum zero-padded regression to these viscoelastic amplitudes is the solid curve, the normalised FE amplitudes are given with dot-dashed standard deviation uncertainty bounds, and the spectrum zero-padded regression to these FE amplitudes is the dot-dashed curve. The FE defect enclosing radius is $r_d = 5\lambda_0$ and the element size is $\mathrm{d}x = \lambda_0/20$.

270°, through equation (5.3.2).

5.5.3 Ideal circular array image reconstruction of volumetric and planar voids in viscoelastic HDPE

Presented here are reconstructed images of simulated two-dimensional volumetric and planar voids, or defects, in the example viscoelastic, HDPE material in which the waveforms are generated using the superposition of viscoelastic point scatterers by implementing Huygens superposition and Fresnel refraction. In all images, the single scattering criterion of equation (5.3.3) is met.

The defect image reconstructions are seen in figures 5.7 to 5.9. In figure 5.7, a small, rough, two-dimensional volumetric defect, with a minimum encircling radius per wavelength of $r_D/\lambda_0 = 0.5$ is reconstructed with use of viscoelastic point scatterers, from equation (5.3.1). The defect is well represented with minimal imaging artefacts or anomalies and its geometric contours are clearly distinguishable down to lengths

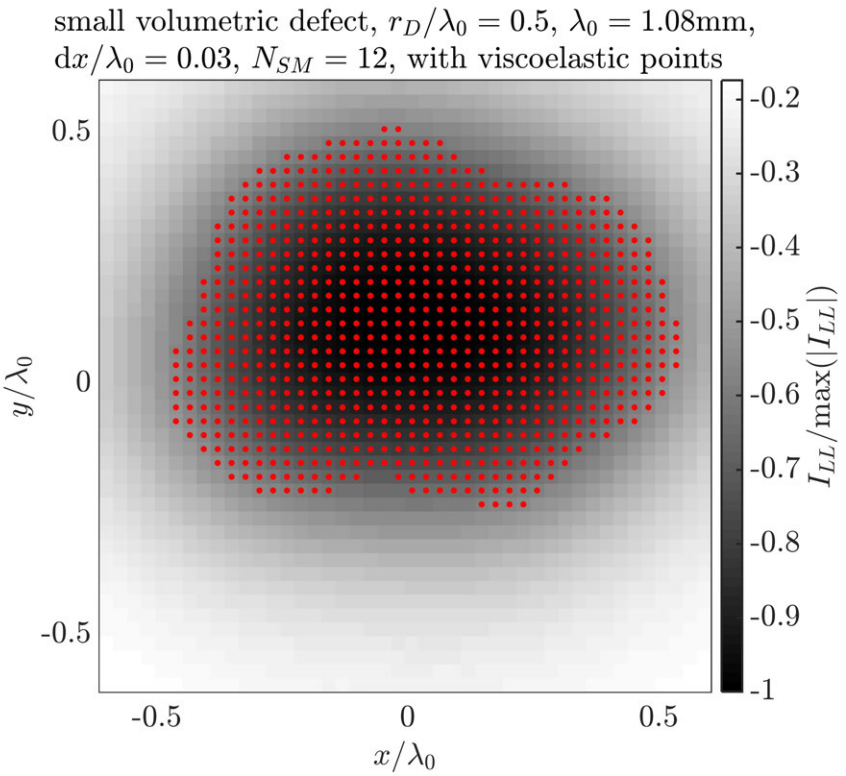

Figure 5.7: Image reconstruction of a small, rough, two-dimensional volumetric defect with use of viscoelastic point scatterers with ultrasonic bulk longitudinal and shear wave anisotropy and orthogonality, from equation (5.3.1). The defect enclosing radius is $r_D/\lambda_0 = 0.5$, for a wavelength at centre frequency, $\lambda_0 = 1.08$mm. The spacing per wavelength of the point scatterers is $\mathrm{d}x/\lambda_0 = 0.03$, in adherence to equation (5.3.3). The number of independent source or monitor locations is $N_{SM} = 12$. The image amplitudes of the defects represented from longitudinal transmitted and received pulses, I_{LL}, have a scale that is quantified on the right greyscale. The dots are the locations of each point scatterer.

below its half-wavelength radius. Amplitude and phase information are retained in the image and therefore the image of the void is correctly close to negative unity in amplitude [25] and increases towards zero away from the defect.

Next, in figure 5.8, a small, planar volumetric defect, with a minimum encircling radius per wavelength of $r_D/\lambda_0 = 0.5$ is reconstructed with use of viscoelastic point scatterers, from equation (5.3.1). As for the rough, volumetric defect of figure 5.7, the small, planar defect is well represented with minimal imaging artefacts or anomalies and its geometric contours are clearly distinguishable down to lengths below its half-wavelength radius.

Last, in figure 5.9, a large, planar volumetric defect, with a minimum encircling radius per wavelength of $r_D/\lambda_0 = 5$ is reconstructed. Again, as for the rough, volumetric defect of figure 5.7 and the small, planar defect of figure 5.8, the large, planar defect is well represented with few imaging artefacts and minimal anomalies.

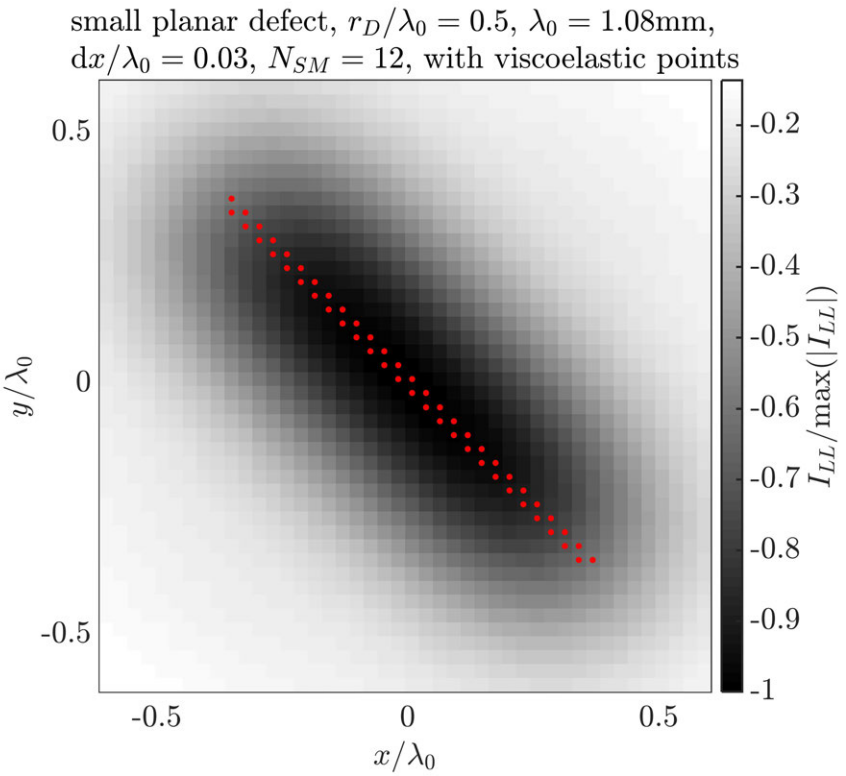

Figure 5.8: Image reconstruction of a small two-dimensional planar defect with use of viscoelastic point scatterers with ultrasonic bulk longitudinal and shear wave anisotropy and orthogonality, from equation (5.3.1). The defect enclosing radius is $r_D/\lambda_0 = 0.5$. All other parameters are the same as in figure 5.7.

The geometric contours of this heterogeneity are clearly distinguishable down to lengths below its wavelength at centre frequency, λ_0.

It is noted that a large, volumetric defect would, with currently available computational technology, need to be simulated with a point scatterer spacing approaching the criterion of equation (5.3.3) to avoid problems caused by limitations in available random access memory. Such achievable accuracy would increase with advancements in computational technology. Similarly, by this method, volumetric defects in three dimensions that are small or large will only currently be representable with reduced accuracy.

5.5.4 Angled ultrasonic array NDE image reconstruction of volumetric and planar voids in viscoelastic HDPE

For this example, angled ultrasonic array NDE of HDPE pipe joint simulated defects, the array has 32 elements, with pitch, $p = 1$mm, and the ultrasonic bulk longitudinal wave centre frequency is $f_0 = 2$MHz.

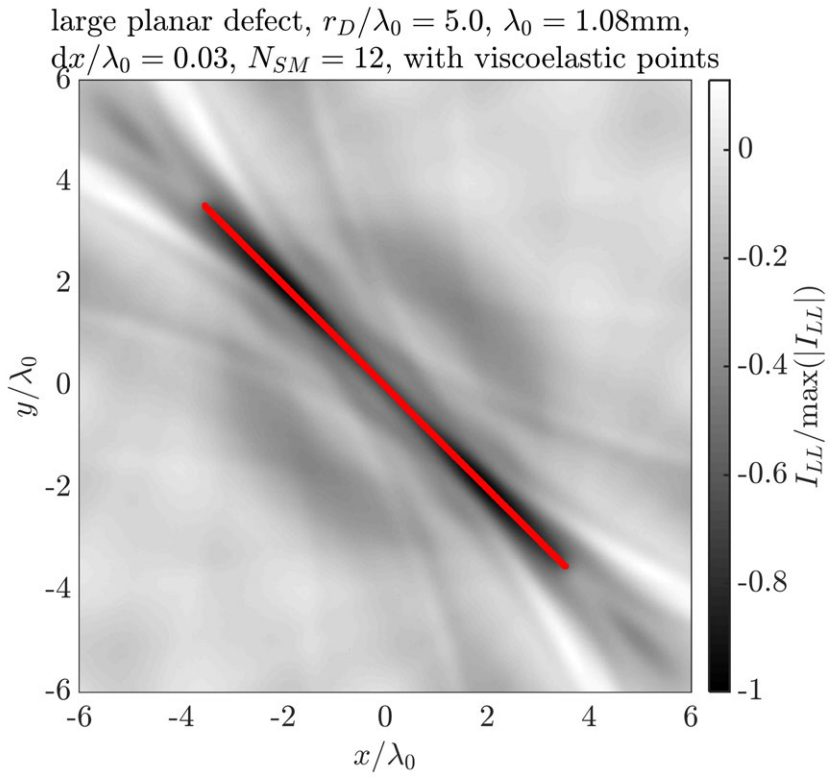

Figure 5.9: Image reconstruction of a large two-dimensional planar defect with use of viscoelastic point scatterers with ultrasonic bulk longitudinal and shear wave anisotropy and orthogonality, from equation (5.3.1). The defect enclosing radius is $r_D/\lambda_0 = 5$. All other parameters are the same as in figure 5.8.

In figure 5.10, viscoelastic point scatterer superposition simulated images of angled ultrasonic array NDE of defects in HDPE pipe joints are shown. The circles and lines are the volumetric and planar viscoelastic point scatterer defect locations respectively. The rough debeaded surface of figure 5.4 is simulated with viscoelastic points at the inner wall, $x = 100$mm. Also, the effect of temperature on the acoustic properties of HDPE pipe material [2], and therefore the ultrasonic array image of HDPE pipe joint defect inspection, is exhibited through a difference in temperature, ΔT, given as input to obtain the acoustic properties of the waveform generation and given as input to obtain the acoustic properties used in imaging. Also, propagation distance attenuation correction, AC, is first not applied, then applied. Last, frequency domain imaging is seen, where the number of independently imaging frequencies is $n_{f,im}$.

In the leftmost image, where there is a temperature discrepancy between waveform generation and imaging and where attenuation correction is not applied, the defects are visible at high inspection angles – shallow through wall depths – but not where

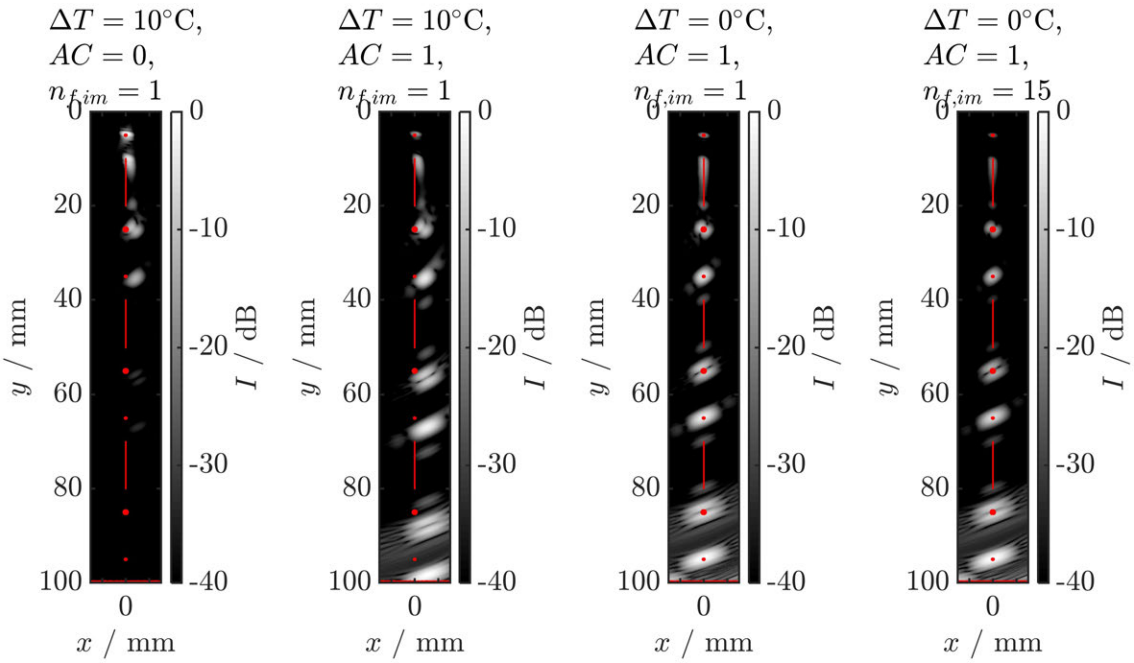

Figure 5.10: Viscoelastic point scatterer superposition simulated images of angled ultrasonic array NDE of defects in HDPE pipe joints. The circles and lines are the volumetric and planar viscoelastic point scatterer defect locations respectively. The rough debeaded surface of figure 5.4 is simulated with viscoelastic points at the inner wall, $x = 100$mm. Far left: $\Delta T = 10°\text{C}$, $AC = 0$, $n_{f,im} = 1$. Centre left: $\Delta T = 10°\text{C}$, $AC = 1$, $n_{f,im} = 1$. Centre right: $\Delta T = 0°\text{C}$, $AC = 1$, $n_{f,im} = 1$. Far right: $\Delta T = 0°\text{C}$, $AC = 1$, $n_{f,im} = 15$.

attenuation is higher because propagation paths are longer. Also, the defect signatures drift to the right of the fusion face of the HDPE pipe joint, $x = 0$, where the defects are located, because of the temperature discrepancy.

In the centre left image, attenuation correction is applied. Consequently, all defects are visible. The lateral resolution inherently reduces with distance from the array – higher depths. The defects signatures drift up to five millimetres from the defect locations. Also, some added noise is made visible by the attenuation correction at the high inspection depths.

The centre right image features a consistent temperature for waveform generation and imaging and attenuation correction. Here the planar and volumetric defects are located and resolved with high accuracy, but, again, with inherently reduced lateral resolution for high depths. A signature from the debeaded surface is also present at the bottom left of the image.

Last, the rightmost image is a frequency domain image with consistent temperature and attenuation correction. This is similar in all but one way to the centre right image, which is because the dispersiveness of HDPE pipe material is low; relative

to time domain image of the centre right image, there may be slight resolution improvement at all depths. Improvements to resolution or signal-to-noise ratio would be more pronounced in a more dispersive medium than HDPE pipe material. As can be seen from left to right, a blended attenuation correction could also provide a more uniform defect signature signal strength with depth, but the parameterisation of such blending would necessarily depend on the inspection configuration.

5.6 Conclusions

The Huygens-Fresnel principle is applied to generalise the simulation of ultrasonic attenuative pulse scattering from two-dimensional volumetric and planar heterogeneities, exemplified with voids, for which the anisotropy and orthogonality of longitudinal and shear wave emission from a point region in a solid is accounted for with the introduction of viscoelastic point scatterers. The viscoelastic point scatterer method is supported with evidence by finite element (FE) analysis – first, the applicability of the anisotropy of the viscoelastic point scatterers for longitudinal wave incidence and scattering and, second, the scattering amplitudes obtained with viscoelastic point scatterer superposition for longitudinal wave incidence and scattering. Further, image reconstruction in an example viscoelastic medium, high-density polyethylene (HDPE), is conducted with viscoelastic point scattering to demonstrate sub-wavelength features of heterogeneities in an ideal ultrasonic circular array imaging setup. Last, this scattering approach is demonstrated with simulated waveform generation and imaging in a HDPE pipe joint setup for the nondestructive evaluation of potential defects.

References

[1] S. Kolkoori, K.C. Venkata, and K. Balasubramaniam, *Quantitative simulation of ultrasonic time of flight diffraction technique in 2D geometries using Huygens–Fresnel diffraction model: Theory and experimental comparison*, Ultrasonics, **55**, 33-41 (2015).

[2] M. Slaney and A.C. Kak, *Limitations of imaging with first-order diffraction tomography*, Microwave Theory and Techniques, IEEE Transactions on, **8**, 860-873 (1984).

[3] D. Plackoa and T. Kundu, DPSM for Modeling Engineering Problems, New Jersey: John Wiley and Sons (2007).

[4] S. Banerjee, T. Kundu, and D. Placko *Ultrasonic Field Modeling in Multilayered Fluid Structures Using the Distributed Point Source Method Technique*, J. Appl. Mech. **73**(4), 598-609 (2005).

[5] A.J.C. Jarvis and F.B. Cegla, *Application of the distributed point source method to rough surface scattering and ultrasonic wall thickness measurement*, J. Acoust. Soc. Am. **132**(3), 1325-1335 (2012).

[6] A. Velichko and P.D. Wilcox, *An analytical comparison of ultrasonic array imaging algorithms*, J. Acoust. Soc. Am. **127**(4), 2377-2384 (2010).

[7] J. Zhang, B.W. Drinkwater, and P.D. Wilcox, *Comparison of ultrasonic array imaging algorithms for nondestructive evaluation*, Ultrasonics, Ferroelectronics, and Frequency Control, IEEE Transactions on **60**(8), 1732-1745 (2013).

[8] C. Fan, M. Caleap, M. Pan, and B.W. Drinkwater, *A comparison between ultrasonic array beamforming and super resolution imaging algorithms for nondestructive evaluation*, Ultrasonics **54**, 1842-1850 (2014).

[9] L.R. Francis Rose, E. Chan, and C.H. Wang, *A comparison and extensions of algorithms for quantitative imaging of laminar damage in plates. I. Point spread functions and near field imaging*, Wave Motion **58**, 222-243 (2015).

[10] P. Wilcox, R. Monkhouse, M. Lowe, and P. Cawley, *The use of Huygens' principle to model the acoustic field from interdigital lamb wave transducers*, Review Progress in Quantitative Nondestructive Evaluation, **17**, 915-922 (1998).

[11] N. Gengembre *Pencil method for ultrasonic beam computation*, WCU 2003, Paris, september 7-10 (2003)

[12] J. Zhang, B.W. Drinkwater, P.D. Wilcox, and A.J. Hunter, *Defect detection using ultrasonic arrays: The multi-mode total focusing method*, NDT&E International **43**, 123-133 (2010).

[13] J.S. Egerton, M.J.S. Lowe, J. Jian, and P. Huthwaite, *Numerical simulation of ultrasonic NDE of sound-damping materials using a multiband time domain approach*, Ultrasonics. [Pre-submission]

[14] J.S. Egerton, M.J.S. Lowe, H.V. Halai, and P. Huthwaite, *A multiband approach for accurate numerical simulation of frequency dependent ultrasonic wave propagation in the time domain*, J. Acoust. Soc. Am. **142**(3), 1270-1280 (2017). [Open Access available]

[15] M.J.S. Lowe, *Plate waves for the NDT of diffusion bonded titanium*, Ph.D. thesis, Imperial College London, 88102 (1992).

[16] B.A. Auld, Acoustic fields and waves in solids Volume II, 2nd ed., Florida: John Wiley and Sons (1990).

[17] J.S. Egerton, M.J.S. Lowe, H.V. Halai, and P. Huthwaite, *Ultrasonic attenuation and phase velocity in high-density polyethylene (HDPE) pipe material*, J. Acoust. Soc. Am. **141**(3), 15351545 (2017).

[18] J. Wu, *Determination of velocity and attenuation of shear waves using ultrasonic spectroscopy*, J. Acoust. Soc. Am. **99**(5), 28712875 (1996).

[19] J.A. Stratton and L.J. Chu, *Diffraction theory of electromagnetic waves*, Physical Review **56**, 99-107 (1939).

[20] D.R. Frey, *A general class of current mode filters*, Circuits and Systems, 1993., ISCAS '93, 1993 IEEE International Symposium on, 1435-1438 (1993).

[21] M.B. Drozdz, *Efficient finite element modelling of ultrasound waves in elastic media*, Ph.D. Thesis, Imperial College London, 182-203 (2008).

[22] R. Courant, K. Friedrichs, and H. Lewy, *Über die partiellen Differenzengleichungen der mathematischen Physik*, Mathematische Annalen (in German), **100**(1), 3274 (1928).

[23] P. Huthwaite, *Accelerated finite element elastodynamic simulations using the GPU*, Journal of Computational Physics, **257**(A), 687-707 (2014).

[24] J.S. Egerton, M.J.S. Lowe, H.V. Halai, and P. Huthwaite, *Ultrasonic attenuation and phase velocity in high-density polyethylene (HDPE) pipe material*, J. Acoust. Soc. Am. **141**(3), 1535-1545 (2017). [Open Access available]

[25] M.J. Grote and C. Kirsch, *Dirichlet-to-Neumann boundary conditions for multiple scattering problems*, Journal of Computational Physics **201**, 630-650 (2004).

Chapter 6

Automated and antidispersive coherent and incoherent noise reduction of waveforms that contain a reference signal

The formulation, implementation, and evaluation of some concepts covered in chapter will be published Open Access as: J.S. Egerton, M.J.S. Lowe, and P. Huthwaite, *Automated and antidispersive coherent and incoherent noise reduction of waveforms that contain a reference signal*, NDT&E International, [Under review].

6.1 Abstract

Fully automated and antidispersive noise reduction of a waveform containing a reference signal is often necessary for more efficient, accurate, and reliable interpretation of signals – such as highly attenuated waves in ultrasonic NDE. This author proposes two methods, pulse specification (PS) and coherent enhanced pulse specification (CEPS), for improving the signal-to-noise ratio (SNR) of coherent pulse amplitudes against both incoherent and coherent noise, as well as apply antidispersive pulse generation (APG) to localise the pulse upon reception. This author has demonstrated their effectiveness using two examples of ultrasonic inspection, by comparison with established methods. This has benefits in applications such as NDE, medical ultrasonics, seismology, and acoustics.

This author deconvolves waveforms using a reference signal time-windowed from said waveforms. These waveforms are convolved with pulses that have centre frequencies and bandwidths that are optimally and automatically specifiable for that unprocessed waveform. This author combines independent measurements of the waveforms using PS and CEPS to maximise the coherent pulse amplitude of known scatterers and minimise the noise content. CEPS also enhances the coherent scatterer amplitude to significantly greater than achieved using an established filtered time shift method – where the time shift is subjective. Unlike such time shift methods, PS and CEPS do not reduce the amplitude of the coherent pulses of scattered signals when reducing noise.

6.2 Introduction

Many signals captured and processed live contain dominant noise, including, for example, ultrasonic, infrasonic, and audible sound waves recorded in nondestructive evaluation (NDE), medical ultrasonics, seismology, and acoustics.

If this unwanted noise is present in the signal, all desired, noise-free content of the signal is somewhat obscured. When processing such signals to reduce noise, the reduction of content at undesired frequencies, without reduction at desired frequencies, from the signal, is optimal. Generally, such processing should be automatable, and therefore have low subjectivity, low sensitivity to variations in key parameters, and high repeatability. The noise reduction aim is distinct from that of ubiquitous de-noising in that I aim for low, not zero, noise and therefore finite, not infinite, signal-to-noise ratio.

Further to this, combined, independent measurements of such signals are often obtained for validation of repeatability, for noise reduction, and many other reasons. In such cases, the combination of these signals may or may not retain the desired signal content, dependent on the combination procedure.

Past approaches to reduction of low and high frequency noise content involve summation in the time or frequency domains of repeat measurements of signals, with or without a constant, subjective time shift applied to all wave pulses. Generally, in the latter, time shift coherent average, methods, the time shift will be based on temporal characteristics of a reference pulse that is common to each waveform record, such as the time when its peak amplitude occurs, the zero-crossing time between its

main positive and negative peaks, or the time when the maximum amplitude of its Hilbert transform occurs, such as in [1].

Conventional frequency filtering reduces certain parts of the signal spectrum, such that it partially reduces both incoherent and coherent content at low and high frequencies. A filter with highly specific frequencies at which reduction occurs (corner frequencies) and gradients of reduction at the corner frequencies (roll-offs) can achieve high reduction in undesired frequencies with low reduction in desired frequencies. However, this process is highly sensitive to these four or more key parameters. The optimum reductions in desired and undesired signal content also necessitates a subjective decision between maximising coherent signal amplitude and maximising noise reduction.

In the noise reduction of signals in geophysics and seismology, radio transmission, nuclear magnetic resonance imaging, coded sequences, and many other fields, it is common to use correlation or convolution techniques, in a procedure sometimes referred to as 'deconvolution interferometry', as instructively reviewed and demonstrated in [2–8]. This may be achieved by a class of deconvolution filters, for which the Wiener filter is considered widely applicable [9]. Further, introduction of a synthetic pulse, often known as a wavelet, allows a synthetic signal to be produced [10–12]. Such wavelets include Gaussian (Morlet) [13] and second order derivative Gaussian (Ricker) [14] envelopes applied to sinusoids. Noise reduction is also achieved through the input of coded sequences applied to NDE inspections [15].

Many of the above applications of deconvolution to noise reduction require significant subjective or circumstantially specific input, often owing to the relatively high complexity of many of the procedures. Some convolution techniques are computed in the time domain, which is more cumbersome to implement than in the frequency domain, and may also be less computationally efficient for live implementation. The iterative and adaptive convolution approaches require a user to specify time ranges within which all pulses occur, and the former requires a specified number of iterations. Some of the above techniques require conventional filtering of the recorded signals, which is a procedure that is sensitive to multiple specified parameters. The potential for coherent enhancement of pulses to yield pulse amplitudes greater than can be achieved using coherent averaging is yet to be presented. Approaches sometimes involve the addition of specific synthetic noise types, for example a constant temporal drift, that is then removed again by filtering, rather than the filtering of

noise inherent in such measurements.

The procedure of this author automatically reduces low and high frequency noise without reducing desired pulse amplitudes. This author deconvolves recorded signals with reference signals that are time-windowed from these signals to obtain transfer functions. These transfer functions are convolved with a synthetic pulse (wavelet) of a similar centre frequency and bandwidth to the reference pulse specifications (PS), to yield a specified, synthetic signal that retains the relative amplitude and phase of the transfer function. These specified signals feature coherent pulse content where such existed in the unprocessed signals, and much reduced noise content. Using a mean average, these specified signals can be combined to one coherent signal, with greater coherent pulse content than would exist in a coherent average of the unprocessed signals, even if optimum frequency filtering were applied to these unprocessed signals. Further to this, this author provides the option of coherent enhanced pulse specification (CEPS) of the waveform. This yields an increase in the coherent pulse amplitude but with a loss of information about the relative amplitudes of separate coherent pulses, achieved using the latter option. Therefore, the potential use of CEPS is specific to applications when maximal signal-to-noise ratio (SNR) is crucial.

The approach of this author to noise filtering and coherent enhancement is compared with the time shift approach this author found to have the highest SNR – peak alignment of the maximum amplitude of the Hilbert transform of the pulse, including also specific, optimised filtering. This is the most suitable comparator for the application of this author, given the various reasons for the above correlation and deconvolution techniques being inapplicable or unsuitable.

For the first, incoherent noise reduction example, this author obtains independent, repeat measurements of ultrasonic waves scattered from cylindrical voids in a viscoelastic NDE 'calibration block' cut from a high-density polyethylene (HDPE) pipe. This author also varies the unprocessed signal recording procedure, such that 10, 32, 100, 316, and 1000 coherent time average waveforms are obtained and analysed. The high noise reduction achieved by the approach of this author renders few coherent time averages feasible in circumstances where many averages would have previously been necessary to achieve acceptable SNR. Further to this, by design, CEPS should readily be capable of improving scatterer detection systems, by allowing potential signals from interrogated geometries or defects to be detected with a higher probabil-

ity of detection (PoD), without significant change to probability of false call (PFC). This is of great importance because ultrasonic inspection of viscoelastic media has wide and growing applications that include medical examination of body tissues; NDE of composites, used for example, in aerospace engineering; and the example of polymer pipes, used, internationally for liquids transportation. Further to this, recording viscoelastic waveforms is a crucial aspect of seismological and geophysical studies.

The second, coherent noise reduction, example is a coarse grained metal alloy block with parallel faces. The large grain size results in significant coherent grain scatter than produces noise that cannot be reduced via coherent time averaging.

For the first, incoherent noise reduction example, in section 6.3.1, this author covers the theory required to formulate the method of this author for incoherent noise reduction and coherent enhancement using pulse specification; in section 6.3.2, the approaches of this author to PS and CEPS are described for incoherent noise reduction; in section 6.3.3, this author shows how the method of this author decreases incoherent noise and increases the coherent pulse amplitudes of known scatterers, beyond what is capable with time shift approaches.

Section 6.4 follows the same structure as section 6.3, but for the second example of coherent noise reduction. The principles of the method of this author are in section 6.4.1; the implementation of the method of this author are in section 6.4.2; and the results and analysis are in section 6.4.3.

In section 6.5, conclusions are drawn and suggestions are made about when best to apply PS or CEPS.

6.3 Incoherent noise reduction example

6.3.1 Principles of method

Within the formulation of the procedure of this author, this author uses a Hilbert transform to window pulses from waveforms and find maxima of pulses; the spectra of the windowed pulses are deconvolved and convolved with other spectra; and the signal-to-noise ratio (SNR) is obtained for evaluated pulses.

The Hilbert transform is here defined using the following convention

$$\text{Hilbert}(\cdot) = (\cdot) + i(\cdot)\exp\left(\frac{i\pi}{2}\right). \tag{6.3.1}$$

Signal convolution $(+)$ and deconvolution $(-)$ in the frequency domain may be defined using multiplication or division of the signal spectra, $S_1(f)$ and $S_2(f)$, as follows,

$$H^{\pm}(f) = S_1(f)S_2^{\pm 1}(f), \tag{6.3.2}$$

where f is the signal frequency and the convolved or deconvolved waveform is the inverse Fourier transform of $H^{\pm}(f)$.

In the wave propagation and scattering example, the signal $S_2(f)$ is the spectrum of the reference signal and $S_1(f)$ is the spectrum of the entire waveform, containing multiple wave pulses. These waveforms are deconvolved using their own noisy reference pulses to obtain their transfer function, $H_{PS}^{-}(f)$, convolved with a noiseless, PS reference, then coherently averaged to produce one mean waveform that has had its incoherent noise reduced and has high coherent pulse amplitude. The PS reference pulse may be any localised pulse with similar centre frequency and pulse duration, or equivalently frequency bandwidth, to the input pulse. For the automated noise reduction system of this author, the centre frequency and pulse duration are obtained from the time-windowed, noisy reference pulse.

To produce a CEPS waveform, the following transfer function is used,

$$H_{CEPS}^{-}(f) = \frac{H_{PS}^{-}(f)}{|H_{PS}^{-}(f)|^m} \tag{6.3.3}$$

where m is the amplitude normalisation order.

The maximum amplitude of the Hilbert transform of an array of variables is

$$\text{mah}(\cdot) = \max(|\text{Hilbert}(\cdot)|). \tag{6.3.4}$$

Respectively, the signal and noise peak amplitudes are defined,

$$\mathrm{mah}_{V_{s,n}} = \mathrm{mah}(V_{s,n}), \tag{6.3.5}$$

where $V_{s,n}$ are the signal and noise voltages within the waveform obtained, at, and distant from, the four wave pulses of figure 6.1.
The SNR is here defined, with voltages not squared voltages, to be,

$$\mathrm{SNR} = \frac{\mathrm{mah}_{V_s}}{\mathrm{mah}_{V_n}}. \tag{6.3.6}$$

Where there is available an accurate description of the frequency dependence of wave phase velocity, v_p, in a medium, as for ultrasound in HDPE pipe material [4], it is possible to transmit a pulse that is maximally localised upon reception, using a chosen target propagation distance of a pulse, $\overline{x}$, such as the path via the region where SNR is lowest, and using the antidispersive pulse generation (APG) transfer function,

$$H_{APG} = \exp\left[-i\left(\frac{2\pi f}{v_p} - \frac{2\pi f}{v_{p0}}\right)\overline{x}\right], \tag{6.3.7}$$

given that $v_{p0} = v_p(f_0)$ and f_0 is the pulse centre frequency.

6.3.2 Implementation of method

This author analyses different specified pulse characteristics, including their pulse envelopes, centre frequencies, and bandwidths (number of cycles), to highlight that the incoherent noise reduction and coherent enhancement procedure of this author is fully automated.
The wave propagation and scattering example, where six spatially independent measurements are taken, for 10-1000 coherent time averages, is shown in figure 6.1. The incident ultrasonic pulse reflects off the flat faces and scatters off the 6mm diameter (5.5 centre wavelengths), cylindrical, air-filled void. The reference signal spectrum of equation (6.3.2), $S_2(f) = S_{F_1}(f)$, is here the front wall spectrum and $S_1(f) = S(f)$

is here the spectrum of the entire waveform, containing the spectrum of all four received pulses.

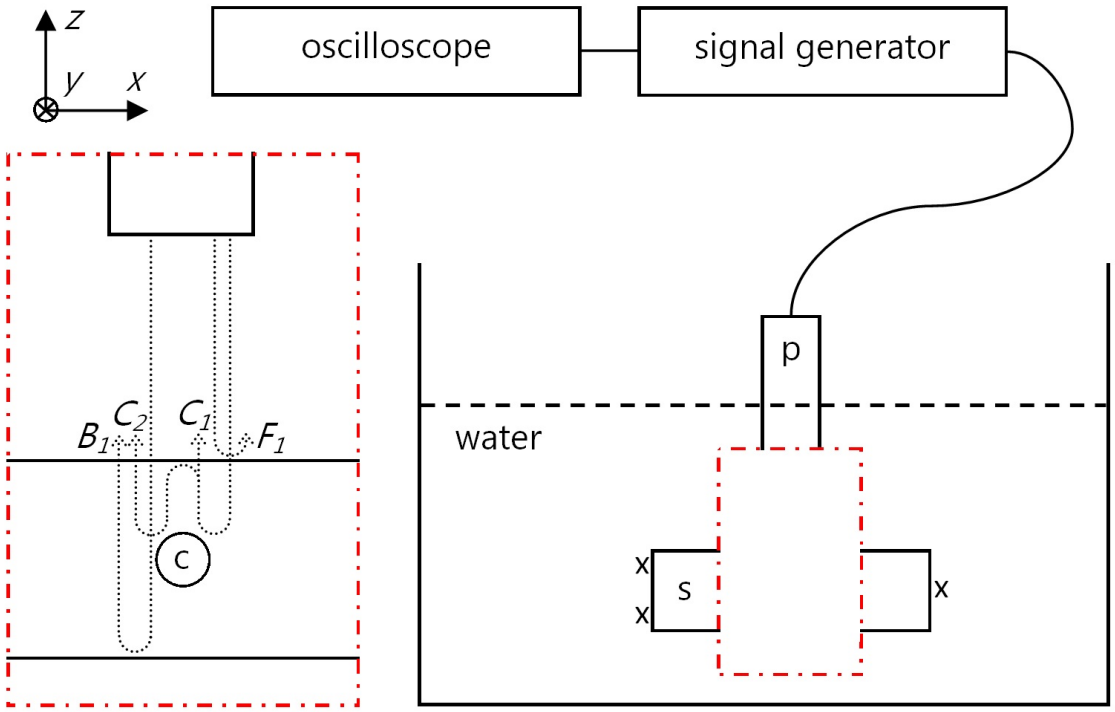

Figure 6.1: A cartoon of the immersion tank, ultrasonic setup used to obtain the waveforms. The dot-dashed region is cut out from the main cartoon. The ultrasonic pulser is p, the high-density polyethylene (HDPE) pipe sample, is s, the centrally located 6mm diameter (5.5 centre wavelengths), cylindrical, air-filled void is c, the front wall reflection of the ultrasound from the sample is F_1, the back wall reflection is B_1, the first scatter from the cylinder is C_1 and, from C_1, after rebounding once more from the front wall and the scatterer, the second scatter, C_2, exits the sample towards the pulser. Three spatially independent measurements are taken in the y-direction for the top and bottom of the sample, each as the front wall, resulting in a total of six independent, repeat measurements. The six measurements are recorded with 10 coherent time averages and then all repeated for 32, 100, 316, and 1000.

The reference signal $F_1(t)$ is automatically time-windowed by finding the maximum amplitude of the Hilbert transform of the entire waveform and centring the window there. This windowing is performed for the six repeat measurements, such that each $S_{F_1}(f)$ is obtained. These and $S(f)$ are deconvolved using equation (6.3.2), to obtain six transfer functions, $H_{PS}^{-}(f)$. An input pulse with automatically specified centre frequency and bandwidth to $S_{F_1}(f)$, but of general envelope, is convolved with each $H_{PS}^{-}(f)$ to obtain specified, synthetic spectra. The chosen pulse types have the following envelopes, cosine (Hann), automated filtered Hann, Blackman-Harris [4, 27], Gaussian (Morlet), and second derivative Gaussian (Ricker). The automated Hann filtering is achieved by setting high- and low-pass filter corner frequencies at the local minima respectively at the lower and higher frequency sides of the

peak spectral amplitude. This may be considered conceptually as optimal noise reduction as preparation of a suboptimal specified pulse. However, it is favourable to the refinement of the Hann pulse to specify a pulse with the desired spectral characteristics, such as the Blackmann-Harris or the Gaussian pulse. Next in the automated noise reduction procedure, the mean average of the six PS or CEPS spectra is taken, and then the inverse Fourier transform, to obtain a waveform with pulse specification that reduces incoherent noise without reducing pulse amplitudes with the waveform, unlike time shift coherent average methods and conventional frequency filtering. Further to this, the coherent amplitude of pulses within the waveform are enhanced relative to the incoherent signal amplitude, using $H^{-}_{CEPS}(f)$ of equation (6.3.3). For incoherent noise reduction, PS and CEPS pulses are applied to the signal both with and without the APG transfer function of equation (6.3.7), because accurate frequency dependence of the ultrasonic phase velocity of HDPE pipe material is provided in [4].

The comparator is a time shift, chosen to be that which makes the six $\text{mah}(F_1(t))$ coincident in time, followed by coherent averaging, followed by low- and high-pass frequency filtering using the sum of two hyperbolic tangent functions [18], with low and high corner frequencies and roll-offs optimised for greatest SNR without a large reduction in mah_{V_s}.

When coherent noise is low or negligible, and incoherent noise is significant in a waveform, it is useful to evaluate the performance of the automated noise reduction system of this author for a range of initial, unprocessed incoherent noise amounts. Therefore, the specified waveforms with 10-1000 coherent time averages are validated against the chosen comparator using the signal-to-noise ratios, SNRs. The lowest SNR pulse, C_2, is most difficult to discern from the noise and therefore chosen for the following analysis of SNRs achieved by the PS and CEPS pulses and the comparator method with specific, optimised filtering and without. The suitability of different pulse (wavelet) spectra is analysed and the influence of this on specified signal quality is demonstrated. This analysis includes the influence of the automated-filtering (AF) of frequency side lobes from the pulse spectra. For which, it should be noted that the input pulse AF for side lobe removal adds negligible specificity; full spectrum noise filtering is highly specific to the parameters used.

6.3.3 Results & analysis

The method for incoherent noise reduction described in section 6.3.2 is implemented, for which the results are here analysed. The unprocessed and conventional frequency filtered waveforms are first provided for both 10 and 1000 coherent time averages, next are the PS and CEPS results for 10 and 1000 coherent time averages, followed by the spectral amplitudes and phases of the unprocessed results, the frequency filtered results, and the PS and CEPS results, and last is quantified SNRs of the comparator methods and the PS and CEPS methods for 10-1000 coherent time averages.

In figure 6.2, the six time shifted waveforms with 10 coherent time averages, their means, and their filtered means are shown. Because in HDPE attenuation increases with frequency, these conventionally filtered means, used throughout the HDPE example, have filter centre frequencies near to 2.1MHz after wave propagation, which is below the input centre frequency of 2.25MHz. The centre of the filter is automatically determined for highest SNR, in this method. Similarly, bandwidth is determined automatically, which, for the example of HDPE, is near to plus and minus a factor of two of centre frequency. The six waveforms have much noise at a 5 millivolt level that significantly obscures C_2 (at $t = 41.5\mu$s) and B_1 (at $t = 46.7\mu$s). Because the waveforms are time shifted for equal maximum amplitudes of their Hilbert transforms, their means do not change the shape or amplitude of F_1 and C_1 significantly. The pulses, C_2 and B_1, in the mean waveforms, are partially distinguishable from the surrounding incoherent noise – where noise is expected to reduce by a factor $\sqrt{6}$. The bottom row is obtained by applying a specific corner frequency and roll-off. There is necessary subjectivity in the selection of the frequencies at which these parameters occur for continuous, multifaceted spectra such as those of waveforms containing multiple pulses. The corner and roll-off are therefore selected based on a compromise between maximising incoherent noise reduction and reducing coherent pulse amplitudes by an acceptably small amount. To reduce the incoherent noise to discern C_2 and B_1 from the noise, the waveform in the bottom row has a maximum amplitude of its Hilbert transform of F_1 that is 86.8% of the mean waveform. This is a loss in coherent pulse amplitude of 13.2%.

In figure 6.3, the six time shifted waveforms with 1000 coherent time averages, their means, and their filtered means are shown. The reduction in incoherent noise

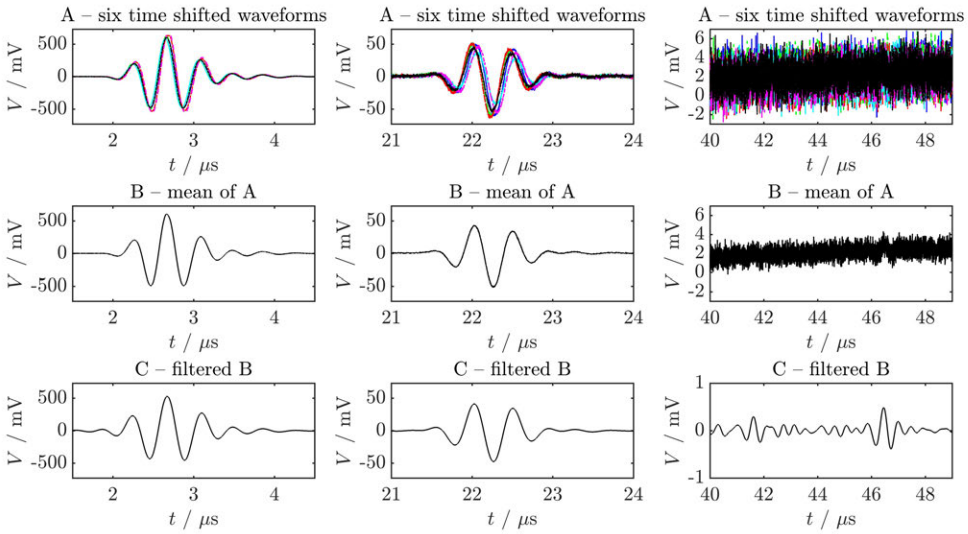

Figure 6.2: Unprocessed waveforms with 10 coherent time averages. Left column: Pulse F_1. Middle column: Pulse C_1. Right column: Pulse C_2 then B_1. Top row: six waveforms time shifted using chosen comparator method. Middle row: the mean of the six time shifted waveforms. Bottom row: the optimised filtered mean of the six time shifted waveforms, with specific corner frequencies and roll-offs.

from 10 to 1000 coherent time averages is of the order 10 and the noise in the six waveforms is at a millivolt level, and approximately a factor $\sqrt{6}$ less than this for the mean waveform. The pulses C_2 and B_1 are highly distinguishable from the incoherent noise in the six waveforms, their mean, and their filtered mean. The filtered coherent pulse amplitudes as percentages of F_1 are the same for 1000 as 10 coherent time averages.

In figure 6.4, the example pulse specifications, for transfer functions that are obtained from the waveforms with 10 coherent time averages, are shown. In the Hann PS waveform, C_2 is indiscernible and B_1 is partially discernible, but significant noise remains in the signal, including high frequency noise and low frequency drift. The Hann CEPS waveform has similar features but with a significantly greater coherent pulse amplitude of C_2. The Hann PS and CEPS waveform that has had its frequency side lobes removed using an automated filtering process has significantly less low and high frequency noise relative to without AF. In the Blackman-Harris PS and CEPS waveforms, B_1 is highly distinguishable from the surrounding noise. The pulse phases of C_2 and B_1 are partially obscured relative to those in the six waveforms with 1000 coherent time averages in figure 6.3. For 10 coherent time averages, C_2 in the Blackman-Harris PS and CEPS waveforms is marginally distinguishable

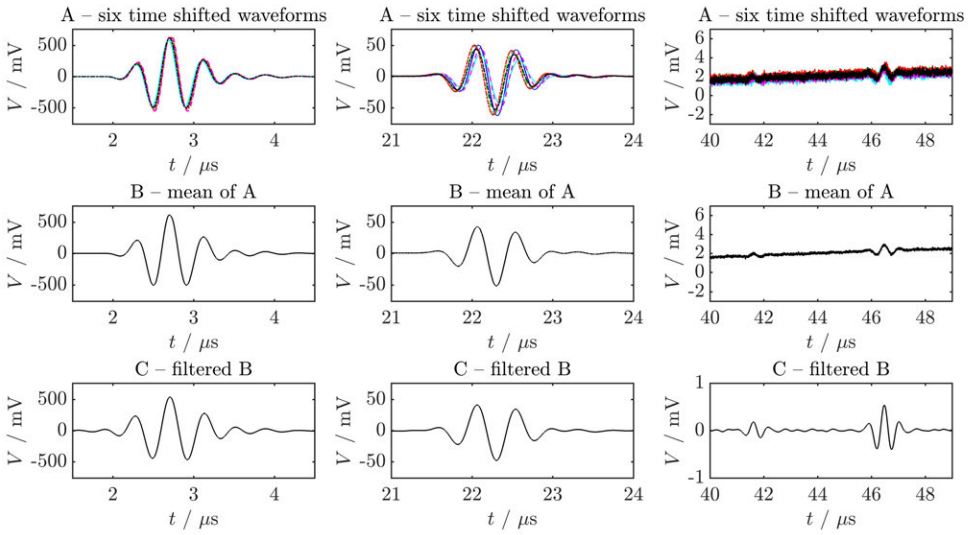

Figure 6.3: Unprocessed waveforms with 1000 coherent time averages. Left column: Pulse F_1. Middle column: Pulse C_1. Right column: Pulse C_2 then B_1. Top row: six waveforms time shifted using chosen comparator method. Middle row: the mean of the six time shifted waveforms. Bottom row: the optimised filtered mean of the six time shifted waveforms, with specific corner frequencies and roll-offs.

from the noise. The same conclusions can be drawn for the Gaussian waveforms as for Blackman-Harris, but more low frequency noise is present in the Gaussian signal. The short duration Ricker pulses in the PS and CEPS waveforms have dispersed significantly in C_1, and C_2 and B_1 are unresolvable because of high dispersion and low and high frequency noise content. Also, significant high frequency noise is present. The non-AF PS waveforms have a maximum amplitude of their Hilbert transforms of F_1 that is 99.8% of the mean waveform. This is a loss in coherent pulse amplitude of 0.2%. The AF Hann PS has a coherent pulse amplitude increase of 1.1% of F_1. Next, in figure 6.5, the example pulse specifications, for transfer functions that are obtained from the waveforms with 1000 coherent time averages, are shown. In the Hann PS waveform, C_2 is indiscernible and B_1 is partially discernible, high frequency noise is very low, but very large low frequency drift is present. In the Hann CEPS both C_2 and B_1 are partially discernible. In the AF Hann PS waveform, C_2 and B_1 are very pronounced and incoherent noise is highly reduced. The AF Hann CEPS waveform have a highly coherent enhanced C_2. The Blackman-Harris and Gaussian PS waveforms have similar C_2 and B_1 pulse shaped to the six waveforms in figure 6.3, but with a very high reduction in incoherent noise, while more low frequency noise is present in the Gaussian signal. The Blackman-Harris and Gaussian CEPS

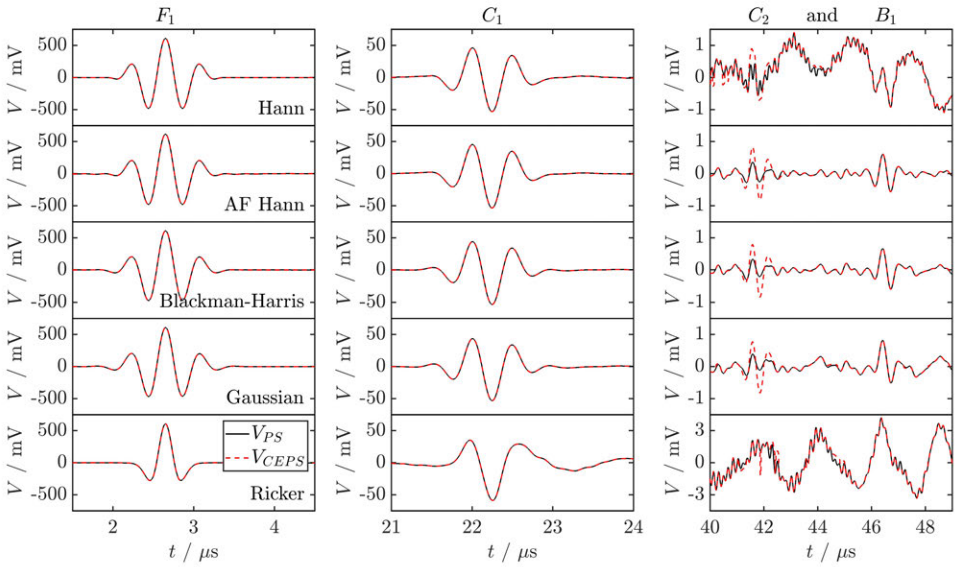

Figure 6.4: Automated noise reduction of the waveforms with 10 coherent time averages. Solid curves are PS and dashed curves are CEPS. Left column: Pulse F_1. Middle column: Pulse C_1. Right column: Pulse C_2 then B_1. First row: cosine (Hann). Second row: cosine (Hann) with AF used to remove frequency side lobes. Third row: Blackman-Harris. Fourth row: Gaussian (Morlet). Fifth row: Second derivative Gaussian (Ricker).

waveforms has a highly coherent enhanced C_2. The short duration Ricker pulse PS waveform has dispersed significantly in C_1, and C_2 and B_1 are unresolvable because of high dispersion and low and high frequency noise content. The coherent pulse amplitude percentages of F_1 are the same for 1000 as 10 coherent time averages.

Shown in figure 6.6, are the example antidispersive pulse specifications, for transfer functions that are obtained from the waveforms with 1000 coherent time averages. The F_1 pulses have reduced phases relative to those of figure 6.5. It is evident that the target pulses C_2 have phases close to those of the input pulses, F_1, of figure 6.5 and, also, the pulse is maximally localised at C_2.

From the above conclusions, AF Hann, Blackman-Harris, and Gaussian appear to be highly useful pulse types for optimally reducing incoherent noise, retaining pulse characteristics, and producing high coherent enhancement in the lowest SNR pulse, C_2. The highly specific, optimised filtering time shift method can reduce incoherent noise, but not without a significant reduction in coherent pulse amplitude. The PS waveforms feature negligible change in coherent pulse amplitude, other than AF Hann, which slightly increases coherent pulse amplitude. Also, the CEPS waveforms feature enhancement of coherent pulse amplitude for C_2.

In figure 6.7, the Hann and automated filtered Hann spectrum amplitudes have

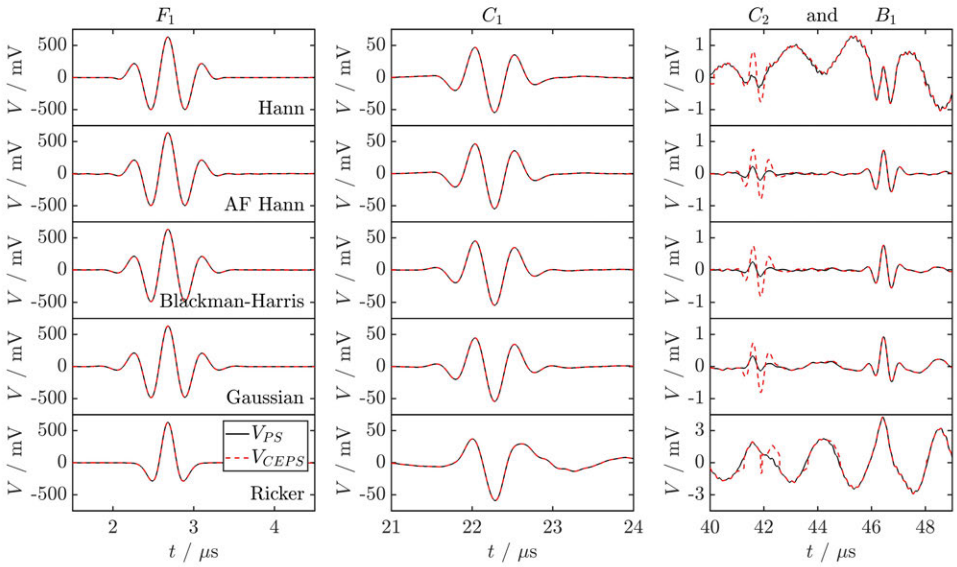

Figure 6.5: Automated noise reduction of the waveforms with 1000 coherent time averages. Solid curves are PS and dashed curves are CEPS. Left column: Pulse F_1. Middle column: Pulse C_1. Right column: Pulse C_2 then B_1. First row: cosine (Hann). Second row: cosine (Hann) with AF used to remove frequency side lobes. Third row: Blackman-Harris. Fourth row: Gaussian (Morlet). Fifth row: Second derivative Gaussian (Ricker).

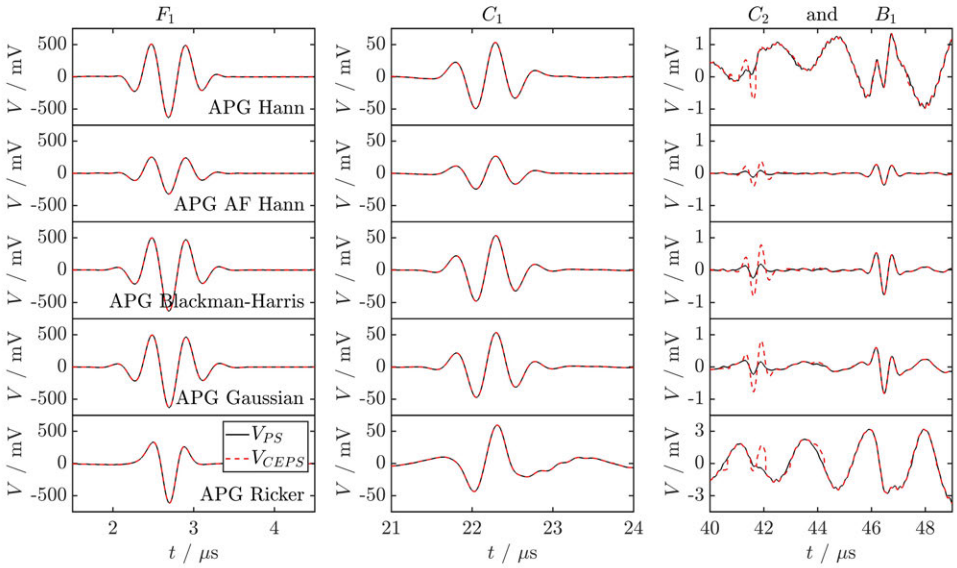

Figure 6.6: Automated noise reduction of the waveforms with 1000 coherent time averages. Solid curves are APG PS and dashed curves are APG CEPS. Left column: Pulse F_1. Middle column: Pulse C_1. Right column: Pulse C_2 then B_1. First row: cosine (Hann). Second row: cosine (Hann) with AF used to remove frequency side lobes. Third row: Blackman-Harris. Fourth row: Gaussian (Morlet). Fifth row: Second derivative Gaussian (Ricker).

similar dominant frequency content and similar bandwidth – number of cycles in time domain – to the unprocessed waveforms; the PS bandwidth can readily be specified to match that of the unprocessed waveforms. The Hann amplitudes have

significant high and low frequency side lobes that contribute to the corresponding poor quality Hann signal in figures 6.3 and 6.4. The AF Hann pulse has the frequency side lobes optimally removed using hyperbolic tangent filters with steep roll-offs. This increased the quality of the AF Hann signals relative to the Hann signals. This filtering has minor effect on the phase at dominant frequencies and creates no major phase discontinuities for frequencies of non-negligible amplitude. The Blackman-Harris spectrum amplitudes are highly similar to those of the unprocessed signals and this smooth reduction in amplitude extends to low and high frequencies where there is significant noise in the unprocessed signals. This results in high signal quality in figures 6.3 and 6.4. Phase is smooth and continuous for frequencies of non-negligible amplitude. This is important because, at frequencies where high spectral amplitudes exist, smooth and continuous variation of spectral phase with frequency is necessary to well-represent a localised signal. The Gaussian spectrum amplitudes has strong automatic high frequency noise reduction but features higher amplitudes in the low frequency noise region than Blackman-Harris. The phase is comparable to Blackman-Harris. The Ricker pulse has moderate high frequency automatic filtering but greatly amplifies low frequency noise. The phase is smooth and continuous for frequencies of non-negligible amplitude. The comparator time shift method with specific filtering parameters successful reduces the low and high frequency noise content of the spectrum amplitudes, but the filtering also extends into the dominant frequency region. This results in reduction of coherent pulse amplitude. The phase is smooth and continuous for frequencies of non-negligible amplitude.

AF Hann, Blackman-Harris, and Gaussian have desired spectral qualities for automatic incoherent noise reduction. This correlates with their high quality signals in figures 6.3 and 6.4. Hann and Ricker amplify, or suboptimally filter, one or more noise region, and therefore their signals are degraded relative to those of AF Hann, Blackman-Harris, and Gaussian. The comparator time shift method has been optimised for good noise reduction, but at the cost of reduction in coherent pulse amplitude.

In figure 6.8, the SNRs of PS AF Hann, Blackman-Harris, and Gaussian are generally higher than the comparator method without filtering and can be higher than the comparator method specific, optimised filtering. The SNRs of CEPS AF Hann, Blackman-Harris, and Gaussian, generally, further improve on this. The shaded

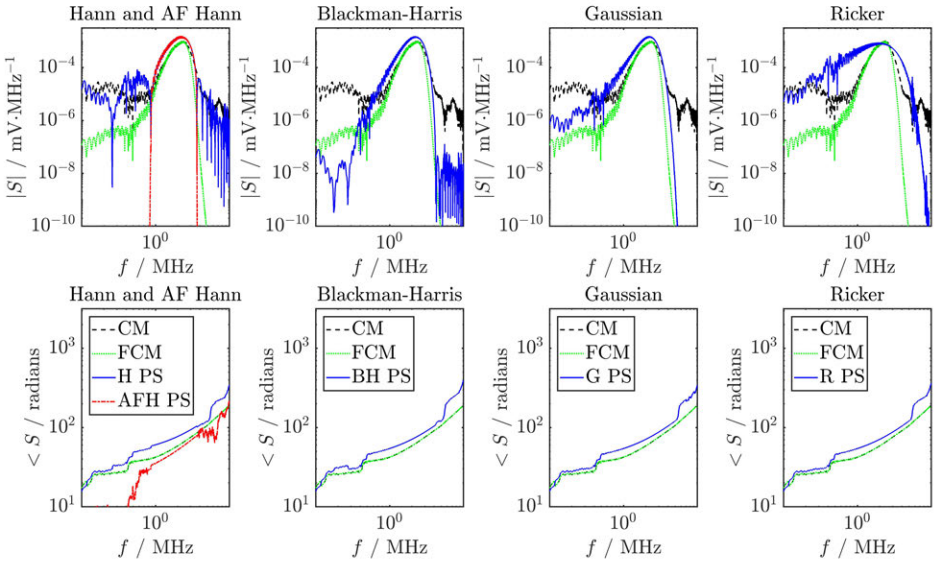

Figure 6.7: Unprocessed waveforms with 10 coherent time averages, and the automated noise reduction of said waveforms. Dashed curves are the mean spectra of the six time shifted waveforms, dotted curves are the filtered mean spectra of the six time shifted waveforms, solid curves are the PS spectra, and dot-dashed curves are the AF cosine (Hann) PS spectra. Top row: spectrum amplitudes. Bottom row: spectrum unwrapped phases. First column: cosine (Hann) and AF Hann. Second column: Blackman-Harris. Third column: Gaussian (Morlet). Fourth Column: Second derivative Gaussian (Ricker).

region bounded by dashed line marks the range of SNRs achievable by the comparators methods, and how certain PS and CEPS methods improve upon those SNRs. The APG SNRs generally exceed cases without for the highest SNR pulse types, AF Hann and Blackman-Harris, especially in the most pertinent, low SNR examples.

6.4 Coherent noise reduction example

6.4.1 Principles of method

The principles behind the coherent noise reduction method of this author are the same as described in section 6.3.1, but there is only one waveform recorded, not six, and therefore the mean is not taken and time shifts are not applied.

6.4.2 Implementation of method

The implementation of the coherent noise reduction method of this author are the same as described in section 6.3.1, other than the following differences. There is only a waveform with 3162 coherent time averages, not 10-1000. This is because 3162

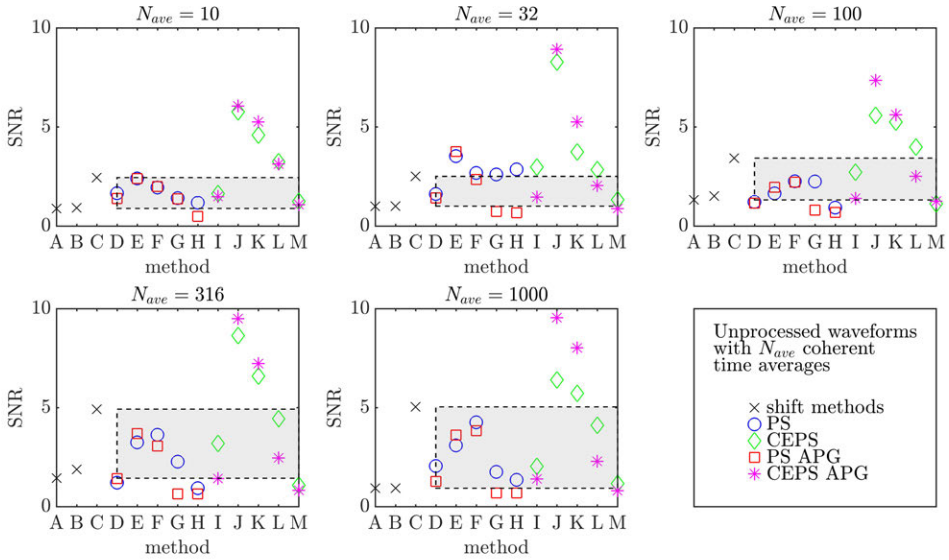

Figure 6.8: Crosses are the shift method SNRs, circles are PS SNRs, and diamonds are CEPS SNRs. The region bounded by the dashed curve represents the range between mean and filtered mean shift method SNRs. Top row, columns 1-3: unprocessed waveforms with 10-100 coherent time averages. Bottom row, columns 1 and 2: unprocessed waveforms with 316 and 1000 coherent time averages. The shaded region bounded by dashed line marks the range of SNRs achievable by the comparators methods, and how certain PS and CEPS methods improve upon those SNRs. Methods, A – mean of SNRs of shifted C_2, B – SNRs of mean of shifted C_2, C – SNRs of filtered mean of shifted C_2, D – SNRs of PS Hann, E – SNRs of PS automated-filtered Hann, F – SNRs of PS Blackman-Harris, G – SNRs of PS Morlet, H – SNRs of PS Ricker, I – SNRs of CEPS Hann, J – SNRs of CEPS automated-filtered Hann, K – SNRs of CEPS Blackman-Harris, L – SNRs of CEPS Morlet, and M – SNRs of CEPS Ricker

coherent time averages is sufficient to reduce coherent noise to negligible amounts within the initial, unprocessed waveforms, such that the performance of the automated noise reduction system of this author can here be evaluated for solely coherent noise reduction. The input frequency is 5MHz not 2.25MHz. This is because the very high material damping in HDPE, that necessitated the prior selection of a 2.25MHz ultrasonic transducer, is not present in the coarse grained metal alloy, and so 5MHz is a suitable input centre frequency. The received waveforms do not include the scattered pulses C_1 and C_2 of figure 6.1. This is because there is no cylindrical void in the coarse grained metal alloy sample, only parallel front and back faces.

6.4.3 Results & analysis

The method for coherent noise reduction described in section 6.4.2 is implemented, for which the results are here analysed. The unprocessed and conventional frequency filtered waveforms are first provided for 3162 coherent time averages, next are the

PS and CEPS results for 3162 coherent time averages, followed by the spectral amplitudes and phases of the unprocessed results, the frequency filtered results, and the PS and CEPS results, and last is quantified SNRs of the comparator methods and the PS and CEPS methods.

In figure 6.9, the unprocessed waveform with 3162 coherent time averages and its filtered mean is shown. The unprocessed waveform has significant coherent noise due to grain scatter, as well as low frequency drift. The back wall reflection, B_1 (at $t = 13.4\mu$s) is clearly distinguishable from the noise. The bottom row is obtained by applying a specific corner frequency and roll-off. There is necessary subjectivity in the selection of the frequencies at which these parameters occur for continuous, multifaceted spectra such as those of waveforms containing multiple pulses. The corner and roll-off are therefore selected based on a compromise between maximising coherent noise reduction and reducing coherent pulse amplitudes by an acceptably small amount. To optimally reduce low and high frequency coherent noise, the waveform in the bottom row has a maximum amplitude of its Hilbert transform of F_1 that is 98.8% of the mean waveform. This is a loss in coherent pulse amplitude of 1.2%.

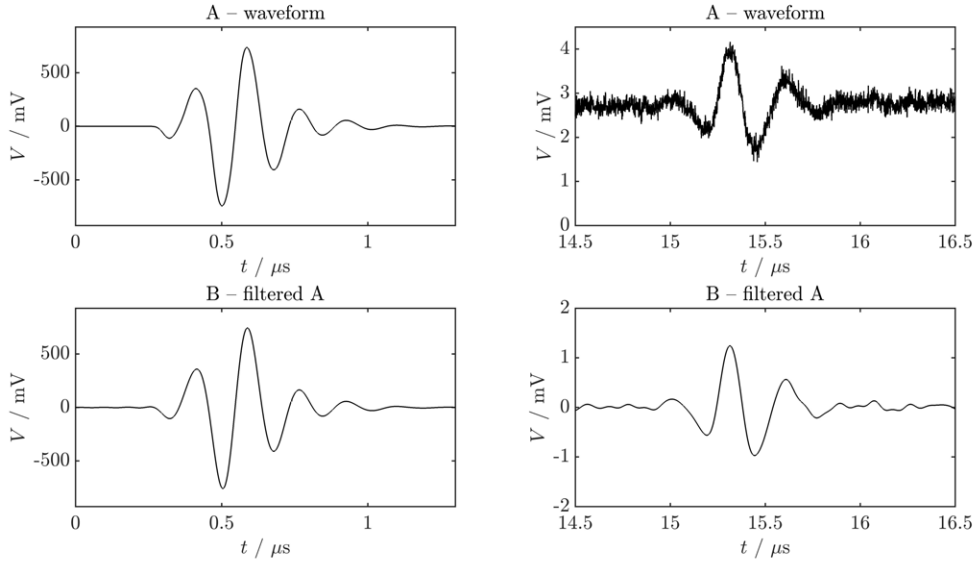

Figure 6.9: Unprocessed waveforms with 3162 coherent time averages. Left column: Pulse F_1. Right column: Pulse B_1. Top row: unprocessed waveform. Bottom row: the optimised filtered waveform, with specific corner frequencies and roll-offs.

In figure 6.10, the example pulse specifications, for transfers functions that are obtained from the waveforms with 3162 coherent time averages, are shown. In the

Hann PS waveform, B_1 is discernible, but some noise remains in the signal, including high frequency noise and low frequency drift. The Hann CEPS waveform is the same as that of PS. The Hann PS and CEPS waveform that has had its frequency side lobes removed using an automated filtering process has less low and high frequency noise relative to without AF. In the Blackman-Harris PS and CEPS waveforms, B_1 is also distinguishable from the surrounding noise. The same conclusions can be drawn for the Gaussian waveforms as for Blackman-Harris. The short duration Ricker pulses in the PS and CEPS waveforms have dispersed significantly in B_1. Also, some noise remains. The non-AF PS waveforms have a maximum amplitude of their Hilbert transforms of F_1 that is 100% of the mean waveform. This is a loss in coherent pulse amplitude of 0%. The AF Hann PS has a coherent pulse amplitude increase of 1.3% of F_1.

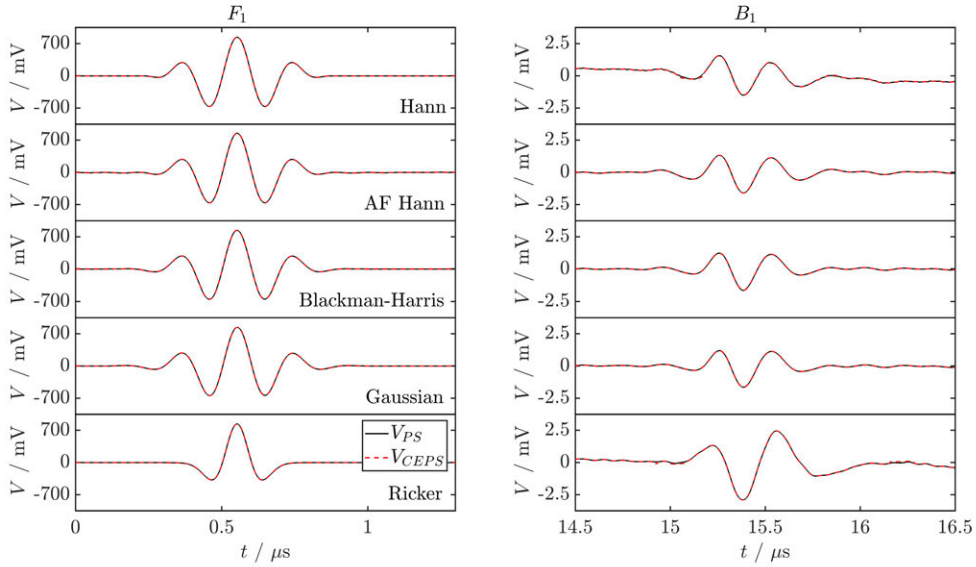

Figure 6.10: Automated noise reduction of the waveforms with 3162 coherent time averages. Solid curves are PS and dashed curves are CEPS. Left column: Pulse F_1. Right column: Pulse B_1. First row: cosine (Hann). Second row: cosine (Hann) with AF used to remove frequency side lobes. Third row: Blackman-Harris. Fourth row: Gaussian (Morlet). Fifth row: Second derivative Gaussian (Ricker).

From the above conclusions, AF Hann, Blackman-Harris, and Gaussian, as with the incoherent noise reduction example, appear to be highly useful pulse types for optimally reducing coherent noise and retaining pulse characteristics in the back wall reflection, B_1. The filtering method can reduce low and high frequency coherent noise, but it is highly specific, using optimised corner frequencies and roll-offs. The PS and CEPS waveforms feature no change in coherent pulse amplitude, other than

AF Hann, which slightly increases coherent pulse amplitude.

The analysis of figure 6.11 results in the same conclusions as for figure 6.7, because the spectrum amplitudes and phases are observed to be similar in all cases. Less high frequency noise results from the high number of coherent time averages of figure 6.11 relative to figure 6.7.

AF Hann, Blackman-Harris, and Gaussian have desired spectral qualities for automatic coherent noise reduction. This correlates with their high quality signals in figure 6.10. Hann and Ricker amplify, or suboptimally filter, one or more noise region, and therefore their signals are degraded relative to those of AF Hann, Blackman-Harris, and Gaussian. The comparator filtering method has been optimised for good noise reduction, but at the cost of high specificity in multiple, key parameters.

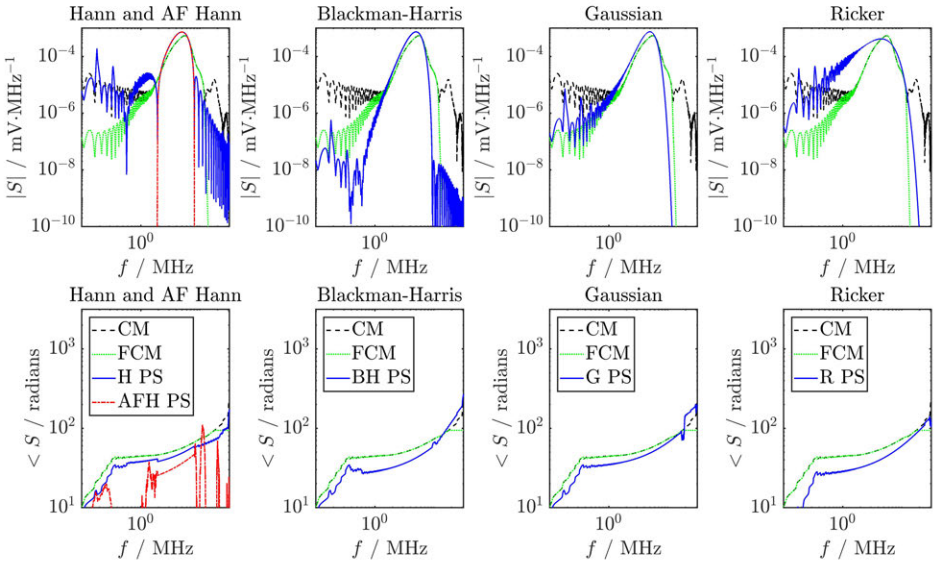

Figure 6.11: Unprocessed waveforms with 3162 coherent time averages, and the automated noise reduction of said waveforms. Dashed curves are the mean spectra of the six time shifted waveforms, dotted curves are the filtered mean spectra of the six time shifted waveforms, solid curves are the PS spectra, and dot-dashed curves are the AF cosine (Hann) PS spectra. Top row: spectrum amplitudes. Bottom row: spectrum unwrapped phases. First column: cosine (Hann) and AF Hann. Second column: Blackman-Harris. Third column: Gaussian (Morlet). Fourth Column: Second derivative Gaussian (Ricker).

In figure 6.12, the SNRs of PS AF Hann, Blackman-Harris, and Gaussian are significantly higher than that of the unprocessed waveform. Also, the PS and CEPS SNRs are significantly higher than that of the specific, optimally filtered waveform. The shaded region bounded by dashed line marks the range of SNRs achievable by the comparators methods, and how certain PS and CEPS methods improve upon those SNRs.

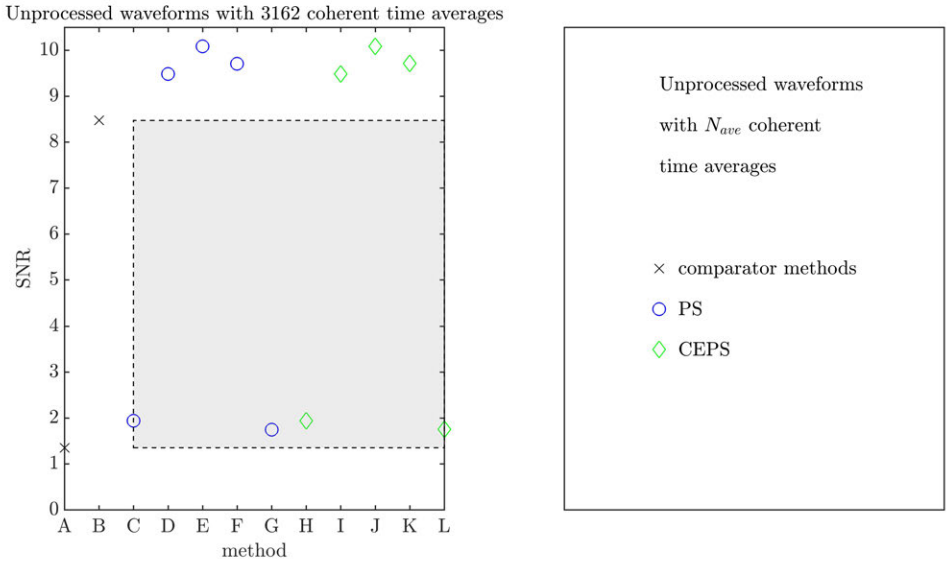

Figure 6.12: Crosses are the shift method SNRs, circles are PS SNRs, and diamonds are CEPS SNRs. The region bounded by the dashed curve represents the range between unprocessed and filtered waveform SNRs. The shaded region bounded by dashed line marks the range of SNRs achievable by the comparators methods, and how certain PS and CEPS methods improve upon those SNRs. Methods, A – mean of SNRs of shifted C_2, B – SNRs of mean of shifted C_2, C – SNRs of filtered mean of shifted C_2, D – SNRs of PS Hann, E – SNRs of PS automated-filtered Hann, F – SNRs of PS Blackman-Harris, G – SNRs of PS Morlet, H – SNRs of PS Ricker, I – SNRs of CEPS Hann, J – SNRs of CEPS automated-filtered Hann, K – SNRs of CEPS Blackman-Harris, L – SNRs of CEPS Morlet, and M – SNRs of CEPS Ricker

6.5 Conclusions

This author has proposed, and demonstrated the effectiveness of, two fully automated noise reduction methods, pulse specification (PS) and coherent enhanced pulse specification (CEPS), for improving signal-to-noise ratio (SNR) of coherent signals in waveforms containing either incoherent or coherent noise. Antidispersive pulse generation (APG) has been devised and demonstrated for further improving the pulse quality upon reception. The effectiveness of these method for reducing incoherent and coherent noise has been exemplified for applications such as NDE, medical ultrasonics, seismology, and acoustics using two examples of ultrasonic inspection. In the first case, high incoherent noise is inherent in the waveforms, but much reduced with the automated noise reduction methods of this author, compared with established methods, especially for the most suitable APG pulses. In the second case, high coherent noise is inherent in the waveforms, but also much reduced with the automated noise reduction methods of this author, compared with established methods.

References

[1] C. Holmes, B.W. Drinkwater, P.D. Wilcox, *Post-processing of the full matrix of ultrasonic transmitreceive array data for non-destructive evaluation*, NDT&E International **38**, 701-711, 2005.

[2] I. Vasconcelos and R. Snieder, *Interferometry by deconvolution, Part 1 – Theory for acoustic waves and numerical examples*, Geophysics, **73**(3), 2008.

[3] I. Vasconcelos and R. Snieder, *Interferometry by deconvolution, Part 2 – Theory for elastic waves and application to drill-bit seismic imaging*, Geophysics, **73**(3), 2008.

[4] G.T. Schuster, *Seismic Interferometry*, Cambridge University Press, Cambridge, 109-123 (2009).

[5] G.A. Morris, *Compensation of instrumental imperfections by deconvolution using an internal reference signal*, Journal of Magnetic Resonance, **80**, 1988.

[6] J. Kivinen, T.O. Korhonen, P. Aikio, R. Gruber, and P. Vainikainen, *Wideband radio channel measurement system at 2 GHz*, Instrumentation and Measurement, IEEE Transactions on, **48**(1), 1999.

[7] T. Thiel, M. Czisch, G.K. Elbel, and J. Hennig, *Phase coherent averaging in magnetic resonance spectroscopy using interleaved navigator scans: Compensation of motion artifacts and magnetic field instabilities*, Magnetic Resonance in Medicine, **47**, 2002.

[8] T.G. Stockham Jr., T.M. Cannon, and R.B. Ingebretsen, *Blind deconvolution through digital signal processing*, Proceedings of the IEEE, **63**(4), 1975.

[9] J. Chen, J. Benesty, Y. Huang, S. Doclo, *New insights into the noise reduction Wiener filter*, Audio, Speech, and Language Processing, IEEE Transactions on, **14**(4), 2006.

[10] N. Kingsbury, *Complex wavelets for shift invariant analysis and filtering of signals*, Applied and Computational Harmonic Analysis, **10**, 2001.

[11] P. Edme and D.F. Halliday, *Near-surface imaging using ambient-noise body waves*, Interpretation, **4**(3), 2016.

[12] M. Antonini, M. Barlaud, P. Mathieu, and I. Daubechies, *Imaging coding using wavelet transforms*, Image Processing, IEEE Transactions on, *1*(2), 1992.

[13] J. Lin and L. Qu, *Feature extraction based on Morlet wavelet and its application for mechanical fault diagnosis*, Journal of Sound and Vibration, **234**(1), 2000.

[14] J.W.J. Hosken, *Ricker wavelets in their various guises*, First Break, **6**(1), 1988.

[15] J. Isla, F. Cegla, *EMAT Phased Array: a Feasibility Study of Surface Crack Detection*, Ultrasonics, 2017.

[16] J.O. Smith III, *Spectral Audio Signal Processing* (W3K Publishing, Lewiston, NY, USA), 57-63 (2011).

[17] J.S. Egerton, M.J.S. Lowe, H.V. Halai, P. Huthwaite, *Ultrasonic attenuation and phase velocity in high-density polyethylene (HDPE) pipe material*, J. Acoust. Soc. Am. **141**(3), 1535-1545 (2017).

[18] D.R. Frey, *A general class of current mode filters*, Circuits and Systems, 1993., ISCAS '93, 1993 IEEE International Symposium on, 1435-1438 (1993).

6.6 Appendices

6.6.1 Concepts of wave deconvolution

The main premise behind such signal deconvolution procedures is that one can reversibly alter the frequency content of a waveform containing many separate waves or pulses, in its entirety, without discarding the relative amplitudes and phases

between each signal; the converse of this is that independent alteration of separate sections of the waveform is inequivalent to this and is here considered a distortion of the recorded information – such procedures will not be conducted or analysed here. Treating the above premise as necessary and sufficient in such signal processing affords significant freedoms; one can feasibly specify any 'reasonable' pulse characteristics for the reference pulse in the waveform and, in the example, observe how such a wave propagates and scatters through the media it interacts with. Equivalently, after waveform deconvolution using the spectrum of the independent, repeatable reference signal, the waveform is convolved with a separate, pulse specified, signal to highlight unique properties of wave interaction with the interrogate media.

When coherent averaging multiple independent, repeatable measurements, the deconvolution of each signal via its own reference signal forces the frequency content of all reference signals to be equal. The extent to which the other waves or pulses in the waveform are coherently enhanced via averaging is coupled to the extent to which experimental procedure and conditions are independent and repeatable between measurements.

Further to this, the extent to which the reference signal, before deconvolution, is unperturbed, relative to the state it is expected or intended to be in, limits the value of the signal measurement for coherent enhancement of signals. An anomalous signal relative to the expected or intended reference signal results from experimental procedure and conditions significantly different to those measurements in which the reference signal is as expected or intended, and therefore this anomalous or perturbed signal will be no more use after deconvolution than in its unprocessed state. For maximum algorithm effectiveness, such signals should be selectively discarded using predefined criteria. An example change in experimental environment is lack of temporal thermal equilibrium. If thermal expansion of a given test material had occurred between independent measurements, and therefore the geometry of the setup had changed, the inherent lack of repeatability in these measurements is expressed through a reduction in coherent signal strength because the pulse separation and phase will have changed.

6.6.2 Signal-to-noise ratio percentages of three superior pulse specifications and comparator methods

The percentages of the three superior methods for PS and CEPS that have SNRs in excess of the comparator method both without and with filtering are shown in table 6.1. In 100% of case the PS and CEPS methods have higher SNRs than the coherent mean of the six time shifted signals. After specific, optimal filtering, the time shift method often has higher SNR than PS, but CEPS generally has a higher SNR than the time shift method. The increased SNRs of PS and CEPS are most dominant for fewer (less than 316) coherent time averages and therefore PS and CEPS are highly beneficial when rapid data acquisition or high quantities of data are required, such that many coherent time averages are not feasible.

↓ SNRs, % above | N_{ave} →	10	32	100	316	1000
(E,F,G)>B	100	100	100	100	100
(J,K,L)>B	100	100	100	100	100
(E,F,G)>C	0	100	0	0	0
(J,K,L)>C	100	100	100	66.7	66.7
(E,F,G)>B	100	100	100	100	100
(J,K,L)>B	100	100	100	100	100
(E,F,G)>C	0	100	0	0	0
(J,K,L)>C	100	100	100	66.7	66.7

Table 6.1: Columns 2-6: Waveforms with coherent time averages, 10-1000. Row 2: Percentage of PS second cylinder scatter, C_2, SNRs that exceed those of the chosen mean shift method. Row 3: Percentage of CEPS second cylinder scatter, C_2, SNRs that exceed those of the chosen mean shift method. Row 4: Percentage of PS second cylinder scatter, C_2, SNRs that exceed those of the chosen mean shift method with specific, optimised filtering applied. Row 5: Percentage of CEPS second cylinder scatter, C_2, SNRs that exceed those of the chosen mean shift method with specific, optimised filtering applied.

The percentages of the three superior methods for PS and CEPS that have SNRs in excess of the unprocessed and filtered waveform are shown in table 6.2. In all cases the PS and CEPS SNRs are in excess of those of the chosen comparator methods.

6.6.3 Pulse specifications inferior to the five analysed

Frequency chirped pulses, which are pulses where the frequency increases or decreases with from earlier to later in the pulse excitation, have bandwidths significantly higher than an equivalent pulse with a fixed centre frequency. Consequently, in a dispersive medium where phase velocity varies with frequency, such as

↓ SNRs, % above	N_{ave} →	3162
(E,F,G)>B		100
(J,K,L)>B		100
(E,F,G)>C		100
(J,K,L)>C		100

Table 6.2: Column 2: Waveforms with coherent 3162 time averages. Row 2: Percentage of PS second cylinder scatter, C_2, SNRs that exceed those of the chosen mean shift method. Row 3: Percentage of CEPS second cylinder scatter, C_2, SNRs that exceed those of the chosen mean shift method. Row 4: Percentage of PS second cylinder scatter, C_2, SNRs that exceed those of the chosen mean shift method with specific, optimised filtering applied. Row 5: Percentage of CEPS second cylinder scatter, C_2, SNRs that exceed those of the chosen mean shift method with specific, optimised filtering applied.

HDPE, chirp pulses delocalise significantly as they propagate. This makes them unfavourable for automated noise reduction, where pulse time-windowing is necessary. Similarly, square pulses have a very large bandwidth, and are therefore unsuitable for localised propagation in dispersive media.

Chapter 7

Numerical simulation of ultrasonic NDE of sound-damping materials using a multiband time domain approach

The formulation, implementation, and evaluation of some concepts covered in chapter will be published Open Access as: J.S. Egerton, M.J.S. Lowe, J. Jian, and P. Huthwaite, *Numerical simulation of ultrasonic NDE of sound-damping materials using a multiband time domain approach*, [Pre-submission].

7.1 Abstract

Ultrasonic array imaging is increasingly favoured and used in the nondestructive evaluation (NDE) of polymer pipes. Simulation of such imaging is considered valuable for validation of the inspection system. However, while numerical simulation of ultrasound NDE is established for typical low-loss engineering materials, such existing numerical simulation techniques are not adequate for high loss materials, such as polymers, because of strong frequency dependence of their properties. Here, to overcome this, an analytical multiband finite element simulation and imaging (MBim) system is demonstrated with nondestructive evaluation of high-density polyethylene (HDPE) pipe joints where compressional waves are sent from water into viscoelastic HDPE pipe material.

MBim waveform simulation is shown to well represent the ultrasonic inspection with accurate ultrasonic scattering, refraction, and reflection.
MBim defect imaging is exemplified for both visual and automated sentencing with ultrasonic images; methods for defect detection, location, sizing, and characterisation by visual sentencing are provided, as are methods for defect detection, location, and sizing by automated sentencing. In all, high accuracy is achieved.

7.2 Introduction

Nondestructive evaluation (NDE) is widely used in industry to detect, locate, size, and characterise potential defects in engineering components such that the likelihood of critical damage or failure is minimised. The development of accurate and reliable NDE methods increasingly uses numerical model simulations.
Conventional explicit time domain FE (TDFE) simulations of ultrasonic wave scattering are broadly considered to be computationally efficient. However, TDFE simulations that are computed with mass proportional damping, stiffness proportional damping, or the combination of the two, are only accurate near the centre frequency of the input ultrasonic pulse. Because they may be solved explicitly, the maximum model size of TDFE simulations is not necessarily a limitation. By contrast, implicit frequency domain FE (FDFE) simulations of ultrasonic wave scattering can potentially be accurate in representing the full frequency dependence of the scattered pulse. Though, this is only possible if there is accurate knowledge of material properties, such as storage and loss moduli [1, 2], at the ultrasonic frequencies of interest. While, experimentally, these material properties are, in general, obtained from cyclic loading at a rate of a few hundred Hertz – far below ultrasonic frequencies – and then extrapolated up to MegaHertz frequencies. Such approaches result in unavoidable inaccuracy from such long extrapolation away from the recorded dataset. Further, FDFE simulations are highly computationally intensive. The largest models cannot be solved using FDFE using current computational equipment, because the implicit method requires simultaneous storage of much information [3].
The multiband finite element (MBFE) method was therefore developed to solve such problems inherent in the described TDFE and FDFE approaches to the simulation of ultrasonic wave scattering. With MBFE the full frequency dependence of the pulse can be accurately represented, with computational efficiency similar to TDFE, and

without the model size limitation of FDFE.

The work presented here arose from a need to perform simulations of ultrasonic NDE of high-density polyethylene (HDPE) pipes using an angled, water-filled wedge and an ultrasonic array, but the method is widely applicable to NDE inspection problems. Therefore, the simulations here combine analytical and finite element (FE) analyses to utilise the best aspects of both approaches.

Simulation of ultrasonic waveforms and imaging, through summation of these waveforms, is important in NDE, especially when an ultrasonic array is used to transmit and receive these waveforms. These waves can scatter from local ultrasonic impedance discontinuities (here material defects), refract upon partial transmission through large-extent ultrasonic impedance discontinuities (here pipe external walls), and partially reflect at such large-extent impedance discontinuities.

In NDE, it is important to accurately simulate such waveforms and accurately produce defect images from such waveforms, because such simulations as these are crucial to the validation of inspection systems.

The work presented here was motivated by the challenge of simulating ultrasonic array imaging of defects in thick-walled polymer (HDPE) pipes, such as are commonly used for water or gas transport. Heat-fused joints of these pipes made on site can be prone to a variety of defects, including contamination, lack of fusion, cracks, and porosity. The proposed simulation geometry for ultrasound array imaging simulation, which closely matches the real inspection setup, is shown in figure 7.1.

Such a simulation study would be very useful in order to investigate the detectability and characterisation potential of the array imaging. The difficulties of performing such a simulation include the strong frequency-dependent attenuation in the HDPE material, the propagation of the sound through a water wedge before reaching the pipe material, the significant propagation distance through the pipe material, the desire to model complex shapes of candidate defects, and the need to perform multiple wave-path simulations in order to compose the set of array signals for the image. In this chapter this author sets out a series of steps to achieve these modelling goals. While these steps are specific to this problem and configuration, the methodology is suitable for such problems in general.

A big saving can be achieved by dividing the problem into analytical and numerical parts. Analytical calculations can be used to propagate the waves accurately over

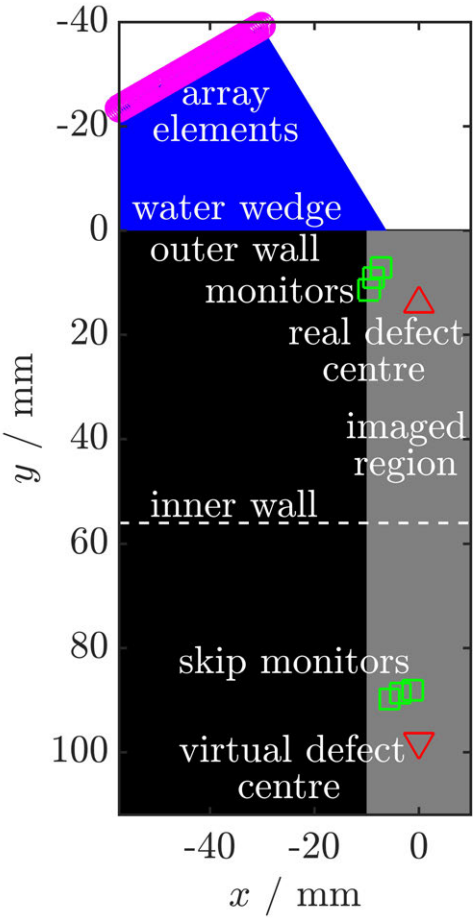

Figure 7.1: Simulation geometry for MBim with an example, simplified depiction of the MBFE region. The overlapping circles at the top of the figure and the angled solid region on which they are located are respectively the ultrasonic array elements and the water-filled wedge that the array is mounted on, with $y < 0$. The outer wall of the HDPE pipe is at $y = 0$. The solid region with $y > 0$ and $-10 < x/\text{mm} < 10$ is the imaged region. The solid region left of the imaged region is a depiction of the HDPE pipe region that is not near the fusion face and is therefore not imaged for the NDE of fusion joint defects. The dashed line at $y = 56$mm is the inner wall of the HDPE pipe. The triangles pointing up and down are the real and virtual defect centres respectively. The squares locate the MBFE direct and skip monitors. The defects and monitors are within the MBFE simulation region, which is smaller than the imaged region that contains an analytical inner wall reflection signature.

large distances of regular material, while numerical calculations are highly suitable for detailing the complex interactions of the waves with defects. This kind of approach has been adopted by others in a number of articles [6–9]. Here this author chooses to deploy an analytical approach for the propagation from the transducer through the water, refracted into the polymer, and then arriving into the region of the defects. The incidence and scattering at the defect is then handled by a local FE model. This whole process requires several innovative modelling techniques.

First, the requirements of the analytical and FE simulation portions of this hy-

bridised simulation technique are detailed. The preceding acoustic properties study conducted by this author [4] provides the necessary acoustic properties for analytical ultrasonic waves propagating in HDPE pipe material. Here, FE simulations also provide accurate and efficient representation of ultrasonic wave scattering from defects, especially when using the MBFE simulation technique of this author [5]. Provided the above acoustic properties and FE simulation technique are available, the efficiency and accuracy of such a hybrid simulation method exceed those of solely FE simulations, including MBFE. Consequently, it is considered highly efficient and accurate to combine analytical wave propagation – plus refraction and reflection, here – with MBFE defect interaction and scattering.

The concept of such a hybrid approach has been addressed in a number of previous studies. Work by Rajagopal, Shi et al. [6, 7] has developed a general purpose hybrid model that uses Green's functions to link separate regions and is versatile to accept any kind of numerical scheme deployed within those separate regions. Zhang, Wilcox et al. [8, 9] addressed imaging interests, again pursuing a general purpose approach, in this case focusing on the construction of scattering matrices for a target defect within a localised region described by a Finite Element representation. These approaches have been developed for complex scatterers surrounded by otherwise straightforward elastic terials. Here there is the challenge of huge attenuation of the propagating sound in the polymer material, and this author develops their hybrid model to link attenuating waves in the HDPE volume with MBFE for the local model and scattering. Furthermore, this author introduces an improved efficiency for the interface with the local region containing the defect.

The next technical progress reported in this chapter relates to the transmission of waves across interfaces in the analytical part of the hybrid model. This has relevance in the application example to the need to propagate through the water wedge and into the HDPE component. The problem of finding the path of a refracted ray from a location in one medium to a location in another is well known and is frustrating in that, although it appears to be a simple task, it is not open to a simple explicit calculation. Calculations can be done by a variety of iterative approaches, including the refraction methods of Ogilvy [14], Schmitz et al. [15], Long et al. [16], Connolly et al. [17], and the method used in the commercial software, *CIVA* [19]. Alternatively, a Fermat mapping method has been applied by Connolly [4], and an eikonal method for obtaining refraction angles has been demonstrated by,

for example, Kalaba [21], Gray et al. [22], and Huthwaite [23]. While these are all reliable, they vary in their efficiency of calculation, and this becomes an important consideration when simulating array image signals in which very many point-to-point routes have to be found. This author proposes here an approach that is based on Fermat's principle to calculate the shortest path, found using a 'range bisection' of the incident location at the interface.

Also, the imaging algorithm for MBim is similar to the multi-mode total focusing method (TFM) [24], and used the principles of TFM. As with MBim, multi-mode TFM may be applied to waves in multi-layered media. Upon transmission and reflection at each interface, an ultrasonic wave is partially mode converted from longitudinal (L) to shear (S), or vice versa. The multi-mode TFM imaging approach is used to obtain separate images of all possible paths, and corresponding modes, the wave could have. MBim provides these reflected and scattered paths in waveform simulation, as well as also providing an image that contains all these paths, in sum, or, as with multi-mode TFM, as separate images.

Last, the MBim approach uniquely combines the limited aperture and the minimal sampling waveform simulation with analytical wave propagation, MBFE wave scattering, and with a combination of a virtual array and virtual defect necessary to represent wave paths known as half- and full-skip. Necessary interface transmission and reflection coefficients are readily determined from, for example, [25] and [26]. For HDPE, where shear waves are very highly attenuated, these paths are, for this example, longitudinal wave incidence and longitudinal reception, after three wave diversions – reflections, refractions, or scatters – LLLL; the same with four diversions, 5L; and the same with five diversions, 6L; corresponding respectively to direct scatter, half-skip and full-skip. Consequently, all non-negligible wave paths that would be present in real ultrasonic array data are simulated and imaged with MBim.

Therefore, the MBim method for combined analytical and MBFE simulation of ultrasonic waveforms, and imaging with these waveforms, utilises unique accurate and efficient approaches to wave scattering, refraction, and reflection.

This chapter is set out as follows. First, in section 7.3, is the background theory required to formulate MBim; next, in section 7.4, is the outline of the MBim method; in section 7.5 are the results and analysis of MBim applied to waveform simulation and imaging of real-world HDPE pipe joint inspections; and in section

7.6 conclusions are drawn.

7.3 Theory

Here this author outlines the theory necessary for the MBim analytical wave propagation and MBFE wave scattering using transfer functions, where, because of its large extent in all dimensions relative to the ultrasonic wavelength, the inner wall of the HDPE pipe, and the ultrasonic reflection from it, are simulated analytically. First, will be a description of the ultrasonic transfer function and dispersion relation used throughout. Next, analytical wave propagation theory is provided. Then, the formulation for multiband finite element description for wave scattering is given. After, are details of how to generate pulses that are antidispersed, such that, once scattered from the defect, the pulses arrive at the monitor with highest temporal resolution or least pulse width. Followed by interface refraction methods including the method used in MBim, details of scattering matrices and how this author makes efficient use of them, and source and monitor locations and separations.
The MBim simulation geometry has been provided and detailed in figure 7.1.

7.3.1 Transfer function and dispersion relation

The transfer function, that maps initial to propagated waves, or otherwise initial to scattered waves, for a 1-D harmonic plane wave may be expressed as

$$H_x(x, f) = \exp(ik_x(f)x), \tag{7.3.1}$$

where x is location, f is frequency, and $k_x(f)$, or tersely $k(f)$, is the dispersion relation,

$$k(f) = \frac{2\pi f}{v_p(f)} + i\alpha(f), \tag{7.3.2}$$

where $v_p(f)$ is phase velocity and $\alpha(f)$ is attenuation. The transfer function is represented tersely as $H(x, f)$.

7.3.2 Analytical wave propagation

Provided here is the theory used to define the ultrasonic acoustic properties of viscoelastic HDPE pipes used in the analytical wave propagation of MBim. In the preceding HDPE pipe acoustic properties study of this author [4] there was presented a description of ultrasonic viscoelastic bulk wave dispersion that conforms to theoretical viscoelastic constraints and that is necessarily causal, using the Kramers-Kronig relation. The variation in acoustic properties with frequency is pertinent for MBim and summarised here – attenuation and phase velocity vary with frequency as follows,

$$\alpha(f) = \alpha_1 f^y, \tag{7.3.3}$$

and

$$v_p(f) = v_{p1} + \left(\frac{v_{p1}}{\pi}\right)^2 \frac{\alpha_1}{y-1} f^{y-1}, \tag{7.3.4}$$

where $0 < \alpha_1$, $1 < y < 2$, and positive phase velocity at zero frequency, $0 < v_{p1}$, are all known empirical coefficients. From equation (7.3.1), general forms of attenuation and phase velocity are,

$$\alpha_{gen}(f) = -\frac{1}{x} \ln \left| \frac{S(f)}{S_0(f)} \right| \tag{7.3.5}$$

and

$$v_{p,gen}(f) = \frac{2\pi f x}{\phi_S(f) - \phi_{S_0}(f)}, \tag{7.3.6}$$

where ϕ_{S_0} and ϕ_S are phases of the initial and propagated waves.

7.3.3 Multiband finite element wave scattering

Provided here is the formulation of the MBFE model, as detailed in [5]. In MBFE, the TDFE dispersion relations of n_{band} different simulations, run at successively increasing frequency bands, are blended to yield the full dispersion relation,

$$k_{blend} = \sum_{n=1}^{n_{band}} b_n \left(\frac{2\pi f}{v_{pn}} + i\alpha_n \right), \tag{7.3.7}$$

where b_n is a linear weighting function. This provides an accurate and efficient input for the transfer function of equation (7.3.1).

7.3.4 Antidispersive pulse generation

The input pulse is a Blackman-Harris [27] windowed sinusoid with 3 periods (cycles), because of its favoured temporal and frequency characteristics, detailed in [4]. Based on the expected average propagation distance of a pulse, $\overline{x}$, a pulse is maximally localised upon reception at the ultrasonic array using the antidispersive pulse generation (APG) transfer function [8],

$$H_{APG} = \exp\left[-i \left(\frac{2\pi f}{v_p} - \frac{2\pi f}{v_{p0}} \right) \overline{x} \right], \tag{7.3.8}$$

given that $v_{p0} = v_p(f_0)$ and f_0 is the pulse centre frequency.

7.3.5 Interface refraction methods

Many existing ray-based refraction methods [14–18, 24] are based on the concept of 'point-and-shoot'. A trial trajectory from the source point – a single known location – is calculated and then its proximity to the target point is used to set the parameters for the next trial. This approach can be subject to a large error in the transmitted wave angle through the interface, even for a small error, or offset, of the angle in the first medium, when waves move from a slower to faster medium. This imposes an increase in the number of trial angles required to obtain a desired precision of the arrival location. This concept is illustrated in figure 7.2; the figure was generated using equations given in appendix 7.7.1. In figure 7.2, the x-axis

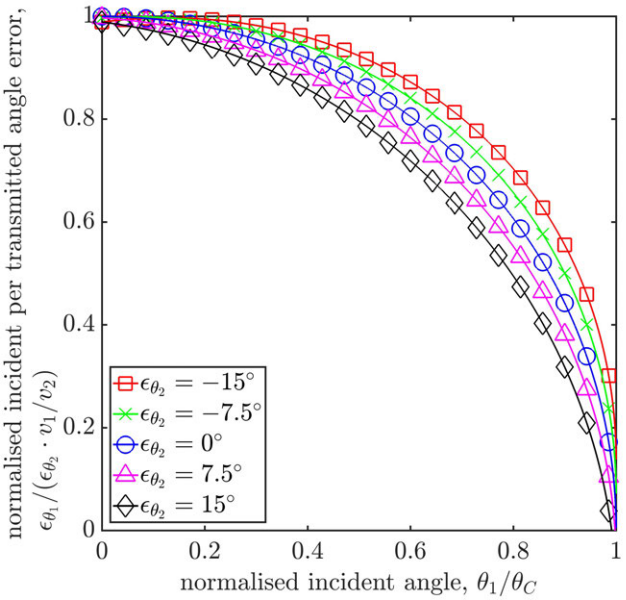

Figure 7.2: Single known location ray tracing and its required increase in angle precision in transmitted wave angle after refraction caused by change in wave velocity, such as at a two-medium interface. The extra required precision from interface 1 to 2, normalised by the ratio of velocities in medium 1 and 2, is $\epsilon_{\theta_1}/(\epsilon_{\theta_2} \cdot v_1/v_2)$. The incident angle at the interface of the wave in medium is θ_1 and the critical angle of total internal reflection at the interface is θ_C.

shows the incident angle, from source to interface, as a fraction of the critical angle at which total internal reflection occurs. The y-axis shows the ratio of errors of the angle from source to interface to the angle from interface to the wave destination in the medium. This quantity is also normalised by the ratio of velocities in the incident and transmitted media. Equivalently, the y-axis shows how small the uncertainty must be on a chosen angle of incidence to yield a desired accuracy in the transmitted medium, meaning low values on the y-axis are undesired for any given simulation technique.

Let us consider the example of a water-HDPE interface, with an angle of incidence of 80% of the critical angle. To achieve a precision of $|\epsilon_{\theta_2}| < 1$ in this example requires an incident angle with precision $|\epsilon_{\theta_1}| < 0.3$. If, for example, the HDPE is replaced by a metal, this necessary precision could be reduced to $|\epsilon_{\theta_1}| < 0.1$ for that same angle of incidence. In regions where multiple interfaces exists, such as a composite, or any heterogeneous medium that is represented discretely, this increase in required angular precision is compounded on an interface-to-interface basis, resulting in a high level of inefficiency to achieve the required accuracy. Further, when conducting single known location ray tracing from a faster to a slower medium, for example

a HDPE-water interface, after wave scattering, it would be impossible to transmit waves at the critical angle. This is because, when only the origin of the wave is used, there is no way to know the point where the wave crosses the interface. This unavoidably results in high-angle imaging errors.

The Fermat spatial map approach by Connolly [4] is an attractive alternative, although the idea of constructing a map of the whole region, while useful for his purpose of examining a generally inhomogeneous region, would be extraordinarily inefficient for the present task of dealing with a single, or multi-layered, interface: in a two-dimensional simulation it would require at least $N_{el} \times N_x \times N_y$ maps, where N_{el} is the number of transmitting array elements and $N_{x,y}$ are the number of spatial x and y grid points in a region that encompasses the array, the interface, and the inspection region.

Next, the eikonal method is also computationally expensive, again requiring at least $N_{el} \times N_x \times N_y$ computations, with the same, large region of interest, and comparable computational time and memory, as with the Fermat map approach. Therefore, it is also considered here less efficient than the chosen method.

The approach this author has taken is use Fermat's principle to calculate the shortest travel time between two known locations – the source point and the imaged point, rather just the source point with a point-and-shoot method. This Fermat path method is considered by this author to be efficient and accurate, especially because the algorithm used employs range bisection of the interface wave incidence location. In this way, the intersection point, and therefore the incident and transmitted angles, are rapidly converged upon. This is applied here to a flat interface, but may readily be applied to a curved or rough interface through consideration of local surface normals and local minima in travel time. Further, two separate, but less efficient approaches, that precede this Fermat approach, are described in appendices 7.7.2 and 7.7.3.

7.3.6 Scattering matrices

The generation of scattering matrices, as conducted by Zhang, Wilcox, et al. [24], is used here. Specifically, their technique requires generation, storage, and use of very large scattering matrices with many elements in each dimension of the matrix. Such scattering matrices, applied to general use, contain a dimension with angles of

incidence, sub-divided into many angular steps; a dimension with angles of reception, sub-divided into many angular steps; a dimension, with a size of 2, for amplitude and phase, or otherwise, real and imaginary components, of the scattered wave; and a dimension with many frequency intervals, given that representation of the full frequency dependence of the wave improves accuracy. By contrast, the multiband finite element simulation and imaging (MBim) approach of this author, applied in the context of angled ultrasonic array inspection, requires generation, storage, and use of a data containing a few incident angles; a few received angles; a dimension with a size of 2, for real and imaginary components of the scattered wave; and a few frequency bands, using MBFE. This implies a major increase in efficiency for MBim over such techniques.

7.3.7 Source and monitor locations and separations

Scattering matrices, and their angular variations, are favourably obtained through the positioning of sources and monitors on a circular arc surrounding the simulated defect. Zhang, Velichko, et al. [10, 11] obtain their scattering matrices only for the transmit and receive angles within the aperture of the ultrasonic array that is being simulated in the given imaging configuration. This is also employed in MBim.
Further efficiency of this scattering matrix approach is achieved by minimising the number of angular steps, as is elsewhere explored by Simonetti [12] and Huthwaite [13]. They demonstrate that an array with half-wavelength element spacing is sufficient to prevent array imaging errors caused by undersampling. Relative to such sampling, used by Simonetti and Huthwaite, for MBim the required number of MBFE excitation locations in the simulation is significantly reduced, by ensuring that the half-wavelength sampling criterion is adhered to on the surface of a minimal-radius sphere in contact with the simulated defect, rather than the sampling criterion being adhered to, more distantly, at the radius of the sources and monitors from the defect.

7.4 Implementation and advancement of theory

First, an overview of MBim waveform simulation approach is provided, through the hybridisation of analytical and MBFE methods. Next, the addition of Gaussian

white noise to the waveforms is detailed. After, the detail of the MBFE implementation for the angled array inspection geometry is given. Then, the scattering matrix approach is optimised for an array aperture with angular limits. The MBFE monitor spacing is specified, to achieve high computational efficiency. The FE geometry for the volumetric and planar defects is described. The Fermat path range bisection method is detailed. The addition to waveform simulation of reflected wave paths and the use of virtual arrays is described.
Then, the MBim imaging approach is given. First, the attenuation correction method is described. Next, transmission and reflection losses, and the correction for them, is detailed. Refraction correction is applied for each media interface interaction. The diffraction of the finite width array elements is corrected for. The simulated waveforms containing reflected paths are summed in example image cases. Image enhancement with resolution upsampling is detailed. A method for improved defect sizing for limited view array inspection is given.

7.4.1 Waveform simulation

Here is provided an overview of the method for simulating waves with MBim, using the example setup in figure 7.1. Each waveform, transmitted and received from each array element, is analytically propagated to and from the MBFE monitors, with associated scattering transfer functions obtained from MBFE simulations between those transmit and receive legs of the propagation path.
For convenience of illustration, this author considers multiple defects through the thickness of the pipe wall, but form the images of these separately. In fact in practice it would be legitimate to consider defects in close proximity as separate and independent, because any secondary scattering is very weak and unlikely to influence the images in such an attenuating material.

Addition of noise in waveform simulation

In highly attenuating media, such as HDPE, amplitudes of received signals are very low, and therefore so is the signal-to-noise ratio (SNR) in such signals. The received SNR is dependent on the inspection system and technique, therefore it is suitable to chose an appropriate artificial noise level for simulations. Gaussian white noise is added to all simulated waveforms at -20dB; this considered by this author to be a

conservatively high level of noise is added to each waveform, upon reception at the array element, to demonstrate the resilience of the imaging system of this author to such signal degradation.

Finite element source lines and simulation region

Figure 7.3 shows examples of the MBFE simulation geometries used in MBim, for a range of wave incidence angles. The plane waves incident on the defect are radially directed towards the defect centre. The simulated region is bounded by a large

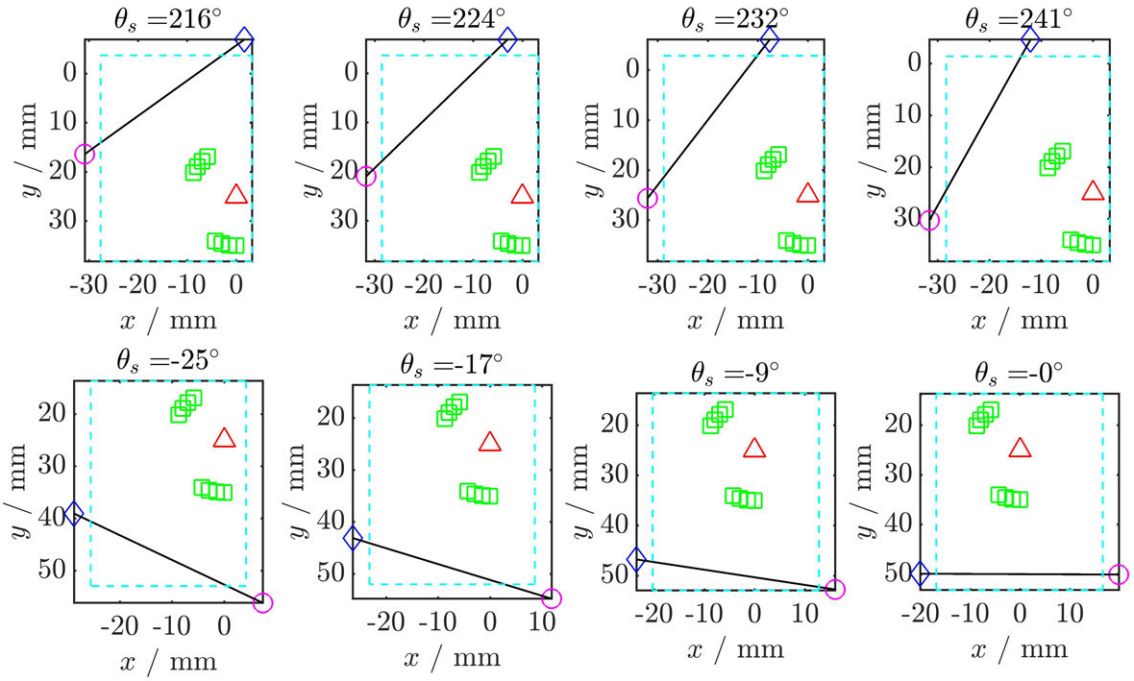

Figure 7.3: Example MBFE simulation geometries used in MBim. The dashed boxes are the boundaries of the absorbing regions. The solid lines with circles and diamonds at their anticlockwise and clockwise ends are the plane wave source lines, with incidence angles θ_s. The triangles are the defect centres. The squares are the monitor locations.

absorptive region that has decreasing stiffness towards the boundary, known as the stiffness reduction method (SRM) [29]. This highly attenuates waves propagating in this region such that boundary reflections are minimal and the resulting wave is not complicated by undesired signals. The SRM was primarily designed for use with elastic materials. In such cases, the damping of the SRM decreases to zero towards the modelled region. This author has adjusted the implementation of the SRM to decrease damping towards the viscoelastic damping of HDPE at the inner edges of the SRM. This ensure damping continuity at the boundary.

The tips of the source line that generates the plane wave are in the absorbing region

to prevent cylindrical waves emanating from them. The radial distance between the source line centres and defect centres is set such that there exists minimal spurious wave content within the ranges of time that the incident and scattered waves pass the monitors. The HDPE pipe outer wall is at $y = 0$ and, being situated within the HDPE pipe material, all monitors have $y > 0$. A range of incident angles are used to fully characterise the defect wave scattering within the feasible angular range. A scattering transfer function at every monitoring angle is obtained for each plane wave transmission angle.

The chosen FE mesh comprises structured triangular plane strain elements. The mesh is describable as fine [30] with element size,

$$\mathrm{d}x \leq \frac{\lambda_0}{20}; \tag{7.4.1}$$

the chosen mesh resolution is

$$\mathrm{d}x = \frac{\lambda_0}{40}. \tag{7.4.2}$$

The CFL condition [31] for numerical method stability is adhered to with time step,

$$\mathrm{d}t = \frac{3}{400 f_0}. \tag{7.4.3}$$

Next, the chosen FE software, Pogo FEA [32], is highly computationally efficient because is uses graphics processors (GPUs) for its time domain calculations. Also, each simulated angle, exemplified in figure 7.3, requires only five million degrees of freedom in these two dimensional simulations.

Finite element wave incidence angles limits

The extremal ultrasonic array element locations define its aperture, as seen in figure 7.1. The angle between straight lines from one extremal location to the defect centre and from the other extremal location to the defect centre is known as the aperture angle. Because ultrasonic waves are only transmitted and received within these

aperture windows, with MBim they are also only simulated with incidence angles within the aperture angular range. As well as this, waves are only monitored on a circular arc centred on the defect centre, within this aperture angular range, with MBim.

Finite element monitor spacing on circular arcs

As seen in figures 7.1 and 7.3, the MBFE incidence angles and monitors are placed on circular arcs and are regularly spaced. This is detailed in figure 7.4. For maximum

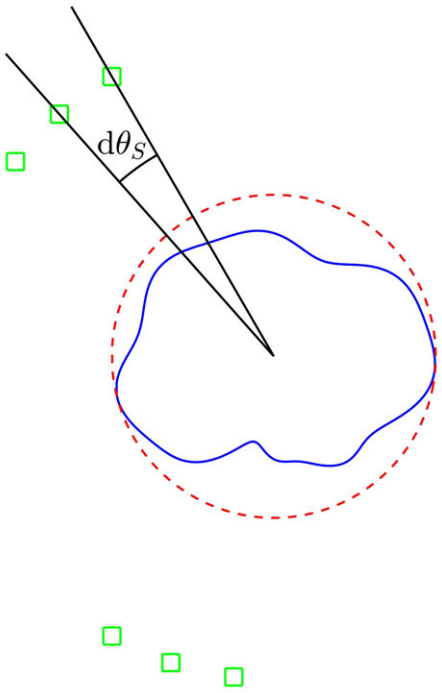

Figure 7.4: Aribtrary defect geometry enclosed by circle of smallest radius, r_d, which is the dashed line. The squares mark the locations where scattered plane waves are monitored. Each different incident wave in MBim is directed through one such square. The angular spacing between adjacent monitors is $d\theta_S$.

efficiency with necessary and sufficient accuracy, there exists an optimal maximum spacing of different incidence angles, $d\theta_S$, to simulate, with a corresponding minimum number of plane waves that avoids undersampling. Because the incident plane waves are radially directed towards the defect centre, and because of the associated radial convergence of the wave, the spatial sampling criterion is most correctly defined at the location of wave incidence on the defect.

The detail of the method for obtaining improved angular sampling of the MBFE monitors is now given. For a general angle of incidence of a radially directed plane

wave, the wave is incident on the defect at a location furthest from the defect centre if the point on the defect surface that is on the radial line of wave incidence is at one of the two points on the defect surface that is furthest from its centre. This is seen in figure 7.4, where the parts of the arbitrary defect furthest from its centre are coincident with the enclosing circle, at those points, which are left and right of the defect in the figure. Though, in the illustrated case, none of the six wave paths from source to defect centre intersect either of the two extremal points on the defect. Therefore, for other angles of incidences, this circle, of radius, r_d, is conservatively large, because the radially directed plane wave is incident on the defect after it crosses this circle.

The optimum angular sampling rate of the square monitors of figure 7.4, which is used in MBim, will here be defined. Over a given aperture angle, θ_A, the number of source locations is

$$N_S = \left\lceil \frac{\theta_A}{\mathrm{d}\theta_S} \right\rceil, \tag{7.4.4}$$

where the angular spacing between source and monitor locations is,

$$\mathrm{d}\theta_S = \frac{\lambda_0}{2N_A r_d}, \tag{7.4.5}$$

for which $\lambda_0 = \lambda(f_0)$ is the wavelength at centre frequency and the number of aperture points, N_A.

Because the monitors are chosen to be radially further from the defect centre than this circle, as seen in figure 7.4, they have a correspondingly reduced spatial sampling rate for the same angular sampling rate – the reciprocal of $\mathrm{d}\theta_S$. Consequently, the circle of radius r_d is conservatively large as the location at which to define the spatial sampling criterion, and is therefore chosen for such in MBim.

Scattering from volumetric and planar defects

In the application of MBim to the simulation and imaging of waveforms in HDPE pipe joints, both cylindrical volumetric and planar defects are analysed. As seen in figure 7.5, the volumetric defects are created in the FE mesh through partitioning and deletion in the region of the defect. The planar defects are represented through

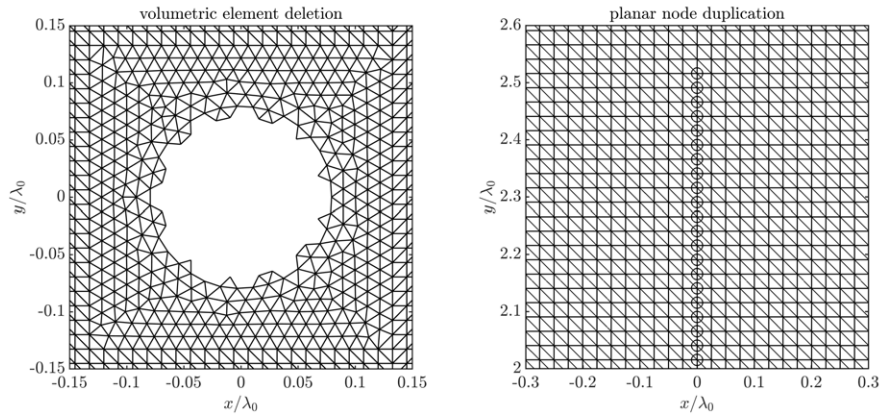

Figure 7.5: Elements are triangles. Left: volumetric element deletion. Right: planar node duplication, where duplicate nodes are circles and only the top tip of the planar defect is shown.

duplication of the selected defect nodes, found at the vertices of finite elements, leaving a line of disconnected nodes.

Refraction angles from Fermat path range bisection

A flat interface between two media of different acoustic velocities is seen at $y = 0$ in figure 7.1. This interface has associated refracted wave paths that are efficiently calculated using Fermat's principle of least travel time in combination with range bisection of the interface wave incidence location. This Fermat path range bisection is depicted in figure 7.6. Fermat's principle implies here that the path, and associated refraction angles, of a wave propagating between such media is that with the least total wave propagation duration. This is efficiently found, using range bisection of the interface wave incidence location, by appropriately selecting minimum and maximum potential wave incident angles and corresponding incidence locations, then finding the minimum propagation duration of those two paths, the left dashed line, ①, and the dot-dashed line, ②, in figure 7.6, and next finding the average incidence location of the two, the right dashed line, ③, and last finding the minimum propagation duration of a path through the average incidence location and that with the previous minimum propagation duration, which is found from the paths $s_{1,2}$ and phase velocities $v_{p,1,2}$, the dotted line, ④. These steps repeat as an iterative loop that rapidly converges on the expected incidence locations and corresponding propagation durations. The high efficiency of the above process is beneficial because it is repeated for every grid point within the imaged region and for every monitor location. The method of this author therefore may require, for example, a duration

of the order of a few seconds to generate of the order of a few million Fermat paths.

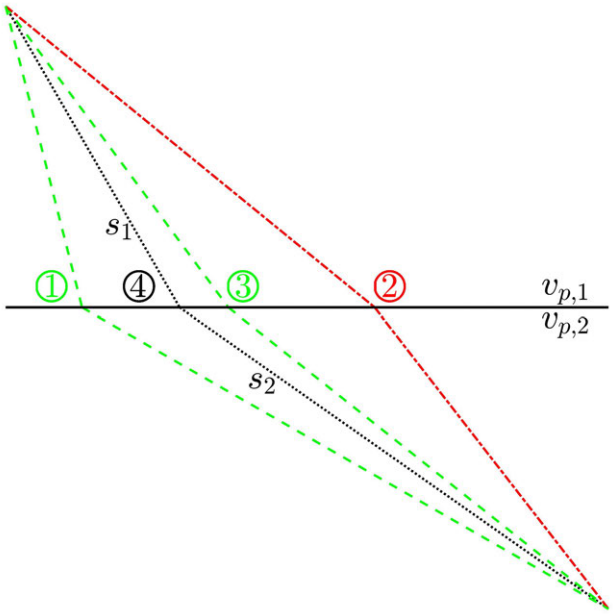

Figure 7.6: Fermat path range bisection. The dotted line, ④, is the target path, $s_1 + s_2$, which has minimum wave propagation duration. This is targeted initially, respectively, by the left dashed line, ①, and the dot-dashed line, ②. Midway between these paths, along the horizontal interface, is a point that the right green dashed line, ③, intersects. In this iteration, the dot-dashed line, ②, is rejected as it has a larger propagation duration than the left dashed line, ①. Repeating this process rapidly converges on the target path.

Reflected paths and virtual arrays

Figure 7.3 shows defect monitors both above (less depth, y, though the pipe wall) and below (greater depth, y, though the pipe wall) the defect. The monitors that are below the defect are found with the aperture angular range of a virtual array that has position that is, to the actual array, symmetric about the HDPE pipe inner wall, which may be located with $y > 0$ and $\mathrm{d}y/\mathrm{d}x = 0$.

The use of an actual and virtual array allows simulation of waves that directly scatter from the defect and are then received at the actual array, but also waves that reflect from the pipe inner wall before, after, or before and after scattering from the defect. These last three cases can be referred to respectively as 'half skip up', 'half skip down', and 'full skip'. All above paths are simulated and imaged with MBim.

The angular transmission and reflection coefficients for the water-HDPE interface and the inner pipe wall used in MBim can be readily determined from, for example, [25] and [26].

7.4.2 Imaging

The imaging algorithm used here with MBim defect scattering, and analytical inner pipe wall reflection, is derived from the TFM described in section 7.2, and features multiple augmentations for the improved ultrasonic array imaging of HDPE pipe joint defects. All the below techniques can be applied both to ultrasonic array waveforms simulated with MBim and waveforms obtained using an ultrasonic array in real NDE applications.

Attenuation correction

The attenuation that the propagated waves have undergone, as in equation (7.3.2), is corrected using the path length in each medium on a point-by-point basis in the imaged region, or otherwise corrected using distance amplitude correction (DAC) using only the depth through the pipe wall, y, of each imaged point.

Transmission and reflection losses correction

Corrections for transmission and reflection losses are implemented for each waveform based on those losses that it experiences on its path through both media, as described in section 7.4.1.

Media interface refraction correction

As described in section 7.4.1, propagation paths to locations in the imaged region have corresponding propagation durations, which can be found using Fermat's principle. Without knowledge of these refracted propagation durations and paths, the defect signature would have a locational offset error and would be less localised, resulting in a reduction in reduced defect detection reliability, and poorer resolution and SNR. These are three major figure of merits for defect detection; with these refracted propagation durations and paths the defect can be reliably and accurately imaged, and located on the fusion face, for HDPE pipe joints.

Array element diffraction correction through a refractive interface

The finite width of ultrasonic array elements results in a diffraction pattern known as directivity. The effective array location in the medium containing these sources,

here water, is determined for the target depth of the inspection region by projecting straight lines back from this location, through the media interface, and into the source medium. Using the effective array dimensions and location, an effective directivity is obtained. This is used to apply array element diffraction correction through the refractive media interface.

Reflected paths

The direct scatter and half- and full-skip paths detailed in section 7.4.1 are all imaged with MBim. They can be viewed independently or through the summation of the individual images. Certain defect types have strong skip defect signatures relative to the direct scatter, and so the choice of individual or summed images can be advantageous.

Image enhancement

The base imaging resolution used is $\mathrm{d}x_i = 0.15\text{mm}$. Further, MBim images feature upsampled resolution. This is achieved by adding, to the two-dimensional spatial Fourier transform of the image, zero bin values to spatial frequencies with higher magnitudes than existed in the original two-dimensional spatial Fourier transform of the image. Image upsampling is here beneficial because such interpolation allows for a more accurate and precise full-width-half-maximum of the maximum amplitude of the Hilbert transform of the image, as described in [5]. This is here used for defect sizing.

Pseudo-two-sided inspection

MBim is here exemplified with a limited-view, single-sided array inspection, where access is only possible to one side of the HDPE pipe fusion joint. Two-sided inspection – two external arrays, one either side of the pipe joint – provides more joint coverage and a larger inspection angle. In such cases where this is not possible, MBim provides pseudo-two-sided inspection. By assuming symmetry about the fusion face, $x = 0$, the summation of a mirrored image to the origin image is used to make possible automated defect location and sizing where it would otherwise be significantly more difficult.

7.5 Results and analysis

MBim simulated defect images are presented and analysed here, for both cylindrical voids and planar defects, in large-walled HDPE pipe joints, 100mm thick – one medium-walled, 56mm thick, example is also provided for comparison. These defects are located at shallow and deep locations within the fusion joint, respectively 1/4 and 3/4 of pipe wall thickness. Imaging methods for visual defect detection, location, sizing, and characterisation are proposed in the following subsections and analysed, as well as methods for automated defect detection, location, and sizing. All defect images shown and used here are based on the methodology detailed in section 7.4, unless otherwise stated.

7.5.1 Defect detectability using signal-to-noise ratio (SNR)

SNR informs defect detectability. Figure 7.7 shows a MBim simulated image of a planar defect, of minimum enclosing radius, $r_d = 2.0\lambda$, located, y_d, at 1/4 through the thickness, y_Δ, of the 100mm HDPE pipe joint. The MBFE monitors of figure 7.1 are shown for direct and reflected paths to the defect, while, in this image, reflected signals are not included, $I_{skip} =$ no.

Figure 7.8 shows a cylindrical void simulated with $n_{band} = 1$. Even for deep defects where lateral resolution is inherently low, and for small defect radius, $r_d = 0.5\lambda$, a simulation with $n_{band} = 1$, which demonstrates the frequency-independent phase velocity approximation of TDFE, is capable of producing a well-localised defect signature. This is because HDPE phase velocity only varies with frequency to the power 0.2 [4], and therefore the frequency-independent approximation (order 0) is expected to be similar, as demonstrated here. However, SNR will be shown below to be simulated with significant inaccuracy for deeper defects with $n_{band} = 1$, as with TDFE simulations, for HDPE pipe joints, because attenuation varies with frequency to the power 1.2 [4].

MBim has first been demonstrated by representing planar and cylindrical defects in HDPE pipe joints. The advantage here of simulating and imaging with MBFE, $n_{band} = 3$, over TDFE, $n_{band} = 1$, is the increased accuracy in SNR, through increased accuracy in amplitude with unchanged noise accuracy, because of increased accuracy in attenuation [5], that the former uniquely provides.

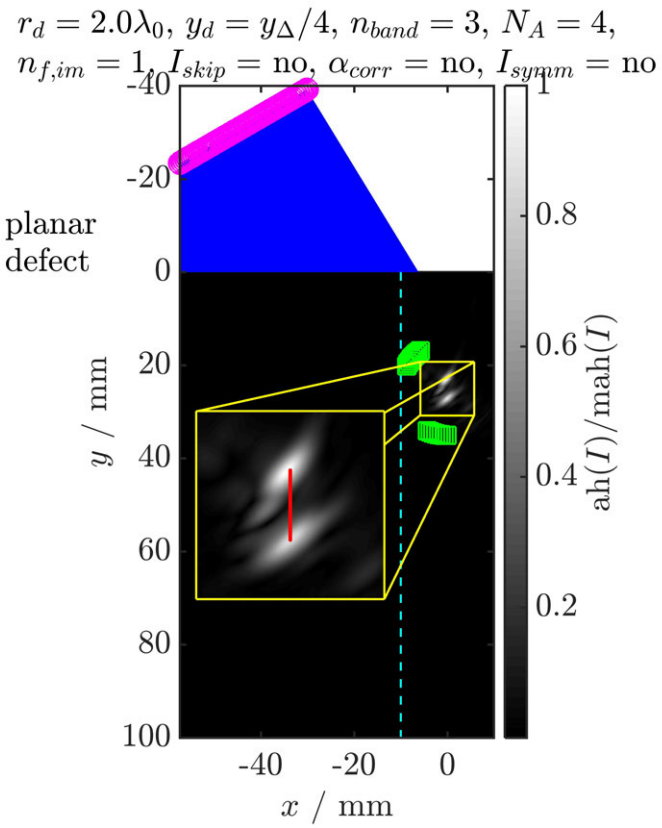

Figure 7.7: MBim planar defect. The imaged region is to the right of the dashed line. The defect, of minimum enclosing radius, $r_d = 2.0\lambda$, is located at $y_d = y_\Delta/4$ in the 100mm HDPE pipe joint and is also shown in the boxed, zoomed image. The line at the centre of the zoomed defect image represents the defect geometry. The absolute of the Hilbert transform of the summed wave, ah(I), is normalised by its maximum in the x-y plane, mah(I) to form the defect image. Reflected signals that scatter from the defect are not included, I_{skip} = no; attenuation correction is not used α_{corr} = no; and symmetry about the fusion face, $x = 0$, is not used, I_{symm} = no.

7.5.2 Defect location and maximum radius using symmetry assumption and gated zone partitioning

Included in figure 7.9 are the summation of reflected (skip) signals into the image, depth-dependent attenuation correction, and image symmetry that is assumed about the HDPE pipe fusion face, $x = 0$. Later, the effect of each of these, in turn, on defect detection, location, sizing, and characterisation is detailed and analysed. In figure 7.9, at the top-left of the circle in the zoomed defect image is the component of MBim image that exists before I_{skip}, α_{corr}, and I_{symm} post-processing techniques are applied. With this alone, defect location and sizing would be a significant challenge. At the bottom of the defect circle is the I_{skip} component. The top-right of the circle features the mirrored (about $x = 0$) image of the original image. Image components originally to the right of $x = 0$ are here also mirrored to the left of $x = 0$, such as

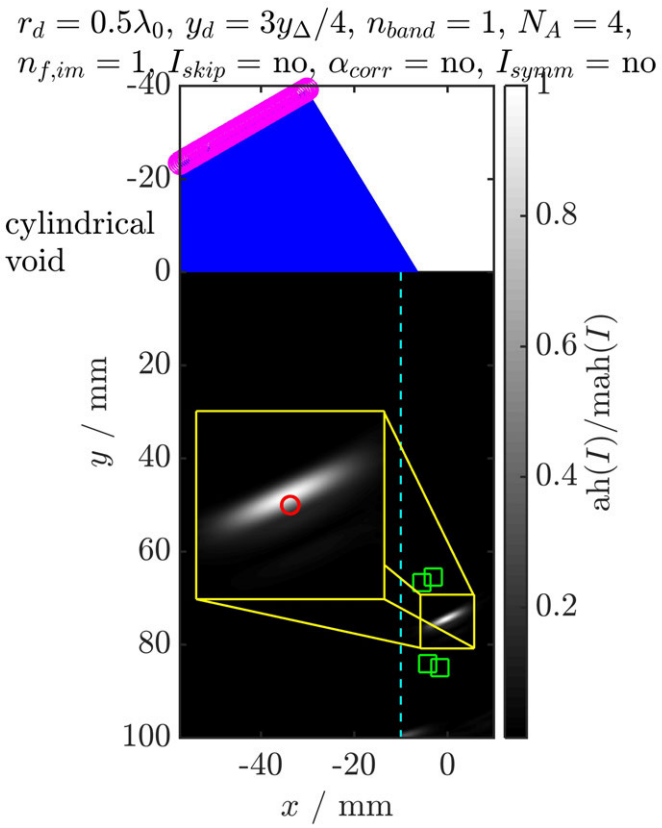

Figure 7.8: MBim cylindrical void. The imaged region is to the right of the dashed line. The defect, of radius, $r_d = 0.5\lambda$, is located at $y_d = 3y_\Delta/4$ in the 100mm HDPE pipe joint and is also shown in the boxed, zoomed image. The circle at the centre of the zoomed defect image represents the defect geometry. The absolute of the Hilbert transform of the summed wave, ah(I), is normalised by its maximum in the x-y plane, mah(I) to form the defect image. Reflected signals that scatter from the defect are not included, I_{skip} = no; attenuation correction is not used α_{corr} = no; and symmetry about the fusion face, $x = 0$, is not used, I_{symm}=no.

left is to right. Upon inclusion of the skip waves and mirrored waves it becomes possible to size the defect, depicted by the red circle, accurately by sight. Despite this, HDPE pipe joint defects could have a greater extent one or other side of the fusion face, therefore sizing by this method must be conducted with awareness of the assumption of symmetry.

Figure 7.10 shows a MBim defect the same as in figure 7.9, except for the thinner pipe wall, which is here 56mm. Here the skip waves have a greater relative contribution to the image than when the pipe inner wall was 100mm from the outer wall, in figure 7.9. Similarly, attenuation correction here increases the amplitude of the defect image and background noise less than for waves propagating to and from the 100mm back wall of figure 7.9. The influence of attenuation correction on defect location and sizing capability is quantified below.

Through the example of a cylindrical void, MBim representation of defect images,

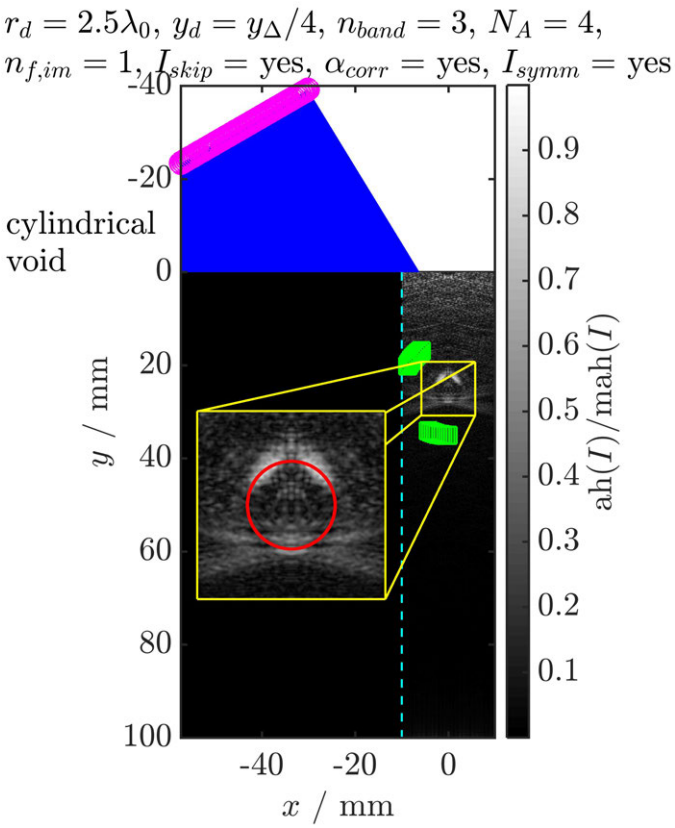

Figure 7.9: MBim cylindrical void. The imaged region is to the right of the dashed line. The defect, of radius, $r_d = 2.5\lambda$, is located at $y_d = y_\Delta/4$ in the 100mm HDPE pipe joint and is also shown in the boxed, zoomed image. The circle at the centre of the zoomed defect image represents the defect geometry. The absolute of the Hilbert transform of the summed wave, ah(I), is normalised by its maximum in the x-y plane, mah(I) to form the defect image. Reflected signals that scatter from the defect are added in the image, I_{skip} = yes; depth-dependent attenuation correction is used α_{corr} = yes; and assumed symmetry about the fusion face, $x = 0$, is used to mirror each side of the image to the other, I_{symm} = yes.

including the summation of reflected skip waves and assumed symmetry about the HDPE pipe joint fusion face have here been shown to significantly facilitate defect location and sizing when visually inspecting the images.

MBim images of a planar defect are shown in figure 7.11 that feature novel visual and automated defect location and sizing. The top image is a MBim defect image, such as have been shown previously. The left image additionally features removal of image content where the wave amplitude is low, using gating, both before and after the addition of low-level Gaussian white noise to the image, to create a dither effect that appears to visually increase greyscale bit depth, which may be considered useful for visual inspection of defect images. The gate levels and dither noise levels are globally chosen to provide high accuracy in automated location and automated sizing for the 480 defect images used in this study. However, these parameters may

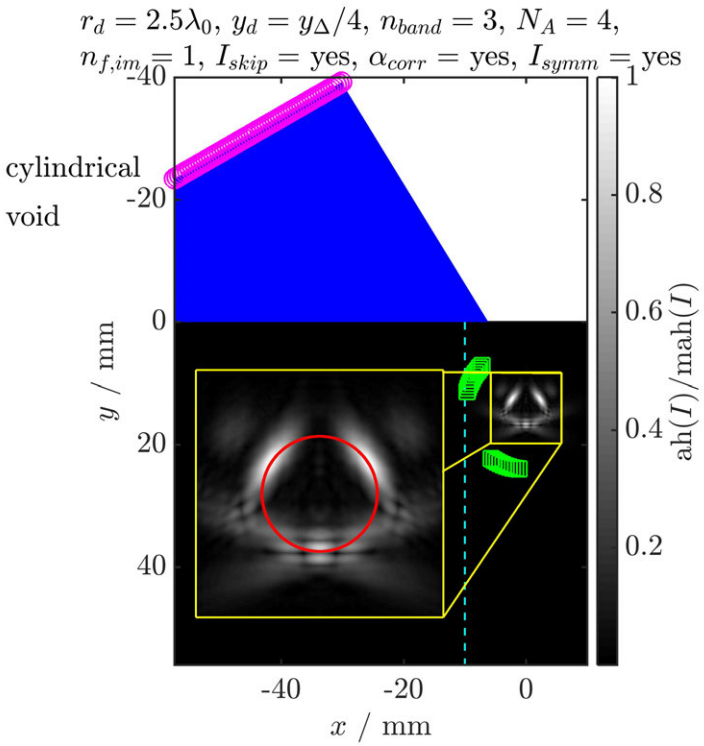

Figure 7.10: MBim cylindrical void. The imaged region is to the right of the dashed line. The defect, of radius, $r_d = 2.5\lambda$, is located at $y_d = y_\Delta/4$ in the 56mm HDPE pipe joint and is also shown in the boxed, zoomed image. The circle at the centre of the zoomed defect image represents the defect geometry. The absolute of the Hilbert transform of the summed wave, ah(I), is normalised by its maximum in the x-y plane, mah(I) to form the defect image. Reflected signals that scatter from the defect are added in the image, I_{skip} = yes; depth-dependent attenuation correction is used α_{corr} = yes; and assumed symmetry about the fusion face, $x = 0$, is used to mirror each side of the image to the other, I_{symm} = yes.

be further optimised with more data. The perimeter points of the gated defect image, without further dither and gating, is used to find distant pairs of points. When a maximum separation, s_{max}, is converged upon, the expected defect extent is set, and also therefore its location, at the centre of the circle that passes through the point pair.

MBim defect representation for visual sentencing, as well as for automated location and automated sizing of defects, has here been demonstrated.

Last, concerning defect characterisation, figures 7.7 to 7.11 show the potential for much increased capability in distinguishing between volumetric and planar defect types, both visually, and potentially also automatically. For visual or automated sentencing with the above defect images, dependence lies on the demonstrated capability in defect sizing and location.

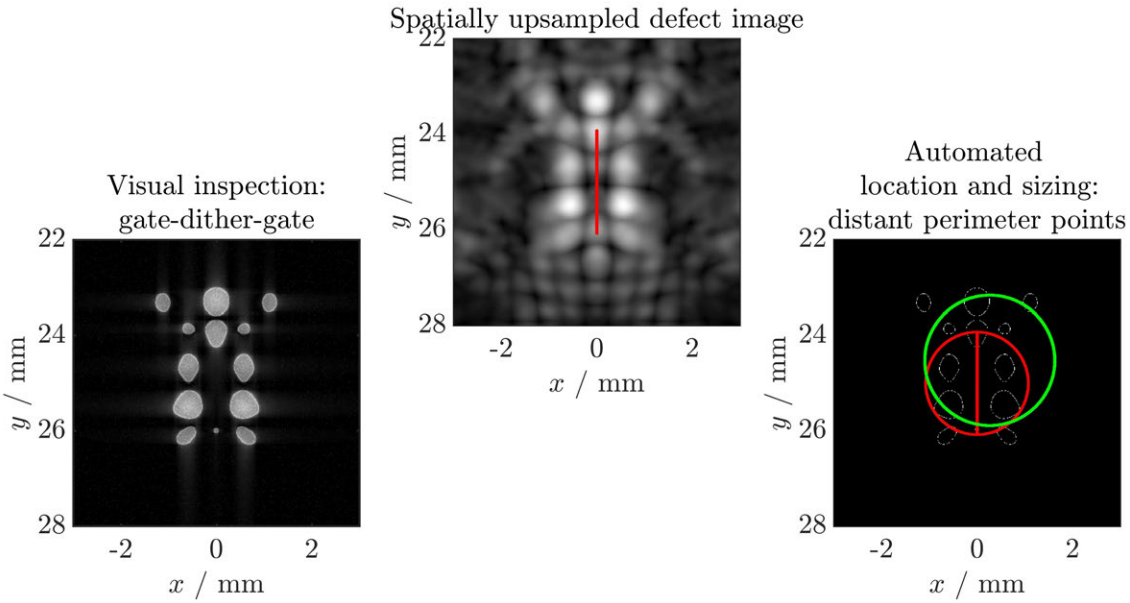

Figure 7.11: Top: MBim image of a planar defect with I_{skip} = yes, α_{corr} = yes, and I_{symm} = yes. Left: A MBim image of the planar defect with amplitude gating before and after Gaussian white noise dithering. Right: automated defect location and sizing using the perimeter of the gated planar defect with distant perimeter points, where the vertical line is the planar defect geometry, the circle bounding it is the simulated defect circle with radius, r_d, and the larger circle marks the automated location and automated size predicted from the defect image.

7.5.3 Discussion

Here is discussed the SNRs from the MBim simulated defect images, and averages of SNRs of certain datasets of images. Shown in figure 7.12, is the ratio of the root mean square of defect signal strength to the root mean square of imaged noise signal strength, the SNR, for cylindrical voids of different defect radii, r_d, and numbers of aperture points, N_A. The similarity of SNRs for $N_A = 2$ and 4 suggests near convergence for that many aperture points, found in equation (7.4.4). Defect radius, r_d, is seen here to have little effect on SNR of cylindrical voids at $y_d = 3y_\Delta/4$, therefore a robust measure of defect detectability could be useful if this trend were further investigated.

Shown in figure 7.13 are the defect signal-to-noise ratio, SNR, means and medians over all defect radii, r_d, and numbers of aperture points, N_A. A-Π first loop through $y_d = y_\Delta/4$ and $3y_\Delta/4$, then from cylindrical void to planar, then both not using and using attenuation correction, next I_{skip} = no and yes, and lastly I_{symm} = no and yes. The mean and median SNRs of A,C,..., the shallower defects, are not significantly different to those of B,D,..., the deeper defects; an optimum array position and wedge angle, as seen in figure 7.1, ensures that the whole inspection region is

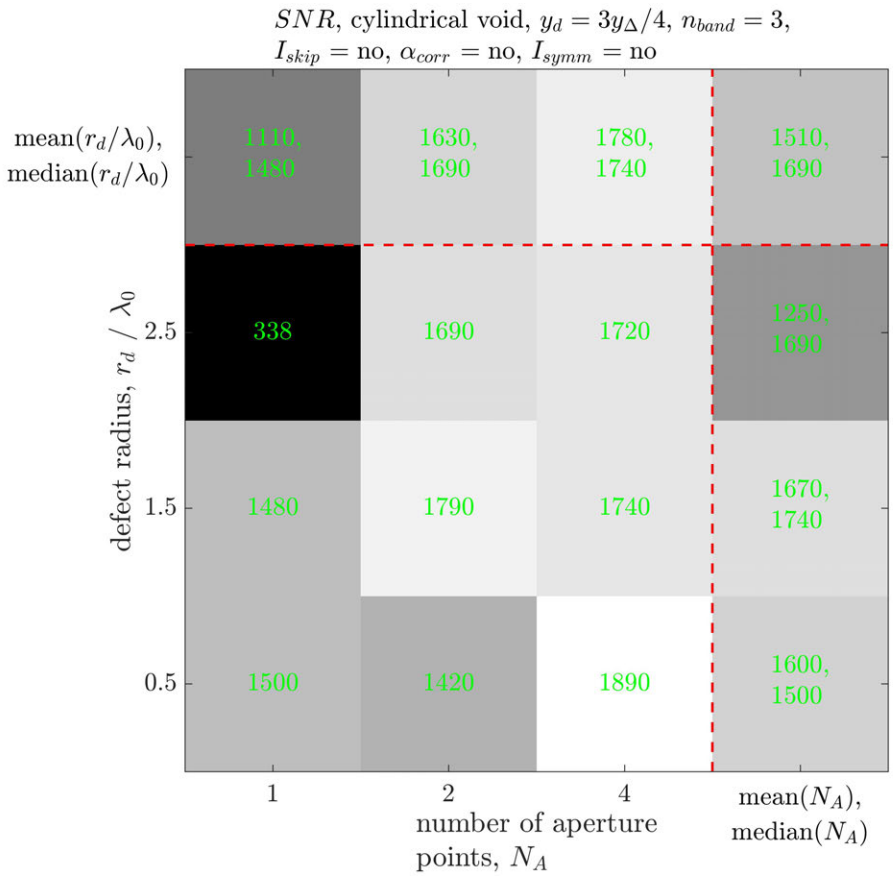

Figure 7.12: SNR variation, $n_{band} = 3$, with defect radius, r_d, and number of aperture points, N_A, for cylindrical voids at a depth of $y_d = 3y_\Delta/4$ in 100mm wall HDPE pipe joints. Means and medians are provided for each row and column, as well as for all tabulated SNRs. Greyscale box shading equates to means in boxes.

well insonified and that regions with higher attenuation – the deeper defects – are at shallower refraction angles, and therefore also well insonified. The cylindrical voids, A,B,E,F,..., are suggested here to be similarly detectable to the planar defects, C,D,G,H,..., where also, the average r_d of both defect types is similar. The defect images with attenuation correction, A-D,I-L,..., have higher SNRs than those with attenuation correction, E-H,M-P,..., because the selection of a noise region, at a certain depth that is different to the signal region will have different relative attenuation corrections applied to them. The defect images without reflected skip signals added to the defect region, A-H and Q-X, have lower SNRs than those without, I-P and Y-Π, because there is partial destructive superposition of the waves when the skip signals are added. The defect images without the addition of an image mirrored about the fusion face, A-P, have similar SNRs to those with such mirroring, Q-Π, because linear summation of two regions with equal SNR does not inherently alter SNR. Defect SNR means and medians for TDFE, $n_{band} = 1$, can

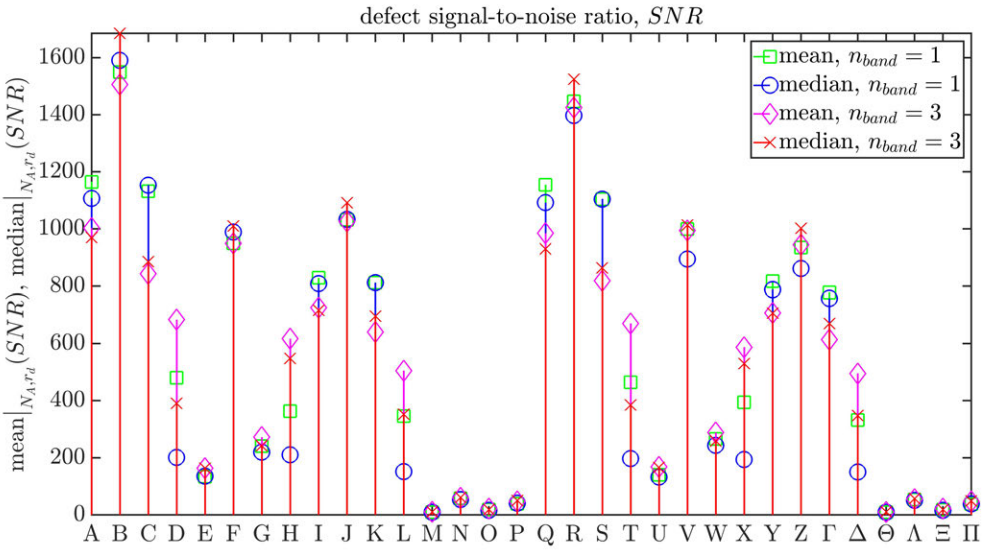

Figure 7.13: Defect SNR means and medians over all defect radii, r_d, and numbers of aperture points, N_A. A-Π first loop through $y_d = y_\Delta/4$ and $3y_\Delta/4$, then from cylindrical void to planar, then both not using and using attenuation correction, next I_{skip} = no and yes, and lastly I_{symm} = no and yes.

range from approximately 70% less to 30% more than those of MBFE, $n_{band} = 3$, where attenuation, and therefore SNR, is of high accuracy.

Shown in figure 7.14 are the means and medians over all defect radii, r_d, and numbers

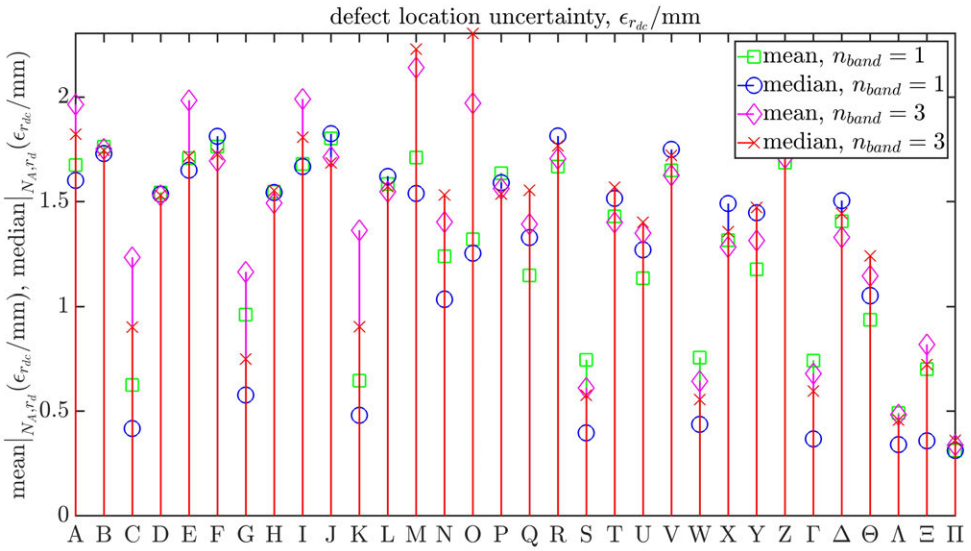

Figure 7.14: Defect location uncertainty, $\epsilon_{r_{dc}}$, means and medians over all defect radii, r_d, and numbers of aperture points, N_A. A-Π first loop through $y_d = y_\Delta/4$ and $3y_\Delta/4$, then from cylindrical void to planar, then both not using and using attenuation correction, next I_{skip} = no and yes, and lastly I_{symm} = no and yes.

of aperture points, N_A, of the defect automated location uncertainty,

$$\epsilon_{r_{dc}}/\text{mm} = \sqrt{(x_{dc} - x_{max})^2 + (y_{dc} - y_{max})^2}, \tag{7.5.1}$$

where subscript 'dc' is defect centre and subscript 'max' denotes locations, separations, and sizes obtained from distant perimeter points, shown in figure 7.14. All automated location uncertainty means and medians are relatively low for 100mm thick HDPE pipes, ranging from approximately 0.5 to 2mm. Sizing between deep and shallow defects is of similar accuracy. The same is true of cylindrical voids and planar defects. Attenuation correction does not conclusively alter defect automated location uncertainty. Without imaging symmetry, adding skip signals is not seen to improve defect automated location uncertainty, while with symmetry, adding these reflected paths to the defect image does reduce this uncertainty. MBim imaging with symmetry overall is seen to improve defect automated location uncertainty. Shown in figure 7.15 are the means and medians over all defect radii, r_d, and numbers

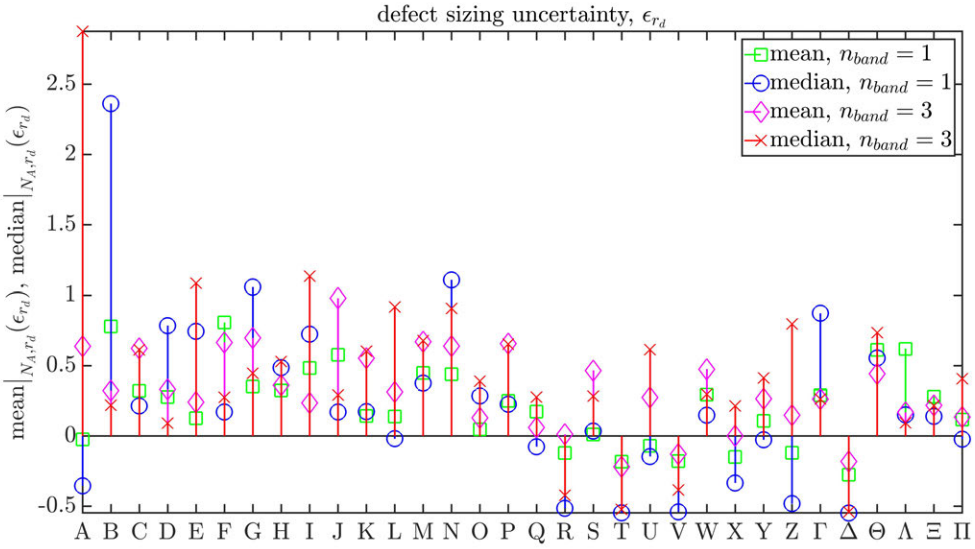

Figure 7.15: Defect sizing uncertainty, ϵ_{r_d}, means and medians over all defect radii, r_d, and numbers of aperture points, N_A. A-Π first loop through $y_d = y_\Delta/4$ and $3y_\Delta/4$, then from cylindrical void to planar, then both not using and using attenuation correction, next I_{skip} = no and yes, and lastly I_{symm} = no and yes.

of aperture points, N_A, of the defect automated sizing uncertainty,

$$\epsilon_{r_d} = \frac{2r_d - s_{max}}{2r_d}. \tag{7.5.2}$$

Automated sizing uncertainty means and medians are generally of the order of less than 50%, while some are up to 100%, and two are larger still. The defect sizing is dependent on the signal amplitude at which the defect perimeter is defined. This would be further optimised using a large library of MBim simulated defect images for the specified inspection conditions.

7.6 Conclusions

The analytical multiband finite element simulation and imaging (MBim) system is demonstrated with nondestructive evaluation of high-density polyethylene (HDPE) pipe joints where compressional waves are sent from water into viscoelastic HDPE pipe material.

MBim waveform simulation is shown to well represent such ultrasonic inspection with accurate ultrasonic scattering, refraction, and reflection. This was not previously possible.

MBim defect imaging is exemplified for both visual and automated sentencing with ultrasonic images; methods for defect detection, location, sizing, and characterisation by visual sentencing are provided, as are methods for defect detection, location, and sizing by automated sentencing. In all, high accuracy is achieved.

References

[1] R.E. Challis, F. Blarel, M.E. Unwin, J. Paul, and X. Guo, *Models of ultrasonic wave propagation in epoxy materials*, Ultrasonics, Ferroelectrics, and Frequency Control, IEEE Transactions on, **56**(6), June 2009.

[2] S. Holm and S.P. Nasholm, *Comparison of fractional wave equations for power law attenuation in ultrasound and elastography*, Ultrasound in Med. & Biol., **40**(4), April 2014.

[3] K.-J. Bathe, *Finite Element Procedures in Engineering Analysis*, Prentice-Hall, New Jersey, 887-1012, 1982.

[4] J.S. Egerton, M.J.S. Lowe, H.V. Halai, and P. Huthwaite, *Ultrasonic attenuation and phase velocity in high-density polyethylene (HDPE) pipe material*, J. Acoust. Soc. Am. **141**(3), 1535-1545 (2017). [Open Access available]

[5] J.S. Egerton, M.J.S. Lowe, H.V. Halai, and P. Huthwaite, *A multiband approach for accurate numerical simulation of frequency dependent ultrasonic wave propagation in the time domain*, J. Acoust. Soc. Am. **142**(3), 1270-1280 (2017). [Open Access available]

[6] P. Rajagopal, E.A. Skelton, W. Choi, M.J.S. Lowe, and R.V. Craster, *A Generic hybrid model for bulk elastodynamics, with application to ultrasonic nondestructive evaluation*, Ultrasonics, Ferroelectrics, and Frequency Control, IEEE Transactions on, **59**(6), 1239-1252 (2012).

[7] F. Shi, M.J.S. Lowe, E.A. Skelton, and R.V. *A time-domain finite element boundary integral approach for elastic wave scattering*, Comput Mech, 1-13 (2017).

[8] J. Zhang, B.W. Drinkwater, and P.D. Wilcox, *Defect characterization using an ultrasonic array to measure the scattering coefficient matrix*, Ultrasonics, Ferroelectrics, and Frequency Control, IEEE Transactions on, **55**(10), 2254-2265 (2008).

[9] P.D. Wilcox and A.Velichko, *Efficient frequency-domain finite element modeling of two-dimensional elastodynamic scattering*, J. Acoust. Soc. Am. **127**(1), 155-165 (2010).

[10] J. Zhang, B.W. Drinkwater, and P.D. Wilcox, *The use of ultrasonic arrays to characterize crack-like defects*, J. Nondestruct. Eval., **29**, 222232 (2010).

[11] A.Velichko, P.D. Wilcox, *Reversible Back-Propagation Imaging Algorithm for Postprocessing of Ultrasonic Array Data*, Ultrasonics, Ferroelectrics, and Frequency Control, IEEE Transactions on, **56**(11), 2492-2503 (2009).

[12] F. Simonetti, L. Huang, and N. Duric, *On the spatial sampling of wave fields with circular ring apertures*, Journal of Applied Physics, **101**, 1-6 (2007).

[13] P. Huthwaite, *Eliminating incident subtraction in diffraction tomography*, Proc. R. Soc. A *472*, 1-25 (2017).

[14] J.A. Ogilvy, *An iterative ray tracing model for ultrasonic nondestructive testing*, NDT&E International, **25**(1), 3-10 (1992).

[15] V. Schmitz, F. Walte, and S.V. Chakhlov, *3D ray tracing in austenite materials*, NDT&E International, **32**, 201213 (1999).

[16] R. Long, J. Russell, P. Cawley, and N. Habgood, *Ultrasonic phased array inspection of flaws on weld fusion faces using full matrix capture*, AIP Conference Proceedings **1096**, 848-855 (2009).

[17] G.D. Connolly, M.J.S. Lowe, J.A.G. Temple, S.I. Rokhlin, *Correction of ultrasonic array images to improve reflector sizing and location in inhomogeneous materials using a ray-tracing model*, J. Acoust. Soc. Am., **127**(5), 2802-2812, (2010).

[18] L.W. Schmerr, *Fundamentals of Ultrasonic Nondestructive Evaluation – A Modeling Approach*, New York: Prenum Press; 91-140, 1998.

[19] A. Lhémery, P. Calmon, R. Raillon, and L. Paradis, *New developments in ultrasonic NDT modeling in CIVA*, Review Progress in Quantitative Nondestructive Evaluation, **17**, 955-962 (1998).

[20] G.D. Connolly, M.J.S. Lowe, J.A.G. Temple, and S.I. Rokhlin, *The application of Fermat's principle for imaging anisotropic and inhomogeneous media with application to austenitic steel weld inspection*, Proc. R. Soc. A, **465**, 34013423 (2009).

[21] R. Kalaba, *Dynamic programming, Fermat's principle, and the eikonal equation*, J. Opt. Soc. Am. **51**, 1150-1151 (1960).

[22] S.H. Gray and W.P. May, *Kirchoff migration using eikonal equation traveltimes*, Geophysics, **59**(5), 810-817 (1994).

[23] P. Huthwaite and F. Simonetti, *High-resolution guided wave tomography*, Wave Motion, **50**, 979-993 (2013).

[24] J. Zhang, B.W. Drinkwater, P.D. Wilcox, and A.J. Hunter, *Defect detection using ultrasonic arrays: The multi-mode total focusing method*, NDT&E International **43**, 123-133 (2010).

[25] B.A. Auld, *Acoustic Fields and Waves in Solids, Volume II*, second ed., Robert E. Krieger Publishing Company, Inc., Florida, 1-61, 1990.

[26] S.I. Rokhlin, D.E. Chimenti, and P.B. Nagy, *Physical Ultrasonics in Composites*, Oxford University Press, Oxford, 3-368, 2011.

[27] J.O. Smith III, *Spectral Audio Signal Processing* (W3K Publishing, Lewiston, NY, USA), 57-63 (2011).

[28] J.S. Egerton, M.J.S. Lowe, and P. Huthwaite, *Automated and antidispersive coherent and incoherent noise reduction of waveforms that contain a reference signal*, The Journal of Sound and Vibration, [Under final review]. [Open Access to be made available]

[29] J.R. Pettit, A. Walker, P. Cawley, and M.J.S. Lowe, *A stiffness reduction method for efficient absorption of waves at boundaries for use in commercial finite element codes*, Ultrasonics, **54**(7), 1868-1879 (2014).

[30] M.B. Drozdz, *Efficient finite element modelling of ultrasound waves in elastic media*, Ph.D. Thesis, Imperial College London, 182-203 (2008).

[31] R. Courant, K. Friedrichs, and H. Lewy, *Über die partiellen Differenzengleichungen der mathematischen Physik*, Mathematische Annalen (in German), **100**(1), 3274 (1928).

[32] P. Huthwaite, *Accelerated finite element elastodynamic simulations using the GPU*, Journal of Computational Physics, **257**(A), 687-707 (2014).

7.7 Appendices

7.7.1 Derivation of single known location ray tracing uncertainty magnification

Snell's law with uncertainties in incident and transmitted wave angles, ϵ_{θ_1} and ϵ_{θ_2}, can be written,

$$\frac{\sin\left(\theta_1 + \epsilon_{\theta_1}\right)}{v_1} = \frac{\sin\left(\theta_2 + \epsilon_{\theta_2}\right)}{v_2}. \tag{7.7.1}$$

Because $\epsilon_{\theta_1} = 0 \Leftrightarrow \epsilon_{\theta_2} = 0$,

$$\theta_2 = \arcsin\left(\frac{v_2}{v_1}\sin\theta_1\right). \tag{7.7.2}$$

Combining equations (7.7.1) and (7.7.2) yields,

$$\epsilon_{\theta_1} = \arcsin\left\{\frac{v_1}{v_2}\sin\left[\arcsin\left(\frac{v_2}{v_1}\sin\theta_1\right) + \epsilon_{\theta_2}\right]\right\} - \theta_1, \tag{7.7.3}$$

as depicted in figure 7.1.

7.7.2 Snell's refraction angles using quartic or expanded solutions

For a two medium region of interest separated by a flat interface,

$$\frac{x}{v_1\sqrt{x^2+y_s^2}} = \frac{x_s - x}{v_2\sqrt{(x_s-x)^2+y_i^2}}, \tag{7.7.4}$$

where x and y are Cartesian coordinates within the region of interest, (x_s, y_s) is the source location, and (x_i, y_i) is the imaged location. This can be solved as a quartic polynomial or with a many-term expansion. These methods have solutions that are variously unstable or not unique, as well as being less computationally efficient than the chosen Fermat path method.

7.7.3 Snell's refraction angles by iteration

The incident angle, θ_1, can be iterated for using,

$$\theta_1 = \arccos\left(\frac{y_s}{y_i}\cdot\frac{\sin\phi_2}{\sin\phi_1}\cdot\cos\theta_2\right), \tag{7.7.5}$$

where θ_2 is defined in equation (7.7.2),
where

$$\phi_1 = \theta_2 - \theta_1 - \phi_2, \tag{7.7.6}$$

$$\phi_2 = \psi_1 - \theta_1, \tag{7.7.7}$$

and

$$\psi_1 = \arctan\left(\frac{x_i - x_s}{y_i - y_s}\right). \tag{7.7.8}$$

This iterative method is stable and convergent, but less computationally efficient than the chosen Fermat path method.

Chapter 8

Experimental array imaging

8.1 Abstract

Angled ultrasonic array imaging of vertically aligned side-drilled holes in a high-density polyethylene (HDPE) pipe test block using an experimental binary array controller is conducted, with moderate defect detection potential, high detected defect location potential, and moderate detected defect sizing and characterisation potential, for necessarily full through wall depth coverage. This is done with the multiband waveform simulation and imaging (MBim) method and pulse specification (PS) noise reduction method. The experimental binary coded sequence array controller and array setup used then had suboptimal lateral resolution and energy input capabilities, so higher defect sizing and characterisation capabilities could otherwise also be expected from these results.

8.2 Introduction

The aim of the EngD project for which this study is conducted is to improve the ultrasonic array inspection of high-density polyethylene (HDPE) heat-fused pipe joints of cooling water pipework that is installed in EDF Energy's nuclear power stations. While ultrasound array inspection is now established for safety-critical metal components, HDPE poses a hugely challenging problem, that the ultrasound waves are heavily attenuated by the material. This impacts multiple aspects of the inspection and of the modelling that is needed to design and qualify inspection. This is shown in this thesis, through improvements to the validation of such inspections using im-

proved and optimised simulation techniques. Also, imaging techniques have been developed and implemented that are useful both with simulated and real ultrasonic array waveforms.

Here the use of these imaging techniques is used, with an experimental binary coded sequence array controller [1] and array system developed at Imperial College London by Dr. Julio Isla and Dr. Fred Cegla, to demonstrate moderate defect detection potential, high detected defect location potential, and moderate detected defect sizing and characterisation potential, for necessarily full through wall depth coverage. This array controller and array setup is chosen because the array controller achieves high signal-to-noise ratio in highly attenuating media, such as HDPE pipe material. HDPE pipe joint inspection capability with an immersed angled ultrasonic array has also been demonstrated for diagonally aligned side-drilled holes at moderate angles of inspection and narrow pipe walls, also with an alternative, Hadamard, coded data acquisition [2, 3], but not with the refraction correction of the MBim method, the noise reduction of the PS method, and full through wall depth coverage, which will be demonstrated here.

8.3 Existing approaches

Described here are the existing approaches required for data acquisition and imaging.

8.3.1 Data acquisition

The ultrasonic array data acquisition hardware and technique is that of [1]. A full matrix of array element transmit and receive combinations is obtained through the correlation of the raw coded sequence data.

The experimental array controller and array setup was, at the stage of use, not yet optimal for HDPE pipe joint inspection. The array had only 16 elements, a pitch of $p = 0.328125$mm, and a consequent array active aperture of $A = 5.25$mm. While there exists a need, discussed respectively in chapters 7 and 9, for large aperture angles and small element pitches; the array aperture was small, $A = 5.25$mm, and therefore so was the array aperture angle. Consequently, the setup could not achieve moderate or high lateral resolution. The array elements also had small surface area and therefore less total energy transmission capability, which is problematic for the

inspection of highly attenuating media such as HDPE.

8.3.2 Imaging technique

The imaging technique is that of [5] described in chapter 7, which implements total focusing [6].

8.4 Method

The method given here includes the manufacture of a HDPE test block, the experimental setup used to acquire the data, and the approach to ultrasonic imaging.

8.4.1 HDPE test block manufacture

First, a test block is cut from a HDPE pipe, retaining the circumferential, axial, and radial orientations of the pipe, as shown in figure 8.1. Next, side-drilled holes are machined into the wall of the test block, again seen in the figure. The surface is smoothed to best represent HDPE pipe outer surfaces. Last, waterproof tape is applied to the SDH ends to maintain an air-filled volume, as would be present in volumetric HDPE pipe joint defects. The HDPE pipe test block with waterproof tape and smoothed outer sufrace is photographed in figure 8.2.

8.4.2 Immersion setup

The immersion setup used is depicted in figure 8.1. It shows angled ultrasonic array inspection of the HDPE pipe block where the array is offset from the SDHs, marked by the solid circles, and the array face and HDPE block are immersed in water. The array elements are the circles, which are separated by a pitch, p, and active aperture, A. The base height of the array is h, the array is offset axially from the fusion face by standoff, s, and the wall thickness between the outer and inner wall of the HDPE pipe is w. The array is angled at θ_1 from normal to the pipe outer wall. The angle at which the maximum amplitude of the ultrasound propagates in the HDPE pipe is θ_2, and this varies a little because of the minor frequency-dependent of ultrasonic bulk longitudinal phase velocity in HDPE pipe material [2]. This is depicted at half, once, and twice the centre frequency to show the dispersiveness of

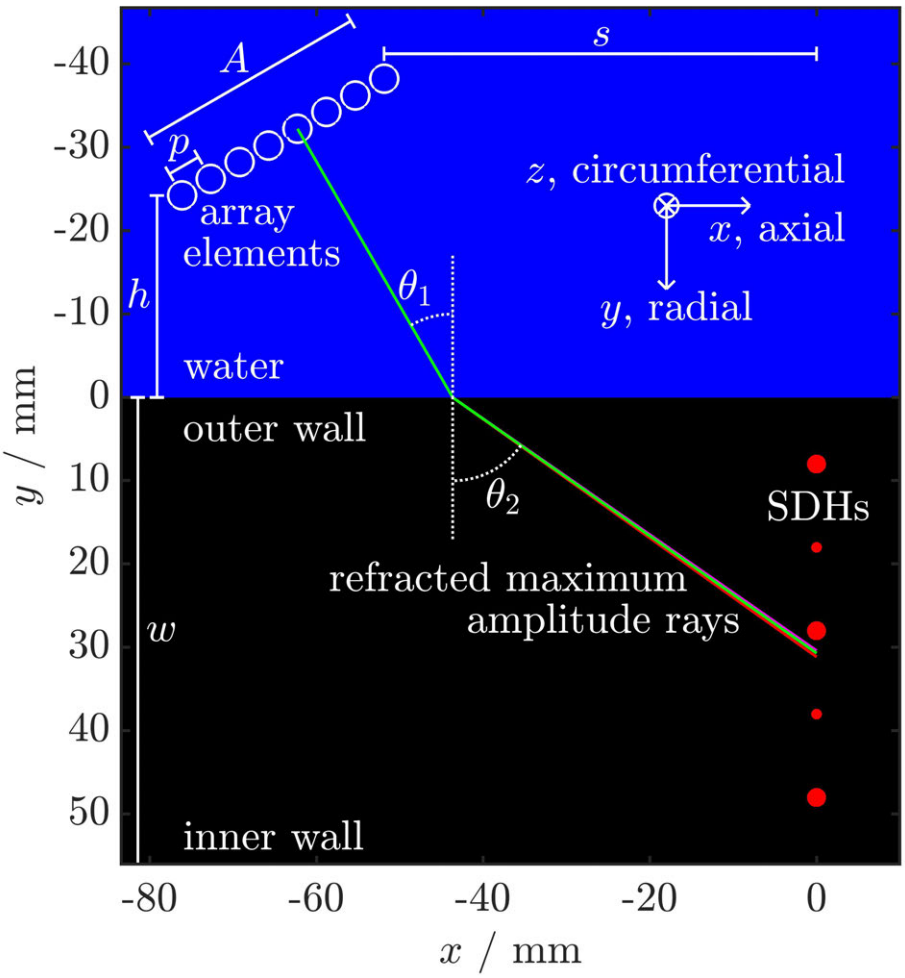

Figure 8.1: Angled ultrasonic binary array inspection of the HDPE pipe block where the array is offset from the SDHs, marked by the solid circles, and the array face and HDPE block are immersed in water. The array elements are the circles, which are separated by a pitch, p, and have an active aperture, A. The base height of the array is h, the array is offset axially from the fusion face by standoff, s, and the wall thickness between the outer and inner wall of the HDPE pipe is w. The array is angled at θ_1 from normal to the pipe outer wall. The angle at which the maximum amplitude of the ultrasound propagates in the HDPE pipe is θ_2. This is depicted at half, once, and twice the centre frequency to show the dispersiveness of the medium; the angle at $f_0/2$, f_0, and $2f_0$ are respectively the bottom, middle, and top rays.

the medium; the angle at $f_0/2$, f_0, and $2f_0$ are respectively the bottom, middle, and top rays.

8.4.3 Imaging method

The imaging technique of [5] described in chapter 7 is applied to the ultrasonic waveform full matrix data. Also, the pulse specification (PS) noise reduction method of [8] is applied to images of the SDHs in the HDPE pipe block. For comparison,

Figure 8.2: HDPE pipe test block SDHs, waterproof tape covering their air gaps, and smoothed outer surface.

an ultrasonic image obtained without the interface refraction and transmission improvements of MBim and PS noise reduction is also provided.

A threshold of -30dB is applied to all images to represent moderately high SNR. SNR improvements would be expected with an optimum array controller and array for the inspection of highly attenuating media, such as HDPE.

8.5 Results

Analysed here is first the angled immersion ultrasonic binary array image of the HDPE pipe test block obtained without the interface refraction and transmission improvements of MBim and without PS noise reduction, then, with the latter, and last, with both.

In figure 8.3, the top SDH, and the two SDHs below it, are partially distinguishable from the noise with -30dB thresholding. The fourth SDH has very low SNR and

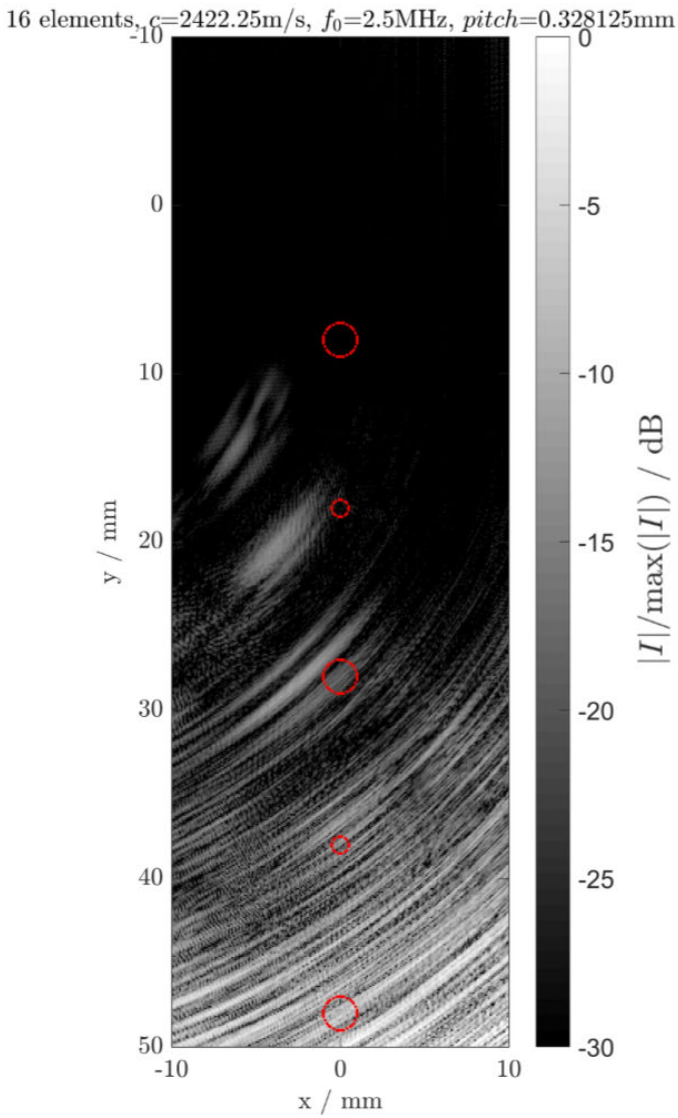

Figure 8.3: Angled immersion ultrasonic binary array image of the HDPE pipe test block obtained without the interface refraction and transmission improvements of MBim and without PS noise reduction. The circles mark the SDHs. These span the full wall thickness, w of the HDPE pipe test block.

the fifth is not discernible. However, the higher defects, at higher inspection angles, are imaged increasingly far to the left of the SDHs without MBim refraction and transmission corrections. Lateral defect resolution is expectedly low.

In figure 8.4, where PS noise reduction is implemented, the SNR of all SDHs increases. The top three SDHs are visible with high SNR. The fourth is possibly present, but with low SNR. The fifth is not discernible. Again, the lack here of refraction and transmission corrections result in skewed defect signatures relative to their locations. The later resolution remains low.

In figure 8.5, where MBim refraction and transmission corrections and PS noise

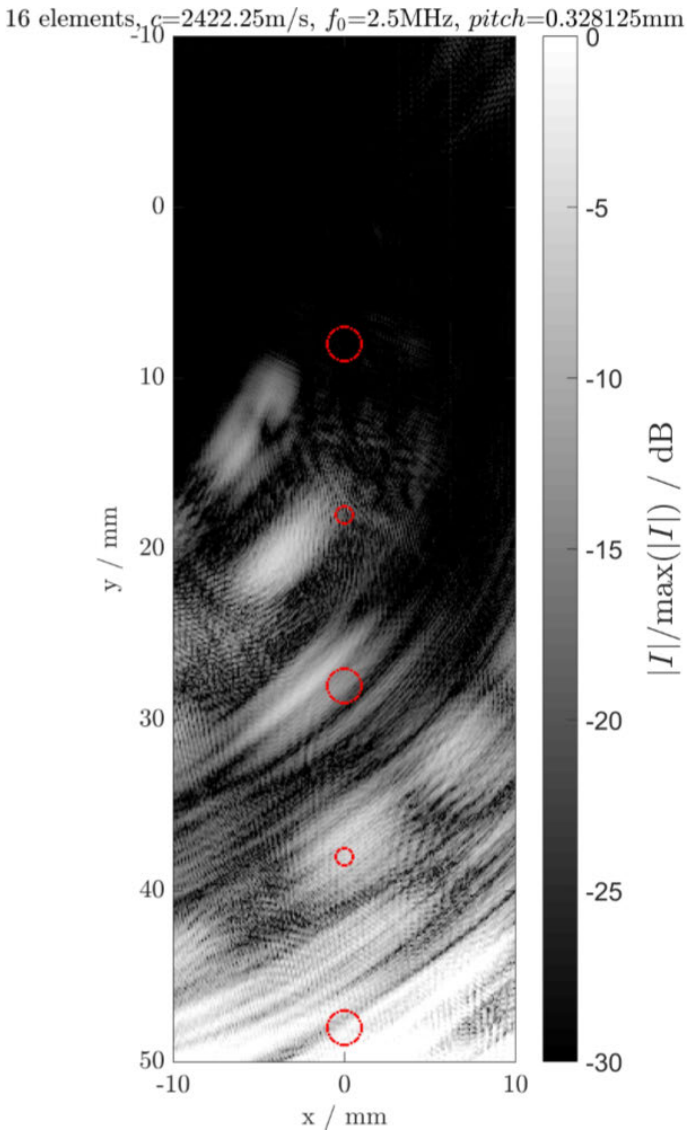

Figure 8.4: Array image of the test block obtained without the interface refraction and transmission improvements of MBim but with PS noise reduction.

reduction are implemented, for the top three SDHs there is similar SNR to the case without refraction and transmission corrections but with PS noise reduction shown in figure 8.4, but the fourth defect signature is more localised. The fifth remains undetected. While the lateral resolution remains inherently low, the SDHs are now located with high accuracy. Consequently, such a NDE inspection of a HDPE pipe joint for fusion interface defects would be able to sentence such defects with higher probability of detection.

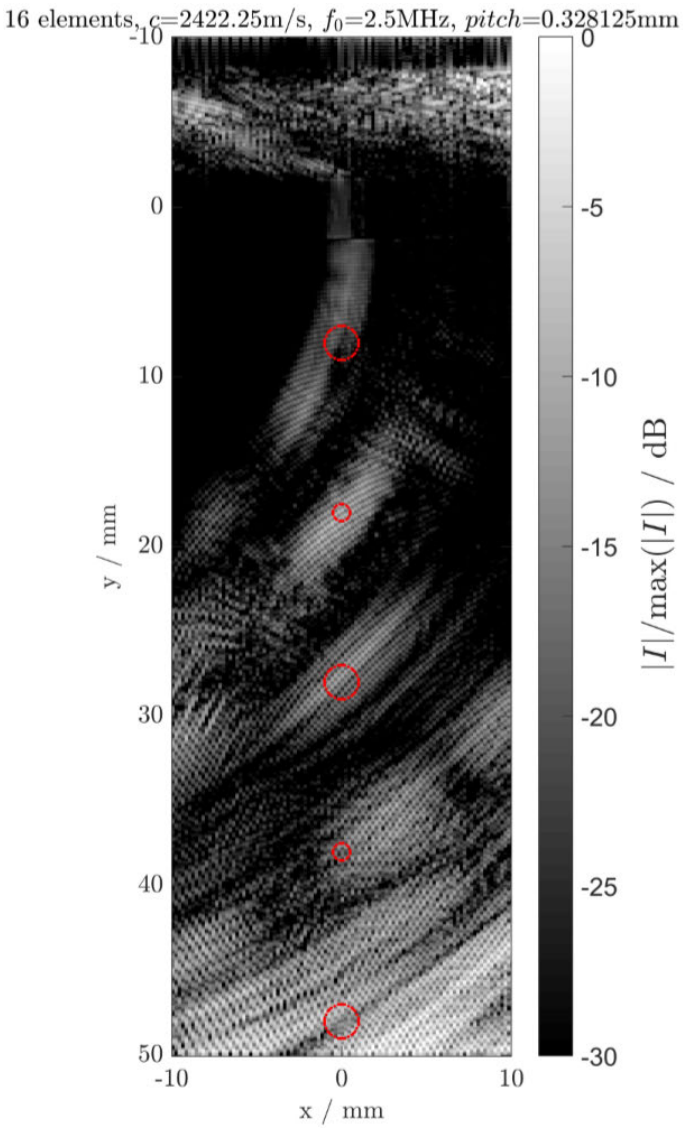

Figure 8.5: Array image of the test block obtained with the interface refraction and transmission improvements of MBim and with PS noise reduction.

8.6 Conclusions

Angled ultrasonic array imaging of vertically aligned side-drilled holes in a high-density polyethylene (HDPE) pipe test block using an experimental binary array controller is conducted, with moderate defect detection potential, high detected defect location potential, and moderate detected defect sizing and characterisation potential, for necessarily full through wall depth coverage. This is done with the multiband waveform simulation and imaging (MBim) method and pulse specification (PS) noise reduction method. The used experimental binary coded sequence array controller and array setup then had suboptimal lateral resolution and energy input

capabilities, so higher defect sizing and characterisation capabilities could otherwise also be expected from these results.

References

[1] J. Isla and F. Cegla, *The use of binary quantization for the acquisition of low SNR ultrasonic signals: a study of the input dynamic range*, Ultrasonics, Ferroelectrics, and Frequency Control, IEEE Transactions on, **63**(9), 1474-1482 (2016).

[2] E. Lopez Villaverde, S. Robert, and C. Prada, *High-frequency total focusing method (TFM) imaging in strongly attenuating materials with the decomposition of the time reversal operator associated with orthogonal coded excitations*, AIP Conference Proceedings 1806, 040002 (2017).

[3] E. Lopez Villaverde, S. Robert, and C. Prada, *Ultrasonic imaging in highly attenuating materials with Hadamard codes and the decomposition of the time reversal operator*, Ultrasonics, Ferroelectrics, and Frequency Control, IEEE Transactions on, **64**(9), 1336-1344 (2017).

[4] G.D. Connolly, M.J.S. Lowe, J.A.G. Temple, and S.I. Rokhlin, *The application of Fermat's principle for imaging anisotropic and inhomogeneous media with application to austenitic steel weld inspection*, Proc. R. Soc. A, **465**, 34013423 (2009).

[5] J.S. Egerton, M.J.S. Lowe, J. Jian, and P. Huthwaite, *Numerical simulation of ultrasonic NDE of sound-damping materials using a multiband time domain approach*, Ultrasonics. [Pre-submission]

[6] J. Zhang, B.W. Drinkwater, P.D. Wilcox, and A.J. Hunter, *Defect detection using ultrasonic arrays: The multi-mode total focusing method*, NDT&E International **43**, 123-133 (2010).

[7] J.S. Egerton, M.J.S. Lowe, H.V. Halai, and P. Huthwaite, *Ultrasonic attenuation*

and phase velocity in high-density polyethylene (HDPE) pipe material, J. Acoust. Soc. Am. **141**(3), 15351545 (2017).

[8] J.S. Egerton, M.J.S. Lowe, and P. Huthwaite, *Automated and antidispersive coherent and incoherent noise reduction of waveforms that contain a reference signal*, The Journal of Sound and Vibration, [Under final review]. [Open Access to be made available]

Chapter 9

Optimum ultrasonic array and water-filled wedge specifications for HDPE pipe joint inspection

9.1 Abstract

Detailed here are guidelines for the optimisation of the HDPE pipe joint angled ultrasonic array inspection standoff – distance from the front array element to the fusion face – for an industrially relevant range of inspection temperatures, ultrasonic frequencies, and pipe wall thicknesses with their corresponding target depths through the pipe wall and water-filled wedge angles. The necessary user input parameters for such are specified and shown in figure 9.1 for this HDPE pipe joint inspection configuration.

9.2 Introduction

Long axial distance inspections, using guided waves have previously been considered for HDPE pipe joint inspections [1]. As described in chapter 1, this method has low resolution and signal-to-noise ratio (SNR) relative to bulk wave ultrasonic array inspection of HDPE pipe joints, exemplified in figure 9.1. However, the ultrasonic array should not be positioned directly over the fusion face, because there the array cannot cleanly transmit or receive ultrasound through the surface profile variation caused by the existence of a bead or debeaded region. The bead is a ridge where

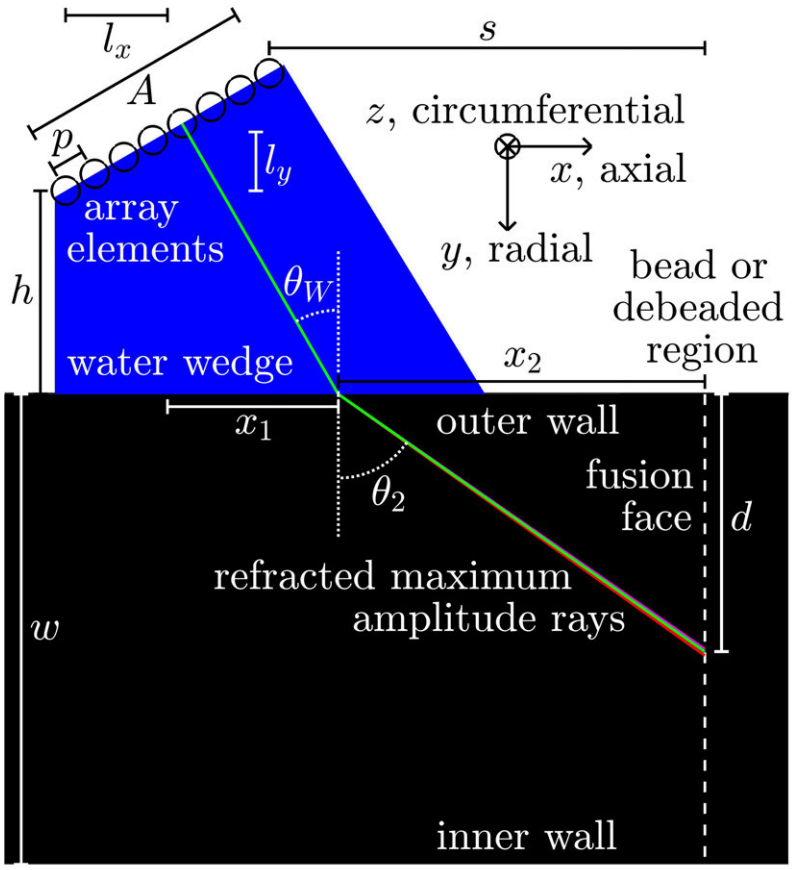

Figure 9.1: Angled ultrasonic array inspection of HDPE pipe heat fused joints where the array is offset from the bead or debeaded region of the joint and the array is mounted on an angled, water-filled wedge directed towards the heat fusion face of the joint. The array elements are the circles, which are separated by a pitch, p, and active aperture, A. The base height of the water wedge is h, the array is offset axially from the fusion face by standoff, s, the wall thickness between the outer and inner wall of the HDPE pipe is w, and the radial depth on the fusion face of the target region is d. The water wedge is angled at θ_W from normal to the pipe outer wall. The angle at which the maximum amplitude of the ultrasound propagates in the HDPE pipe is θ_2. This is depicted at half, once, and twice the centre frequency to show the dispersiveness of the medium; the angle at $f_0/2$, f_0, and $2f_0$ are respectively the bottom, middle, and top rays.

melted material cooled after being squeezed from the heat fused joint. The two pipe ends contract during cooling, more so around the bead than the nearby pipe material, thus forming two dips adjacent to the bead. These dips, or troughs, prevent most ultrasonic transmission and reception. Even when the bead has been removed to leave a flat region, there is still likely to be imperfection, or surface roughness, which will be highly problematic for ultrasound transmission. For these reasons ultrasonic inspection normal to fusion face is highly impractical.

An array normal to the fusion face, but offset adjacently, along the length of the pipe, can achieve some fusion joint coverage, but high inspection angles, near the outer wall of the pipe, shown in figure 9.1, would receive very little ultrasound bulk longitudinal wave energy, due to the directionality of the array elements. Also, shear wave types are extremely highly attenuated in viscoelastic media, such as HDPE [3], such that they propagate only the shortest of distances and are impractical for ultrasonic inspection, for example, using surface waves. Such surface waves signals would also be inherently coincident with the joint bead or debeaded signal, and therefore defects would be difficult to detect using surface waves.

Therefore, inspection with a wedge is considered the best available option. However, shallow angle wedges with wedge angle, $\theta_W < 21^\circ$ for a water-HDPE interface, are subject to multiple reverberation from array to material face and back again. Consequently, such shallow inspection angles result in long durations before ultrasonic signals can be received, after these reverberations subside, from external inspected regions.

Concerning wedge material, conventionally used polymers have a similar ultrasound phase velocity to HDPE. This means the wave would not be refracted forwards towards the fusion face, but instead propagate with little deviation. There would be low ultrasound energy at high angles of inspection in this low refraction scenario, and, therefore low defect detection probability for the full joint region. Conversely, a water-filled wedge may be used, as is done here and in similar industrial inspections. This results in the required ultrasound steering and high area coverage of the fusion joint. This approach should give a high probability of detection for fusion face defects.

9.3 Theory

The refraction angle in HDPE, θ_2, is determined using the ultrasound bulk longitudinal phase velocities at a given frequency in water and HDPE, respectively $v_{p,1,2}$, and the wedge angle, θ_W, with Snell's law,

$$k_1 \sin\theta_W = k_2 \sin\theta_2, \tag{9.3.1}$$

where the real components of the dispersion relations, $k_{1,2}$, are inversely proportional to the velocities, $v_{p,1,2}$, in each medium. These dispersion relations vary significantly with frequency and temperature, in HDPE pipe material [2], while the bulk longitudinal phase velocity varies little with frequency, as described above.

9.4 Method

The method for obtaining the optimum HDPE pipe joint angled ultrasonic array inspection standoff, s, which is the distance from the front array element to the fusion face, is given here. The necessary user input parameters for such are shown in figure 9.1. First, because shallow inspection angles, $\theta_W < 21°$ for a water-HDPE interface, result in multiple wedge reverberations, this optimum standoff algorithm warns users against input of wedge angles below this threshold with a conditional if-statement in the algorithm that seeks angles below said threshold.

The optimisation is conducted for the paths through each medium over which the peak amplitude of the wave propagates along, the 'ray path' of the wave. This is done at centre frequency, f_0, as well as at half and double this frequency, as shown in figure 9.1, illustrating the wave dispersion of these components. This shows, using the acoustic properties of HDPE [2], that there is low bulk wave dispersiveness in HDPE.

Next is a list of configurable array and wedge parameters. The number of array elements, N_{el}, may be specified by the user; the pitch, p, or spacing between adjacent array elements is also specified by the user; and the array active aperture is set from the former two parameters,

$$A = N_{el}p. \tag{9.4.1}$$

The base height of the array, h, is chosen by the user, which is the radial distance from the bottom of the wedge to the centre of the array element closest to the base. Last, the water-filled wedge angle, θ_W, is chosen by the user.

Concerning the targetted region of the fusion face, there exists low sound energy at high angles of refraction and therefore at regions of the fusion face near the outer wall of the HDPE pipe. Also, ultrasound amplitude decays exponentially with wave

propagation distance and is therefore lower at the fusion face near the inner wall of the HDPE pipe. These effects are opposing and are known to be of similar order. Consequently, the target depth, d, within the fusion face should be specified by the user to be half radial depth through the wall thickness, w, for the highest probability of detection for full joint coverage.

Below is the algorithm used to obtain the optimum standoff, s, for inspection of HDPE pipe joints. It is seen in figure 9.1 that the centre of the array is a distance $A/2$ from elements at either end of the array. This location is defined here to be an axial distance left of the array element that has least axial distance, s, from the fusion face,

$$l_x = \frac{A}{2} \cos \theta_W. \tag{9.4.2}$$

This location is also defined here to be a radial height above the array element that has least radial distance, h, from the interface,

$$l_y = \frac{A}{2} \sin \theta_W. \tag{9.4.3}$$

It is seen in the figure that the axial projections of the two ray paths are x_1 and x_2, within the wedge and the pipe respectively. Summing these yields the distance of the centre of the array from the fusion face,

$$x_1 + x_2 = s + l_x. \tag{9.4.4}$$

The axial distance between the centre of the array and this intersection point, trigonometrically, is

$$x_1 = (h + l_y) \tan \theta_W, \tag{9.4.5}$$

The axial distance between this intersection point and the fusion face, trigonomet-

rically, is

$$x_2 = d \tan \theta_2, \tag{9.4.6}$$

where θ_2 is found using equation (9.3.1). Consequently, the standoff, s, is obtained through combination of equations (9.4.4) to (9.4.6); equation (9.4.4) may be restated as follows,

$$s = x_1 + x_2 - l_x. \tag{9.4.7}$$

The above approach has aided the design of two optimum ultrasonic arrays for the inspection of the fusion joints of small-to-medium and medium-to-large wall thickness, w, HDPE pipes, as well as an optimum water-filled wedge, with Imasonic SAS, France. Below, the above algorithm is deployed for industrially relevant pipe wall thicknesses, w, and therefore half wall thickness target depths, d, to provide guidelines for the optimum standoffs, s, at which to inspect HDPE pipe joints.

9.5 Results

The optimum pitch, p, should be of the order of half a wavelength at centre frequency, λ_0, to avoid unwanted wave diffraction known as grating lobes [4]. For example, for a centre frequency of $f_0 = 2.25$MHz the ultrasonic bulk longitudinal wavelength is $\lambda_0 = 1.08$mm, leading to a suggested maximum pitch of $p = 0.54$mm. The pitch, $p = 0.5$mm, used below and in the arrays designed and built with Imasonic SAS, adhere to this condition.

The optimum standoffs, s, for HDPE pipe joint inspection are given here for a range of potential inspection temperatures, ultrasonic frequencies, and half wall thickness target depths, d, for typical pipe wall thicknesses used in industry, w. The array and wedge parameters are chosen to be $p = 0.5$mm, $N_{el} = 64$, $A = 32$mm, $\theta_W = 30°$,

and $h = 23.4$mm. Consequently, the uncertainty of optimum standoffs is,

$$\epsilon_s = \mathrm{E}(s)\epsilon_{v_p}, \tag{9.5.1}$$

where E(s) is the expected value of the standoff, and the attenuation and phase velocity fractional uncertainties are found in [2] and chapter 2.

The guideline standoffs for 5°C increments from 5°C to 40°C, for centre frequencies $f_0 = 1, ..., 5$MHz, and for a small wall thickness pipe with radial target depth, $d = 13$mm, are given in table 9.1. The optimum standoff uncertainty is $\epsilon_s = 0.4$mm.

T/°C f/MHz	1	2	3	4	5
5	25.2	25.4	25.6	25.6	25.7
10	24.4	24.7	24.8	24.9	24.9
15	23.6	23.9	24.0	24.1	24.1
20	22.7	23.0	23.1	23.2	23.2
25	21.8	22.1	22.2	22.3	22.4
30	21.0	21.3	21.4	21.5	21.5
35	20.3	20.6	20.7	20.8	20.8
40	19.7	20.0	20.1	20.2	20.2

Table 9.1: Optimum wedge standoffs, s, in millimetres, for HDPE pipe joint inspection at a target depth of $d = 13$mm, for a range of inspection temperatures and ultrasonic frequencies. The array and wedge parameters are chosen to be $p = 0.5$mm, $N_{el} = 64$, $A = 32$mm, $\theta_W = 30°$, and $h = 23.4$mm. Therefore, the optimum standoff uncertainty is $\epsilon_s = 0.4$mm.

As can be seen in table 9.1, and is shown in figure 9.2, when the phase velocity of HDPE is higher and therefore further from that of water – at low temperatures and high frequencies – the required standoff increases. This can be significant when velocity variation is high for a give step in frequency or temperature, which occurs for low values of both parameters. Consequently, a high standoff is required to achieve full joint coverage at low temperatures or higher ultrasonic frequencies.

Next, the guideline standoffs for a medium wall thickness pipe with radial target depth, $d = 28$mm, are given in table 9.2. The optimum standoff uncertainty is $\epsilon_s = 0.7$mm. The conclusions for the small wall thickness pipe hold for this medium wall pipe.

Last, the guideline standoffs for a large wall thickness pipe with radial target depth, $d = 50$mm, are given in table 9.3. The optimum standoff uncertainty is $\epsilon_s = 1.2$mm. The conclusions for the small and medium wall thickness pipes hold for this large

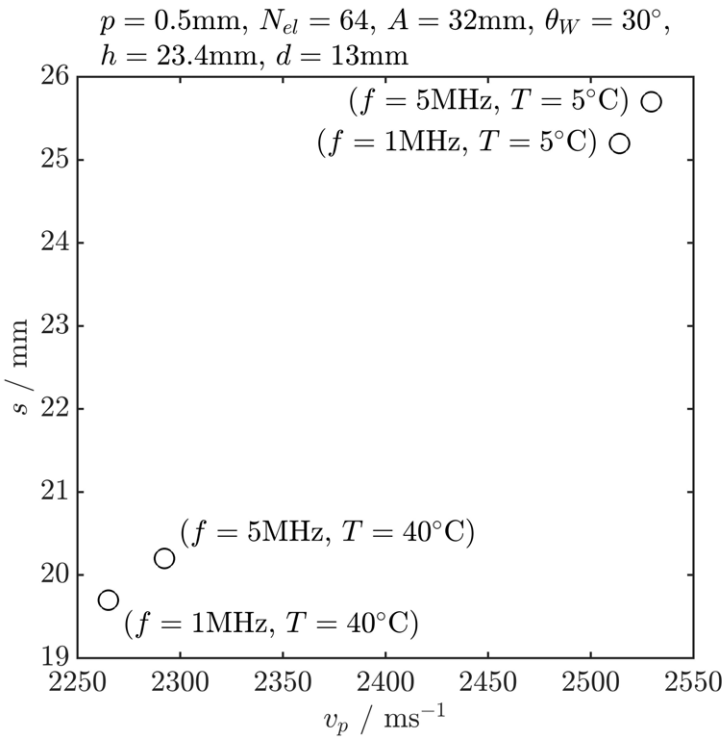

Figure 9.2: Ultrasonic bulk wave phase velocity, v_p, at low and high frequencies, f, and low and high temperatures, T, and the corresponding changes in standoff, s for target depth, $d = 13$mm.

T/°C f/MHz	1	2	3	4	5
5	49.3	49.9	50.2	50.3	50.3
10	47.7	48.3	48.6	48.7	48.8
15	45.9	46.5	46.8	46.9	47.0
20	44.0	44.6	44.9	45.0	45.1
25	42.1	42.7	43.0	43.1	43.2
30	40.4	41.0	41.2	41.4	41.5
35	38.9	39.4	39.7	39.8	39.9
40	37.6	38.1	38.4	38.5	38.5

Table 9.2: Optimum wedge standoffs, s, in millimetres, for HDPE pipe joint inspection at a target depth of $d = 28$mm, for a range of inspection temperatures and ultrasonic frequencies. The optimum standoff uncertainty is $\epsilon_s = 0.7$mm and all other parameters are the same as for table 9.1.

wall pipe.

9.6 Conclusions

Guidelines for the optimum inspection of HDPE pipe joint fusion face defects using an ultrasonic array and water-filled wedge are provided. The distance of the front of the array from the fusion face, known as the standoff, is given for an indus-

T/°C f/MHz	1	2	3	4	5
5	84.7	85.8	86.2	86.4	86.5
10	81.8	82.9	83.3	83.6	83.7
15	78.6	79.7	80.2	80.4	80.6
20	75.2	76.3	76.8	77.0	77.2
25	71.9	72.9	73.4	73.7	73.8
30	68.8	69.8	70.3	70.5	70.7
35	66.1	67.1	67.5	67.8	67.9
40	63.7	64.1	65.1	65.4	65.5

Table 9.3: Optimum wedge standoffs, s, in millimetres, for HDPE pipe joint inspection at a target depth of $d = 50$mm, for a range of inspection temperatures and ultrasonic frequencies. The optimum standoff uncertainty is $\epsilon_s = 1.2$mm and all other parameters are the same as for tables 9.1 and 9.2.

trially relevant range of inspection temperatures, ultrasonic frequencies, and pipe wall thicknesses with their corresponding target depths through the pipe wall and water-filled wedge angles.

References

[1] C.W. Chan, *The Ultrasonic Nondestructive Evaluation of Welds in Plastic Pipes*, Ph.D. Thesis, Imperial College London, London, March 1996.

[2] J.S. Egerton, M.J.S. Lowe, H.V. Halai, and P. Huthwaite, *Ultrasonic attenuation and phase velocity in high-density polyethylene (HDPE) pipe material*, J. Acoust. Soc. Am. **141**(3), 15351545 (2017).

[3] J. Wu, *Determination of velocity and attenuation of shear waves using ultrasonic spectroscopy*, J. Acoust. Soc. Am. **99**(5), 28712875 (1996).

[4] W.F. Kremkau and K.J. Taylor, *Artifacts in ultrasound imaging*, J. Ultrasound Med., 227-237 (1986).

Chapter 10

Conclusions

Here is the review of outcomes of this Engineering Doctorate (EngD) project that are provided in this thesis and potential future works that could be conducted to advance this area of research.

10.1 Thesis Review

The aim of the project was to improve the ultrasonic array inspection of high-density polyethylene (HDPE) heat-fused pipe joints of cooling water pipework that is installed in EDF Energy's nuclear power stations. Whereas ultrasound array inspection is now established for safety-critical metal components, HDPE poses a hugely challenging problem, that the ultrasound waves are heavily attenuated by the material. This impacts multiple aspects of the inspection and of the modelling that is needed to design and qualify inspection. The thesis reports a range of research that was needed to overcome this challenge.

Within the thesis, first accurate acoustic properties of HDPE were obtained that are necessary for improved simulated or real ultrasonic array imaging of HDPE pipe joints. Accuracy of a few percent has been achieved here. Next in the thesis, a simulation technique has been developed for representing ultrasound in such inspections that has both high accuracy and efficiency. Further, analytical analysis of ultrasound scattering from cylindrical voids from elastic media has been extended to general, attenuative media, as well as provided a new method for image recon-

struction of said cylinders. Also, the Huygens-Fresnel principle has been used to represent ultrasound scattering from volumetric and planar voids, to image sub-wavelength features of these defects in an ideal circular array setup, and to image angled ultrasonic array nondestructive evaluation (NDE) of potential defects occurring in HDPE pipe joints. An automated and antidispersive system for reducing coherent and incoherent noise in waveforms with an isolated wave reflection signal has been devised. An imaging and analysis method for ultrasonic array NDE that can represent defects in a refractive, reflective, and scattering environment in attenuating media, which is applied to data from the above developed simulation technique has been produced. The work of the thesis applied much of the above imaging and analysis method to defects machined into HDPE pipe material, with an experimental ultrasonic array controller, yet with an array of limited suitability. Last, parameters have been specified for ultrasonic arrays and a water-filled wedge, which are optimum for HDPE pipe joint inspection, and have been designed and built by Imasonic SAS, France, for research use at Imperial College London.

10.2 Main Findings

The main findings from the project are provided here on a chapter-by-chapter basis, excepting the first chapter, which comprises an introduction and review of existing literature, and the tenth and final chapter that is this chapter, which provides conclusions.

The acoustic properties of HDPE pipe joints are obtained to provide improved accuracy and efficiency of interpretation and calibration of real ultrasonic NDE data, as well as to provide a necessary foundation for accurate simulation and modelling of ultrasonic NDE of HDPE pipe joints. Accuracy of a few percent has been achieved here. These acoustic properties have been used in all simulations throughout this project.

Conventional time domain finite element (FE) and conventional frequency domain FE simulation techniques could not provide such benefits as high computational accuracy, efficiency, and large model size. To do so, the multiband finite element (MBFE) modelling technique is developed. Comprising so few as three time domain simulations, MBFE provides ultrasonic simulation accuracy improvements of factors from approximately 1.5 to 10 over one time domain FE simulation, as has been

demonstrated in HDPE for a computational duration a few times that of a time domain finite element simulation.

In the consideration of a breadth of simulation techniques, within the categories of FE and analytical, analytical ultrasonic scattering from a cylindrical void is implemented for simulated elastic media and generalised to viscoelastic media to provide alternative and efficient accurate analytical simulation of such scattering in HDPE pipe material. A new method for image reconstruction of such scatterers is shown to be effective for the cylindrical geometry found in this idealised ultrasonic transmit-receive configuration, where waves propagate to and from the scatterer at all angles.

In further consideration of analytical approaches for the accurate and efficient simulation of ultrasonic scattering in viscoelastic media such as HDPE pipe material, the Huygens-Fresnel principle is used to represent ultrasound scattering from volumetric and planar voids. This is therefore more general than prior analysis of scattering from cylindrical voids. With an ideal circular arc distribution of ultrasonic transmitters and receivers around the scatterer, imaging of sub-wavelength features of the defects in HDPE pipe material, or scatterers, is conducted that is representative of those that could be found during real ultrasonic NDE of HDPE pipe joints.

For highly attenuating media such as HDPE pipe material, the signal-to-noise ratio of received ultrasonic NDE waves can be undesirably low. Consequently, an automated and antidispersive system for reducing coherent and incoherent noise in waveforms with an isolated wave reflection signal is developed. For incoherent noise in HDPE and for coherent noise in a large grained metal alloy, improvements in signal-to-noise ratio (SNR) of factors of approximately 5 and 3 are demonstrated relative to unprocessed waveforms and waveforms with an optimised frequency filtering technique.

Imaging of potential defects is fundamental in much accurate and reliable ultrasonic NDE, including when using array technology, as is done for HDPE pipe joint inspection. Further, accurate and reliable simulation of the data acquisition and imaging of HDPE pipe joints can demonstrate capability in potential defect detection, location, sizing, and characterisation of defect type when validated by equivalent and comparable real ultrasonic array NDE. With this method, simulated planar and volumetric defects in HDPE pipe joints are demonstrated as potentially detectable and sizeable through pipe wall thicknesses of up to 100mm and defect sizes down to a few millimetres or less.

Development of ultrasonic array data acquisition and imaging of HDPE pipe material that contains representative potential defects, and that contains machined standard geometries, such as side-drilled holes and notches, is provided. This is conducted with available, limited suitability hardware but still assists in the validation of the simulation and imaging techniques of this project. For example, despite the limited suitability of the data acquisition hardware, volumetric defects in HDPE pipe material are demonstrated as detectable through pipe wall thicknesses up to 56mm and defect sizes down to a millimetre or less. These are also located with millimetre accuracy when the developed imaging refraction correction is implemented. For the ultrasonic array NDE of HDPE pipe joints where a water-filled wedge is used to direct the ultrasound towards the HDPE pipe joint, by existing or newly developed techniques, provided here are optimum distances of the wedge from the HDPE pipe fusion joint for realistic temperatures and frequencies. From this optimisation method, arrays and a water-filled wedge have been designed and built by Imasonic SAS, France, for research use at Imperial College London.
Each area of study in this thesis provides advancements for the ultrasonic inspection of highly attenuating media and for the ultrasonic array NDE of HDPE pipe joints.

10.3 Future work

Outlined here are aspects of the project the author thinks would benefit from future research work.
The overall goal of this future work would be to improve the ultrasonic inspection of highly attenuating media through further research into simulation techniques for ultrasonic waves in said media. The NDE of HDPE pipe joints should be advanced through inspection simulations and laboratory-based feasibility studies, leading towards the demonstration of a site-ready, advanced ultrasonic HPDE pipe joint imaging system.

10.3.1 Potential approaches to future work

While the potential of ultrasonic inspection of highly attenuating media has been advanced very significantly by the original work in multiple topics reported in this thesis, improvement is always possible, both in the implementation of new techniques

and in the optimisation of these techniques towards industrial goals.

Consequently, in advancement of the simulation tool that has arisen from the work in this thesis, which describes ultrasonic waves in viscoelastic media and their interaction with heterogeneities in said media, it would be beneficial to develop user-friendly software tools that make this simulation tool more readily accessible. Also, the improved quantification of imaged defect detectability would be worthwhile to pursue. This could involve sentencing through four quantifiable themes: defect detection, location, sizing, and characterisation. Detection capability may be quantified with receiver operating characteristic (ROC) curves, location with the detection of defect maxima applied to defect images or waveforms, sizing with the analysis of ultrasonic amplitude obtained from the defect, and characterisation through the analysis of defect structure and comparison with a known defect library. The sentencing of these four nondestructive evaluation (NDE) quantities may be conducted visually by an operator or partially automated with algorithms. The four NDE quantities should be sought with increased accuracy in future work and the provided methods for sentencing should be further validated and improved through scientific procedure. A defect library should be built for representative defects in relevant NDE scenarios such as the ultrasonic inspection of HDPE pipe joints.

A presently underexploited technique in NDE is data fusion. Data from all sources can provide a more precise quantification of the four NDE quantities detailed above. For the example of linear ultrasonic array inspection, the multiple images obtained in a set of data acquisitions, such as when moving on a scanning frame with encoded location around the circumference of a pipe, may readily be summed to create a three dimensional image of the inspected volume. This is very data efficient when compared with using matrix (two-dimensional) ultrasonic arrays that acquire data at each inspection location and it should yield a comparable three-dimensional image of the inspected volume.

The NDE procedures of existing HDPE pipe joint inspection could be updated to include a temperature measurement, such that temperature correction, using the methods and data of this thesis, can be applied to the ultrasonic data interpretation obtained in routine inspections. The procedure could also be updated to have required distances of the array from the HDPE pipe joint that are based on the methods and data of this thesis.

The work and progress of this thesis should be continued on an academic and re-

search level, in close collaboration with industrial partners, such that the aim of improved ultrasonic inspection of highly attenuating media, and of HDPE pipe joints, should be achieved.

List of Publications

[P1] J.S. Egerton, M.J.S. Lowe, H.V. Halai, and P. Huthwaite, *Improved FE simulation of ultrasound in plastics*, AIP Conference Proceedings 1706, 120001 (2016).

[P2] J.S. Egerton, M.J.S. Lowe, H.V. Halai, and P. Huthwaite, *Ultrasonic attenuation and phase velocity in high-density polyethylene (HDPE) pipe material*, J. Acoust. Soc. Am. **141**(3), 1535-1545 (2017).

[P3] J.S. Egerton, M.J.S. Lowe, H.V. Halai, and P. Huthwaite, *A multiband approach for accurate numerical simulation of frequency dependent ultrasonic wave propagation in the time domain*, J. Acoust. Soc. Am. **142**(3), 1270-1280 (2017).

[P4] J.S. Egerton, M.J.S. Lowe, and P. Huthwaite, *Automated and antidispersive coherent and incoherent noise reduction of waveforms that contain a reference signal*, The Journal of Sound and Vibration, [Under final review].

[P5] J.S. Egerton, M.J.S. Lowe, J. Jian, and P. Huthwaite, *Analytical multiband finite element waveform simulation and imaging (MBim) of ultrasonic scattering, refraction, and reflection*, [Pre-submission].

[P6] J.S. Egerton, M.J.S. Lowe, J. Jian, and P. Huthwaite, *Analytical simulation of ultrasonic scattering from heterogeneities using the Huygens-Fresnel principle, with image reconstruction of sub-wavelength features*, [Pre-submission].